Deterministic Approach to Polarization Mode Dispersion

by

Poh-Boon Phua

Submitted to the Department of Electrical Engineering and Computer Science
in partial fulfillment of the requirements for the degree of

Doctor of Philosophy

at the

MASSACHUSETTS INSTITUTE OF TECHNOLOGY

August 2004

Author . . . .
Poh-Boon Phua
Department of Electrical Engineering and Computer Science
August 18, 2004

Certified by . . . .
Erich P. Ippen
Elihu Thomson Professor of Electrical Engineering, Professor of Physics
Thesis Supervisor

Accepted by . . . .
Arthur C. Smith
Chairman, Department Committee on Graduate Students

Deterministic Approach to Polarization Mode Dispersion

by

Poh-Boon Phua

Submitted to the Department of Electrical Engineering and Computer Science
on August 18, 2004, in partial fulfillment of the
requirements for the degree of
Doctor of Philosophy

Abstract

Polarization Mode Dispersion (PMD) is considered to be one of the most serious obstacles in the high speed optical telecommunication systems. This thesis focuses on a deterministic approach to both compensation and emulation of PMD. Most PMD compensation schemes in the literature rely on feedback loops to search for the optimum control parameters in the compensator. These schemes often suffer from slow response time and are limited to compensating the low orders of PMD. Adding control parameters to enable higher-order PMD compensation further increases the complexity of the feedback algorithm and its response time. As PMD can vary as fast as on a millisecond time scale, a potential method to alleviate this problem is to employ a deterministic approach to PMD compensation where the PMD parameters are first diagnosed and the compensator then set accordingly.

One of the most challenging problems to this deterministic approach is the real-time monitoring of the PMD information. We propose an improved version of the PMD estimation technique using polarization scrambling and optical filtering. Once the PMD parameters are characterized, for first order PMD compensation, we present a novel module that can produce variable Differential Group Delay (DGD) without any second order PMD. We also discuss a feed-forward PMD compensator for first and second order PMD compensation. To allow for hybrid feed-forward and feedback PMD compensation scheme, we propose to decouple the first and second order PMD compensation by using a module that produces variable second order PMD without any first order PMD. To extend the compensation to all orders of PMD, instead of concatenating birefringent segments, we look into a compensator that is based on four stages of flexible frequency-dependent polarization rotations. These stages can be implemented using polarization beam splitting in combination with spatial light modulators or all-pass filters. For transmission systems where Polarization Dependent Loss (PDL) is an issue, we present a deterministic broadband PDL compensation.

Another important area of research in PMD is its emulation. Traditional PMD emulators are built by cascading a large number of birefringent elements via polarization scramblers. There are two issues with these emulators. Firstly, they are costly and bulky due mainly to the large number of polarization scramblers involved. We present a combinatorial approach to build polarization scramblers which significantly reduce the number of phase-plates required. Secondly, it is difficult to use such emulators to determine the system's outage probability since we need to explore an extremely large number of possible configurations to obtain a reliable estimate of the outage probability. A deterministic approach to PMD emulation is therefore a better option. The ability to "dial-in" a desired PMD state to an emulator allows one to quickly examine a PMD compensator by investigating only PMD states that are of interest. In this thesis, we present two deterministically controlled PMD emulators. One of them has the dial-in feature for arbitrary set of first and second order PMD while the other can accept arbitrary spectrum of PMD vectors.

Thesis Supervisor: Erich P. Ippen
Title: Elihu Thomson Professor of Electrical Engineering, Professor of Physics

Acknowledgments

To me, writing the acknowledgement seems to be the most difficult part of the thesis. I worry that I may not do a good job in expressing my gratitude to the late Prof. Haus, Prof. Ippen and all the friends who had helped to make this "journey" a pleasant and fruitful one.

Time flies! The memory of my first arrival at MIT 4 years ago is still so vivid. After so many wonderful opportunities to interact with brilliant individuals whom I will never get to meet in abundance in other parts of the world, now it is time to go. MIT is indeed the focus of the global intellectual power.

When I first came to MIT, I was excited because I knew I would join the group that built the shortest pulse laser in the world and I would be working under the then President of Optical Society of America, Prof. Erich Ippen. I have always held high regards for the Optical Society of America ever since I started my research career in Optics. The opportunity to learn from Prof. Ippen, one of the pioneers and experimentalists who set the world record for the ultra-short pulse, is what attracted me to MIT. Unfortunately, Lady Luck was not on my side, there was no vacancy for the laser projects in Prof. Ippen's group. The students whom I spoke to in the group, only had praises for Prof. Ippen as a mentor and as a scientist. This positive feedback only strengthens my belief that Prof Ippen is the ideal advisor for me. I was determined to join the group even if it meant I would have to move into a field of optics other than laser research. Finally Prof. Ippen had a vacancy in the PMD project, working closely with Prof Haus.

Looking back, this seems to be a good move because venturing into a new research area in optics every few years, can inject refreshing ideas and new perspectives to the understanding of light. And I believe this is how Prof. Haus acquired a profound insight into so many different areas of optics.

All along I have known that Prof. Haus was a great theorist, the father of the theory of modelocked laser, and was a MIT Institute Professor. But as I started out as an experimentalist for my research career in DSO National Laboratories (Singapore), I worried that my level of understanding of physics and standard of mathematics may not be up to his expectation. Moreover, PMD is totally a new ball game for me. Nevertheless, my first contact with Prof. Haus was really exciting. Personally, I felt he treated me as if I was already an expert in PMD despite my limited knowledge in polarization. In the meeting, I was overwhelmed by the subtleties of PMD. He "drowned" me with difficult concepts such like Principal State of Polarization and his own analogy of describing the Different Group Velocity as "sausages". This meeting was daunting as I only managed to understand less than 20 % of what he told me, mostly due to the "impedance mismatch" in our levels of understanding. Fortunately, this "impedance mismatch" decreased as the days passed.

Prof Haus was always so approachable and was always there in his office even though he had retired. His office is beside mine. Most of the times when I passed by his office, I would see him in such intense concentration solving equations at his desk. He liked to solve them on clean sheets of paper which later became his memo with a serial number.

Prof. Haus always impressed me with his deep understanding on almost everything. He had an amazingly good memory. He was always able to recall the details of our discussions weeks or months ago which I myself might not have remembered. Another interesting observation was that he took our weekly group presentation more seriously than anyone else. Every presenter in our weekly group meeting seemed to have learnt something from him, or to get their problem solved after the presentation.

I always felt that he treated me more like his friend and research collaborator than his student. He had given me many good research directions which had yielded fruitful results. At the same time, he respected my quest to explore my own ideas. Prof Haus was very enthusiastic to pursue a broadband PMD compensation by treating all PMD vectors simply as first order PMD varying with frequency. He encouraged me to look into the details of how to build such compensator. However, at the time, I was busy running simulations on my new idea of handling the low-order PMD. Despite his keen interest in this all-frequency compensation approach, he still gave me full attention in our discussion of my new idea. However, after each discussion, he would often shift gears trying to explain to me the importance of the all-frequency PMD approach. But one thing he never did, was ask me what I had done on his idea, even though I believed he knew that I had yet to spend more thought on his idea. He persistently sold me this idea for 4 or 5 times. On one occasion, when we took a stroll back after lunch with the one of the invited speakers for the Optics seminar, he told me that he had been thinking over the idea on his bed the night before, and the more he thought of it the more feasible he felt it was. At this point, I really felt bad that I did not do much on this idea yet even after his many persuasions. The saddest thing was it happened to be one of our last discussions on this topic before his sudden departure a few weeks later. I worked on this idea right after his funeral. With much difficulty, I finally managed to come out with the architecture of such an All-Frequency PMD compensator. I am not sure whether this is what he wanted. Maybe there is a better architecture. Anyway, from simulation, the architecture seems promising and it has given me the better performance than all the other compensators that I have explored.

Prof. Haus was a great teacher who had inspired me in many ways especially his pursuit for academic excellence, his passion for science and his enthusiasm in overcoming challenging problems. To me, he was just like the giant "float" which you can always rely on in the sea of knowledge. Prof. Haus had not only inspired me academically, he had also inspired me as someone who had led a fruitful life and enjoyed it to the fullest. He amazed me as a person who dedicated his whole career life to MIT and his private life to a successful marriage that lasted for more than 50 years. It really touches me when Mrs Haus cried out "he's my life" at the cemetery when she accompanied my family to pay respect to Prof. Haus after my thesis defense. I will always keep Prof. Haus in remembrance and use his teaching as a guide in my future research career.

Prof. Ippen took over my project and I was happy for this increased chances of interaction with him. I am impressed by Prof. Ippen's ability to explain difficult concepts in a simple manner. Besides his profound technical knowledge and good intuition in optics, I admired him for his charismatic leadership, his sincerity toward people and the warmth he showered. I am always so comfortable with him. From him, I have learnt how to be a good professor well-liked by his peers and students. While I treasured the freedom he has given me in pursuing the research, he is always there to guide and help. I will also miss Prof Ippen's sense of humor, sometimes his humorous comments during group meeting just brighten up everyone.

I would also like to thank Prof. Rajeev Ram and Prof. Franz Kartner for their willingness to be in my thesis committee. Their valuable comments have helped to make this thesis a better one. I also like to thank Mike Watts and HanFei Shen for being such wonderful officemates; Milos Popovic and Mike Watts for their helpful discussion in optical filter and waveguides; Peter Rakich, Jason Sicker and Juliet Gopinath for their help in the experiment; Dorothy and Donna for all their help in the administrative issues and many friends in the optics group that have helped me in one way or another. I will definitely miss the Oktoberfest at Prof. Ippen's house: Mrs Ippen's cooking and Prof. Ippen's barbecue cook-out. And of course, Mrs Kartner's cooking at the Christmas Party held at Prof. Kartner's house.

Last but not least, I would like to thank my wife Aina and my daughter D'alene. They have given me so much support and family warmth to keep me going. Aina has made me realize that work is not everything, family life is just as important. They are the "de-stressing" tools of my life. I have always believed this helps in my creativity and productivity. They share my ups and downs. I am glad that we have the opportunity to travel quite a bit as a family in US. Aina has always instilled the right attitudes and my outlook in life. She once said "Simplicity is beauty" which works for me in my research ideas too. Usually simple ideas turn out to be great ideas. Although this acknowledgement is not a love letter, I really hope that Prof. Haus and Mrs Haus have set a good example for our marriage. Mrs Haus had said "it's a love affair" even after 50 years of marriage to Prof. Haus. So I hope if I "go" before you, you would still say to people "he's my life". So, Mrs Dr. Phua, this thesis is dedicated to you and D'alene. D'alene, I hope you will keep and cherish all the good memories of how you spent your early childhood years in US, if you happen to read this many years from now. You are the most beautiful experimental result that I have ever attained.

Getting a PhD has been one of my goals for academic excellence since I was young, I am grateful that DSO had helped me to attain this achievement with its scholarship. I would also like to acknowledge 3M for their funding.

Contents

List of Figures

List of Tables

Chapter 1

Outline of Thesis

Polarization mode dispersion (PMD) is one of the most challenging problems when the bit rate of a telecommunication channel approaches 10 Gbit/s and beyond. It broadens and distorts the signal propagating through the fiber. This leads to inter-symbol interference which causes detection errors. PMD has its origin in optical birefringence. Chapter 2 describes the various intrinsic and extrinsic perturbations on the fibers that create the optical fiber birefringence. It also reviews the fundamental concepts and basic theory of PMD using the Jones and Stokes space representation, and shows the elegant use of Pauli spin matrices to connect the two spaces. Extrinsic perturbations, such as environment temperature and mechanical vibration, cause these induced birefringences to vary stochastically in time. Due to this statistical nature, PMD compensators (or emulators) have to be adjustable and adaptive. This makes PMD particularly difficult to manage. Thus, we also discuss in Chapter 2 the statistics of PMD, and gives a brief literature survey of the various technique used to mitigate and/or compensate PMD.

Most current PMD compensation schemes rely on feedback loops to search for the optimum control parameters in the compensator. The feedback configuration often suffers from slow response time since it requires dithering of the signal to find an optimal point. Most feedback compensators are therefore limited to using a small number of control parameters ($\sim$ 2-3 degrees of freedom) for mainly first-order PMD compensation. However, as the bit rate of the channel increases, a compensator that cancels first order PMD is no longer sufficient since higher order PMD dominates the signal's degradation. Adding control parameters to enable higher-order PMD compensation increases the complexity of the feedback algorithm and also lower its response time. As PMD can vary as fast as on a millisecond time scale, there are difficult tracking problems associated with too many search parameters and too little feedback information. One potential method to alleviate this tracking problem is to employ a deterministic approach to PMD compensation. A deterministic approach to PMD compensation means that the PMD parameters have to be first characterized, and then the compensator is set accordingly to compensate for the fiber PMD [2, 3]. This scheme is also known as feed-forward in contrast to the feedback scheme.

One of the most challenging problems in feed-forward PMD compensation schemes lies in the real-time monitoring of the required information. In order to make this monitoring non-intrusive to the operation of the telecommunication link, we utilize the spectrum of the telecommunication signal. In Chapter 3, we present an in-line monitoring of the output PMD vector that is based solely on the measurements carried out at the output end of the fiber [4, 5]. One of the main advantages of this monitoring technique is that no knowledge of the input polarization is required. This facilitates the use of polarization scrambling at the input end which can substantially improve the accuracy of the monitoring. The input polarization scrambling also helps to avoid the case where the fiber has a large amount of PMD but the signal's polarization is aligned with one of the input Principal State of Polarizations (PSPs) so that no PMD information can be deduced. After knowing the output PMD of the transmission fiber, we need to operate the compensator appropriately in order to exercise the PMD compensation. There are various versions of PMD compensation. One of them relies on the principle of aligning the input state of polarization (SOP) with the composite sum of the transmission fiber PMD and the local PMD in the compensator transformed to the input plane. This version of compensation is not attractive in our deterministic approach, especially if polarization scrambling is used in the real-time PMD monitoring. This is because the compensator's local PMD has to be adjusted at the rate of the scrambling in order to maintain constant alignment of the composite

PMD vector with the input SOP. And the rate of polarization scrambling used is often a few times faster than the drift rate of the fiber PMD. The preferred version of PMD compensation is the exact cancellation of the fiber PMD. In this case, the composite PMD vector of the transmission fiber and the compensator is zero. And the compensator only needs to be adjusted at the drift rate of the fiber PMD. In this thesis, we will only concentrate on this exact cancellation of the fiber PMD.

A typical first order PMD compensator consists of a polarization controller with a birefringence segment that has a tunable differential group delay (DGD). The common approach to generating a variable DGD is to separate the two orthogonal polarization components using a polarization beam splitter and to introduce a path difference between them. The two polarization components are then recombined using a polarization beam combiner. This approach requires mechanical movements, and tends to suffer from slow speed (sub-second), large output polarization fluctuation and poor control stability. Alternatively, one can generate a variable DGD by concatenating two fixed DGD segments via a polarization controller. However, this results in a second order PMD vector perpendicular to the resultant 1^{st} order PMD vector, which causes rotation of the principal state of polarization as one moves away from the center wavelength. In Chapter 4, we present a symmetrical way of concatenating 4 identical fixed DGD segments so that the resultant DGD is variable while no second order PMD is produced [6, 7]. In addition, the third order PMD produced is only half the value of the one produced in the concatenation of two fixed segments with the same DGD tuning range.

As the channel's bit rate increases, a compensator that cancels first order PMD is inadequate. In Chapter 5, we look into a compensator that is capable of full compensation for both 1^{st} and 2^{nd} order PMD [8]. This compensator consists of three first order PMD segments, one of which is adjustable, concatenated via polarization controllers. As this compensator works in a feed-forward manner, the 1^{st} and 2^{nd} order PMD vectors need to be characterized before the compensator can act. However, from Chapter 3, one can see that the 2^{nd} order PMD may not be characterized as accurately as the 1^{st} order PMD. Thus, instead of trying to compensate both orders simultaneously in a feed-forward scheme, another viable option is to have a hybrid feed-forward/feedback scheme, where the 1^{st} order PMD compensation is carried out in a feed-forward manner and feedback compensation is used for the second order PMD. To decouple these compensation schemes, we also propose in Chapter 5 a module that produces a variable 2^{nd} order PMD without generating any 1^{st} order PMD [9, 1]. This allows the second order PMD compensator to search for the optimum without affecting the first order PMD compensation which is already accomplished in a feed-forward manner.

For broadband PMD compensation, all orders of PMD need to be considered. In Chapter 6, we propose the architecture of a broadband PMD compensator in a feed-forward compensation scheme [10]. In this compensator, we avoid expressing the PMD as a Taylor expansion about the center frequency, ω_o, since this introduces complicated higher-order PMD terms such as $\frac{d\vec{\tau}}{d\omega}$, $\frac{d^2\vec{\tau}}{d\omega^2}$ etc. Instead we simply treat the whole PMD spectrum as first order PMD vectors that vary from frequency to frequency. For this reason, we choose to call the proposed scheme “All-Frequency”, instead of “All-Order”, PMD compensator. It is comprised of three stages of flexible frequency dependent polarization rotation. In Stokes space, the net effect of the first two stages is equivalent to a frequency dependent polarization rotation that aligns all PMD vectors into a common direction. The third stage compensates the frequency dependent variable DGD. One practical implementation of this broadband PMD compensator is based on Optical-integrated All-Pass Filters (APFs). APFs are promising due to their compactness and economy of production. For broadband applications, the number of APFs involved can be as large as 50. To find the optimum of the large number of parameters involved, we need a fast and efficient algorithm based on recursive equations. We also present in Chapter 6 a fast recursive algorithm using complex cepstrums [11].

Another important area of research in PMD is its emulation. This area is interesting because the evaluation of PMD mitigation techniques requires a method of emulating PMD of installed fiber links, especially since “legacy” fiber with high PMD installed in the 1980’s is no longer commercially available. Traditional PMD emulators are built by cascading a large number of birefringent elements via polarization scramblers. There are two main issues with these emulators. Firstly, it is bulky, costly and complicated to build and control such emulators due to the large number of segments and scramblers involved. In Chapter 7, we present a novel PMD emulator that adopts a combinatorial approach to build polarization scramblers between the birefringent elements [12]. This approach can reduce the required number of phase-plates and their corresponding controls significantly, thus reducing the cost, size and complexity. It exploits the fact that rotation matrices are non-commutative which gives many different ways of building polarization controllers out of just a few phase-plates. Although these polarization controllers are correlated, we show, numerically and experimentally, that there is sufficient polarization scrambling between segments to achieve the important key properties of a PMD emulator. Secondly, these emulators often tend to lack in repeatability, unable to adjust for varying PMD statistics and lacking a “dial-in” feature. The temporal variation of the optical fiber’s birefringence produces penalties that change randomly with time. In system design, a maximum penalty ($\sim$1-3 dB) is usually assigned to PMD, and one would demand that the probability of the PMD induced penalty exceeding this allowed value (also known as the outage probability) to be very small, typically around 10^{-6}. Because of this stringent requirement, it is difficult to use an emulator that uses random polarization scrambling between segments to determine the system’s outage probability since an extremely large number of possible configurations need to be explored in order to obtain a reliable estimate. A deterministic approach to PMD emulation is therefore a better option. The ability to “dial-in” a desired PMD state to an emulator allows one to quickly examine a PMD compensator by investigating only PMD states that are of interest. One useful way to employ such emulator with a “dial-in” feature is to use Monte-Carlo simulation with importance sampling technique to generate the extremely rare events that occur in the tail of PMD distribution, and then “dial-in” these PMD states into the emulator which then produces them physically. In Chapter 8, we investigate a four-segment PMD emulator that can be deterministically controlled to produce the desired 1^{st} and 2^{nd} order PMD vectors [13]. In Chapter 9, we present a deterministic broadband PMD emulator that can approximate a desired PMD vector for every frequency within a certain band of interest. In the other words, one can arbitrarily “dial-in” the spectrum of a PMD vector that comprises all orders of PMD [14].

Until now, we have assumed negligible Polarization Dependent Loss (PDL) present in the fiber. In reality, there are always distributed PDL from components at the amplifier sites in a multi-span system and from components at the receiver. In situations where PDL is non-negligible, the system penalty due to the coexistence of PMD and PDL is known to be higher than the summation of PMD-only penalty and PDL-only penalty. In addition, the presence of PDL may discount the performance of some PMD compensators. The physics of the mutual interaction of PMD and PDL is complex. Fortunately, polar decomposition of the fiber transmission matrix allows lumped PDL followed by lumped PMD compensation at the receiver’s end. Thus, we present in Chapter 10, the architecture of a broadband PDL compensator in a feed-forward compensation scheme [15]. This module consists of three stages. Stage 1 and 2 are the frequency-dependent polarization rotators that align all the different PDL vectors into the $\{1, 0, 0\}$ direction in Stokes space. Stage 3 eliminates both the PDL magnitude and the frequency dependence of the isotropic attenuation by introducing different frequency-dependent variable attenuation to the linear horizontal and vertical polarizations. By applying the known Mueller transformations of the PDL compensator to the monitored polarimetric data, we show that the composite PMD spectrum can be deduced for subsequent broadband PMD compensation described in Chapter 6. Therefore no additional monitoring is required for PDL compensation since it utilizes the same set of polarimetric data measured in the case of PMD compensation.

Chapter 2

Polarization Effects in Lightwave System

2.1 Background

Polarization effects, such as PMD and PDL, have historically played a minor role in the development of lightwave system. The main reason is that commercial optical receivers detect optical power rather than the field and are thus insensitive to polarization. In recent years, the deployment of optical amplifiers together with numerous improvements in the related optical transmission technologies, has led to a dramatic increase in the capacity and distance of transmission. With the large increase in the optical path length, and the number of optical elements that light encounters during transmission, formerly small effects such as PMD and PDL can accumulate to a point where they become significant sources of network impairment. This is especially true when the carriers begin to deploy high bit rate transmission systems ($>$ 10 Gbit/s per channel) in older generation fibers. While fibers manufactured today can have mean PMD coefficients less than 0.05ps/$\sqrt{km}$, these older generation fibers installed in the 1980s may exhibit PMD coefficients higher than 0.8ps/$\sqrt{km}$.

There are three sources of polarization-related impairments: Polarization Mode Dispersion (PMD) [16, 17, 18, 19], Polarization Dependent Loss (PDL) [20, 21, 22] and Polarization Dependent Gain (PDG) [16, 23]. Of these, PMD is the main problem.

PMD is caused by optical birefringence and the random variation of its orientation along the fiber . It causes different group delays for different polarizations. When this difference in delays approaches a significant fraction of the bit period, pulse distortion and system penalties occur [24, 25, 26, 27, 28]. Environmental changes including temperature and stress cause the PMD to vary stochastically in time [29, 30, 31], making PMD particularly difficult to manage. This means a system can randomly wander in and out of the high-penalty states. The goal of PMD compensation is to reduce the probability that the penalty will exceed a certain level to a negligible value (typically $<$1 minute per year) [32, 33, 34].

Research on PDL effects when it coexists with PMD is relatively recent and is beginning to attract serious attention [20, 21, 35, 36, 37]. This area is especially interesting since PDL can amplify the system penalties due to PMD . Various inline optical components such as switches, isolators, couplers, filters, and circulators, may have non-negligible PDL (i.e $>$ 0.2 dB) [22]. When the optical pulse passes through these optical components, it splits between two orthogonal polarization modes which are attenuated differently for each polarization. Therefore, an obvious effect of PDL is the optical power variation when there is polarization fluctuation due to the dynamically changing birefringence in the fiber. PDG, on the other hand, is due to the anisotropic gain saturation in fiber amplifiers. Polarization hole burning arises in an amplifier when a saturating signal causes selective de-excitation of erbium ions that are aligned with the polarization of the saturating signal. This causes the gain seen by the unpolarized ASE noise accompanying the signal to be reduced for the components of the noise parallel to the signal and enhanced for components orthogonal to the signal. This leads to the orthogonal noise component growing at the expense of the signal power, which leads to a reduction in the signal-to-noise ratio at the receiver [23] .

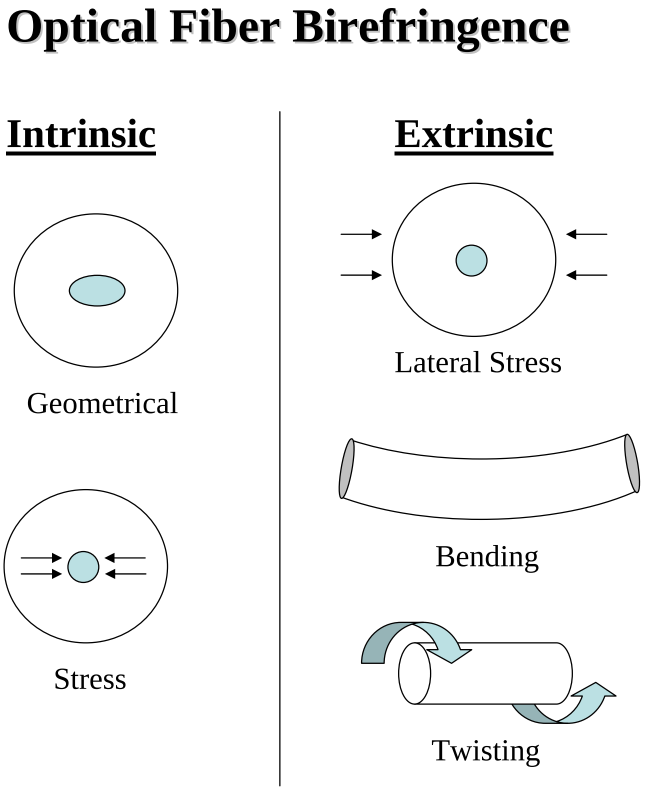

Figure 2-1: Intrinsic and extrinsic birefringence in optical fiber

2.2 Origin of PMD

In a single mode fiber, an optical wave of arbitrary polarization can be represented as the linear superposition of two orthogonally polarized HE_{11} modes [38, 39]. In an ideal fiber, the two HE_{11} modes are indistinguishable (degenerate) in terms of their propagation properties owing to the cylindrical symmetry of the waveguide. However, in reality, fibers have some amount of asymmetry due to the imperfections in the manufacturing process and or mechanical stress on the fiber after manufacture [40, 18, 16, 41, 42, 43]. This asymmetry breaks the degeneracy of the orthogonally polarized HE_{11} modes, resulting in birefringence: a difference in the phase and group velocities of the two modes. Both intrinsic and extrinsic perturbations can cause birefringence in optical fiber. The manufacturing process sets up permanent, intrinsic perturbations in the fiber. There are two main forms of intrinsic birefringence: geometrical and stress birefringence as shown in Figure 2-1. Non-circular fiber geometry can usually be traced to the preform from which the fiber is drawn. In telecommunication fiber, deviation of less than 1% in the circularity of the core can translate into noticeable effects in lightwave systems. Consequently, even extremely small imperfections in the processing of the preform can have a significant impact on the fiber performance.

Stress birefringence caused by a non-circularly symmetrical stress field in the core region typically arises in combination with a non-circular fiber geometry. The necessarily different chemical composition of the core relative to the cladding usually results in slightly different thermal expansion coefficient for the two regions. This gives rise to radially directed stresses when the fiber is cooled after being drawn. In an ideal circularly symmetrical fiber, these stress fields are symmetrical and thus do not cause anisotropy. However, if there is a noncircular shape to either the core and cladding in the preform, the drawn fiber will have internal stress that are not circularly symmetrical. Extrinsic birefringence, on the other hand, is created when the fiber is spooled, cabled, or embedded in the ground. This is due to the extrinsic perturbations such as lateral stress, bending, or twisting. These external perturbations vary due to the changes in the environment, thus making PMD a stochastic process.

2.3 Representations of Polarization and its Evolution

As a preparation, we first examine the two common representations of polarization in the 2-D complex-valued space of the Jones vector (known as Jones space) and the 3-D real-valued space of Stokes vector (known as Stokes space) and the connection between the two [17, 44, 45]. In Jones space, the propagation through the fiber is represented by a complex-valued 2×2 transmission matrix $\mathbf{T}$, and the complex-valued 2-D output State of Polarization (SOP) $|t\rangle$ is related to the input SOP $|s\rangle$ by

$$|t\rangle = \mathbf{T}\,|s\rangle = e^{-j\phi_o}\mathbf{U}\,|s\rangle \tag{2.1}$$

where the real part of ϕ_o represents the isotropic phase term while its imaginary part represents the isotropic loss or gain term. **U** is the complex Jones matrix. If one assumes no PDL, **U** will be unitary and has $\det(\mathbf{U}) = 1$. The equivalent of unitary **U** in Stokes space is a real-valued 3×3 rotation matrix **R**. This is also known as the Mueller matrix. The SOP is represented by a real-valued 3-D vector so that the output SOP Stokes vector $\hat{t}$ is related to the input SOP $\hat{s}$ by

$$\hat{t} = \mathbf{R}\hat{s} \tag{2.2}$$

The isomorphic pairings of operators such as these are not new and have been widely used elsewhere in mechanics, quantum mechanics and even in the unification of quantum theory and general relativity. Pauli spin matrices and spin vectors are the key to connect these two spaces. The 2×2 Pauli spin matrices are defined as

$$\sigma_{\mathbf{1}} = \begin{pmatrix} 1 & 0 \\ 0 & -1 \end{pmatrix} \tag{2.3a}$$

$$\sigma_{\mathbf{2}} = \begin{pmatrix} 0 & 1 \\ 1 & 0 \end{pmatrix} \tag{2.3b}$$

$$\sigma_{\mathbf{3}} = \begin{pmatrix} 0 & -j \\ -j & 0 \end{pmatrix} \tag{2.3c}$$

And they allow us to write the components s_i of the Stokes vector corresponding to $|s\rangle$ in a compact form

$$s_i = \langle s|\, \sigma_{\mathbf{i}} \,|s\rangle \tag{2.4}$$

If we define a Pauli spin vector in Stokes space as $\vec{\sigma} = (\sigma_{\mathbf{1}}, \sigma_{\mathbf{2}}, \sigma_{\mathbf{3}})$, the Stokes vector is simply

$$\hat{s} = \langle s|\, \vec{\sigma} \,|s\rangle \tag{2.5}$$

Spin matrices are Hermitian and unitary (i.e $\sigma_{\mathbf{i}} = \sigma_{\mathbf{i}}^{\dagger}$ and $\sigma_{\mathbf{i}}\sigma_{\mathbf{i}}^{\dagger} = \mathbf{I}$) and have zero trace. They obey the well-known multiplicative rules

$$\sigma_{\mathbf{i}}^{\mathbf{2}} = \mathbf{I} \tag{2.6a}$$

$$\sigma_{\mathbf{i}}\sigma_{\mathbf{j}} = -\sigma_{\mathbf{j}}\sigma_{\mathbf{i}} \tag{2.6b}$$

$$\sigma_{\mathbf{i}}\sigma_{\mathbf{j}} = j\sigma_{\mathbf{k}} \tag{2.6c}$$

The assumption of no PDL and isotropic loss/gain gives unitary **T**, **U** and **R** (i.e $\mathbf{TT}^{\dagger} = \mathbf{I}$, $\mathbf{UU}^{\dagger} = \mathbf{I}$, $\mathbf{RR}^{\dagger} = \mathbf{I}$), normalized Jones vector (i.e $\langle t \mid t \rangle = \langle s \mid s \rangle = 1$) and unit norm of the Stokes vector (i.e $\left|\hat{t}\right| = |\hat{s}| = 1$). It is worth noting that, in the presence of PDL, **T** and **U** lose their unitary property and, in order to account for the power intensity change in the Stokes Space, we need to use the complete 4×4 Mueller matrix. Table 2.1 shows a few examples of SOP expressed in 2-D Jones vector $|s\rangle$ and its corresponding representation in Stokes space $\hat{s}$ related by equation (2.4). Stokes space can give a good 3-D visualization of the SOP. Figure 2-2 shows the various SOPs on the unit Poincaré sphere presented in Stokes space. For completely polarized light, it lies on the unit Poincaré sphere. For partially polarized light, it lies within the unit Poincaré sphere. Orthogonal polarizations are diagonally opposite one another on the sphere. For example, horizontal linear polarization is in the {1,0,0} direction while vertical linear polarization is in the {-1,0,0} direction. Linear SOPs lie on the equator. The right-handed circularly polarized light occupies the north pole while the left-handed circularly polarized light occupies the south pole. All other states are elliptical. They are on the upper hemisphere if they are right-handed and on the lower hemisphere if they are left-handed.

The evolution of SOP through a medium in Jones space is represented by the Jones matrix **U** as in eqn. (2.1). The equivalent picture in Stokes space is a rotation **R** of the Stokes vector as in eqn. (2.2). The rotation axis $\hat{r}$ of **R** corresponds to the slow eigen-states of **U** while the rotation angle φ corresponds to the difference in the phase accumulated by the two eigen-states. This phase difference is often called the retardation angle for the case of a birefringent element. For example, the change

Jones Vector $\left\vert s \right\rangle$	**Stokes Vector** $\hat{s}$	**Description**
$\left\vert \begin{matrix} 1 \\ 0 \end{matrix} \right\rangle$	$\begin{pmatrix} 1 \\ 0 \\ 0 \end{pmatrix}$	Horizontal Linear Polarization
$\left\vert \begin{matrix} 0 \\ 1 \end{matrix} \right\rangle$	$\begin{pmatrix} -1 \\ 0 \\ 0 \end{pmatrix}$	Vertical Linear Polarization
$\frac{1}{\sqrt{2}}\left\vert \begin{matrix} 1 \\ 1 \end{matrix} \right\rangle$	$\begin{pmatrix} 0 \\ 1 \\ 0 \end{pmatrix}$	45^o Linear Polarization
$\frac{1}{\sqrt{2}}\left\vert \begin{matrix} 1 \\ -1 \end{matrix} \right\rangle$	$\begin{pmatrix} 0 \\ -1 \\ 0 \end{pmatrix}$	135^o Linear Polarization
$\frac{1}{\sqrt{2}}\left\vert \begin{matrix} 1 \\ e^{j\pi/2} \end{matrix} \right\rangle$	$\begin{pmatrix} 0 \\ 0 \\ 1 \end{pmatrix}$	Right-Handed Circular Polarization
$\frac{1}{\sqrt{2}}\left\vert \begin{matrix} 1 \\ e^{-j\pi/2} \end{matrix} \right\rangle$	$\begin{pmatrix} 0 \\ 0 \\ -1 \end{pmatrix}$	Left-Handed Circular Polarization
$\left\vert \begin{matrix} s_x \\ s_y \end{matrix} \right\rangle$	$\begin{pmatrix} s_x s_x^* - s_y s_y^* \\ s_x s_y^* + s_x^* s_y \\ j\left(s_x s_y^* - s_x^* s_y\right) \end{pmatrix}$	General Elliptical Polarization

Table 2.1: Example of SOPs in both Jones and Stokes Spaces

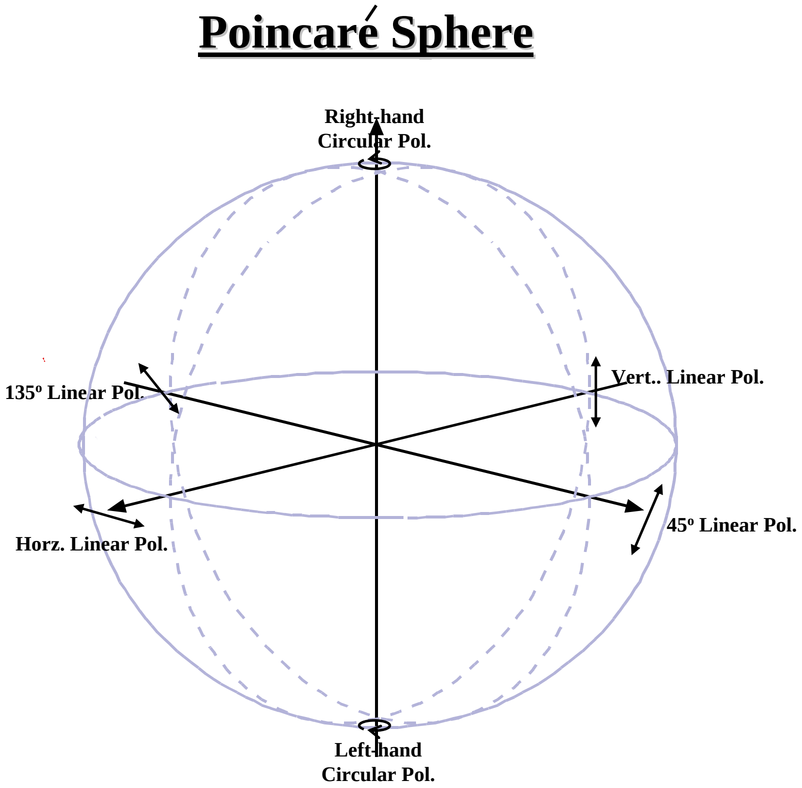

Figure 2-2: Various SOPs in Poincaré sphere representation

of SOP when light propagates through a birefringent half-wave plate with horizontal slow birefringence axis in physical space, corresponds to a 180^o rotation about $\{1,0,0\}$ in Stokes space. If the slow axis is turned to 45^o in physical space, the 180^o rotation is now about the $\{0,1,0\}$ axis. If we now change the half-wave plate to a quarter-wave plate but maintain the same orientation for the slow birefringence axis, the rotation angle becomes 90^o about the $\{0,1,0\}$. In terms of Pauli-spin matrices, the relation of **U** and **R** can be shown [17] as

$$\mathbf{R}\vec{\sigma} = \mathbf{U}^{\dagger}\vec{\sigma}\mathbf{U} \tag{2.7}$$

There are two convenient and useful equations to express **U** and **R**, if the rotational axis $\hat{r} = \{r_1, r_2, r_3\}$ and the rotation angle φ [17] are known

$$\mathbf{U} = \mathbf{I}\cos\left(\varphi/2\right) - j\hat{r}.\vec{\sigma}\sin\left(\varphi/2\right) \tag{2.8}$$

and

$$\mathbf{R} = \hat{r}\hat{r} + \sin(\varphi)(\hat{r}\times) + \cos(\varphi)(\hat{r}\times)(\hat{r}\times) \tag{2.9}$$

where the 3D dyadic $\hat{r}\hat{r}$ is the projector operator

$$\hat{r}\hat{r} = \begin{pmatrix} r_1r_1 & r_1r_2 & r_1r_3 \\ r_2r_1 & r_2r_2 & r_2r_3 \\ r_3r_1 & r_3r_2 & r_3r_3 \end{pmatrix} \tag{2.10}$$

and $(\hat{r}\times)$ is the cross-product operator

$$(\hat{r}\times) = \begin{pmatrix} 0 & -r_3 & r_2 \\ r_3 & 0 & -r_1 \\ -r_2 & r_1 & 0 \end{pmatrix} \tag{2.11}$$

Table 2.2 lists some useful examples of **U** and their corresponding **R**. In birefringent elements, the retardation angle is expressed as

$$\varphi = \frac{(n_e - n_o)\omega l}{c} \tag{2.12}$$

where $(n_e - n_o)$ is the birefringence, l is the length of the birefringent element, ω is the angular frequency and c is the speed of light. The retardation angle has a linear dependence on frequency if we assume negligible frequency dependence in the birefringence. Even with fixed input polarization, there is a change with frequency of the output polarization. This explains why zero-order wave-plate which has the smallest length l, can be used for a broader bandwidth than higher-order wave-plates. Another important consequence of equation (2.12) is that the concatenation of birefringent elements can create frequency dependence in the eigenstates of the composite **U**, even if the eigenstates of the individual birefringent element are independent of frequency. Furthermore, the retardation angle of the composite **U** departs from a linear frequency dependence to acquire a more general dependence. It is this frequency dependence in **U** (and **R**) that gives rise to PMD.

Description	**Rotation Axis $\hat{r}$**	**Rot. Angle φ**	**Jones Mat. U**	**Stokes Mat. R**
a) Half-wave plate with horizontal slow birefringent axis	$\begin{pmatrix} 1 \\ 0 \\ 0 \end{pmatrix}$	180^o	$\begin{pmatrix} -j & 0 \\ 0 & j \end{pmatrix}$	$\begin{pmatrix} 1 & 0 & 0 \\ 0 & -1 & 0 \\ 0 & 0 & -1 \end{pmatrix}$
b)Quarter-wave plate with slow birefringent axis oriented at 45^o in physical space	$\begin{pmatrix} 0 \\ 1 \\ 0 \end{pmatrix}$	90^o	$\frac{1}{\sqrt{2}}\begin{pmatrix} 1 & -j \\ -j & 1 \end{pmatrix}$	$\begin{pmatrix} 0 & 0 & 1 \\ 0 & 1 & 0 \\ -1 & 0 & 0 \end{pmatrix}$
c)Quarter-wave Plate with slow birefringent axis oriented at -45^o in physical space	$\begin{pmatrix} 0 \\ -1 \\ 0 \end{pmatrix}$	90^o	$\frac{1}{\sqrt{2}}\begin{pmatrix} 1 & j \\ j & 1 \end{pmatrix}$	$\begin{pmatrix} 0 & 0 & -1 \\ 0 & 1 & 0 \\ 1 & 0 & 0 \end{pmatrix}$
d)Birefringent plate with tunable retardation angle θ and horizontal slow birefringent axis	$\begin{pmatrix} 1 \\ 0 \\ 0 \end{pmatrix}$	θ	$\begin{pmatrix} e^{-j\theta/2} & 0 \\ 0 & e^{j\theta/2} \end{pmatrix}$	$\begin{pmatrix} 1 & 0 & 0 \\ 0 & \cos\theta & -\sin\theta \\ 0 & \sin\theta & \cos\theta \end{pmatrix}$
e)Birefringent plate with tunable retardation angle and slow birefringent axis oriented at 45^o in physical space	$\begin{pmatrix} 0 \\ 1 \\ 0 \end{pmatrix}$	θ	$\begin{pmatrix} \cos\frac{\theta}{2} & -j\sin\frac{\theta}{2} \\ -j\sin\frac{\theta}{2} & \cos\frac{\theta}{2} \end{pmatrix}$	$\begin{pmatrix} \cos\theta & 0 & \sin\theta \\ 0 & 1 & 0 \\ -\sin\theta & 0 & \cos\theta \end{pmatrix}$
Concatenation of birefringent plates (b)→(d)→(c)	Effectively $\begin{pmatrix} 0 \\ 0 \\ 1 \end{pmatrix}$	θ	$\begin{pmatrix} \cos\frac{\theta}{2} & -\sin\frac{\theta}{2} \\ \sin\frac{\theta}{2} & \cos\frac{\theta}{2} \end{pmatrix}$	$\begin{pmatrix} \cos\theta & -\sin\theta & 0 \\ \sin\theta & \cos\theta & 0 \\ 0 & 0 & 1 \end{pmatrix}$

Table 2.2: Useful examples of **U** and their corresponding **R**

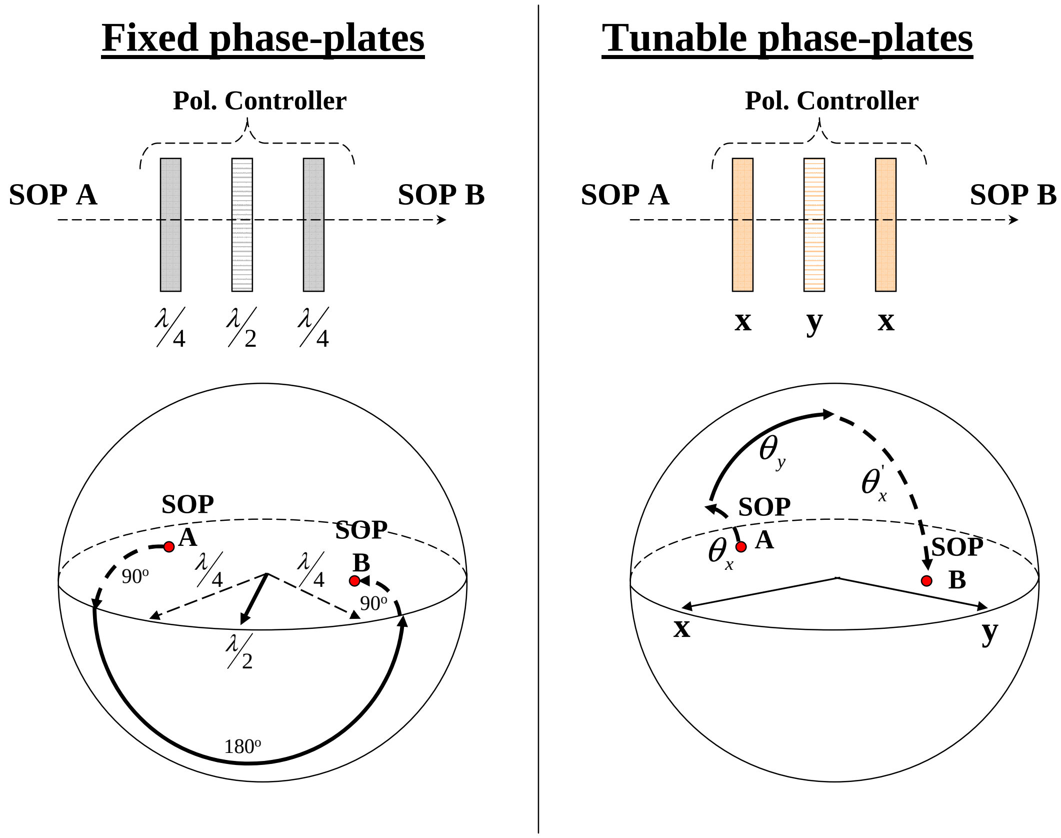

Figure 2-3: Two typical types of polarization controller

2.4 Polarization Controller

There are two typical types of polarization controller for altering the polarization of light [44, 46, 47]. One is based on a combination of three fixed phase-plates where a half-wave plate is sandwiched between two quarter-wave plates, and the other is based on a combination of three tunable phase-plates whose birefringence axes are in {1,0,0}, {0,1,0} and {1,0,0} in Stokes space. The operation of each polarization controller is obvious using the Stokes space representation as shown in Figure 2-3. For a fixed phase-plate polarization controller, we can transform any polarization state to any polarization state on the Poincaré sphere by changing the angular orientations of their birefringent axes. For tunable phase-plate polarization controller, we fix the birefringence axes, but tune their phase angles to carry out any polarization transformation on the Poincaré sphere. It is worthwhile to note that the rotation operation to map any input SOP to any output SOP is not unique and Figure 2-3 shows only two of the more common configurations. To simplify practical implementation, either the input or output SOP is fixed to {1,0,0}. This reduces the degree of freedom and thus reduces the required number of phase-plates to two. Many practical phase-plates often have a finite range of adjustments. The tunable phase-plate, for example, may have a limited range of rotation on the sphere. As the SOP varies with time, such a phase-plate may approach the end of its tunable range. To maintain an endless control, most polarization controllers include one or two more redundant phase-plates to tackle this engineering issue [48, 49, 47]. The redundant phase-plates allow "unwinding" of any of the phase-plates to the center of the operation range before they reach their range limit. This "unwinding" is the key to endless control of the polarization controller using phase-plates with finite tuning range.

2.5 Principal State Model

A fiber is often visualized or modeled as a sequence of random birefringent sections whose birefringence axes and magnitude change randomly with z (along the fiber). There are two different manifestations of PMD depending on the view taken. In the frequency domain view one sees, for a fixed input polarization, a change with frequency ω of the output polarization of the input pulse. In the time domain one observes a mean time delay of a pulse traversing the fiber which is the function of the polarization of the input pulse. The two phenomena are intimately connected.

In 1986, Poole and Wagner [19] introduced the Principal States model using the Jones matrix and the frequency domain view. Equation (2.1) describes the relationship of the input and output Jones vectors $|s\rangle$ and $|t\rangle$. As the pulses are described by wave-packets with a finite frequency band, we need to consider the frequency dependence of $|t\rangle$. We assume fixed input polarization and phase ($|s\rangle_\omega = 0$), as is appropriate for a simple pulse entering the fiber at time zero. By differentiating eqn.

(2.1) and eliminating $|s\rangle$, we obtain for the change of output Jones vector

$$|t\rangle_\omega = -j\left(\frac{d\phi_o}{d\omega} + j\mathbf{U}_\omega\mathbf{U}^\dagger\right)|t\rangle \tag{2.13}$$

To first order, the output polarization $|t\rangle$ generally changes with frequency unless $|t\rangle$ is a eigenvector of $j\mathbf{U}_\omega\mathbf{U}^\dagger$. The frequency derivative of the common phase ϕ_o gives a mean group delay τ_o common to all polarizations ($\tau_o = d\phi_o/d\omega$). One can show [17] two important properties of the matrix $j\mathbf{U}_\omega\mathbf{U}^\dagger$: (1) it is hermitian and (2) it has zero trace. Therefore both eigenvalues of $j\mathbf{U}_\omega\mathbf{U}^\dagger$ are real and their sum is zero. If we denote the eigenvalues as $\pm\tau_g/2$ and corresponding eigenvectors as $|p_\pm\rangle$. When the output polarization $|t\rangle$ happens to align with one of these eigenvectors, then

$$|p_\pm\rangle_\omega = -j\left(\frac{d\phi_o}{d\omega} \pm \frac{\tau_g}{2}\right)|p_\pm\rangle \tag{2.14}$$

so that by first-order Taylor's approximation,

$$|p_\pm\rangle(\omega) \approx |p_\pm\rangle(\omega_o) + |p_\pm\rangle_\omega(\omega-\omega_o) \approx e^{-j\left(\frac{d\phi_o}{d\omega}\pm\frac{\tau_g}{2}\right)(\omega-\omega_o)}|p_\pm\rangle(\omega_o) \tag{2.15}$$

In the time-domain view, the first order approximation shows that the effect of the propagation through a fiber is simply a group delay when the output polarization is in one of the eigenstates of $j\mathbf{U}_\omega\mathbf{U}^\dagger$. This special orthogonal pair of polarizations is called the Principal State of Polarizations (PSPs) of the output. Light launched in a PSP does not change polarization at the output to first order in ω. These PSPs have group delays which are maximum and minimum mean time delays of the time domain view. The difference between these two delays is called the Differential Group Delay (DGD) τ_g. The PMD vector $\vec{\tau}$ describes both the PSPs and the DGD in the fiber. It is a Stokes vector $\vec{\tau}$ pointing in the direction of the slow PSP $\hat{p} = \langle p_+|\vec{\sigma}|p_+\rangle$ with a length equal to the DGD, thus

$$\vec{\tau} = \tau_g\hat{p} \tag{2.16}$$

As we have discussed earlier, in Stokes space, orthogonal polarizations are diagonally opposite in the Poincaré sphere, thus the fast PSP is given as $\langle p_- | \vec{\sigma} | p_- \rangle = -\hat{p}$. Since the determinant of a Hermitian matrix is the product of its eigenvalues, we have $\det\left(j\mathbf{U}_\omega\mathbf{U}^\dagger\right) = -\tau_g^2/4$. From this, noting that $\det(\mathbf{U}) = 1$, we can extract an expression for

$$\tau_g = 2\sqrt{\det(\mathbf{U}_\omega)} \tag{2.17}$$

In general any 2×2 matrix **M** can be expanded in the form

$$\mathbf{M} = a_o\mathbf{I} + \vec{a}.\vec{\sigma} \tag{2.18}$$

where $a_o = Trace\,(\mathbf{M})/2$ and $a_i = Trace\,(\sigma_{\mathbf{i}}\mathbf{M})/2$. This is the well-known $\vec{\sigma}$-expansion of a matrix used commonly in quantum mechanics. Since the eigenvectors $|p_+\rangle$ and $|p_-\rangle$ of the matrix $j\mathbf{U}_\omega\mathbf{U}^\dagger$ constitute a complete orthogonal set of Jones vectors, we can express $j\mathbf{U}_\omega\mathbf{U}^\dagger$ using its eigenvalues $\pm\tau_g/2$ and its corresponding eigenvector as $|p_\pm\rangle$ as

$$j\mathbf{U}_\omega\mathbf{U}^\dagger = \frac{\tau_g}{2}\,|p_+\rangle\,\langle p_+| - \frac{\tau_g}{2}\,|p_-\rangle\,\langle p_-| \tag{2.19}$$

Using $Trace\,(|q\rangle\,\langle p|) = \langle p \mid q\rangle$ and with eqn. (2.19), one can see that

$$Trace\left(\sigma_{\mathbf{i}}\left(j\mathbf{U}_\omega\mathbf{U}^\dagger\right)\right) = \tau_g\hat{p}_i = \vec{\tau}_i \tag{2.20}$$

Using the fact that $j\mathbf{U}_\omega\mathbf{U}^\dagger$ has zero trace and equation (2.20), the $\vec{\sigma}$-expansion of $j\mathbf{U}_\omega\mathbf{U}^\dagger$ yields

$$j\mathbf{U}_\omega\mathbf{U}^\dagger = \frac{1}{2}\vec{\tau}.\vec{\sigma} \tag{2.21}$$

This is a useful equation for the Jones Matrix characterization technique of PMD.

It is also worthwhile to note that the concepts such as group velocity and group delay, as pointed out by Haus [50, 51] and Gordon [17], have a strict definition for an individual mode only. Thus these concepts are appropriate only when the polarization is aligned with the PSPs. For other polarizations, the PMD phenomenon can split an input pulse into two or more pulses at the fiber output, leading to polarization-dependent pulse shapes. In these cases, the moments of the output signals are more appropriate descriptions of the signal delays in systems involving two or more modes of propagation [17]. In addition, the reader should not confuse the eigenstates of $\mathbf{U}$ with the principal states of PMD. The principal states of PMD are the eigenstates of $j\mathbf{U}_\omega\mathbf{U}^\dagger$ at the output or eigenstates of $j\mathbf{U}^\dagger\mathbf{U}_\omega$ at the input. Only for very special cases, such as phase-plates, are these eigenstates the same as the principal states.

2.6 The Law of Infinitesimal Rotation

A useful law of infinitesimal rotation relates the change of polarization of light at fiber location z due to a small length increment dz of the fiber. Over this small length increment, the birefringence [40] can be assumed to be constant in magnitude and direction . As mentioned in Section 2.3, the evolution of SOP through a constant birefringent element corresponds to a rotation of the Stokes vector in Stokes space. The rotation axis corresponds to the slow birefringent axis $\hat{\beta}$ while the rotation angle corresponds to the retardation angle $\frac{(n_e-n_o)\omega dz}{c}$. Thus the change of polarization with distance z over this small increment length can be written in the form of a precession about $\hat{\beta}$ with

$$\frac{d\hat{t}}{dz} = \vec{\beta} \times \hat{t} \tag{2.22}$$

where $\left|\vec{\beta}\right| = \frac{(n_e-n_o)\omega}{c}$. This is the law of infinitesimal rotation for birefringence with distance. On the other hand, the change of the output SOP $\hat{t}$ with frequency can be expressed as

$$\hat{t}_\omega = \langle t|_\omega \vec{\sigma}\,|t\rangle + \langle t|\,\vec{\sigma}\,(|t\rangle)_\omega \tag{2.23}$$

Combining (2.13) and (2.21) into (2.23), and applying the spin vector identities

$$\begin{aligned} \vec{\sigma}\,(\vec{a}.\vec{\sigma}) &= \vec{a}\mathbf{I} + j\vec{a}\times\vec{\sigma} && (2.24a) \\ (\vec{a}.\vec{\sigma})\,\vec{\sigma} &= \vec{a}\mathbf{I} - j\vec{a}\times\vec{\sigma} && (2.24b) \\ \langle s|\,\vec{a}\times\vec{\sigma}\,|s\rangle &= \vec{a}\times\langle s|\,\vec{\sigma}\,|s\rangle && (2.24c) \end{aligned}$$

we can derive the important law of infinitesimal rotation [17]

$$\frac{d\hat{t}}{d\omega} = \vec{\tau} \times \hat{t} \tag{2.25}$$

This precession equation describes the evolution of the output SOP with frequency in Stokes space. The geometrical interpretation of this simple law is a rotation of the output Stokes vector on the Poincaré sphere as frequency changes. The rotation axis is the PSP $\hat{p}$ and the rate of rotation is the DGD τ_g. This infinitesimal rotation law allows us to express the PMD vector in term of the rotation (Mueller) matrix **R** that relates the input and output Stokes vector $\hat{s}$ and $\hat{t}$. We differentiate eqn. (2.2) with frequency (while keeping fixed input $\hat{s}$) and obtain

$$\hat{t}_\omega = \mathbf{R}_\omega \hat{s} = \mathbf{R}_\omega \mathbf{R}^\dagger \hat{t} \tag{2.26}$$

The comparison of (2.25) and (2.26) yields the useful operator relationship

$$\vec{\tau}\times = \mathbf{R}_\omega \mathbf{R}^\dagger \tag{2.27}$$

The above discussion has focused on expressions for the PMD vector at the fiber output. There are practical cases where the corresponding PMD vector at the input is needed. This can be obtained by a simple transformation. The relation between the PSPs in Jones space is

$$|p_{out}\rangle = \mathbf{T}\,|p_{in}\rangle \tag{2.28}$$

and in Stokes space

$$\vec{\tau}_{out} = \mathbf{R}\vec{\tau}_{in} \tag{2.29}$$

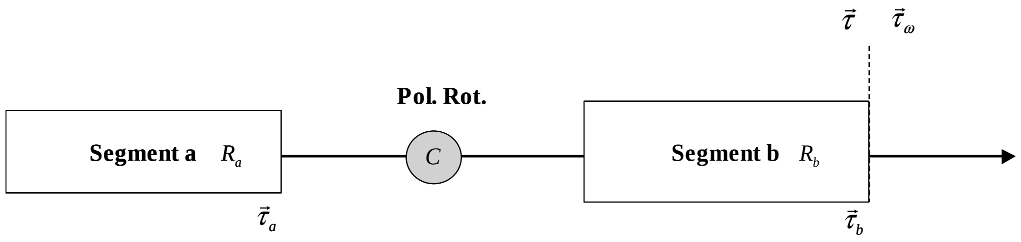

Figure 2-4: Concatenation of two fiber segments

2.7 PMD Concatenation Rule and Dynamical PMD Equation

The PMD vector concatenation rules are a powerful set of simple tools that allow the determination of the PMD vector of an assembly of concatenated fiber sections when the PMD vectors of the individual sections are known [17, 52, 53]. Among their uses are the analysis of the evolution of the PMD vector with fiber length, statistical PMD modeling, PMD simulation, and the design of multi-section PMD compensators.

Consider two concatenated fiber sections with Muller rotation matrices $\mathbf{R}_a$ and $\mathbf{R}_b$ as shown in Figure 2-4. The output PMD vectors of each of the individual sections are $\vec{\tau}_a$ and $\vec{\tau}_b$. There is a polarization rotator at their junction whose rotation matrix is denoted as $\mathbf{C}$. The rotation matrix $\mathbf{C}$ is assumed to be frequency independent over the frequency range of interest. Our goal is to determine the output PMD vector of the combined assembly. The rotation matrix $\mathbf{R}$ of the two-section concatenation is the matrix product

$$\mathbf{R} = \mathbf{R}_b\mathbf{C}\mathbf{R}_a \tag{2.30}$$

Combining this with (2.27), we find that the PMD vector $\vec{\tau}$ of the assembly that

$$\vec{\tau}\times = \mathbf{R}_\omega\mathbf{R}^\dagger = \mathbf{R}_{\omega b}(\mathbf{C}\mathbf{R}_a)(\mathbf{C}\mathbf{R}_a)^\dagger\mathbf{R}_b^\dagger + (\mathbf{R}_b\mathbf{C})\mathbf{R}_{\omega a}\mathbf{R}_a^\dagger(\mathbf{R}_b\mathbf{C})^\dagger \tag{2.31}$$

Applying $(\mathbf{C}\mathbf{R}_a)(\mathbf{C}\mathbf{R}_a)^\dagger = \mathbf{I}$, equation (2.27) for the individual sections, and a trans-

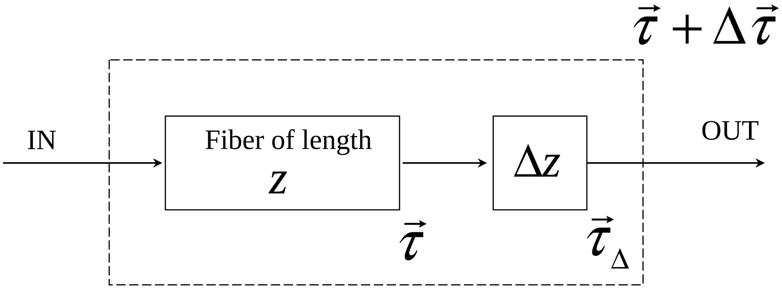

Figure 2-5: A long piece of fiber concatenated to a differentially small fiber addition of length Δz

formation of matrix operation of

$$(\mathbf{R}_b\mathbf{C})\mathbf{R}_{\omega a}\mathbf{R}_a^\dagger(\mathbf{R}_b\mathbf{C})^\dagger = (\mathbf{R}_b\mathbf{C})(\vec{\tau}_a\times)(\mathbf{R}_b\mathbf{C})^\dagger = (\mathbf{R}_b\mathbf{C}\vec{\tau}_a)\times \tag{2.32}$$

we can simplify equation (2.31) into the form

$$\vec{\tau} = \vec{\tau}_b + \mathbf{R}_b\mathbf{C}\vec{\tau}_a \tag{2.33}$$

This is the basic concatenation rule for the first order PMD vector. The rule is very similar to that for the impedances of a transmission line. To get the PMD vector of an assembly, transform the PMD vectors of each individual section to a common reference plane and take the sum of all those vectors. It can be transformed to the input of the fiber. It can also be generalized to multiple sections as well as differentially small sections. When it is applied to the case of differentially small sections, it gives the dynamical PMD equation [53].

To be more specify, we apply the two-section concatenation rule to a long piece of fiber with output PMD vector $\vec{\tau}$ and a differentially small fiber addition of length Δz as shown in Figure 2-5. From equation (2.22), the change $\Delta\hat{t}$ of the Stokes vector $\hat{t}$ entering the element is

$$\Delta\hat{t} = \Delta z\vec{\beta}\times\hat{t} \tag{2.34}$$

The output Stokes vector $\hat{t} + \Delta\hat{t}$ can be expressed in terms of rotation matrix $\mathbf{R}_\Delta$ as,

$$\hat{t} + \Delta\hat{t} = \mathbf{R}_\Delta \hat{t} \tag{2.35}$$

Substitute equation (2.34) into equation (2.35) gives

$$\mathbf{R}_\Delta = (\mathbf{I} + \Delta z \beta \times) \tag{2.36}$$

The corresponding PMD vector $\vec{\tau}_\Delta$ of this small element can be found from R_Δ and its derivative as in equation (2.27). By dropping the second order term in Δz, we obtain

$$\vec{\tau}_\Delta = \Delta z \vec{\beta}_\omega \tag{2.37}$$

Using the PMD concatenation rule equation (2.33), in combination with equation (2.36) and equation (2.37), we get

$$\vec{\tau} + \Delta\vec{\tau} = \vec{\tau}_\Delta + \mathbf{R}_\Delta \vec{\tau} = \Delta z \vec{\beta}_\omega + \left(\mathrm{I} + \Delta z \vec{\beta} \times\right) \vec{\tau} \tag{2.38}$$

And this simplifies to give the dynamical PMD equation

$$\frac{\Delta\vec{\tau}}{\Delta z} = \vec{\beta}_\omega + \vec{\beta} \times \vec{\tau} \tag{2.39}$$

2.8 Higher-Orders PMD

In first order approximation, $\vec{\tau}$ in eqn. (2.25) can be approximated as a constant vector over a small bandwidth about the center frequency. In this approximation, $\vec{\tau}$ is commonly known as the first-order PMD and the bandwidth over which the approximation holds is called the bandwidth of the principal state of polarization or PSP bandwidth $\Delta\omega_{PSP}$. The concept of PSP bandwidth is important for frequency-domain measurement of PMD vectors where measurements of the output SOP at two or more frequencies are required. These frequencies have to be confined to the PSP bandwidth in order to reduce inaccuracy caused by higher-order PMD. On the

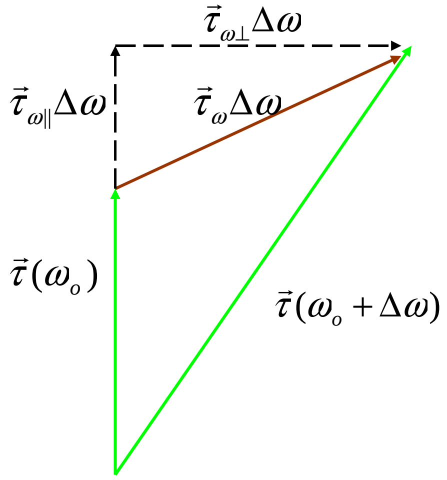

Figure 2-6: A vector diagram of the second order PMD and its components

other hand, in statistical PMD measurements, the samples of $\vec{\tau}(\omega)$ are deemed to be statistically independent if their frequencies are at least six times the PSP bandwidth apart. While different constants have been reported [54, 55, 56, 57], a good practical estimate for $\Delta\omega_{PSP}$ is given by

$$\Delta\omega_{PSP}\cdot\bar{\tau}_{DGD}=\frac{\pi}{4} \tag{2.40}$$

where $\bar{\tau}_{DGD}$ is the mean DGD of the fiber. The correlation function of the PMD vectors $\vec{\tau}(\omega_o)$ and $\vec{\tau}(\omega_o+\Delta\omega)$ recently reported in [56, 58] provides an elegant confirmation and interpretation of the $\Delta\omega_{PSP}$ concept and its practical implications. When the bandwidth of interest is larger than $\Delta\omega_{PSP}$, the first order PMD approximation no longer holds and $\vec{\tau}$ varies with the optical frequency. This frequency dependence in $\vec{\tau}$ causes the precession direction and the precession rate in equation (2.25) to change with frequency. This gives rise to higher-order PMD. A Taylor expansion of $\vec{\tau}(\omega)$ about the carrier frequency ω_o has been commonly used to describe this frequency dependence [59],

$$\vec{\tau}(\omega_o+\Delta\omega)=\vec{\tau}(\omega_o)+\vec{\tau}_\omega(\omega_o)\Delta\omega+\frac{1}{2}\vec{\tau}_{\omega\omega}(\omega_o)\Delta\omega^2+... \tag{2.41}$$

where the subscript ω indicates differentiation. $\vec{\tau}\left(\omega_o\right)$, $\vec{\tau}_\omega\left(\omega_o\right)$ and $\vec{\tau}_{\omega\omega}\left(\omega_o\right)$ are commonly called the first-, second-, and third- order PMD. Using eqn. (2.16), the second-order PMD can be expressed as

$$\vec{\tau}_\omega\left(\omega_o\right)=\left.\frac{d\vec{\tau}}{d\omega}\right|_{\omega_o}=\left.\frac{d\tau_g}{d\omega}\right|_{\omega_o}\hat{p}\left(\omega_o\right)+\tau_g\left(\omega_o\right)\hat{p}_\omega\left(\omega_o\right) \tag{2.42}$$

It has two terms. The first term on the right-hand side of equation (2.42) is $\vec{\tau}_{\omega||}$, the component of $\vec{\tau}_\omega$ that is parallel to $\vec{\tau}\left(\omega_o\right)$, whereas the second term $\vec{\tau}_{\omega\perp}$ is the component of $\vec{\tau}_\omega$ that is perpendicular to $\vec{\tau}\left(\omega_o\right)$. Figure 2-6 shows a vector diagram of the second order PMD vector and its components. The magnitude of the first term, $\left.d\tau_g/d\omega\right|_{\omega_o}$ is the change of the DGD with frequency. This term creates polarization-dependent chromatic dispersion [60] which, in the presence of chirp, can cause either pulse compression or broadening depending on the polarization. The second term in equation (2.42), $\vec{\tau}_{\omega\perp}$, describes the PSP depolarization, a rotation of PSP with frequency. Pulse distortions caused by PSP depolarization include overshoots and generation of satellite pulses [18]. It can also have a detrimental effect on first order PMD compensators. Second- and third- order PMD can also be concatenated. By differentiating eqn. (2.33), we get

$$\vec{\tau}_\omega=\vec{\tau}_{\omega b}+\mathbf{R_b C}\vec{\tau}_{\omega a}+\mathbf{R_{\omega b}C}\vec{\tau}_a=\vec{\tau}_{\omega b}+\mathbf{R_b C}\vec{\tau}_{\omega a}+\mathbf{R_{\omega b}R_b^\dagger R_b C}\vec{\tau}_a \tag{2.43}$$

By using $\vec{\tau}_b\times=\mathbf{R_{\omega b}R_b^\dagger}$, we obtain the concatenation rule for the second order PMD, $\vec{\tau}_\omega$, as

$$\vec{\tau}_\omega=\vec{\tau}_{\omega b}+\mathbf{R_b C}\vec{\tau}_{\omega a}+\vec{\tau}_b\times\mathbf{R_b C}\vec{\tau}_a=\vec{\tau}_{\omega b}+\mathbf{R_b C}\vec{\tau}_{\omega a}+\vec{\tau}_b\times\vec{\tau} \tag{2.44}$$

By differentiating equation 2.44, we get

$$\begin{aligned}\vec{\tau}_{\omega\omega} &= \vec{\tau}_{\omega\omega b}+\mathbf{R_{\omega b}C}\vec{\tau}_{\omega a}+\mathbf{R_b C}\vec{\tau}_{\omega\omega a}+\vec{\tau}_{\omega b}\times\vec{\tau}+\vec{\tau}_b\times\vec{\tau}_\omega && \text{(2.45a)}\\ &= \vec{\tau}_{\omega\omega b}+\mathbf{R_{\omega b}R_b^\dagger R_b C}\vec{\tau}_{\omega a}+\mathbf{R_b C}\vec{\tau}_{\omega\omega a}+\vec{\tau}_{\omega b}\times\vec{\tau}+\vec{\tau}_b\times\vec{\tau}_\omega && \text{(2.45b)}\end{aligned}$$

By using $\vec{\tau}_b \times = \mathbf{R}_{\omega\mathbf{b}}\mathbf{R}_{\mathbf{b}}^{\dagger}$, we obtain the concatenation rule for the third order PMD, $\vec{\tau}_{\omega\omega}$, as

$$\vec{\tau}_{\omega\omega} = \vec{\tau}_{\omega\omega b} + \mathbf{R}_{\mathbf{b}}\mathbf{C}\vec{\tau}_{\omega\omega a} + \vec{\tau}_b \times \mathbf{R}_{\mathbf{b}}\mathbf{C}\vec{\tau}_{\omega a} + \vec{\tau}_{\omega b} \times \vec{\tau} + \vec{\tau}_b \times \vec{\tau}_{\omega} \tag{2.46}$$

2.9 PMD Characterization Technique

The three most common PMD characterization techniques used in the laboratory are: 1) Jones Matrix Eigenanalysis, 2) the Mueller Matrix Method and 3) Poincaré Sphere Analysis. Jones Matrix Eigenanalysis [61] uses a set of pre-determined input polarization states to determine the complete Jones Matrix $\mathbf{U}$ of the fiber at each frequency. By measuring the Jones matrix at closely spaced frequency intervals, one can compute its frequency derivative $\mathbf{U}_{\omega}$, and then determine the matrix product $j\mathbf{U}_{\omega}\mathbf{U}^{\dagger}$. Using the σ-expansion in equation (2.21), one can determine the full PMD vector.

The Mueller Matrix Method [57] measures PMD in much the same way as the Jones matrix method. The difference is it works entirely in Stokes space, and measures the rotation matrix $\mathbf{R}$ as a function of frequency. In this way, one can compute $\mathbf{R}_{\omega}$ and the matrix product $\mathbf{R}_{\omega}\mathbf{R}^{\dagger}$. Using equation (2.27) and the matrix form of the cross-product operator similar to equation (2.11), one can determine the full PMD vector.

The Poincaré Sphere Analysis [30] measures the precession of an output SOP about $\vec{\tau}$ as a function of frequency as seen in equation (2.25). Using two different input SOPs, the corresponding output SOP $\hat{t}_i$ and $\hat{t}_j$ are measured at each frequency. The PMD vector can then be computed using eqn. (2.25) and the vector identity $\vec{a} \times \vec{b} \times \vec{c} = (\vec{a}.\vec{c})\,\vec{b} - \left(\vec{b}.\vec{a}\right)\vec{c}$ to be

$$\vec{\tau} = \frac{\frac{d\hat{t}_i}{d\omega} \times \frac{d\hat{t}_j}{d\omega}}{\left|\frac{d\hat{t}_i}{d\omega} \cdot \hat{t}_j\right|} \tag{2.47}$$

The main difference between the Poincaré Sphere Analysis and the other two techniques is that no knowledge of the input SOP is required to determine the output

PMD vector. This is evident in equation (2.47).

The above three techniques belong to the generic class of "polarimetric techniques" in the frequency domain. They find both the DGD and the PSP by measuring the frequency-dependent rotation of the output polarization state. To measure the output polarization, a polarimeter is needed. Figure 2-7 shows the schematic of a polarimeter. In order to understand the working principle of a polarimeter, we need to know the transmission through a perfect polarizer in Stokes space. For an incoming light of polarization $\vec{r}$ passing through a perfect polarizer whose transmission axis is $\hat{p}$, the intensity transmission [17] expressed in Stokes space representation is given by

$$T = \frac{1}{2}\left(1 + \vec{r} \cdot \hat{p}\right) \tag{2.48}$$

To measure an unknown polarization $\vec{r} = \{r_1, r_2, r_3\}$, three polarizers are needed, one for each component: for r_1, a polarizer with horizontal transmission axis $\hat{p} = \{1, 0, 0\}$; for r_2, a polarizer with transmission axis aligned at 45^o with $\hat{p} = \{0, 1, 0\}$; for r_3, a polarizer with $\hat{p} = \{0, 0, 1\}$. This can be achieved by a quarter-wave plate with vertical slow axis followed by a polarizer with transmission axis oriented at 45^o. By measuring the intensity transmission through each polarizer (i.e. $\frac{I_i}{I_0}$), we can deduce the respective component of the polarization using eqn. (2.48). This should explain the required layout of the polarimeter shown in Figure 2-7.

For perfectly polarized light, $\vec{r}$ has a unit norm and lies on the surface of the unit Poincaré sphere. The degree of polarization (DOP) defined as

$$DOP = \sqrt{r_1^2 + r_2^2 + r_3^2} \tag{2.49}$$

is unity for this case. In general, due to the response time of detectors, the polarimeter intrinsically measures the SOP averaged over the pulse duration (or equivalently, over the pulse spectrum). Thus $\vec{r}$ is in fact a weighted average of the Stokes vector $\hat{s}(\omega)$ across the spectrum of the signal given by

$$\vec{r} = \int \frac{d\omega}{2\pi} \left|H(\omega)\right|^2 \hat{s}(\omega) \tag{2.50}$$

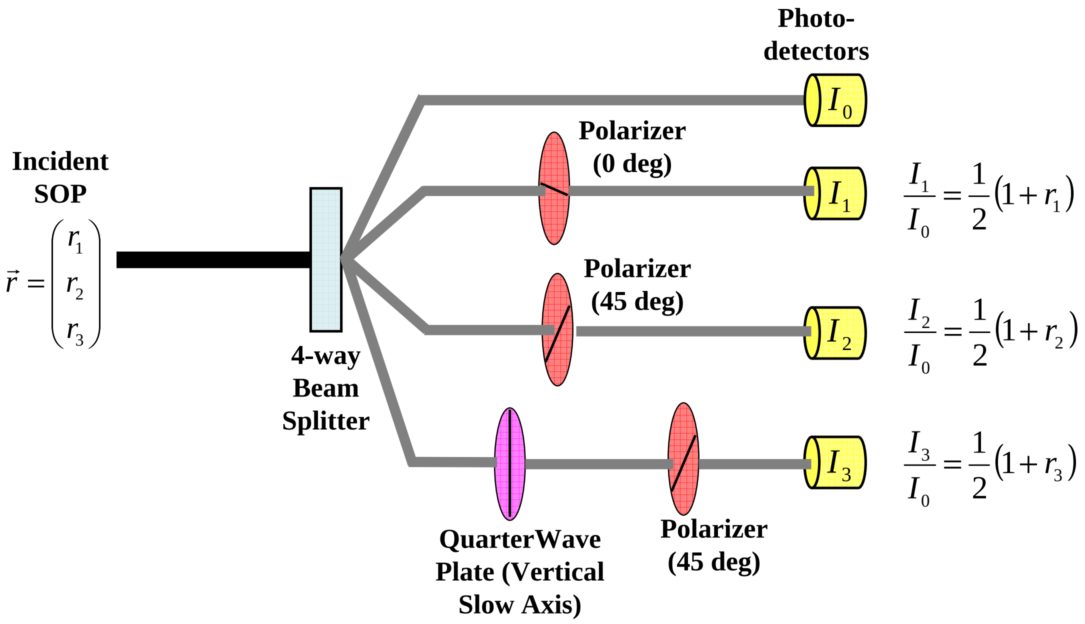

Figure 2-7: Schematics of a polarimeter

where $|H(\omega)|^2$ is the signal spectrum normalized to $\int d\omega\, |H(\omega)|^2/2\pi = 1$. This makes $\vec{r}$ generally lies inside the unit Poincaré sphere with DOP less than 1. An exception is when $\hat{s}(\omega) = \hat{s}(\omega_o)$ for all frequency in the pulse, which results in $\vec{r} = \hat{s}(\omega_o)$.

2.10 Statistics of PMD

Compared to other system impairments, the impairment due to PMD is much more challenging to deal with since it is changing stochastically with wavelength and time. This means that one cannot predict the impairment of the system at any particular wavelength and time but resort to a statistical description. Tolerance of worst-case impairment is rarely possible when PMD is a significant source of impairment. The probability densities for PMD in most situations have asymptotic tails extending to unacceptably large impairment. Hence, the system cannot be designed to handle the worst-case PMD impairment and must instead be designed for a specified outage probability. For similar reasons, the goal of PMD compensation cannot be to eliminate the impairment but rather to reduce the PMD outage probability. To understand and predict the system outage probabilities, to design compensators, and

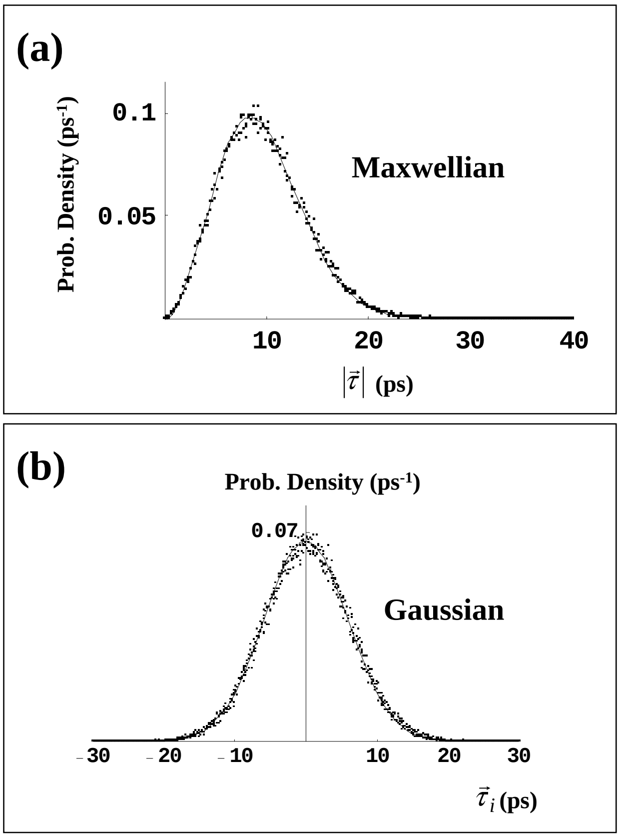

Figure 2-8: Maxwellian probability distributions for the DGD and Gaussian distribution for each of the components of the PMD vector

to accurately measure PMD in systems, one must understand the statistics of the phenomena associated with PMD.

The first statistical property of PMD to attract interest was the mean DGD [19, 62]. It is time consuming and tedious to obtain an accurate estimate of the mean DGD by repeatedly measuring the DGD at one wavelength over time. Instead, the DGD is averaged over wavelength and the result is assumed to be equal to the time average. This assumption is of crucial importance. Virtually every measured mean DGD value quoted in the literature was obtained by wavelength averaging.

The probability density of the DGD is shown in Figure 2-8. For fully random PMD, the problem can be reduced to that of the probability density of the magnitude of the sum of 3-D vectors having random orientation and length. The result is the well-known Maxwellian distribution for the DGD shown in Figure 2-8 given by [59]

$$pdf\left(|\vec{\tau}|\right)=\frac{8}{\pi^2\left\langle|\vec{\tau}|\right\rangle}\left(\frac{2\left|\vec{\tau}\right|}{\left\langle|\vec{\tau}|\right\rangle}\right)^2 e^{-(2|\vec{\tau}|/\langle|\vec{\tau}|\rangle)^2/\pi} \tag{2.51}$$

and each of its vector components, $\vec{\tau}_i$, follows a Gaussian function

$$pdf\left(|\vec{\tau}_i|\right)=\frac{2}{\pi\left\langle|\vec{\tau}|\right\rangle}e^{-(2|\vec{\tau}_i|/\langle|\vec{\tau}|\rangle)^2/\pi} \tag{2.52}$$

where $\langle|\vec{\tau}|\rangle$ is the mean DGD of fiber. Statistical properties of the higher-order PMD can be found in [63].

The required speed of the PMD compensators depends on the time rate of change of the PMD in the fiber. A number of groups [29, 31, 64, 65] have made long-term PMD measurements. The consensus is that temperature changes in embedded fibers are slow in general, and thus cause slow PMD variations on the time scale of hours to days. On the other hand, human operation in buildings, mechanical vibrations, or wind for aerial fibers can cause much rapid PMD fluctuations on the timescale of milliseconds [29] to seconds [64] depending on the mechanism of the perturbation.

2.11 System effects of PMD

Fiber PMD can cause a variety of impairments in optical fiber transmission systems. For a single channel, intersymbol interference impairment is caused by the DGD between the two pulses propagating in the fiber when the input polarization of the signal is not aligned to the fiber's PSP [66]. For larger signal bandwidth, systems impairments can occur due to second- and higher-order PMD, particularly when these PMD components combine with the chromatic fiber dispersion or signal chirp [60, 55].

The outage criterion is defined as the maximum ratio of mean DGD to bit interval (i.e $\bar{\tau}/T$) that one can tolerate without any compensation. The generally accepted value for this outage criterion is approximately $\bar{\tau}/T \leqslant 0.1$. As the signal bandwidth Δf is roughly equal to $\sim 1/T$, and $\bar{\tau}$ is related to the PSP bandwidth by eqn. (2.40), the outage criterion is roughly equivalent to $\Delta f \leqslant \Delta f_{PSP}$. Since the effects of second order PMD are insignificant as long as the bandwidth of the signal Δf is smaller than the PSP bandwidth. This implies that second order penalties are negligible as long as the first order outage criterion is met. This important observation has been confirmed repeatedly by experiments and simulations [67]. In the other words, it means that there is no worry about second order PMD as long as there is no need for first order PMD compensation. However, when the outage criterion is not met, there is a need for PMD compensation as well as a need for concern about second order PMD impairments.

The system impacts of the second order PMD have been studied in Ref. [60, 55, 67, 68, 69]. The simplest second-order impairment is the polarization dependent chromatic dispersion. The PCD increases or decreases the effective chromatic dispersion of the transmission system depending on the input state of polarization. However, statistically this effect is a relatively minor component of the second order PMD. The dominant impairment mechanism is caused by the PSP depolarization term [60, 55]. This depolarization term leads to pulse overshoots and satellite pulses. Statistical analyses and numerical simulations of system impairments indicate a strong interaction between chromatic dispersion in the fiber and its second order PMD in general [60]. Similarly, it has been found that chirp in the transmitted signal has a significant impact on second order PMD impairments [67].

The stochastic fluctuations of PMD in optical fibers compel systems designers to allocate a power margin (typically 1 or 2dB) in their link budget in order to avoid error bursts caused by large signal distortions due to PMD. However, there is always a finite probability (often called the outage probability) that distortions exceed the allocated margin. The outage probability increases with $\bar{\tau}/T$, the ratio of the mean DGD and the bit interval of the transmitted signal. When the outage probability exceeds the value specified by the system operator, larger margin should be allocated or PMD mitigation technique is required. PMD can also cause impairments in WDM systems because it changes the relative polarization of the different wavelength channels as they propagate along the fiber. Thus in WDM systems where adjacent wavelength channels are launched with orthogonal polarizations to suppress nonlinear impairments such as cross-phase modulation or four wave mixing, PMD destroys the orthogonality of these polarizations [70]. Another example is in system where polarization multiplexing is used for close packing of WDM channels in order to achieve high bandwidth efficiency. Here PMD induces coherent cross-talk between multiplexed channels leading to system impairments [71, 72].

2.12 PMD Mitigation

One of the simplest and potentially least costly ways of reducing PMD impairment is to deploy fiber having low PMD. For example, fiber link having DGD less than 2% of the current bit rate would have sufficiently low PMD for the current systems, as well as the next generation systems assuming that the bit rates will increase by a factor four. Since less than 1% core ellipticity and the associated stress can result in significant birefringence, much work in fiber manufacturing has focused on reducing deviations in the circularity of the fiber preform. Much of this work is proprietary information. As further reduction in the intrinsic fiber birefringence becomes difficult, attention is shifted to mitigating it. One method used to reduce the effect of intrinsic birefringence is spinning [73]. An intuitive explanation of how spinning reduces PMD uses the model of fiber being a cascade of N randomly oriented birefringent element $\Delta\tau$. The mean DGD of the concatenation is $\Delta\tau\ \sqrt{N}$ [74]. Spinning the fiber during the drawing process decreases the coupling length of the fiber. For the same length of fiber, this gives smaller $\Delta\tau$ but larger N. However, the mean DGD scales as $\sqrt{N}$ and linearly as $\Delta\tau$, therefore spinning results in a smaller mean DGD. These efforts devoted to the reduction of fiber PMD have been rewarded with great success. Field measurements indicate that some production fiber manufactured in the late 1980's had PMD well beyond 1ps/$\sqrt{km}$ [18]. It is currently possible to purchase large quantities of fiber having PMD less than 0.1ps/$\sqrt{km}$ on the spool and considerably less than that when cabled.

Other approaches that are actively pursued to mitigate the PMD effect include the use of novel modulation formats than the conventional NRZ format [26, 75, 76], soliton transmission [77, 78], Forward Error Correction [79, 80], and simply increasing the power margin. Data formats such as RZ, carrier-suppressed RZ, chirped NRZ, chirped RZ, phase-shaped binary transmission are more resistant to PMD than the conventional NRZ format [81]. Generally, there seems to be a consensus that formats with low duty cycle (eg. Chirped RZ and RZ) are more resistant to PMD as it takes more DGD for these pulses to leak out into the neighbouring bit slots while data formats with small spectral width such as NRZ are more effectively compensated in optical compensators.

The use of FEC is another way to improve the system performance when it is already suffers from a high BER. Even though FEC is not a PMD compensator technique it can mitigate the effects of PMD in terms of outage probability in a similar way as an increased power margin. The use of FEC in systems limited by PMD has been studied [79, 80].

Soliton transmission was first introduced to compensate for chromatic dispersion by taking advantage of the nonlinear effects. However, solitons are also resistant to other kinds of perturbations, such as PMD. The two orthogonal polarization states that are differentially delayed as an effect of PMD, induce a nonlinear phase shift due to cross-phase modulation that mutually shifts one-another frequencies in opposite directions. Through the chromatic dispersion, the two polarization states will travel at different speeds that fortunately counteract the PMD-induced delay. This phenomenon is sometimes referred to as soliton trapping and works optimally in polarization maintaining fibers. However, in real telecom fibers, where the solitons must adapt to the random birefringence, the solitons will shed some of their energy to dispersive wave radiation. The inherent robustness of soliton to PMD has been studied in both conventional and dispersion-managed systems [77, 78].

2.13 PMD Compensation

In some cases, the mitigation techniques discussed in the above section are inadequate and active PMD compensation must be employed. The main challenge in active PMD compensation lies in the fact that the temporal drift of the PMD parameters forces any active compensation technique to dynamically adapt to changes while the system is in operation.

There are a number of optical [82, 83, 84] and electronic [85, 86] PMD compensators being proposed. Integrated electronics solutions have the advantage that they consist of small and fast circuits that can be incorporated in the receiver, which can also compensate for other types of distortions such as chromatic dispersion. Electronics PMD mitigation is preferred over optical PMD compensation at 10 Gbit/s due to its lower cost. However, when the bit rate is increased to 40Gbit/s per channel and beyond, the required electronics is still immature. This makes its implementation difficult and expensive. Furthermore, even though the components in the electrical domain are generally faster and more flexible than bulk optics, the phase information is lost after detection. This results in non-zero dispersion penalty even when optimal equalizers are used. Therefore optical PMD compensators may have larger potential as the PMD, in theory, can be completely compensated in the optical domain. For optical domain compensation, compensators generally fall into three main categories: (1) PSP transmission method, (2) Post compensation in feedback scheme, (3) Post compensation in feed-forward scheme.

The PSP transmission method is obtained by aligning the input SOP to one of the input PSP [81] of the transmission fiber. This scheme effectively has two degree of freedoms (DOF). The main disadvantage of this method is that it requires a control signal to be fed from the receiver all the way back to the input, and thus making this scheme inherently slow. Post-compensation at the receiver's end is therefore desirable and has been an active research field.

Most post-compensation techniques in the literature [87, 88, 81, 89, 90] work in a feed-back scheme. They vary in the degree of freedom (DOF) used in the compensator and the type of feedback control signal used. The most commonly demonstrated method is of the polarization controller + fixed DGD type. It has two degrees of freedom from the polarization controller [89]. Its advantage lies in its simplicity and the small number of DOF. With a fixed DGD in the compensator, it cannot cancel the complete PMD vector. Instead, its working principle is to effectively create an appropriate combined PMD of the transmission line and the compensator so that when this combined PMD is transformed to the input plane, it is aligned with input SOP. The main disadvantage is that the compensator may create a large combined PMD, thus introducing more higher-order PMD to the system. Another variation employs an additional DOF by replacing the fixed DGD by a variable one [88]. Other variety increases the DOF to account for higher-order PMD [87, 91].

Some of the most common feedback signals used are (1) Degree of Polarization [92]: from equation (2.25), PMD introduces different polarizations for different spectral components in the signal thereby reducing the DOP as seen in equation (2.50). The feedback algorithm works to increase the DOP; (2) "Spectral line" feedback: it is based on the analysis of the electrical spectrum. Since PMD generates a minimum in the spectrum at the frequency 0.5/DGD [88], the maximization of spectrum samples, eg. at $1/4$ or $1/2$ of the bitrate, indicates a decrease in the residual PMD distortion, and (3) Eye-diagram: the analysis of the detected eye diagram at decision time provides a measure with the best correlation to the BER. This can be accomplished by an electronic eye monitor which allows one to extract the eye opening or to estimate the Q-factor at PMD output [93].

The inherent challenge in PMD compensation based on feed-back schemes lies in finding the global optimum and tracking it in all situations. There is often a risk that the compensator loses track and ends up in an unfavourable position, either because it is too slow or because the error signal is associated with sub-optima. Therefore, feedback schemes are often restricted to the use of a small number of DOF and compensation is mainly for the first-order PMD. As the bit rate of a single channel increases, a compensator that cancels first order PMD is no longer sufficient since higher order PMD dominates the signal's degradation. Typical higher order PMD compensators are multistage devices that have many degrees of freedom [87, 91, 8]. If the compensation scheme relies on feedback loops, the complexity involved in searching the optimum of many parameters may hinder the development of a fast and stable compensator. Thus, a feed-forward approach to PMD compensation appears more desirable when higher- order PMD has to be compensated. In this thesis, we focus on this deterministic approach that diagnoses the PMD vectors and use this information to carry out the appropriate compensation.

2.14 PMD Emulation

Although modern fibers have PMD values ~0.1ps/$\sqrt{km}$, many of the previously installed fiber spans have higher PMD values. A critical problem for designers of high performance systems is to measure the performance degradations due to the high-PMD fiber spans [22]. Unfortunately, these high-PMD fibers are not readily available. Moreover, even if they are available, it would be hard to rapidly explore the large number of different fiber ensembles that is required to determine the distribution of penalty due to PMD. For testing of optical systems that may be affected by PMD and especially for the performance study of PMD compensators, it is critical to be able to accurately emulate the first and higher-order PMD and quickly cycle through a large number of different fiber states.

The fiber is typically modelled as a concatenation of randomly coupled linear birefringent sections. Consequently, a device to emulate fiber PMD may be constructed by concatenating many birefringent elements [94, 95]. These elements may be sections of polarization maintaining fiber, birefringent crystals or any other device that provides a differential group delay between the two orthogonal polarization axes (e.g. a polarization beam splitter followed by two paths of differing lengths and a polarization beam combiner). To achieve different PMD states, some properties of the emulator must be varied between samples, such as the polarization coupling between sections or the birefringence of each section. With a sufficient number of these sections, the PMD statistics of the emulator will mimic those of a real fiber. Reference [95] concludes that a 15-section emulator with rotatable sections presents a good compromise between meeting the theoretical design criteria and practical implementation. For example, to obtain an emulator of root mean square DGD of DGD_{rms} using a concatenation of N birefringent element (for $N > 15$), the required DGD per element

ΔDGD is given by [74]

$$\Delta DGD = \frac{DGD_{rms}}{\sqrt{N}} \tag{2.53}$$

To avoid an undesired periodicity in the frequency autocorrelation function [56], the DGD of each section is randomly chosen from a Gaussian distribution with a mean of ΔDGD and a standard deviation that is 20% of ΔDGD.

However, the main disadvantage of the above many-element emulator is that it is too time consuming to perform enough trials to evaluate the effects of extremely rare PMD events that cause outage probability of 10^{-6} (<1 min/yr) or less. Therefore, the tool of importance sampling [32, 33, 34] has recently attracted much attention. Importance sampling is a powerful tool for obtaining very low probability events with relatively few sample points. This is accomplished by altering the method of obtaining the random samples to concentrate the measured results in the area of interest in the sample space. This distorts the probability distribution of the measured results, so that each sample must then be appropriately weighted to map the measured values back onto the proper distribution function. With this importance sampling technique, one is strongly motivated to develop a programmable PMD emulator that has the ability to "dial-in" any PMD state [96, 13, 14] so that one can quickly investigate the PMD states of interest. One useful way to employ such emulator with a "dial-in" feature is to use Monte-Carlo simulation with importance sampling to generate the extremely rare events that occur in the tail of PMD distribution, and then "dial-in" these PMD states into the emulator and produce them physically. In this thesis we focus on this deterministic approach of emulation.

2.15 PMD in the presence of PDL

Polarization-Dependent Loss (PDL) of various inline optical components, such as switches, isolators, couplers, filters and circulators can be as high as 0.3 dB or more. When the optical pulse passes through an optical component with non-negligible PDL, it splits between two orthogonal polarizations that attenuate each optical pulse replica differently. Therefore in the presence of PDL, the full 4-parameters Stokes vector $\{S_0, S_{1,} S_{2,} S_3\}$ and the 4×4 Mueller matrix have to be employed in the Stoke space representation.

Pure PDL can cause deleterious effects in fiber links including: 1) optical power fluctuations resulting from OSNR variation due to polarization state wandering during propagation [97], induced gain ripple [98], and 3) limited PMD compensator performance [99]. Recent publications have also showed via theoretical and experimental results that the mutual interaction between PMD and PDL leads to significant performance degradation in long distance systems [36, 21]. These degradations are aggravated when low-frequency polarization scrambling ($\sim$ 20 kHz) is used at the transmitter end [100, 101, 102]. Polarization scrambling of the input State-Of-Polarization (SOP) may be applied for various reasons: to suppress the polarization-hole burning in erbium-doped fiber amplifiers [100, 101], and to facilitate the real-time monitoring of PMD in feed-forward PMD compensation schemes [103, 2, 4, 104]. In terms of real-time monitoring of PMD, the presence of PDL also has its deleterious effects. It causes the loss of orthogonality between the two Principal States-of-Polarization (PSPs), and makes them no longer represent the fastest and slowest propagating polarization states [20]. This affects the accuracy of the PMD characterization and thus compromises the effectiveness of the feed-forward PMD compensation.

Due to the complexity of PDL interacting with PMD, most works on PMD compensation ignore the presence of PDL to simplify the physics. However, studies show that PDL may compromise the effectiveness of some PMD compensators [99] and magnify the PMD-alone induced penalty [36]. In this thesis, we adopt the same approach of first ignoring the presence of PDL, and then in the last chapter of the thesis, we show how to account for, and compensate for, PDL.

Chapter 3

Real-Time PMD Monitoring

3.1 Background

One of the most challenging problems in feed-forward PMD compensation schemes is the real-time monitoring of the PMD information. Previous graduate students (Patrick Chou and John Fini) had proposed a method [2] that estimates the Principal State of Polarization (PSP) of the fiber, using polarization scrambling of the input State of Polarization (SOP). The measured values of the output averaged SOP were fitted to an ellipsoid in Stokes space. The intersection of the major axis of the ellipsoid with the unit Poincaré sphere gives the orientation of the PSP.

In this chapter, we present an improved version of the PMD estimation technique [4]. Figure 3-1 shows the schematic of the measurement. It involves a sequence of optical filtering of the tapped output signal, before the averaged SOP is measured using a polarimeter. It makes use of the spectrum of telecommunication signals. Three filters are used: a high-pass filter, a low-pass filter and a narrowband filter. The averaged SOP's of the filtered signals are then measured using a polarimeter. We repeat the measurement for several different input SOPs using a polarization scrambler at the input of the fiber. From these measurements, we deduce the first order PMD, and subsequently the second order PMD. Instead of fitting the output averaged SOP to an ellipsoid, we make use of the vectors that lie in the planes perpendicular to the PSP.

By numerical simulations, we show major improvements over the previous ellipsoid method [2]: (i) We substantially reduce the number of input SOPs required to achieve at the similar estimation accuracy of the PMD parameters. For example, to estimate the PSP within an angle deviation of $\sim 9^o$, the previous ellipsoid method [2] required at least forty input SOPs. However, in the current PMD estimation technique, we can achieve comparable estimation accuracy by using only three input SOPs. This implies faster characterization and a lower required scrambling rate of the polarization scrambler; (ii) We can distinguish the fast and slow PSP in the current PMD estimation technique, which is not possible in the previous method; (iii) We can accurately estimate the DGD; (iv) With a polarimeter of adequate accuracy, second order PMD estimation is possible; (v) The current PMD estimation technique uses a simple search algorithm that requires little computation time.

3.2 Theory of First Order PMD Characterization

We neglect the effect of polarization dependent loss. Due to the response time of detectors, the polarimeter intrinsically measures the SOP averaged over the pulse duration (or equivalently, pulse spectrum). We denote the averaged SOP as $\vec{r}$ and it is given as a weighted average of the Stokes vector $\hat{s}(\omega)$ across the spectrum of the signal,

$$\vec{r} = \int \frac{d\omega}{2\pi} |H(\omega)|^2 \hat{s}(\omega) \tag{3.1}$$

where $|H(\omega)|^2$ is the signal spectrum normalized to $\int d\omega |H(\omega)|^2/2\pi = 1$, so that for the case of $\hat{s}(\omega) = \hat{s}(\omega_o)$ for all ω, $\vec{r} = \hat{s}(\omega_o)$. The PMD Stokes vector, $\vec{\tau}(\omega)$ [17], describes the motion on the Poincaré sphere of the output SOP, $\hat{s}(\omega)$, as a function of angular frequency ω

$$\frac{d\hat{s}(\omega)}{d\omega} = \vec{\tau}(\omega) \times \hat{s}(\omega) \tag{3.2}$$

The magnitude $|\vec{\tau}|$ is the DGD while its direction $\hat{\tau}$ is the PSP direction. Taking a Taylor expansion of $\hat{s}(\omega)$ around the center angular frequency, ω_o, up to second order,

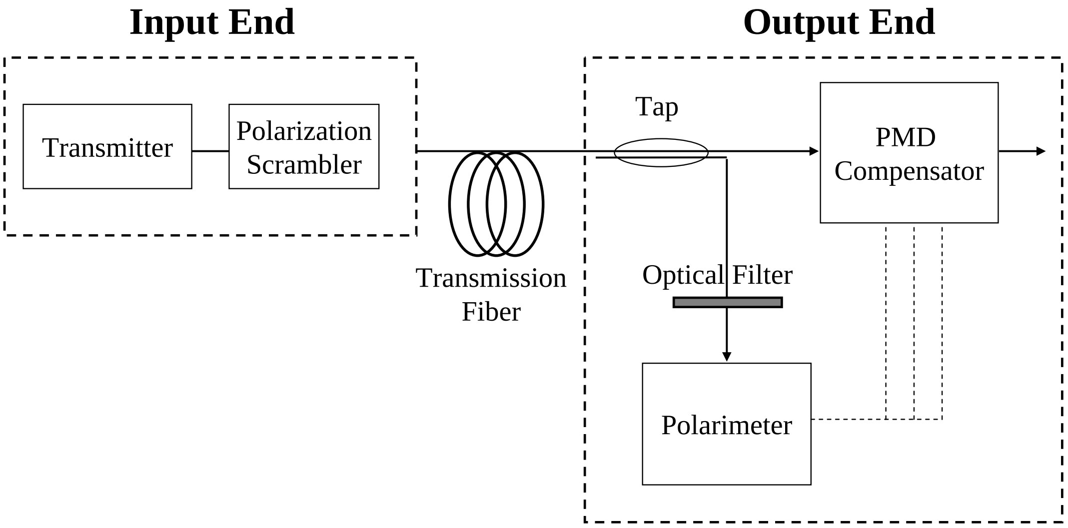

Figure 3-1: Schematics of the new PMD estimation technique. At the output end of fiber, signal is tapped and filtered. Its averaged SOP is measured using a polarimeter. Various input SOP are generated using a polarization scrambler at the input end of fiber.

substituting into (3.1) and making use of (3.2), we obtain the averaged SOP as

$$\vec{r} \cong \hat{s}(\omega_o) + \overline{\Delta\omega}\,[\vec{\tau}(\omega_o) \times \hat{s}(\omega_o)] + \tfrac{1}{2}\overline{\Delta\omega^2}\,[\vec{\tau} \times [\vec{\tau} \times \hat{s}(\omega_o)] + \vec{\tau}_\omega \times \hat{s}(\omega_o)] + ... \tag{3.3}$$

where $\overline{\Delta\omega} = \int d\omega\,|H(\omega)|^2\,(\omega - \omega_o)/2\pi$, $\overline{\Delta\omega^2} = \int d\omega\,|H(\omega)|^2\,(\omega - \omega_o)^2/2\pi$ and $\vec{\tau}_\omega = \frac{d\vec{\tau}}{d\omega}$ is the second order PMD.The polarimeter intrinsically measures the SOP $\vec{r}$, as given by (3.3). To measure the narrowband output SOP, $\hat{s}(\omega_o)$, one has to place a narrowband filter about ω_o before the polarimeter.

This PMD estimation technique makes use of the filtered signal spectrum [105, 106, 107]. Figure 3-2 shows a typical optical spectrum of a 10Gbit/s RZ pseudo-random bit sequence of length 2^7-1. Each '1' bit is a Gaussian pulse of 30ps FHWM pulse-width. This approximates the spectrum of the real telecommunication signal. In this figure, the signal spectrum is symmetrical about the carrier frequency. However, our estimation technique is equally valid when the signal spectrum is asymmetrical. For simplicity, we shall first consider this symmetrical signal spectrum.

The signal is tapped at the output of the fiber as shown in Figure 3-1. For every SOP generated by the polarization scrambler at the input of the fiber, we carry out

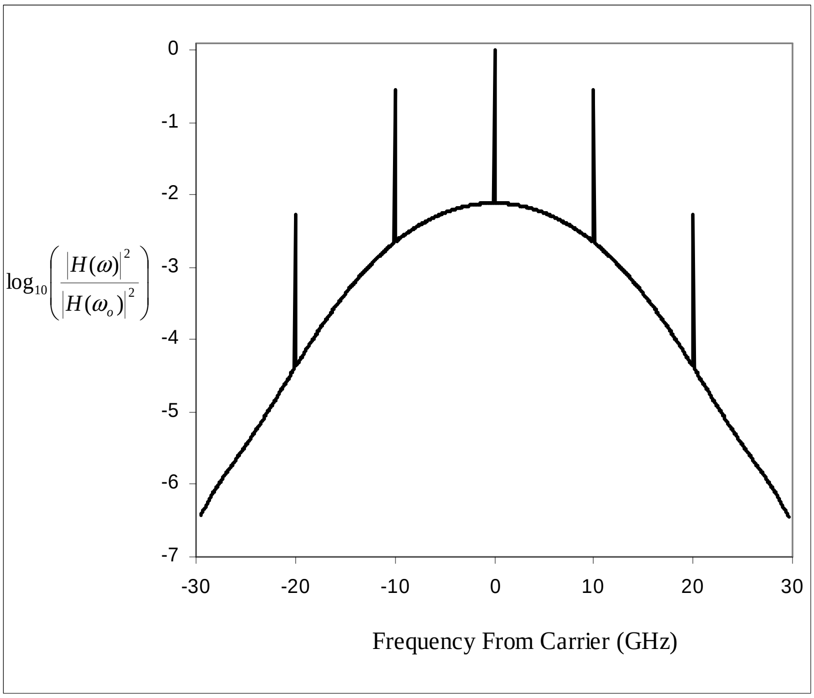

Figure 3-2: Optical Spectrum of a 10 Gbit/s RZ pseudo-random bit sequence of length (2^7-1). Each '1' bit is a Gaussian pulse of 30ps FWHM pulse-width.

three polarimeter measurements: 1) we measure the output $\hat{s}(\omega_o)$ with a narrowband filter about ω_o, and 2) the averaged SOP of signal filtered by a high-pass optical filter and (3) the averaged SOP of signal filtered by a low-pass optical filter. For simplicity, we assume the transmission curves of these filters are of rectangular profiles with the same transmission frequency bandwidth Δf_F as shown in Figure 3-3. A discussion of the use of realistic filter transmission profiles is given in the later portion of the chapter. The high-pass filter transmits frequency f within the range $f_o < f \leqslant f_o + \Delta f_F$ while the low-pass filter transmits $f_o - \Delta f_F \leqslant f < f_o$. We assume these optical filters are polarization insensitive. Figure 3-4 shows the simulated normalized average power transmitted by the high-pass (or low-pass) optical filters for various Δf_F. The normalized average power within the peak of the carrier frequency, f_o, is calculated to be 32%. Since the transmission of the high-pass (or low-pass) filter excludes f_o, the upper limit of the normalized averaged powers transmitted by the filter is therefore 34% for this symmetrical spectrum.

The transmitted signal using the high-pass filter has $\overline{\Delta\omega} = \overline{\Delta\omega_T}$ and $\overline{\Delta\omega^2} = \overline{\Delta\omega_T^2}$

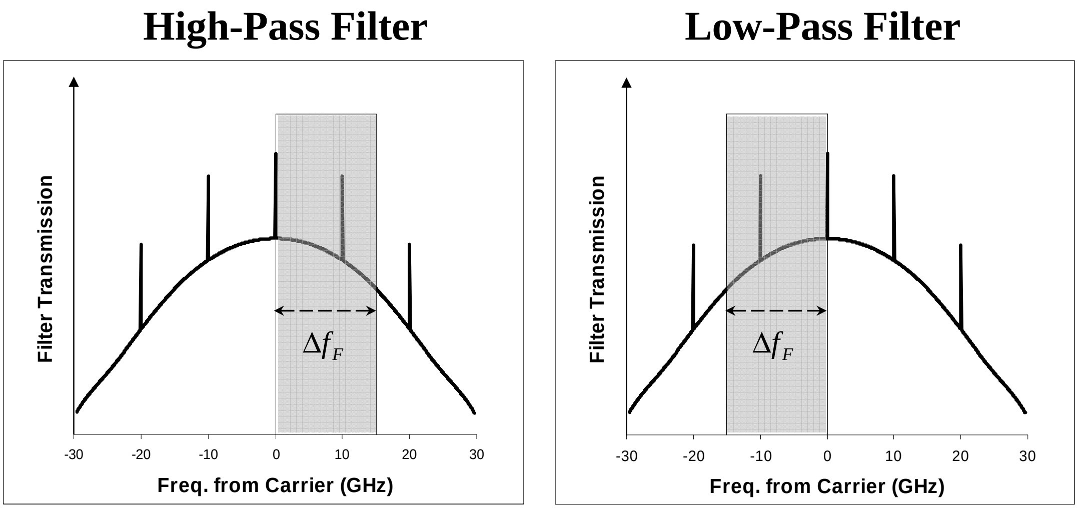

Figure 3-3: Transmission profiles of the high-pass filter and low-pass filter used in the PMD estimation techniques

while, the filtered signal using the low-pass filter has $\overline{\Delta\omega} = -\overline{\Delta\omega_T}$ and $\overline{\Delta\omega_T^2} = \overline{\Delta\omega_T^2}$. Thus the polarimeter measures the averaged SOP of these filtered signals as

$$\vec{r}_{HP} = \hat{s}(\omega_o) + \overline{\Delta\omega_T}\,[\vec{\tau}\times\hat{s}(\omega_o)] + \frac{1}{2}\overline{\Delta\omega_T^2}\,[\vec{\tau}\times[\vec{\tau}\times\hat{s}(\omega_o)] + \vec{\tau}_\omega\times\hat{s}(\omega_o)] + \ldots.. \tag{3.4}$$

for the high-pass filter and

$$\vec{r}_{LP} = \hat{s}(\omega_o) - \overline{\Delta\omega_T}\,[\vec{\tau}\times\hat{s}(\omega_o)] + \frac{1}{2}\overline{\Delta\omega_T^2}\,[\vec{\tau}\times[\vec{\tau}\times\hat{s}(\omega_o)] + \vec{\tau}_\omega\times\hat{s}(\omega_o)] + \ldots.. \tag{3.5}$$

for the low-pass filter. By taking the difference of $\vec{r}_{HP}$ and $\vec{r}_{LP}$, we obtain a vector

$$\vec{\tau}(\omega_o)\times\hat{s}(\omega_o) \cong \frac{(\vec{r}_{HP} - \vec{r}_{LP})}{2\overline{\Delta\omega_T}} \tag{3.6}$$

which lies in the plane normal to $\vec{\tau}(\omega_o)$. Polarization scrambling of the input SOP gives us several vectors $(\vec{r}_{HP} - \vec{r}_{LP})_i$ lying in different planes normal to $\vec{\tau}(\omega_o)$. By using a simple search algorithm to find the unit vector $\hat{p}$ that is perpendicular to all these $(\vec{r}_{HP} - \vec{r}_{LP})_i$, we determine the orientation of the PSP (i.e.$\hat{\tau}(\omega_o) = \hat{p}$). Ideally,

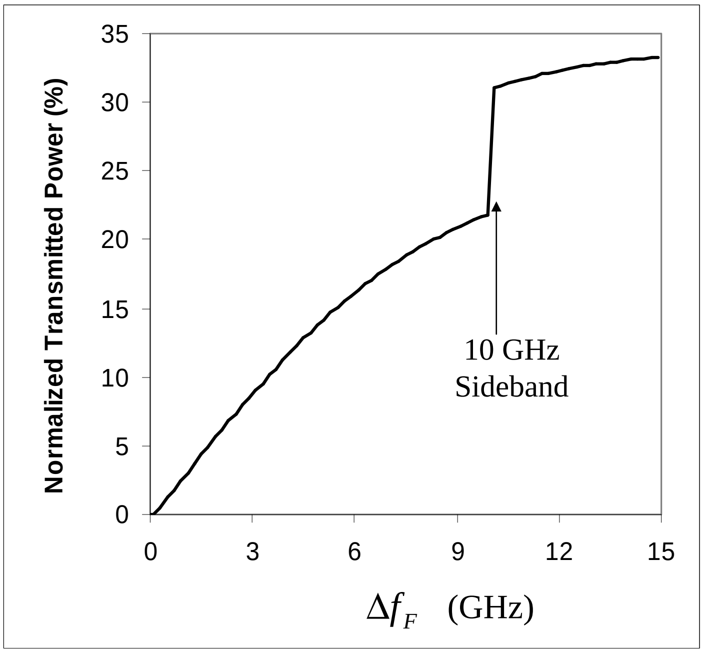

Figure 3-4: Normalized average power transmitted by the optical filters for various Δf_F.

$(\vec{r}_{HP} - \vec{r}_{LP})_i.\hat{p} = 0$. Because of errors in measurements, the $\hat{p}$ that satisfies

$$\sum_{i}^{All\ Input\ SOP} ((\vec{r}_{HP} - \vec{r}_{LP})_i.\hat{p})^2 = minimum \tag{3.7}$$

is the optimal estimate of the PSP $\hat{\tau}(\omega_o)$. Since the search involves only two parameters, it requires little computational time, and therefore it is suitable for fast real-time PMD characterization. In addition, since we know $(\vec{r}_{HP} - \vec{r}_{LP})$ and $\hat{s}(\omega_o)$, we can also distinguish the fast and slow PSP from equation (3.6),

After the PSP $\hat{\tau}(\omega_o)$ is determined, the angle subtended by $\vec{r}_{HP}$ and $\vec{r}_{LP}$ is projected onto the plane perpendicular to the PSP. This projected angle is given as

$$\cos(\theta) = \frac{\vec{r}_{HP\perp}.\vec{r}_{LP\perp}}{|\vec{r}_{HP\perp}|\,|\vec{r}_{LP\perp}|} \tag{3.8}$$

where $\vec{r}_{HP\perp} = \vec{r}_{HP} - (\vec{r}_{HP}.\hat{\tau})\hat{\tau}$ and $\vec{r}_{LP\perp} = \vec{r}_{LP} - (\vec{r}_{LP}.\hat{\tau})\hat{\tau}$. The DGD is then given as

$$DGD = |\vec{\tau}(\omega_o)| = \frac{\theta}{2\overline{\Delta\omega_T}} \tag{3.9}$$

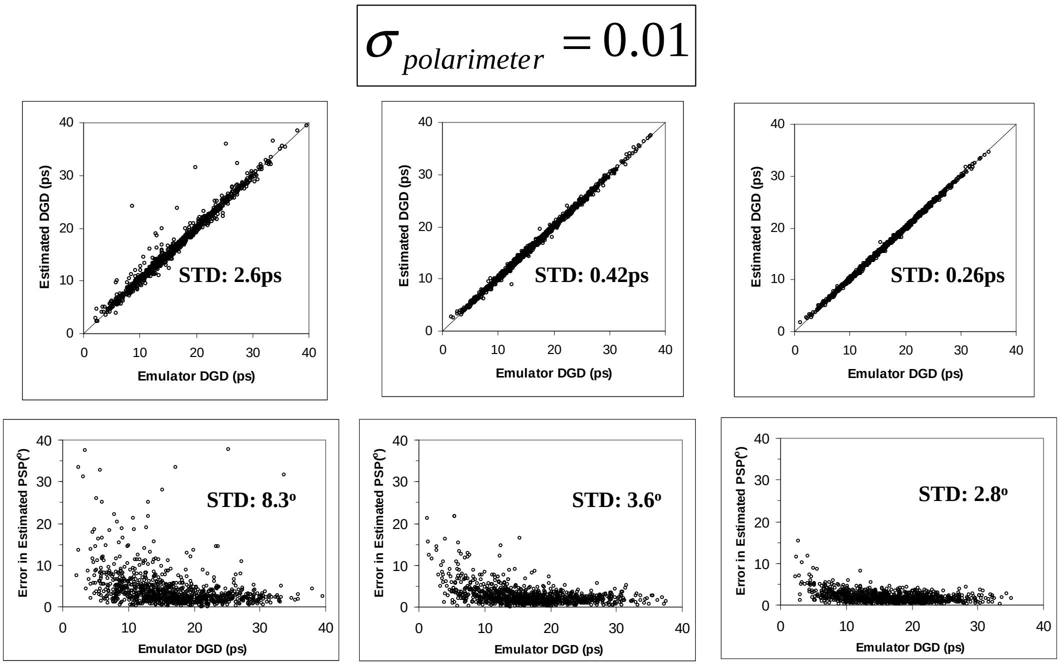

(a) 3 Input SOP **(b) 5 Input SOP** **(c) 10 Input SOP**

Figure 3-5: Graphs in the top row show the estimated DGD versus the emulator's DGD while the graphs in the bottom row show the errors in the estimation of the output PSP (in terms of degrees of arc length from the emulator's output PSP). PMD estimation using various numbers of input SOP: a) 3, b) 5 and c) 10. The standard deviation, $\sigma_{polarimeter}$, of the polarimetric measurement is kept constant at 0.01.

We estimate the final DGD of the fiber by averaging the DGD values measured for the various input SOPs. When the input SOP happens to be close to the input PSP, we have small $|(\vec{r}_{HP} - \vec{r}_{LP})|$, thus equation (3.8) tends to be more sensitive to errors in the polarimetric measurements. With this in mind, the averaging of the DGD is weighted by a factor of $|(\vec{r}_{HP} - \vec{r}_{LP})|$ to improve the accuracy in the estimation.

3.3 Theory of Second Order PMD Characterization

Second order PMD is defined as $\vec{\tau}_\omega(\omega_o) \equiv d\vec{\tau}/d\omega$. By adding equation (3.4) and equation (3.5), we obtained

$$\vec{r}_{HP} + \vec{r}_{LP} = 2\hat{s}(\omega_o) + \overline{\Delta\omega_T^2}\left[\vec{\tau}\,(\omega_o) \times [\vec{\tau}\,(\omega_o) \times \hat{s}(\omega_o)] + \vec{\tau}_\omega(\omega_o) \times \hat{s}(\omega_o)\right] + \ldots.. \tag{3.10}$$

Thus

$$\vec{\tau}_\omega(\omega_o) \times \hat{s}(\omega_o) \cong \frac{(\vec{r}_{HP} + \vec{r}_{LP}) - 2\hat{s}(\omega_o)}{\overline{\Delta\omega_T^2}} - (\vec{\tau}(\omega_o) \times [\vec{\tau}(\omega_o) \times \hat{s}(\omega_o)]) \tag{3.11}$$

Since we have already determined the first order PMD, $\vec{\tau}(\omega_o)$, the R.H.S. of equation (3.11) is a known quantity. Therefore we have obtained a vector that lies in the plane normal to $\vec{\tau}_\omega(\omega_o)$. As in the case of first order PMD characterization, polarization scrambling gives us different $\vec{\tau}_\omega(\omega_o) \times \hat{s}(\omega_o)$ for the various input SOPs. Thus using a least-squared fit algorithm in similar form to that of equation (3.7), we can find the vector that is perpendicular to all these $\vec{\tau}_\omega(\omega_o) \times \hat{s}(\omega_o)$. This determines the orientation of the $\vec{\tau}_\omega(\omega_o)$. The magnitude of second order PMD for each input SOP can also be obtained from equation (3.9). Similarly, we estimate the final magnitude of second order PMD by averaging the second order PMD magnitudes measured for the various input SOPs.

3.4 Simulations

Figure 3-5 shows the Monte Carlo simulations of our current PMD estimation technique. These computer simulations were carried out with 10Gbit/s RZ pseudo-random bit sequences of Gaussian pulses of 30ps (FHWM) pulse-width. For each graph, 1000 PMD states are randomly "generated" using an emulator of 10 fixed DGD segments. The DGD of each segment is 5.15ps and polarization scramblers are placed between segments. This emulator produces a mean DGD of 15ps. This

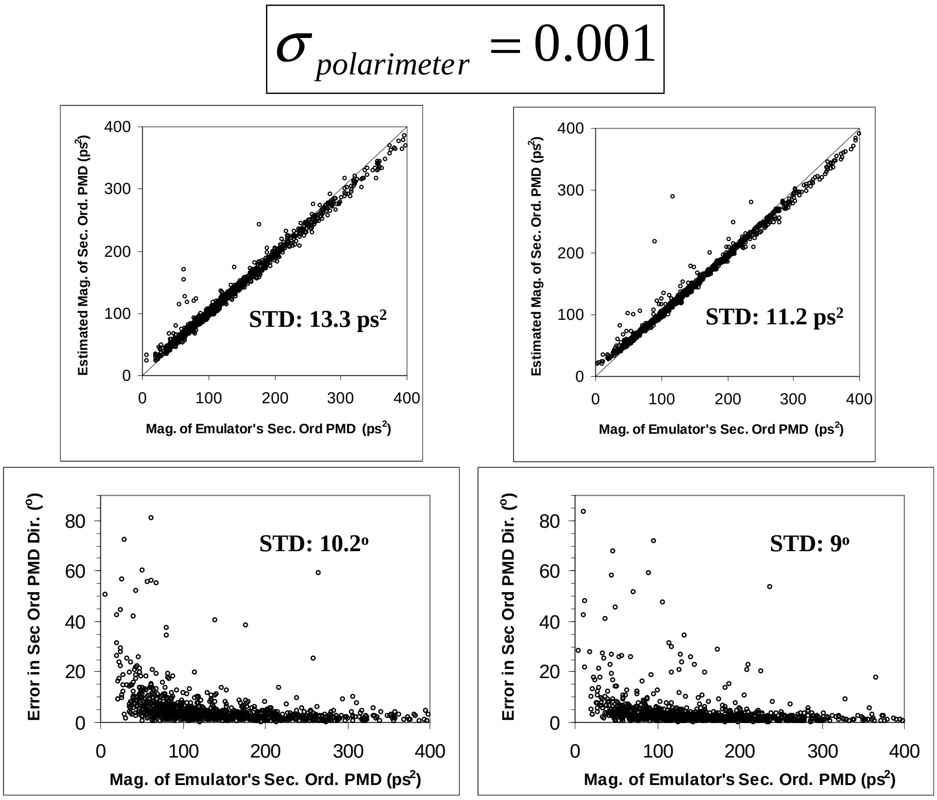

(a) 10 Input SOP **(b) 25 Input SOP**

Figure 3-6: Estimation of the second order PMD using a) 10 and b) 25 input SOP's. Standard deviation $\sigma_{polarimeter}$ used in the simulation is 0.001. The filter bandwidth Δf_F is 5 GHz.

corresponds to a PSP bandwidth of 8.3 GHz. Different input SOP's are randomly generated to simulate the polarization scrambling at the input end of the emulator. For each input SOP, the signal is filtered after propagating through the emulator with three rectangular optical filters: a high-pass filter, a low-pass filter (see Figure 3-3) and a narrowband filter. In order to capture second order PMD without much variation in the first order PMD, we choose the total transmission bandwidth covered by both high- and low-pass filters to be ~1.2 times the PSP bandwidth. Thus in these simulations, Δf_F of both filters is 5 GHz. The normalized averaged powers transmitted by these high- and low-pass filters are ~14% (see Figure 3-4). The narrowband filter has a frequency bandwidth of 0.5 GHz centered at the carrier frequency.

To simulate the polarimetric measurement, the averaged SOPs of the filtered signals after propagating through the emulator are computed. In addition, to simulate the random noise in the polarimetric measurements, we introduce independent random Gaussian distributed errors of standard deviation $\sigma_{polarimeter}$ to each component of the computed averaged SOP vector. Based on these randomly perturbed averaged SOP, we carry out the PMD estimation using equations (3.6), (3.8), (3.9) and (3.11) and the algorithms discussed in the previous section.

This standard deviation $\sigma_{polarimeter}$ could be used to include other noise sources in the fiber link. However, for the following discussion, we simply assume the noise originates mainly from the polarimetric measurements. Currently, polarimeters of accuracy of $\sigma_{polarimeter} \sim 0.01$ with sub-millisecond measurement speed are commercially available. This corresponds to a standard deviation of SOP angular errors of 0.81^o. Thus we choose $\sigma_{polarimeter}= 0.01$ for our simulations. We assume the errors of measuring $\overline{\Delta\omega_T}$ and $\overline{\Delta\omega_T^2}$ are small.

The graphs in the top row of Figure 3-5 show the estimated DGD versus the emulator's DGD while the graphs in the bottom row show the errors in the output PSP estimation (in terms of degrees of arc length from the emulator's output PSP). The number of input SOPs used for each PMD characterization are (a) 3, (b) 5, (c) 10. By increasing the number of input SOP's from 3 to 10, the standard deviation of the errors of the estimated DGD improves from 2.6ps to 0.26ps while the standard deviation of the PSP angular errors improves from 8.3^o(corresponding to polarization extinction ratio of –22.8dB) to 2.8^o (corresponding to polarization extinction ratio of -32.2dB). By using three input SOPs, we have achieved accuracy in PSP estimation in Figure 3-5a comparable to that in Reference [2] where forty input SOP's were used.

Generally, we would expect less accurate PMD estimation when the emulator's DGD is small. This is due to the reduced magnitude of $|(\vec{r}_{HP} - \vec{r}_{LP})|$ which tends to be more sensitive to noise in the polarimetric measurements, thus leading to relatively large deviation of the PMD estimation from the actual value when the DGD is small. Occasionally, one can also observe large deviations of the PMD estimation even when the DGD of the emulator is large. These are mainly due to random occurrences of the input SOPs that are too close to the input PSP, which result in reduced $|(\vec{r}_{HP} - \vec{r}_{LP})|$.

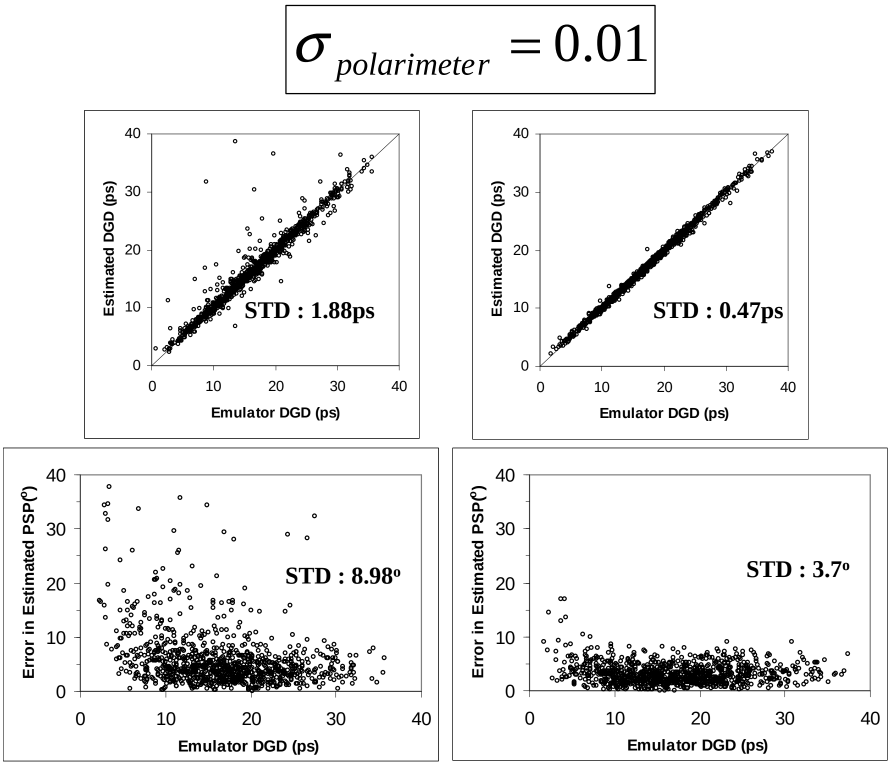

(a) 3 Input SOP **(b) 10 Input SOP**

Figure 3-7: Estimation of first order PMD when Lorentzian filters are used. The low-pass filter has a bandwidth of 3 GHz (FWHM) while the high-pass filter has a bandwidth of 2.5 GHz (FWHM). Both filters are centered 3.5 GHz away from f_o. The narrowband filter has a bandwidth of 0.5 GHz (FWHM) centered at f_o. Standard deviation $\sigma_{polarimeter}$ used in the simulation is 0.01. The number of input SOP's used are (a) 3 and (b) 10.

This situation improves significantly when we increase the number of input SOPs used in the PMD estimation, as shown in Figure 3-5. In principle, the minimum number of input SOP's needed for PMD characterization is two. However, due to i) the possibility of the input SOP being too close to the input PSP and ii) measurement inaccuracy of the polarimeter and other sources of noise, better estimation can be achieved with a larger number of input SOPs.

Estimation accuracy of second order PMD is expected to be less than that of first order PMD characterization. This is because second order PMD is a second order effect in averaged SOP (see equation (3.3)), and, in addition, its estimation depends on how well the first order PMD had been determined. Therefore, a larger number of input SOP's and more precise polarimetric measurements are required. We have only managed to achieve reasonable accuracy in the estimation of second order PMD when $\sigma_{polarimeter}$ is reduced to < 0.003. Figure 3-6 shows the estimation of the second order PMD with $\sigma_{polarimeter}$ of 0.001 when the number of input SOPs used for each PMD characterization are a) 10 and b) 25. When the number of input SOP's increases from 10 to 25, the standard deviation of the errors of the estimated magnitude of second order PMD improves from 13.3ps^2 to 11.2ps^2 while the standard deviation of the angular errors of the second order PMD direction improves from 10.2^o (corresponding to polarization extinction ratio of –21 dB) to 9^o (corresponding to polarization extinction ratio of –22 dB).

As mentioned earlier, for simplicity in illustrating our estimation technique, we considered a symmetrical signal spectrum about the carrier frequency with identical rectangular high- and low- pass filters as shown in Figure 3-3. In the case of an asymmetrical signal spectrum or non-identical high and low-pass filters, equation (3.6) must be modified

$$\left(\frac{\overline{\Delta\omega_{LP}^2}}{\overline{\Delta\omega_{HP}^2}}(\vec{r}_{HP} - \hat{s}(\omega_o))\right) - (\vec{r}_{LP} - \hat{s}(\omega_o)) \cong [\vec{\tau}(\omega_o) \times \hat{s}(\omega_o)]\left(\overline{\Delta\omega}_{HP}\frac{\overline{\Delta\omega_{LP}^2}}{\overline{\Delta\omega_{HP}^2}} - \overline{\Delta\omega}_{LP}\right) \tag{3.12}$$

while equation (3.9) becomes

$$DGD = |\vec{\tau}(\omega_o)| = \frac{\theta}{(\overline{\Delta\omega}_{HP} - \overline{\Delta\omega}_{LP})} \tag{3.13}$$

where $\overline{\Delta\omega}_{HP}$ and $\overline{\Delta\omega_{HP}^2}$ are defined in the same manner as $\overline{\Delta\omega}$ and $\overline{\Delta\omega^2}$ (see equation (3.3)) but evaluated using the transmitted spectrum of the high-pass filter, while $\overline{\Delta\omega}_{LP}$ and $\overline{\Delta\omega_{LP}^2}$ are evaluated using the transmitted spectrum of the low-pass filter. The remaining procedures for PMD characterization are the same. The technique works with filters of any transmission profiles as long as they are polarization insensitive. Figure 3-7 shows a simulation where the filters are of Lorentzian transmission profiles. The low-pass filter has a bandwidth of 3 GHz (FWHM) centered at 3.5 GHz from the carrier frequency f_o while the high-pass filter has a bandwidth of 2.5 GHz

(FWHM) centered at 3.5 GHz from f_o. The narrowband filter has a bandwidth of 0.5 GHz (FWHM) centered at f_o. The standard deviation $\sigma_{polarimeter}$ is 0.01 and the number of input SOP's used for each PMD estimation are (a) 3 and (b) 10. Equations (3.12) and (3.13) were used instead of equations (3.6) and (3.8) in the simulation. From Figure 3-7, when the number of input SOP is increased from 3 to 10, the standard deviation of the errors of the estimated DGD improved from 1.88 ps and 0.47 ps while the standard deviation of the PSP angular errors improved from 8.98°(corresponding to polarization extinction ratio of –22dB) to 3.7°(corresponding to a polarization extinction ratio of –29.8dB). Thus, this shows that comparable estimation accuracy is achievable with non-identical realistic high- and low-pass filters.

3.5 Broadband PMD Monitoring

The above sections focus on the real-time characterization of 1^{st} and 2^{nd} order PMD vectors. However, for broadband applications such as a multi-channel WDM system or fiber with large mean DGD, compensation of PMD up to second- order may not be sufficient and all orders of PMD have to be considered. To avoid the complexity of introducing higher-order PMD terms, we do not express the PMD vector as a Taylor expansion about the center frequency ω_o. Instead we simply treat the whole PMD spectrum as 1^{st} order PMD vector that varies from frequency to frequency. This results in the All-Frequency PMD compensation scheme described in Chapter 6. To diagnose the PMD vector spectrum over a certain frequency range of interest, we utilize the same non-intrusive SOP monitoring schemes shown in Figure 3-1.

For a frequency ω and its nearby frequencies $\omega \pm \Delta\omega$, the trajectories of the polarimetric output state of polarization (SOP) can be approximated by an arc on the Poincaré sphere. The axis of the arc is along the direction of the output principal state of polarization (PSP) $\hat{\tau}_f(\omega)$ and the arc length is proportional to the differential group delay (DGD) $|\vec{\tau}_f(\omega)|$. So, in principle, the knowledge of the output SOP as a function of frequency is sufficient to determine the output PMD vector $\vec{\tau}_f(\omega)$ as a function of frequency.

A portion of the telecommunication signals is tapped out at the output end of the fiber for measurements. This tapped signal then passes through an optical filter placed before a polarimeter. The averaged output SOP of this filtered signal is $\vec{r}(\omega)$. By scanning the optical filter through the spectrum of interest, the averaged output SOP $\vec{r}(\omega)$ can be measured as a function of frequency. From equation (3.6), the output PSP at frequency ω_o can then be obtained by the direction of the cross product of differential SOP vectors $(\vec{r}(\omega_o) - \vec{r}(\omega_o - \Delta\omega))$ and $(\vec{r}(\omega_o + \Delta\omega) - \vec{r}(\omega_o))$. The DGD at frequency ω_o can be deduced from the length of these differential SOP vectors. In practice, this cross-product often does not give a good estimation of $\vec{r}_f(\omega)$ due to the presence of higher order PMD and the fact that it is difficult to measure the small change in the differential SOP vectors with frequency. To improve the estimation accuracy, we make use of the random scrambling of the launched SOP at the transmitter end of the fiber. Since the input polarization scrambling does not change the fiber's properties, it will not affect the PMD of the fiber. On the other hand, the trajectory of the averaged output SOP of the filtered signal changes to $\vec{r}(\omega)'$. For a given frequency, the trajectories of $\vec{r}(\omega)$ and $\vec{r}(\omega)'$ produce different arcs, however, both arcs possess a common axis. This common axis gives the PSP at that frequency, and can be found by the cross product of $(\vec{r}(\omega_o + \Delta\omega) - \vec{r}(\omega_o - \Delta\omega))$ and $(\vec{r}(\omega_o + \Delta\omega)' - \vec{r}(\omega_o - \Delta\omega)')$. Once the PSP is determined, the DGD can be deduced from the arc length of $(\vec{r}(\omega_o + \Delta\omega) - \vec{r}(\omega_o - \Delta\omega))$. Often, more than two different input SOPs are used to improve the estimation. Using equation (3.7), one can find the optimum unit vector that is normal to all the various differential SOP vectors, $(\vec{r}_j(\omega_o + \Delta\omega) - \vec{r}_j(\omega_o - \Delta\omega))$. Thus this determines their common axis (which is aligned to the PSP) with much better accuracy. The DGD estimation can also be improved by averaging the individual DGD value deduced from the various $(\vec{r}_j(\omega_o + \Delta\omega) - \vec{r}_j(\omega_o - \Delta\omega))$.

With the above monitoring scheme, it is clear that we do not need to know the input SOP. Thus, the polarization scrambling at the transmitter end can be arbitrary and need not be in a pre-arranged sequence. This is a major advantage of characterizing the output PMD in Stokes Space as compared to characterizing the Jones

Matrix of the fiber, since the latter requires the knowledge of the input SOP. In the case of Jones Matrix characterization, even if the input SOP can be scrambled in a pre-arranged sequence, the detected output SOP must still be synchronized with the input SOP. On the other hand, for the case of the output PMD characterization in Stoke space, there is no need for such synchronization except that the measurement of $\vec{r}(\omega)$for the entire frequency range of interest, has to be completed before the next input SOP is launched. In other words, if the time to measure $\vec{r}(\omega)$ over a certain band of interest is T_{SOP}, the scrambling rate cannot be faster than $1/T_{SOP}$.

Since this PMD monitoring scheme utilizes the telecommunication spectrum, the accuracy of the SOP measurement naturally depends on the power spectral density of the frequency components. Due to the signal-to-noise ratio, frequency components that have large power spectral density are expected to be monitored with better accuracy than those of lower power spectral density. However, frequency components, that do not have sufficient power spectral density for accurate SOP measurement, are also components that have lesser impact on the signal's degradation. Therefore, their PMD compensation is less important.

The accuracy of the PMD estimation also depends on the DGD values. Frequency components that have larger PMD are expected to be monitored with better accuracy due to the larger differential SOP vectors $(\vec{r}_j(\omega_o + \Delta\omega) - \vec{r}_j(\omega_o - \Delta\omega))$. However, frequency components that have small DGD are components that have little impact on the signal's degradation. Thus, their PMD compensation is also immaterial.

Since feed-forward PMD compensator acts after the characterization, there is a time lag between the monitoring and the compensation. For the case of continuous monitoring and compensation, this time lag is determined by the time required to measure the PMD spectrum. To avoid data loss due to the delayed action of the compensator, the time lag must be smaller than the time scale over which the PMD spectrum changes significantly. This time scale varies from few ms to few minutes [29, 31, 64] depending on the environment in which the fiber is being deployed (whether aerial or buried fiber). To speed up the polarimetric SOP measurement, instead of scanning the optical filter through the frequency range of interest, one can

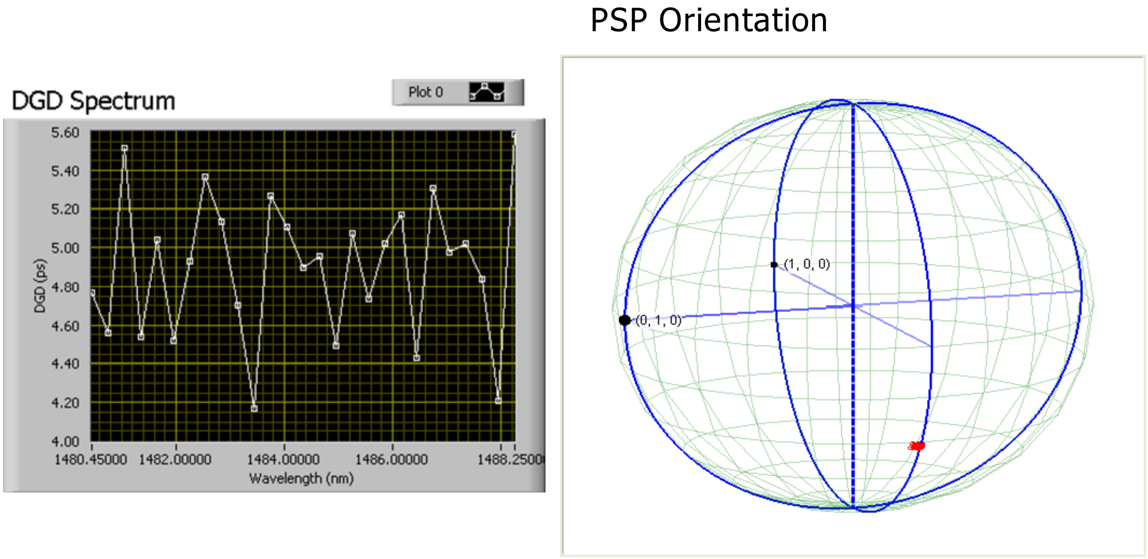

Figure 3-8: Measured DGD and PSP as a function of wavelength. The calibrated emulator's DGD setting is 5ps

build a polarimeter that uses dispersive elements to spatially disperse the frequency components onto detector arrays. Reference [108] has recently demonstrated that such a scheme allows SOP measurements of 256 different wavelengths within 1 ms.

It may be useful to estimate the time required for the characterization of the spectrum of PMD vectors. The optical frequency step size Δf required for the characterization depends on the bandwidth of the PSP. This PSP bandwidth [18] is given as $\Delta f_{PSP} = 1/8\bar{\tau}$ where $\bar{\tau}$ is the mean DGD value. Over this bandwidth, the PMD vector stays reasonably constant. Thus the maximum value of the step size Δf is limited by Δf_{PSP}. A conservative step-size is $\sim \Delta f_{PSP}/8$ and this step-size is typically used in simulations discussed in Chapter 6. For a single channel, we need to monitor the PMD spectrum for an optical frequency range of 3/T about the center frequency of the channel. Note that T is the bit period. If we require N_{pol} different input SOPs for every PMD spectrum characterization, the total number of polarimetric SOP measurements needed for a single characterization of the PMD spectrum is $192 N_{pol}\bar{\tau}/\mathrm{T}$. For example, if one uses 3 input SOPs for each characterization of the PMD spectrum of a fiber whose mean DGD is 50% of the bit period, the total required number of polarimetric SOP measurements is ~288. In practice, it may be

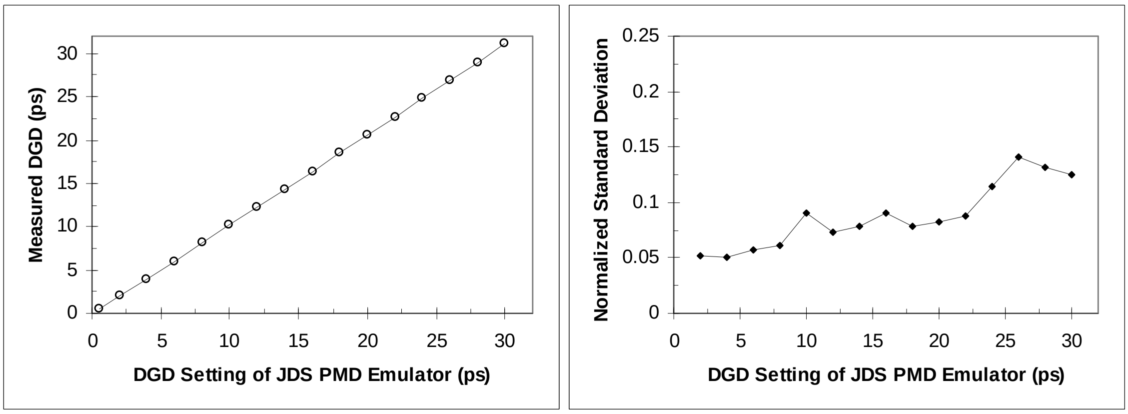

Figure 3-9: Measured DGD and its errors for the various emulator's DGD setting

feasible to achieve this many polarimetric SOP measurements on a millisecond time scale since Reference [108] has demonstrated 256 polarimetric SOP measurements in 1 ms. In summary to the real-time monitoring, we believe real-time monitoring of PMD vectors is comparatively easier than the monitoring of the complete Jones Matrix (as required in Reference [109]) since no knowledge of the input SOP is required. However, to perform it on a millisecond time scale may be challenging but still feasible.

3.6 Experimental Demonstration

We first demonstrate the accuracy of the characterization technique for first-order PMD using a calibrated JDS Uniphase PE4 PMD emulator which generates pure first order PMD by separating the two orthogonal polarization components using a polarization beam splitter, introducing a path difference between them in free space and then recombining them using a polarization beam combiner. In the measurement setup, instead of optically filtering a telecommunication signal at the output end as described in Section 3.2, we use a Santec scanning wavelength laser at the input end. The polarization of the laser is randomly scrambled with a General Photonics polarization scrambler (Polarite II) before launching into the emulator. The output polarization is measured with a HP 8509B polarimeter. From the SOP measurements

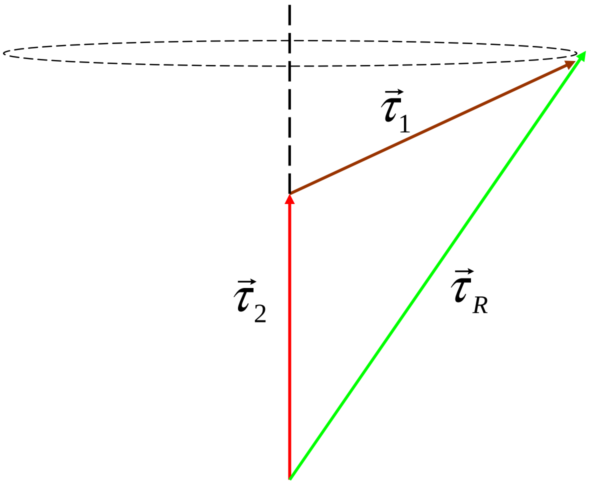

Figure 3-10: Vector diagram showing the precession of the resultant PMD vector with wavelength for a two-segment concatenation

with frequency, we deduce the spectrum of the PMD vectors using the same algorithms described in Section 3.2. Figure 3-8 shows the measured DGD as a function of wavelength. The calibrated emulator's DGD setting is 5ps. In principle, the pure first-order PMD is independent of wavelength. In fact, the variation in the DGD spectrum is due to the measurement errors that mainly arise from the reading of the Santec laser wavelength. Its manufacturer warrants an accuracy of wavelength read-out up to $\sim \pm 0.02$ nm. This translates to a $\sim \pm 5$ % error in the DGD measurements when a wavelength step-size of 0.4 nm is used, thus explaining the observed DGD variation in the spectrum. On the other hand, the PSP can be characterized more accurately since it is based solely on the polarimetric measurements (see equation 3.7). The measured PSP is shown on the Poincaré sphere in Fig 3-8 for the various wavelengths. As expected, the PSP does not vary with the wavelength. Figure 3-9 shows the measured DGD and the corresponding errors for the various emulator's DGD setting. It shows good agreement with the calibrated emulator's DGD. In our experiment, we use a smaller wavelength step-size for the larger DGD setting, thus producing a larger error for these larger DGD settings. Since all orders of PMD can be generated simply by concatenating two first-order PMD segments [51], we verify the characterization technique for the higher-order PMD using a two-segment con-

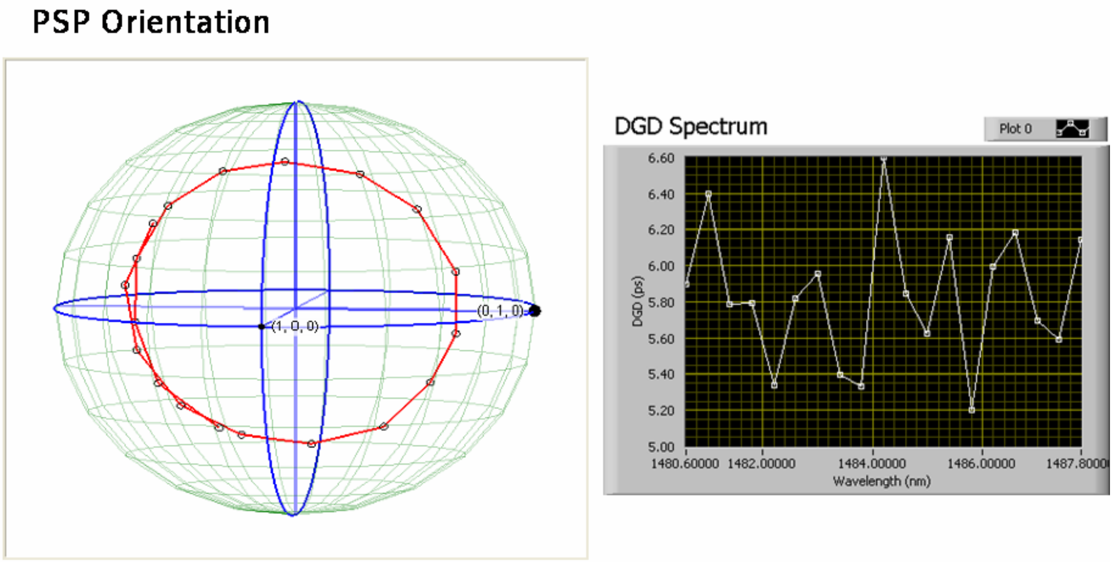

Figure 3-11: The measured PSP and DGD as a function of wavelength for a two-segment concatenation

catenation. By PMD concatenation rule, the resultant PMD of this concatenation is

$$\vec{\tau}_R = \vec{\tau}_2 + R_2\vec{\tau}_1 \tag{3.14}$$

where $\vec{\tau}_1$ and $\vec{\tau}_2$ are the first order PMD for the first and second segment respectively. They have negligible wavelength dependence. R_2 is the rotation due to the second segment. The rotation axis is along the slow birefringent axis of the second DGD segment, and the rotation angle is the retardation angle of segment 2 and is wavelength dependent. As a result, when the wavelength varies, the resultant PMD vector precesses about the birefringent axis of the second segment as shown in Figure 3-10. The rate of precession with frequency is determined by the DGD of the second segment. On the other hand, the magnitude of the resultant PMD vector is wavelength-insensitive for this two-segment concatenation. Another interesting point to make about equation 3.14 is that a change in the first segment's DGD may change the resultant PMD vector but it has no effect on the precession of the resultant PMD vector. In the experiment, we use a variable DGD for the first segment and a fixed DGD for the second segment. The variable DGD is produced by the JDS Uniphase

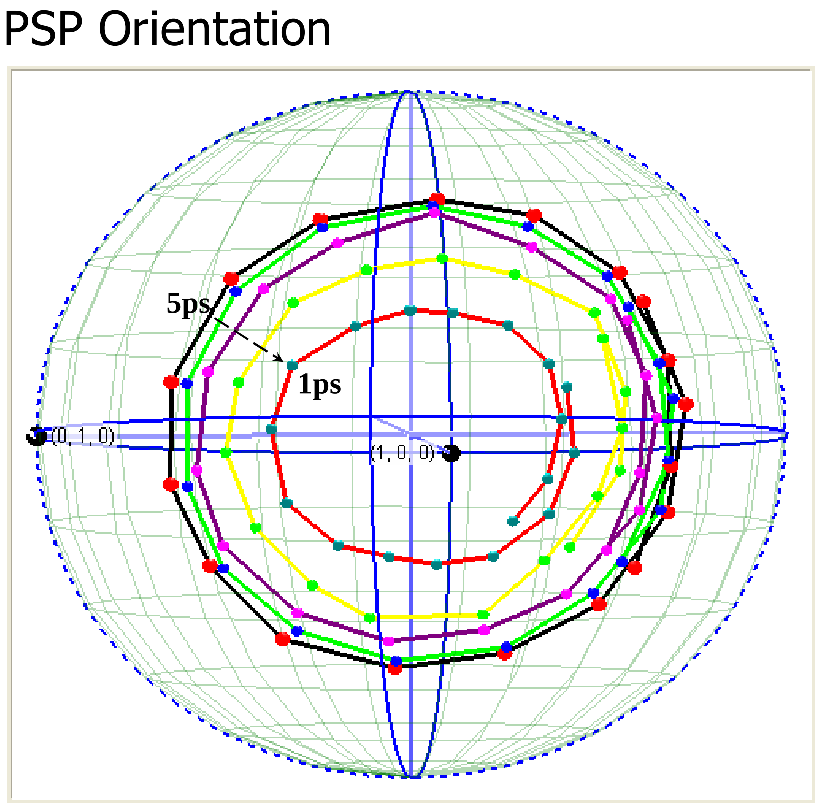

Figure 3-12: Measured resultant PSP as a function of wavelength for different setting of the first segment's DGD

PE4 PMD emulator while the fixed DGD is a fixed length of 3M Tiger polarization maintaining fiber. The measured DGD of the Tiger PM fiber is 1.27ps. Figure 3-11 shows the measured resultant PMD vector of the concatenation. As expected, we observed the precession of the PSP of the resultant PMD. In addition, the measured DGD of the resultant PMD vector remain constant at 5.8 ps (within the measurement errors) when the wavelength changes. Figure 3-12 shows the measured resultant PMD vector when we vary the DGD of the first segment. It matches our expectation that the rate of precession and precession axis remain constant despite the change in the resultant PMD vector. To check the capability of the technique for characterizing higher-order PMD, we deduce the DGD of the second segment from the precession rate and its PSP from the precession axis of the resultant PMD vectors. After knowing the PMD of the second segment, we deduce the DGD of the first segment from the measured resultant PMD vector. These are then compared to the known DGD

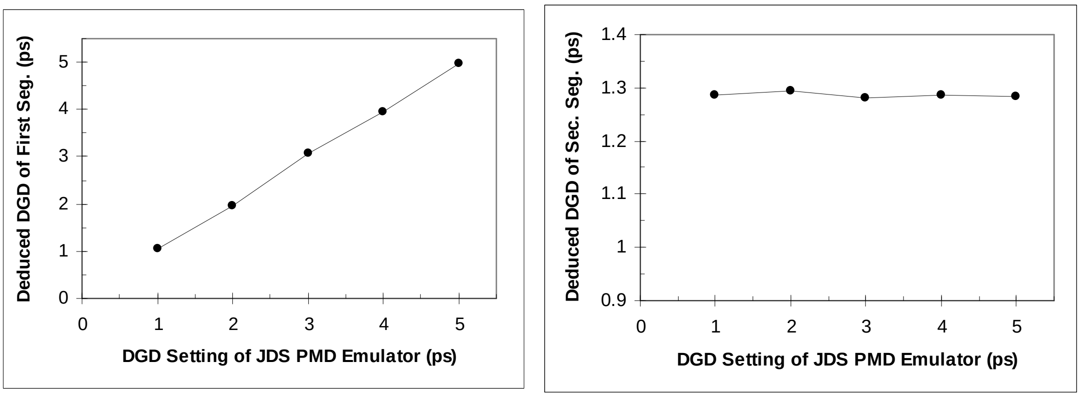

Figure 3-13: Deduced DGD of the individual segment

values of each segment. Figure 3-13 shows the deduced DGD of the first segment and the second segment using various DGD settings of the JDS emulator. The deduced DGD value of segment 1 agrees well with the known calibrated values from the JDS emulator. In addition, for all the various DGD settings of the JDS emulator, the deduced DGD of the second segment is constant at 1.28ps. This value also agrees well with the measured 1.27 ps for the Tiger PM fiber. Therefore we have verified the accuracy of the characterization technique for the prediction of first and higher-order PMD.

3.7 Conclusion

We have presented a real-time estimation technique to predict the first order and second order PMD parameters. At the output end of the fiber, the signal is tapped and filtered. Three filters are used: a high-pass filter, a low-pass filter and a narrowband filter. The averaged SOP of the filtered signals are then measured using a polarimeter. We repeat the measurement for several different input SOP's using a polarization scrambler at the input end of the fiber. From these measurements, we deduce the first order PMD, and subsequently the second order PMD. Using Monte Carlo simulations, we have shown that this technique offers significant improvements over the previous ellipsoid method [2] in terms of measurement accuracy, lower required polarization scrambling rate and capability to estimate more PMD parameters. The search algorithm used is simple and requires little computation time, thus making the technique feasible for real-time PMD characterization. In addition, we discuss how to extend the scheme to monitor the spectrum of the PMD vector which is required for All-Frequency PMD compensation discussed in Chapter 6. We also demonstrate the accuracy of the characterization technique experimentally using well-calibrated first- and higher-order PMD sources.

Chapter 4

A Variable DGD Module for First Order PMD

4.1 Background

Due to the statistical nature of polarization mode dispersion (PMD), PMD compensators and emulators have to be adjustable. For first order PMD, a typical compensator [88] or emulator [74] consists of a polarization controller and a birefringence segment that has a tunable differential group delay (DGD). To generate the variable DGD, a common approach is to separate the two orthogonal polarization components using a polarization beam splitter, introduce a path difference between them and then recombine them using a polarization beam combiner [88, 8, 87, 110, 111]. This approach requires mechanical movements and therefore suffers from slow speed (sub-second), large output polarization fluctuation and poor control stability. Another popular option is to concatenate two fixed DGD segments via a polarization controller to generate the tunable DGD. However, this results in a second order PMD vector perpendicular to the resultant 1^{st} order PMD vector, which causes rotation of the principal state of polarization as one moves away from the center wavelength [17, 68]. The most recent approach to variable DGD is based on concatenation of 6 birefringent crystals whose lengths increase in a binary power series [112]. Nevertheless, there remains a substantial amount of 2^{nd} order PMD ($\sim$80ps^2).

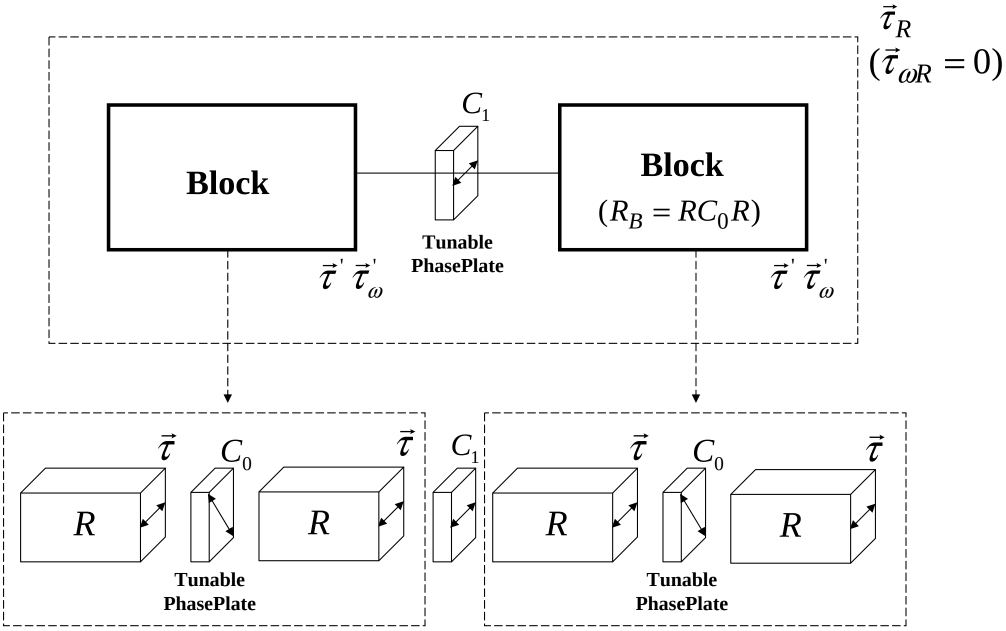

Figure 4-1: Schematic of the variable DGD module. It consists of two identical blocks concatenated via C_1. Each block itself consists of two identical fixed DGD segments concatenated via C_0.

In this chapter, we propose a symmetrical way of concatenating 4 identical fixed DGD segments so that the resultant DGD is variable while no second order PMD is produced. In addition, the third order PMD produced is only half the value of the one produced in the concatenation of two fixed segments with the same DGD tuning range.

4.2 Theory

The schematic of the module is shown in Figure 4-1. Two identical blocks are concatenated via a tunable phase-plate, C_1, whose rotation axis is the x-direction in Stokes space (equivalent to horizontal linearly polarized birefringence axis). Each block consists of two identical fixed DGD segments of negligible second order PMD. They are concatenated via C_0, which is a tunable phase-plate whose rotation axis is the y-direction (equivalent to a 45^o linearly polarized birefringence axis). In Stokes space representation, each fixed DGD segment has first order PMD, $\vec{\tau} = \{|\vec{\tau}|, 0, 0\}$,

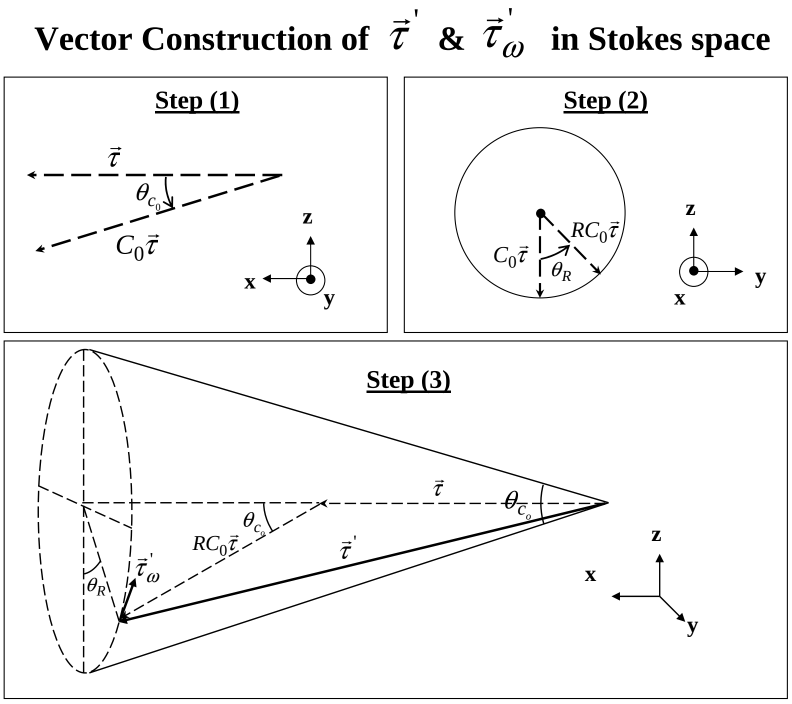

Figure 4-2: Construction of $\vec{\tau}\,'$ and $\vec{\tau}_\omega'$ in Stokes space. Step 1 is the C_0 transformation of $\vec{\tau}$, which correspond to a rotation of θ_{C_0} about y-axis. Step 2 is the R transformation of $C_0\vec{\tau}$ which corresponds to a rotation of θ_R about x-axis. In Step 3, vector addition of $\vec{\tau}$ and $RC_0\vec{\tau}$ gives $\vec{\tau}\,'$ while vector product $\vec{\tau}$ of and $RC_0\vec{\tau}$ give $\vec{\tau}_\omega'$.

and a rotation matrix, R, whose rotation axis is the x-direction and rotation angle is θ_R. The block produces first order PMD, $\vec{\tau}\,'$, and second order PMD,$\vec{\tau}_\omega'$

$$\vec{\tau}\,' = \vec{\tau} + RC_0\vec{\tau} \tag{4.1}$$

$$\vec{\tau}_\omega' = \vec{\tau} \times \vec{\tau}\,' \tag{4.2}$$

Note that $\vec{\tau}\,'$ and $\vec{\tau}_\omega'$ are perpendicular to each other. We will make use of this property to cancel the second order PMD of the entire structure. Figure 4-2 illustrates the construction of $\vec{\tau}\,'$ and $\vec{\tau}_\omega'$ in Stokes space. Step 1 is the transformation via C_0 of $\vec{\tau}$ which corresponds to a rotation of θ_{c_0}about the y-axis. Step 2 is the R transformation of $C_0\vec{\tau}$ which corresponds to a rotation of θ_R about the x-axis. In Step 3, vector addition of $\vec{\tau}$ and $RC_0\vec{\tau}$ gives $\vec{\tau}\,'$while the vector product of $\vec{\tau}$ and $RC_0\vec{\tau}$ give $\vec{\tau}_\omega'$. The rotation matrix of the block is $R_B = RC_0R$.

Since the module is constructed with tunable phase-plates, which can either be electro-optic or magneto-optic, high speed tuning of DGD is possible as shown in [112]. Moreover, instead of using polarization-maintaining fibers as fixed DGD segments, one could use birefringent crystals, which promise compactness and stability. Alternatively, one could integrate the whole variable DGD module on a wafer based on MEMS technology, since the fixed DGD segments are simply fixed delay lines in free space while the tunable phase-plates are finely-adjustable delay lines in free space as shown in [113].

When the two identical blocks of $\vec{\tau}\,'$ and $\vec{\tau}_\omega{}'$ are concatenated via C_1, the resultant first order PMD vector, $\vec{\tau}_R$, and resultant second order PMD vector, $\vec{\tau}_{\omega R}$, are

$$\vec{\tau}_R = \vec{\tau}\,' + R_B C_1 \vec{\tau}\,' \tag{4.3}$$

and

$$\vec{\tau}_{\omega R} = \vec{\tau}_\omega{}' + R_B C_1 \vec{\tau}_\omega{}' + \vec{\tau}\,' \times \vec{\tau}_R \tag{4.4}$$

Now, if we tune C_1 so that

$$R_B C_1 \vec{\tau}\,' = \vec{\tau}\,' \tag{4.5}$$

and

$$R_B C_1 \vec{\tau}_\omega{}' = -\vec{\tau}_\omega{}' \tag{4.6}$$

Then

$$\vec{\tau}_R = 2\vec{\tau}\,' \tag{4.7}$$

and

$$\vec{\tau}_{\omega R} = 0 \tag{4.8}$$

Thus, our approach to produce variable DGD without second order PMD can be summarized as follows: For any designated DGD value, we tune C_0 so that each block produces half of the designated DGD value, and then we tune C_1 so that the first order PMD vectors of the two identical blocks add to give the designated DGD value, while their second order PMD vectors cancel one another. The total tunable

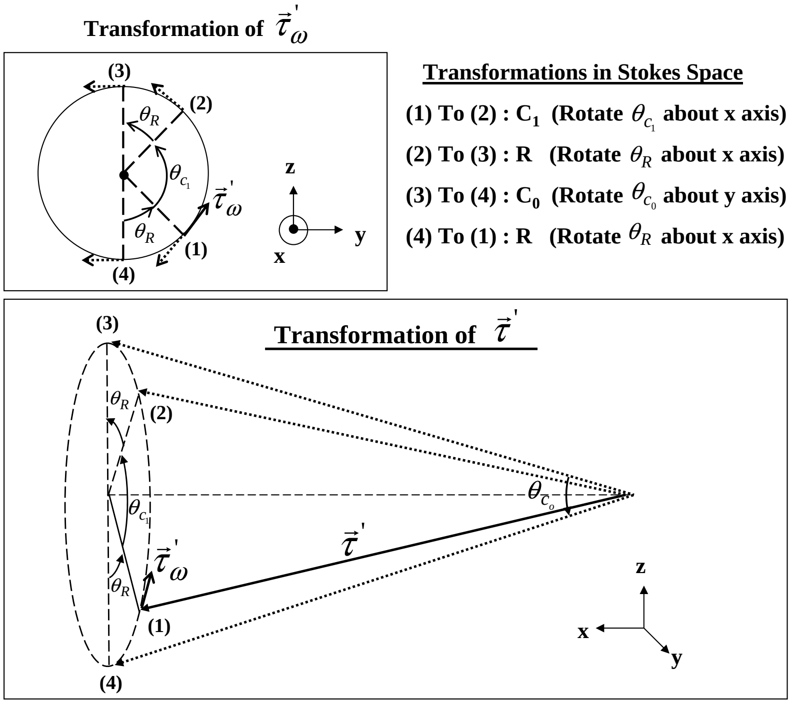

Figure 4-3: $\vec{\tau}\,'$ and $\vec{\tau}_{\omega}'$ under $R_B C_1 (= R C_0 R C_1)$ transformation in Stokes space. Point (1) to Point (2): $\vec{\tau}\,'$ and $\vec{\tau}_{\omega}'$ are transformed by C_1 which corresponds to a rotation of θ_{C_1} about x-axis. Point (2) to Point (3): R transformation which corresponds to a rotation of θ_R about x-axis. Point (3) to Point (4): C_0 transformation which corresponds to a rotation of θ_{C_0} about y-axis. Point (4) back to Point (1): another R transformation.

DGD range of the module is $4|\vec{\tau}|$. For any designated DGD value, $|\vec{\tau}_R| = 2\left|\vec{\tau}\,'\right|$, we can solve the required rotation angle of C_0 using simple vector algebra (see Figure 4-2),

$$\cos\left(\frac{\theta_{C_0}}{2}\right) = \frac{|\vec{\tau}_R|}{4\,|\vec{\tau}|} \tag{4.9}$$

Note that $\vec{\tau}\,'$ and $\vec{\tau}_{\omega}'$ are perpendicular to each other. Thus equations (4.5) and (4.6) are satisfied by a rotation transformation, $R_B C_1$, that uses $\vec{\tau}\,'$ as its rotation axis and rotation angle of π. Since we know R_B and $\vec{\tau}\,'$, we can compute C_1 as

$$C_1 = R_B^{\dagger} T = (R C_0 R)^{\dagger} T \tag{4.10}$$

where T is a rotation by π about $\vec{\tau}\,'$. In general, to implement C_1 to satisfy equation (4.10), one would require at least three tunable phase-plates due to the 3 parameters

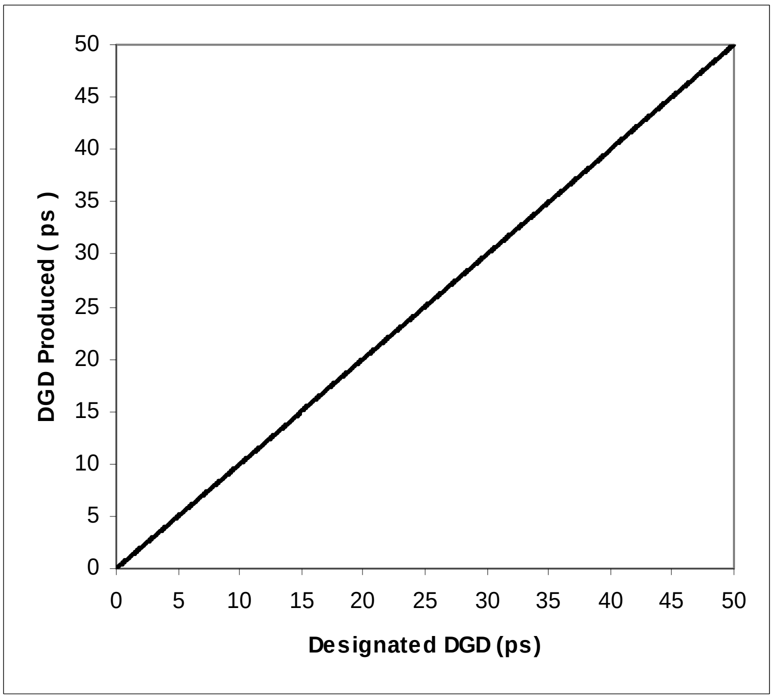

Figure 4-4: DGD produced by the 4-segment module for various designated DGD values.

contained in an arbitrary rotation transformation. However, due to the symmetry involved in our configuration and our selection of the rotation axes of C_0 and R, C_1 is a rotation about the x-axis with fixed rotation angle of

$$\theta_{c_1} = \pi - 2\theta_R \tag{4.11}$$

This angle remains constant independent of changes in C_0 needed to achieve different DGD. The simplicity of the solution of C_1, favors practical implementation of the module. Figure 4-3 depicts visually the vector transformation, $R_B C_1 (= RC_0RC_1)$ of $\vec{\tau}\,'$and $\vec{\tau}_\omega'$ in Stokes space to explain the solution of C_1 in equation (4.11). From point (1) to point (2), $\vec{\tau}\,'$ and $\vec{\tau}_\omega'$ are transformed by C_1 which corresponds to a rotation of θ_{c_1} about the **x**-axis. They are further transformed by R from point (2) to point (3), which corresponds to a rotation of θ_R about the **x**-axis. This is followed by a rotation of θ_{c_0} about the **y**-axis via C_0 from point (3) to point (4) and, finally, from point (4) back to point (1) via R. With the rotation angle of C_1 given by equation (4.11), $\vec{\tau}\,'$

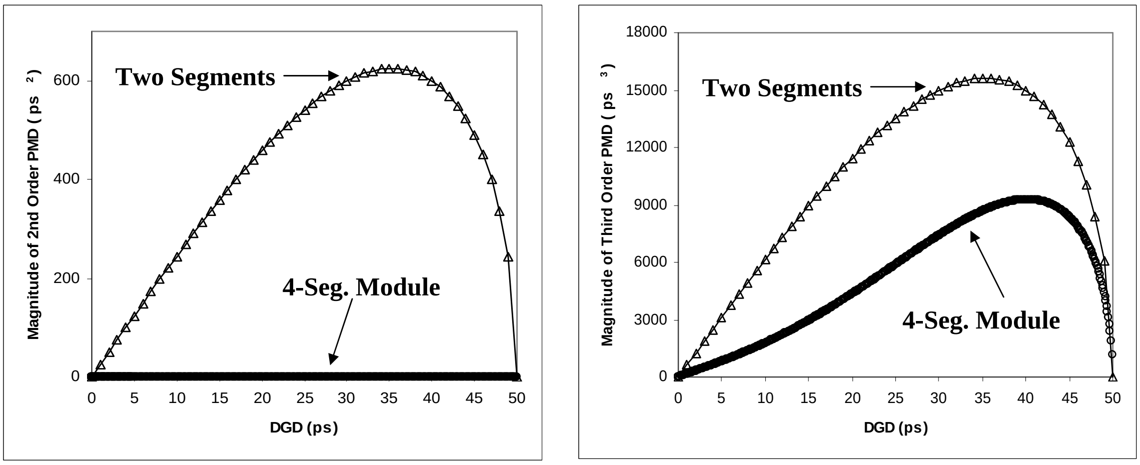

(a) **(b)**

Figure 4-5: Higher-orders PMD produced the 4-segment module. (a) Magnitude of second order PMD vector. (b) Magnitude of third order PMD vector. For comparison purposes, we have also plotted higher-orders PMD produced by the conventional concatenation of two 25 ps DGD segments via a polarization controller, to produce the same DGD tuning range of 50 ps.

acquires its original direction while $\vec{\tau}_{\omega}{}'$ is reversed in direction. Therefore the first order PMD vectors of the two identical blocks add to give the designated DGD value, while their second order PMD vectors cancel. Now, if C_0 is varied to achieve another different DGD value, one can repeat the whole transformation procedure visually to see that the same rotation angle of C_1, as in equation (4.11), again satisfies both equations (4.5) and (4.6). Thus, to vary the DGD of the 4-segment module, we only need to control the rotation angle of C_0.

4.3 Simulations

Figure 4-4 shows the DGD values produced by 4-segment module for various designated DGD values using the method discussed above. The DGD, $|\vec{\tau}|$, is 12.5ps for all four identical segments. Obviously, the 4-segment module can produce the designated DGD within the whole tuning range of zero to $4|\vec{\tau}|$, which, in this case, is 50ps. Figure 4-5a shows the second order PMD produced by the 4-segment module. For comparison, we have also plotted the second order PMD produced by concatenating two 25ps DGD segments via a polarization controller, to produce the same DGD tuning range of 50 ps. The 4-segment module does not produce any second order PMD while the maximum magnitude of second order PMD produced by the conventional 2-segment concatenation is $\sim$ 625 ps^2. The result for third order PMD is shown in Figure 4-5b. The 4-segment module produces half the value of the conventional two-segment concatenation.

In practical implementation, to get identical $\vec{\tau}$ for all four segments may not be an issue but one may have difficulty in achieving the same rotation angle, θ_R, for all the segments. Thus, for cases where we have different rotation angles for the various segments, the solution of C_1 can be worked out to be

$$\theta_{c_1} = \pi - \theta_R^{Seg2} - \theta_R^{Seg3} \tag{4.12}$$

Again the solution is a constant over the whole DGD tuning range, and it is independent of the rotation angle of the first and last segment. Figure 4-6a shows the numerical solution of the required rotation angle of C_0 for the various designated DGD values. Obviously, for zero DGD, the rotation angle of C_0 has to be π so that $\vec{\tau}$ of each segment in the block must cancel and produce no DGD for the segment block. On the other hand, to produce the maximum DGD value, which is 50ps in this case, $\vec{\tau}$ of each segment must be aligned, thus the rotation angle of C_0 has to be zero. Also note that the solution of C_0 is continuous, and there is no transient DGD fluctuation [112] when one changes the DGD settings. Figure 4-6b shows the required rotation angle of C_1 for three different cases: (1) Rotation angle of all segments are equal to 2.23 rad; (2) –2.8 rad (first segment), -1.7 rad (second segment), 3.3 rad (third segment), 5.1 rad (fourth segment); (3) 4.5 rad (first segment), 2.5 rad (second segment), -3.5 rad (third segment), 1.5 rad (fourth segment). For case (2) and (3), the rotation angles are randomly chosen for illustration of equation (4.12). These solutions of C_1 in the figure are numerically computed using equation (4.10) and they agree with equation (4.12). And more importantly, they remain constant for the whole DGD

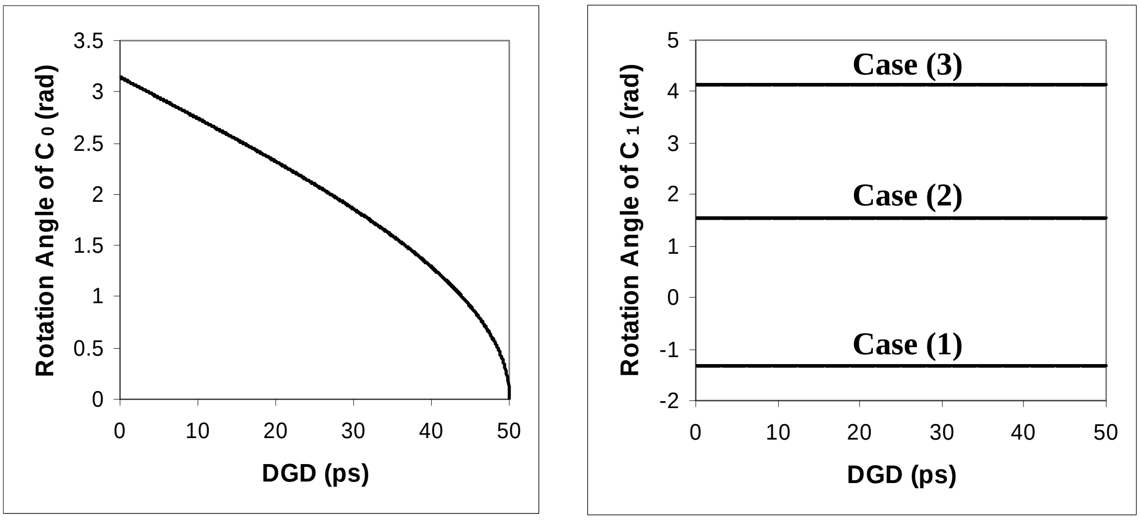

(a) **(b)**

Figure 4-6: (a) Numerical solutions of rotation angle of C_0 for various designated DGD values using equation (4.9). (b) Numerical solution of rotation angle of C_1 for three different cases: case (1): Rotation angle of all segments are equal to 2.23 rad; case (2): -2.8 rad (first segment), -1.7 rad (second segment), 3.3 rad (third segment), 5.1 rad (fourth segment); case (3): 4.5 rad (first segment), 2.5 rad (second segment), -3.5 rad (third segment), 1.5 rad (fourth segment). Solutions are computed using equation (4.10).

tuning range. However, the above discussion is only valid when the rotation angles of these segments do not drift over time. If there are drifts in these angles, continuous tuning of C_1 is necessary using equation (4.12). One should avoid these drifts so that the rotation angle of C_0 is the only variable control for the module. Drifts could be avoided by a temperature controlled and mechanically stabilized environment.

In the control of C_0 to produce the designated DGD, there are bound to be some inaccuracies in the setting, especially since it is dynamically changing. Thus, for practical purposes, it is useful to know the sensitivity of our module to these deviations and to know the required angular accuracy in the rotation of C_0. We assume we have successfully aligned C_1 and the rotation angles of all segments do not vary with time. To study this angular sensitivity, we first solve exactly the required angle of C_0. We then introduce random Gaussian distributed angular errors of standard deviation

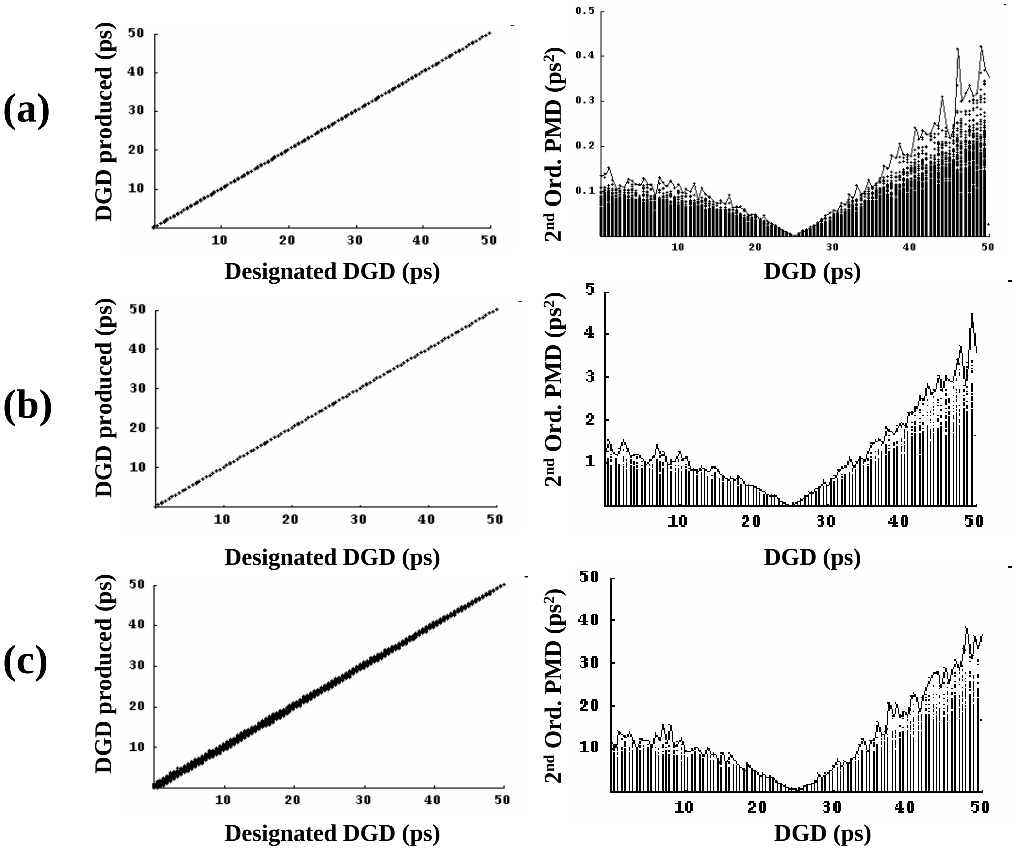

Figure 4-7: First and second order PMD generated for various angle standard deviation σ_{angle} of (a) 0.01°, (b) 0.1° and (c) 1°. All segments have identical $|\vec{\tau}|$ of 12.5ps and R.

σ_{angle} to the C_0 in both blocks. Their perturbations are independent. Using these perturbed angles, we calculate the first and second order PMD produced by the 4-segment module. Figure 4-7 shows the 1^{st} and 2^{nd} order PMD magnitudes generated for various standard deviation σ_{angle} of (a) 0.01°, (b) 0.1° and (c) 1°. All segments have identical $|\vec{\tau}|$ of 12.5ps and R. For each designated DGD, we perform 500 Monte-Carlo simulations. From these figures, one may conclude that for reasonable practical implementation, σ_{angle} of 0.1° may be sufficient, as the DGD is close to the designated value while the magnitude of the second order PMD is still tolerably small ($\sim$ 4 ps^2) when compared to the 625 ps^2 of conventional two-segments concatenation.

The DGD of a variable delay line in free space has no frequency dependence. However, due to the presence of third and higher orders of PMD, the 4-segment module has structure in its spectra of DGD and second order PMD magnitude, as shown in Figure 4-8. For these graphs, each segment in the module has $|\vec{\tau}|$ of 5ps and the total DGD tuning range is 20ps. From the graphs, the DGD and the magnitude of second order PMD of the module are oscillatory functions of frequency. Their periods are $1/2\,|\vec{\tau}|$, for this case, 100GHz. To explain this frequency dependence, one has to note that equation (4.11), which maintains the condition of variable DGD without second order PMD, is only satisfied at a particular center frequency. While θ_{c_1} can be assumed to be frequency-independent since the phase-plate has a negligible DGD, the rotation angle of the fixed DGD segment, θ_R, depends on the optical frequency, and has a periodicity of $1/\,|\vec{\tau}|$, Thus when the optical frequency moves away from this center frequency, equation (4.11) is no longer satisfied, and the first order PMD vectors from the two blocks are not aligned. This leads to variation of DGD with optical frequency as shown in Figure 8a. Moreover, the second order PMD of the module appears as in Figure 4-8, since the vectors of the blocks no longer cancel one another completely. However, equation (4.11) is again satisfied when the rotation angle of the fixed DGD segment becomes $\theta_R + m\pi$ (where m is an integer). This explains the periodicity of $1/2\,|\vec{\tau}|$ in Figure 4-8.

To show that the module has sufficient bandwidth for PMD compensation, we perform a simulation of first order PMD compensation at 10GHz using 2^7 pseudo-random Gaussian pulse trains. The Gaussian pulses have pulse-widths of 40ps (FWHM). A variable delay line in free space is used as a first order PMD emulator. The first order PMD compensator consists of the 4-segment module and a polarization controller, which is placed between the emulator and the module. The 4-segment module produces the necessary DGD while the polarization controller carries out the necessary alignment for complete cancellation of first order PMD. In Figure 4-9, the emulator's DGD is set at 15ps. The input state of polarization is chosen to be perpendicular to the input principal state of polarization (in Stokes Space), which corresponds to the worst case scenario. Each segment in the 4-segment module has $|\vec{\tau}|$ of 5ps and the total DGD tuning range is 20ps. The simulation is carried out with three different frequency chirps of the pulse: i) no chirp, ii) positive frequency chirp of 245 GHz/ns and

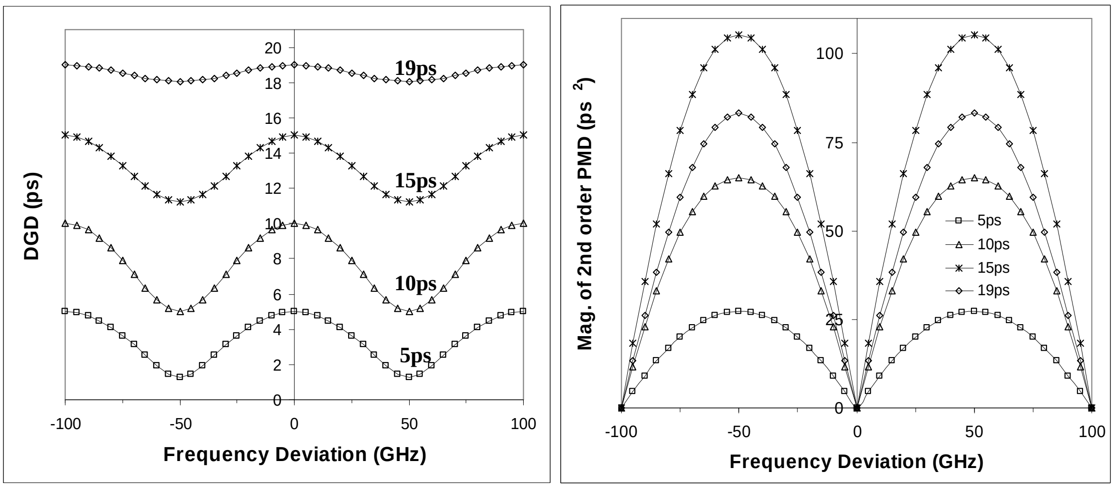

(a) **(b)**

Figure 4-8: a) DGD and b) Magnitude of second order PMD vary periodically when the optical frequency is shifted from the center frequency. Four different DGD values (at the center frequency) are shown: 5 ps, 10 ps, 15 ps and 19 ps. Each segment in the module has DGD of 5 ps and the total DGD tuning range is 20 ps.

iii) negative frequency chirp of 245 GHz/ns. Figure 4-9a shows that the 4-segment module can restore the pulse to its original shape regardless of the frequency chirp. For comparison, we have also simulated in Figure 4-9b, the performance of the conventional two-segment concatenation when it is used for PMD compensation under the same frequency chirp conditions. The DGD of each segment is 10ps so that it can produce the same tuning range of 20ps. The 2-segment concatenation can fully restore the pulse only when there is no frequency chirp. When there is either a negative or positive 245 GHz/ns frequency chirp, the pulse, after passing through the compensator, is distorted from the input pulse-shape, and the distortion depends on the chirp. This chirp-dependence distortion is due to the substantially large second order PMD generated by the 2-segment concatenation. When the first order PMD of the system is compensated, the second order PMD of the system effectively becomes a polarization dependent chromatic dispersion. Poole and Giles [60] have shown that this effect is more significant when the signal is chirped. C. Vassallo [28] had derived similar results theoretically. So when there is a positive frequency chirp, we observe pulse compression while we observe pulse broadening when there is negative chirp.

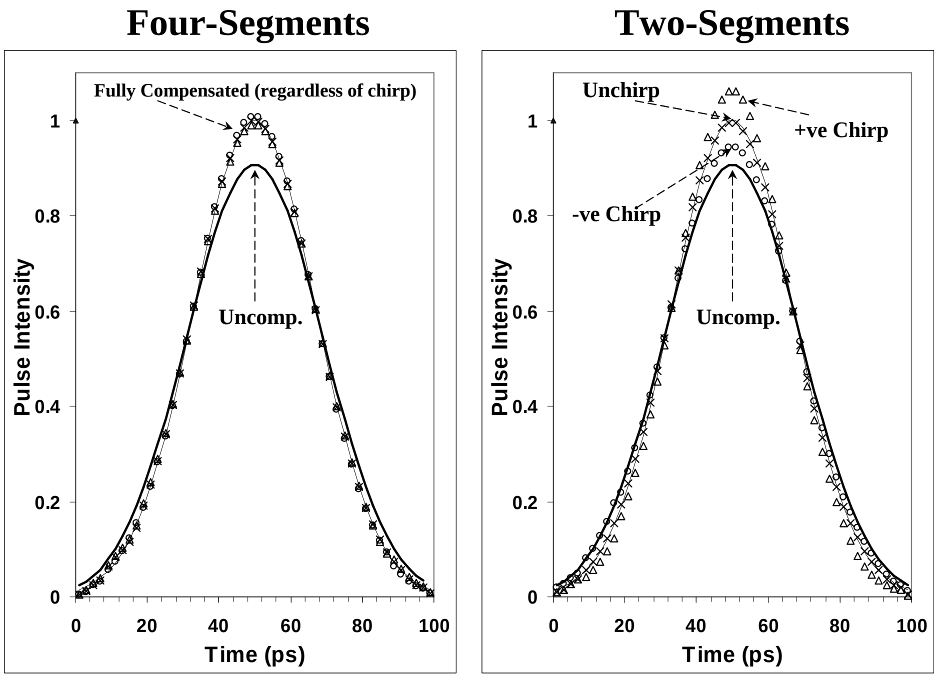

(a) (b)

Figure 4-9: a) 4-segment module used in first order PMD compensation; b) Conventional 2-segment concatenation used in first order PMD compensation. Due to the 15ps DGD presented in the first order emulator, the pulses after emulator are distorted (shown as the bottom dark solid line). The upper light solid line is the input pulse-shape. Triangles are for the case of positive 245 GHz/ns frequency chirp, circles are for the case of negative 245 GHz/ns frequency chirp while crosses are for the case of zero frequency chirp. For 4-segment module, full restoration of the pulse is observed regardless of the frequency chirp while chirp-dependent distortion is observed for the conventional 2-segment concatenation.

For the case of zero chirp, the effect of second order PMD is not so significant and thus the compensator manages to restore the pulse to its original shape. In the case of the 4-segment module, no second order PMD is generated, thus full compensation is achieved regardless of the frequency chirp. From Figure 4-9, in the presence of frequency chirp, we have illustrated the better performance of the 4-segment module over the conventional 2-segment concatenation in first order PMD compensation.

4.4 Conclusion

We presented a way to concatenate four identical fixed DGD segments so that the resultant DGD is variable while no second order PMD is produced. In addition, the third order PMD is only half the value of the one produced by two fixed segments achieving the same DGD tuning range. Since the 4-segment module is based totally on tunable phase-plates and fixed DGD segments, there are two practical implementations that promise high speed, compactness and stability: (1) using birefringent crystals with electro-optic or magneto-optic tunable phase-plates and (2) integrating the whole variable DGD module on a wafer based on MEMS technology. We also analyzed the required accuracies of the tunable phase-plates used in this variable DGD module and illustrated that the 4-segment module has better performance in PMD compensation than the conventional two-segment concatenation, when there is frequency chirp presented in the system.

Chapter 5

PMD Compensation Up to Second Order

5.1 Background

As the channel's bit rate increases from 10 Gbit/s and beyond, a compensator that cancels first order PMD may no longer be sufficient. This is especially true in the upgrading of existing transmission lines where high PMD values are common. The mostly discussed optical techniques to compensate PMD are based on the first-order approximation. This can be assumed valid for a narrow bandwidth. When the transmitted bandwidth of the optical signal and the transmission distance become large, the effects of the higher-order PMD need to be taken into account. Thus in this chapter, we propose a compensator that is capable of full compensation for both 1^{st} and 2^{nd} order PMD. As a set of 1^{st} and 2^{nd} order PMD vectors have six degrees of freedom, to avoid the complexity of tracking the optimum of such many free parameters in a feedback scheme, we propose to diagnose the transmission fiber's 1^{st} and 2^{nd} order PMD vectors using the technique described in Chapter 3. This information is then fed forward to the compensator to eliminate the PMD. This deterministic approach may have an advantage over currently used feedback schemes [88, 93, 90] that adjust a compensator in a way to achieve maximum system performance such as the minimum Bit Error Rate (BER). The many adjustable parameters of the compensator may lead the compensation to a local minimum of BER that is not the real optimum during the PMD tracking process. The feed-forward scheme avoids this and calls for action only when the PMD becomes excessive. Particularly, the rarely occurring catastrophic accumulations of PMD can be anticipated and compensated.

A two-segment PMD compensator [114, 111] cannot compensate the full second order PMD because of its frequency-independent differential group delay (DGD) characteristic. This frequency-independent DGD characteristic results from the fact that the second order PMD vector generated by a two-segment compensator is always normal to its first order PMD vector. Thus, we need at least three concatenated first order PMD segments for full PMD compensation up to second order. In this chapter, we study a particular compensator consisting of three first order PMD segments, one of which is adjustable, concatenated via polarization rotators. And, for the feed-forward technique we need to know how to set this compensator after determining the PMD parameters. Thus, in the following section, we solve analytically the required individual rotation matrices of the polarization rotators and the required DGD for the variable delay line in the compensator.

5.2 Theory

The compensator consists of three pure first order PMD concatenated segments as shown in Figure 5-1. $\{\vec{\tau}_1,R_1\}$, $\{\vec{\tau}_2, R_2\}$ and $\{\vec{\tau}_3,R_3\}$ are the first order PMD vectors and the Mueller rotation matrices for each segment. They are fixed parameters of the compensation system, except for $|\vec{\tau}_1|$ which is adjustable. The adjustable first order PMD segment can be a variable delay line in free space. We assume negligible second order PMD for each of the individual segments. Thus segments 2 and 3 could be fixed group velocity delay lines in free space or polarization maintaining fiber with negligible second order PMD. There are two polarization rotators in the compensator whose rotation matrices are given by C_1, and C_2. The resulting PMD vectors for the compensator are represented by $\vec{\tau}_c$ for first order PMD, $\vec{\tau}_{\omega c}$ for second order PMD and R_c for its rotation matrix (which is equal to $R_3C_2R_2C_1R_1$). C_0 is the rotation matrix

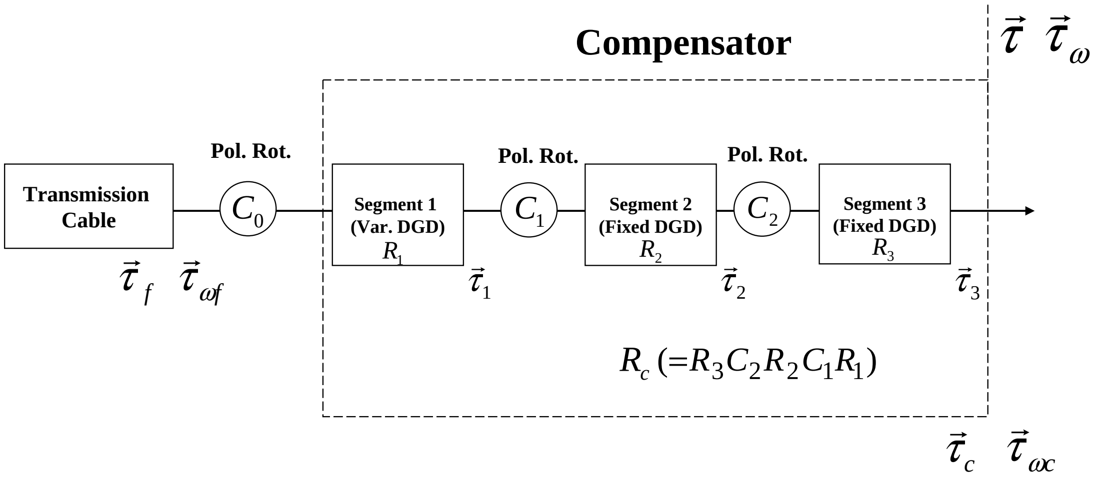

Figure 5-1: The three-segment compensator consisting of three first order PMD segments and two polarization rotators. The first segment is of adjustable DGD. $\vec{\tau}_f$ and $\vec{\tau}_{\omega f}$ are the first and second order PMD of transmission cable while $\vec{\tau}_c$ and $\vec{\tau}_{\omega c}$ are those of the compensator. For PMD compensation, we need to set C_0 and the compensator appropriately so that the net PMD vectors, $\vec{\tau}$ and $\vec{\tau}_\omega$, equal to zero.

of the polarization rotator between the transmission cable and the compensator. The rotation matrices, C_0, C_1, and C_2, are assumed to be frequency independent over the frequency range of interest.

In this paper, we neglect polarization-dependent loss or gain in the link, and we assume we have monitored the first order PMD, $\vec{\tau}_f$, and second order PMD, $\vec{\tau}_{\omega f}$, of a long haul transmission cable in real time. After knowing $\vec{\tau}_f$ and $\vec{\tau}_{\omega f}$, we need to work out the Mueller rotation matrices for the required polarization rotations, C_0, C_1, C_2, and the DGD, $|\vec{\tau}_1|$, of the variable delay line in order to achieve the necessary compensation. From Figure 5-1, the total first and second order PMD vectors, $\{\vec{\tau}$, $\vec{\tau}_\omega\}$ for both the transmission cable and the compensator together, are found using the PMD vector concatenation rules,

$$\vec{\tau} = \vec{\tau}_c + R_c C_0 \vec{\tau}_f \tag{5.1}$$

$$\vec{\tau}_\omega = \vec{\tau}_{\omega c} + R_c C_0 \vec{\tau}_{\omega f} + \vec{\tau}_c \times \vec{\tau} \tag{5.2}$$

For total PMD compensation, we require $\vec{\tau}$and $\vec{\tau}_\omega$to be zero. This implies

$$\vec{\tau}_c = -R_c C_0 \vec{\tau}_f \tag{5.3}$$

$$\vec{\tau}_{\omega c} = -R_c C_0 \vec{\tau}_{\omega f} \tag{5.4}$$

Since $\vec{\tau}_f$ and $\vec{\tau}_{\omega f}$ are known from our real time PMD characterization technique, the compensator just needs to generate a pair of $\vec{\tau}_c$ and $\vec{\tau}_{\omega c}$ vectors, such that $\vec{\tau}_c.\vec{\tau}_{\omega c} = \vec{\tau}_f.\vec{\tau}_{\omega f}$, $|\vec{\tau}_c| = |\vec{\tau}_f|$ and $|\vec{\tau}_{\omega c}| = |\vec{\tau}_{\omega f}|$. And again from PMD vector concatenation rules, the PMD vectors of the three-segment compensator can be expressed as

$$\vec{\tau}_c = \vec{\tau}_3 + R_3 C_2 \vec{\tau}_2 + R_3 C_2 R_2 C_1 \vec{\tau}_1 \tag{5.5}$$

$$\vec{\tau}_{\omega c} = (\vec{\tau}_3 \times \vec{\tau}_c) + R_3 C_2 \vec{\tau}_2 \times R_3 C_2 R_2 C_1 \vec{\tau}_1 \tag{5.6}$$

To simplify notation, we denote

$$\vec{B} = R_3 C_2 \vec{\tau}_2 \tag{5.7}$$

$$\vec{A} = R_3 C_2 R_2 C_1 \vec{\tau}_1 \tag{5.8}$$

Thus equations (5.5) and (5.6) become

$$\vec{\tau}_c - \vec{\tau}_3 = \vec{B} + \vec{A} \tag{5.9}$$

$$\vec{\tau}_{\omega c} - (\vec{\tau}_3 \times \vec{\tau}_c) = \vec{B} \times \vec{A} \tag{5.10}$$

The vector $\vec{B}$ is adjustable in orientation using the rotation matrix C_2. The vector $\vec{A}$ is arbitrarily adjustable in orientation and magnitude using the rotation matrix C_1 and the adjustable group delay $|\vec{\tau}_1|$. Our aim is to solve for $\vec{A}$ and $\vec{B}$, so that we can compute their respective rotation matrices, C_2 and C_1, from equation (5.7) and (5.8), since we know R_3, $\vec{\tau}_2$ and R_2 of the individual segment. We also know the direction of $\vec{\tau}_1$. However, its magnitude is only known when we have solved for $\vec{A}$ (i.e. $|\vec{\tau}_1| = \left|\vec{A}\right|$).

The procedure is simplified if we use another available degree of freedom, the rotation matrix C_0 of the polarization rotator preceding the compensator. For any given $\vec{\tau}_f$ and $\vec{\tau}_{\omega f}$ of the fiber cable to be compensated, C_0 can be used to turn $\vec{\tau}_c$ and $\vec{\tau}_{\omega c}$ into a plane containing $\vec{\tau}_3$, according to equation (5.3) and (5.4). Thus, we can arbitrarily fix $\vec{\tau}_c$ and $\vec{\tau}_{\omega c}$ to lie on any convenient plane that contains $\vec{\tau}_3$ while maintaining the condition of $\vec{\tau}_c.\vec{\tau}_{\omega c} = \vec{\tau}_f.\vec{\tau}_{\omega f}$, $|\vec{\tau}_c| = |\vec{\tau}_f|$ and $|\vec{\tau}_{\omega c}| = |\vec{\tau}_{\omega f}|$. However, from equation (5.9) and (5.10), we also know that $\vec{\tau}_c - \vec{\tau}_3$ and $\vec{\tau}_{\omega c} - (\vec{\tau}_3 \times \vec{\tau}_c)$ must be perpendicular to one another. Thus by taking the dot product of $\vec{\tau}_c - \vec{\tau}_3$ and $\vec{\tau}_{\omega c} - (\vec{\tau}_3 \times \vec{\tau}_c)$, and setting it to zero, we get the condition,

$$(\vec{\tau}_{\omega c} - (\vec{\tau}_3 \times \vec{\tau}_c)).(\vec{\tau}_c - \vec{\tau}_3) = \vec{\tau}_{\omega c}.(\vec{\tau}_c - \vec{\tau}_3) = 0 \qquad (5.11)$$

Therefore, the compensator can only produce pairs of $\vec{\tau}_c$ and $\vec{\tau}_{\omega c}$ that satisfy condition (5.11). Denote by $\theta_{\omega 3}$ the angle between $\vec{\tau}_{\omega c}$ and $\vec{\tau}_3$, and by ϕ the angle between $\vec{\tau}_c$ and $\vec{\tau}_{\omega c}$ (which is required to be the same as that between $\vec{\tau}_f$ and $\vec{\tau}_{\omega f}$) (See Figure 5-2a). Then we find from (5.11)

$$\cos\theta_{\omega 3} = \frac{|\vec{\tau}_c|}{|\vec{\tau}_3|}\cos\phi = \frac{|\vec{\tau}_f|}{|\vec{\tau}_3|}\cos\phi \qquad (5.12)$$

This fixes the vectors $\vec{\tau}_c$ and $\vec{\tau}_{\omega c}$ in that chosen plane. Thus now we know what 1^{st} and 2^{nd} order PMD vectors, $\vec{\tau}_c$ and $\vec{\tau}_{\omega c}$, need to be produced by the compensator so that, by applying a suitable rotation matrix, C_0, we can satisfy both equations (5.3) and (5.4) and eliminate the net 1^{st} and 2^{nd} order PMD. With the known $\vec{\tau}_c$ and $\vec{\tau}_{\omega c}$, we can now solve for $\vec{A}$ and $\vec{B}$, and thus the corresponding C_1 and C_2 for the compensator to produce them. To visualize that solutions of $\vec{A}$ and $\vec{B}$ exist, we have also illustrated the relative orientations of vectors that are discussed above in Figure 5-2a. Due to C_2, $\vec{B}$ can be of any direction with fixed magnitude $|\vec{\tau}_2|$ while, due to $C_1$and variable $|\vec{\tau}_1|$, $\vec{A}$ can be of any direction and of any magnitude. In Figure 5-2a, the solutions of $\vec{A}$ and $-\vec{B}$ point from the center of spheres to a common point on the ring of intersection of the two spheres so as to satisfy equation (5.9) and (5.10) simultaneously.

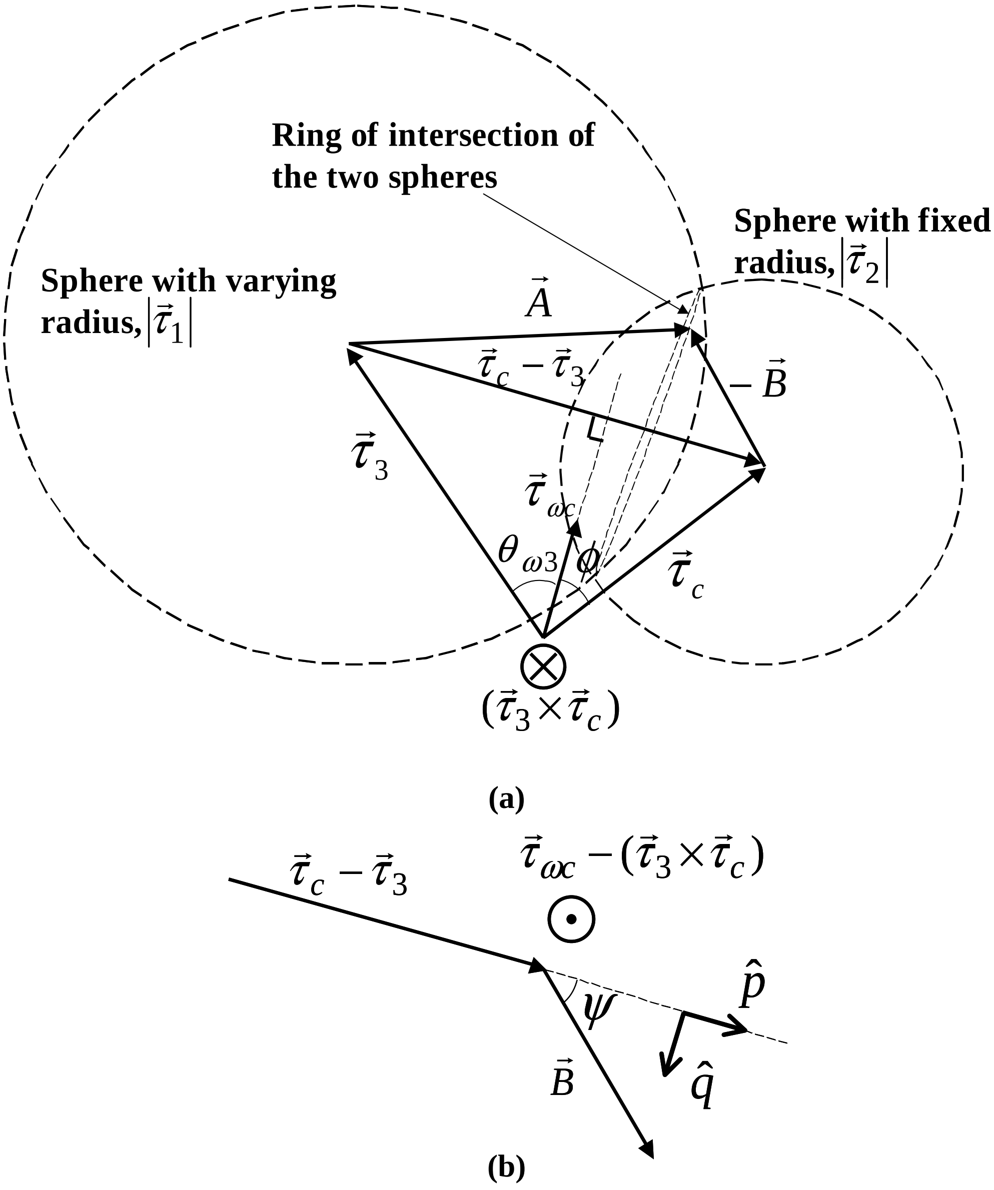

Figure 5-2: (a) Relative orientations of $\vec{\tau}_c$, $\vec{\tau}_{\omega c}$, $\vec{\tau}_3$, $\vec{A}$ and $\vec{B}$. ϕ is the angle between $\vec{\tau}_c$ and $\vec{\tau}_{\omega c}$ which is required to be the same as that between $\vec{\tau}_f$ and $\vec{\tau}_{\omega f}$. Condition (5.11) requires $\vec{\tau}_{\omega c}$ to be perpendicular to $\vec{\tau}_c - \vec{\tau}_3$. C_0 allows us to arbitrarily fix $\vec{\tau}_c$ and $\vec{\tau}_{\omega c}$ on any arbitrary plane that contains $\vec{\tau}_3$. Vectors $\vec{A}$ and $-\vec{B}$ point from centre of spheres to a point on the ring of intersection of the two spheres so as to satisfy equation (5.9) and (5.10) simultaneously. (b) The cross product of $\vec{B}$ and $\vec{\tau}_c - \vec{\tau}_3$ gives $\vec{\tau}_{\omega c} - (\vec{\tau}_3 \times \vec{\tau}_c)$. Vector $\hat{q}$ is the unit vector in the direction of $[(\vec{\tau}_c - \vec{\tau}_3) \times (\vec{\tau}_{\omega c} - (\vec{\tau}_3 \times \vec{\tau}_c)]$ while $\hat{p}$ is the unit vector in the direction of $(\vec{\tau}_c - \vec{\tau}_3)$.

Thus from Figure 5-2a, one should be able to see geometrically that solutions of $\vec{A}$ and $\vec{B}$ always exist (under the assumption that the required magnitude $|\vec{\tau}_1|$ is available in the set-up). Mathematically, we can solve for $\vec{A}$ and $\vec{B}$ in the following way. Substitute equation (5.9) into (5.10), we have

$$\vec{\tau}_{\omega c} - (\vec{\tau}_3 \times \vec{\tau}_c) = \vec{B} \times (\vec{\tau}_c - \vec{\tau}_3) \tag{5.13}$$

Note that according to equation (5.7) $\left|\vec{B}\right| = |\vec{\tau}_2|$. Thus the solution of $\vec{B}$ is

$$\vec{B} = |\vec{\tau}_2| \left(\cos\psi \hat{p} + \sin\psi \hat{q}\right) \tag{5.14}$$

where $\hat{p}$ is the unit vector in the direction of $(\vec{\tau}_c - \vec{\tau}_3)$, $\hat{q}$ is the unit vector in the direction of $[(\vec{\tau}_c - \vec{\tau}_3) \times (\vec{\tau}_{\omega c} - (\vec{\tau}_3 \times \vec{\tau}_c)]$ and ψ is the angle between $\vec{B}$ and $(\vec{\tau}_c - \vec{\tau}_3)$ (see Figure 5-2b) given by

$$\sin\psi = \frac{|(\vec{\tau}_{\omega c} - (\vec{\tau}_3 \times \vec{\tau}_c)|}{|\vec{\tau}_2|\,|\vec{\tau}_c - \vec{\tau}_3|} \tag{5.15}$$

After solving for $\vec{B}$, we solve for $\vec{A}$ using equation (5.9). Since we are using a variable DGD segment for $\vec{\tau}_1$, we can accommodate whatever magnitude $\vec{A}$ is needed to satisfy equation (5.9). And the magnitude of $\left|\vec{A}\right|$ solution gives the required DGD setting, $|\vec{\tau}_1|$, of the segment 1. It is worth noting that to ensure robust PMD compensation, we need to choose the magnitude of $\vec{\tau}_2$ and $\vec{\tau}_3$ appropriately so that we can always have solutions for equation (5.12) and (5.15) with any anticipated magnitude of $\vec{\tau}_f$ and $\vec{\tau}_{\omega f}$. Since we know R_3, $\vec{\tau}_2$, R_2, $\vec{\tau}_1$ of the individual segments, using equation (5.7), we can solve for the rotation matrix C_2 from

$$C_2\vec{\tau}_2 = R_3^{\dagger}\vec{B} \tag{5.16}$$

And then, using equation (5.8), we can solve for C_1

$$C_1\vec{\tau}_1 = (R_3C_2R_2)^{\dagger}\vec{A} \tag{5.17}$$

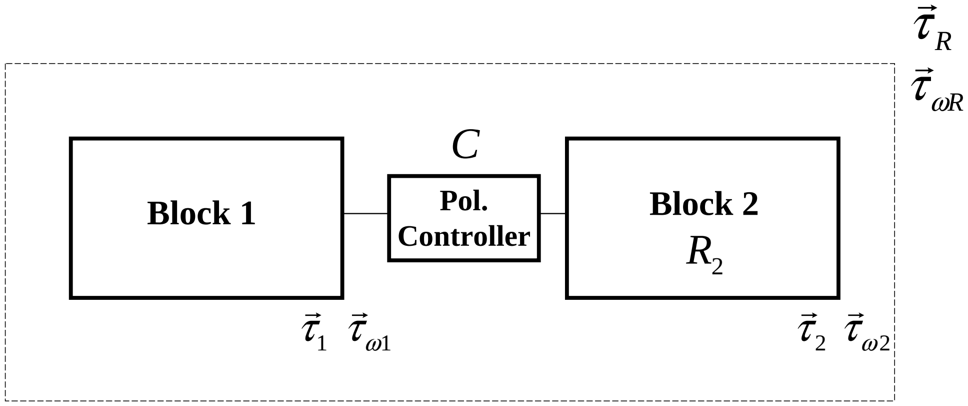

Figure 5-3: Block diagram of two PMD blocks concatenated via polarization controller.

Now we can compute

$$R_c = R_3 C_2 R_2 C_1 R_1 \tag{5.18}$$

and using equations (5.3), (5.4) and (5.18), we can solve for C_0 that satisfies both

$$C_0 \vec{\tau}_f = -(R_c)^\dagger \vec{\tau}_c \tag{5.19a}$$

$$C_0 \vec{\tau}_{\omega f} = -(R_c)^\dagger \vec{\tau}_{\omega c} \tag{5.19b}$$

so that the net 1^{st} and 2^{nd} order PMD are eliminated. Thus we have found all the required rotation matrices, C_0, C_1, and C_2 (from equation (5.16), (5.17), and (5.19) of the 3 polarization rotators as well as the required DGD value for segment 1, in order to compensate any 1^{st} order PMD, $\vec{\tau}_f$, and 2^{nd} order PMD, $\vec{\tau}_{\omega f}$, of the transmission cable. It should be noted that this 3-segments compensator is expected to introduce loss of several dB, especially since a variable DGD is used. Hence, an optical amplifier may be needed.

5.3 Hybrid Feed-forward and Feedback Scheme

In the feed-forward PMD compensation scheme, one needs accurate PMD characterizations of both first and second order PMD in order to carry out PMD compensation for both orders. However, from Chapter 3, one can see that the second order PMD cannot be characterized as accurately as the first order PMD. Thus, instead of compensating both orders simultaneously in a feed-forward scheme, an alternative is a hybrid feed-forward and feedback PMD scheme, where first-order PMD compensation is carried out in a feed-forward manner and feedback compensation is used for the second order PMD. To decouple these compensation schemes, a module that produces variable second order PMD without generating any first order PMD is needed. This allows the second order PMD compensator to search for the optimum without affecting the first order PMD compensation which is already accomplished in a feed-forward manner. In this section, we present a module that can be controlled to produce variable magnitude of second order PMD without generating any first order PMD. When it is used with an additional polarization controller, it can generate an arbitrary second order PMD vector within its designed operation range. Another application of such a module is in PMD emulation. In some studies, one may need to investigate the effects of first and second order PMD separately, thus decoupling of first order and second order PMD emulation is necessary.

Figure 5-3 shows the schematics of the module. Two blocks are concatenated via polarization controller C. Block 1 has first order PMD, $\vec{\tau}_1$, and second order PMD,$\vec{\tau}_{\omega 1}$ while Block 2 has first order PMD, $\vec{\tau}_2$, second order PMD, $\vec{\tau}_{\omega 2}$, and a polarization rotation matrix, R_2. By PMD concatenation rules, the resultant first order PMD vector, $\vec{\tau}_R$, of the module is

$$\vec{\tau}_R = \vec{\tau}_2 + R_2 C \vec{\tau}_1 \tag{5.20}$$

while the resultant second order PMD, $\vec{\tau}_{\omega R}$, is

$$\vec{\tau}_{\omega R} = \vec{\tau}_{\omega 2} + R_2 C \vec{\tau}_{\omega 1} + \vec{\tau}_2 \times \vec{\tau}_R \tag{5.21}$$

Now if we control the polarization controller C so that

$$R_2 C = I \tag{5.22}$$

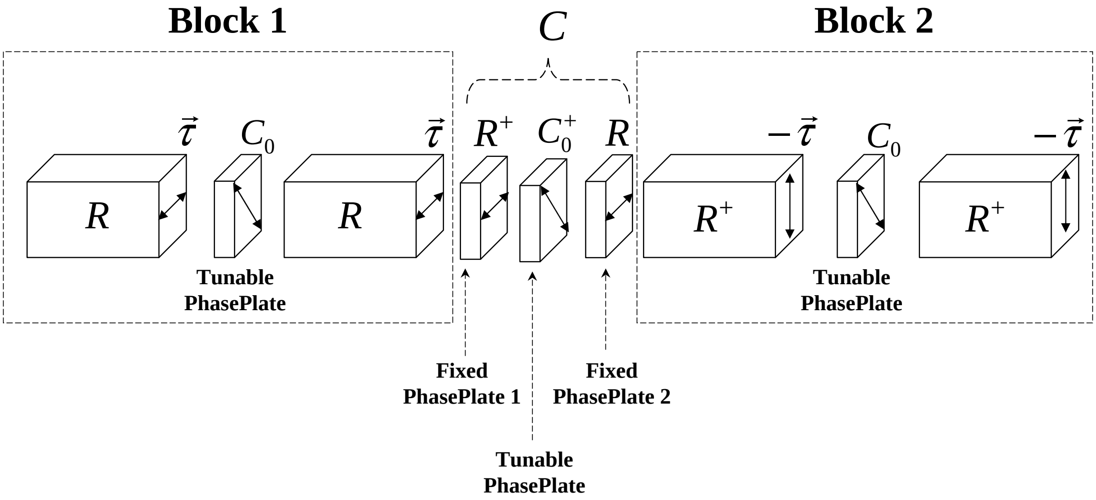

Figure 5-4: Schematic of our proposed module that produces variable magnitude of second order PMD without first order PMD. It consists of 4 identical fixed DGD segments arranged in a symmetrical manner. The first and second fixed DGD segments of PMD $\vec{\tau}$ are concatenated via C_o to form the Block 1 while Block 2 is formed by the third and fourth segment of PMD $-\vec{\tau}$, concatenated using another C_o. The polarization controller C between the two blocks is made up of two fixed phase plates and one tunable phase-plate $C_o^\dagger$.

and if the blocks are adjusted so that

$$\vec{\tau}_2 = -\vec{\tau}_1 \tag{5.23}$$

$$\vec{\tau}_{\omega 2} = \vec{\tau}_{\omega 1} \quad , \tag{5.24}$$

the resultant first order PMD vanishes while the second order PMD is given by

$$\vec{\tau}_{\omega R} = 2\vec{\tau}_{\omega 2} \tag{5.25}$$

Figure 5-4 shows the detailed composition of each block and of the polarization controller. All four identical fixed DGD segments are assumed to have negligible second order PMD. The first and second fixed DGD segments are concatenated via C_0 to form Block 1. In Stokes space representation, these fixed DGD segment have first order PMD, $\vec{\tau} = \{|\vec{\tau}|, 0, 0\}$, equivalent to having the slow birefringence axes oriented in the horizontal direction in physical space. They have rotation matrices, R, whose rotation axis is in the x-direction in Stokes space. C_0 is a tunable phase-plate whose rotation axis is along the y-direction in Stokes space (equivalent to a 45 degree linearly polarized birefringence axis). Block 2 is formed of another two segments (i.e. the third and fourth segment) concatenated using another C_0. Both of these segments have first order PMD, $-\vec{\tau}$. This is equivalent to having the same birefringence segments as Block 1 except that their slow birefringence axes are now in the vertical direction in physical space. Thus, these segments have rotation matrices, $R^\dagger$. With this arrangement, we can compute for Block 1,

$$\vec{\tau}_1 = \vec{\tau} + RC_0\vec{\tau} \tag{5.26}$$

$$\vec{\tau}_{\omega 1} = \vec{\tau} \times RC_0\vec{\tau} \tag{5.27}$$

And for Block 2

$$\vec{\tau}_2 = -\vec{\tau} - R^\dagger C_0\vec{\tau} = -R^\dagger R^\dagger(RR\vec{\tau} + RC_0\vec{\tau}) = -R^\dagger R^\dagger \vec{\tau}_1 \tag{5.28}$$

$$\vec{\tau}_{\omega 2} = -\vec{\tau} \times R^\dagger C_0(-\vec{\tau}) = R^\dagger R^\dagger(RR\vec{\tau} \times RC_0\vec{\tau}) = R^\dagger R^\dagger \vec{\tau}_{\omega 1} \tag{5.29}$$

We have made use of the fact that the rotation transformation of R has no effect on $\vec{\tau}$ since its rotation axis is along $\vec{\tau}$ (the x-axis in Stokes Space). Substituting equation (5.28) into (5.20) and (5.29) into (5.21), we obtain

$$\vec{\tau}_R = \vec{\tau}_2 - R_2CRR\vec{\tau}_2 \tag{5.30}$$

$$\vec{\tau}_{\omega R} = \vec{\tau}_{\omega 2} + R_2CRR\vec{\tau}_{\omega 2} + \vec{\tau}_2 \times \vec{\tau}_R \tag{5.31}$$

So if $R_2CRR = I$, we have successfully removed the first order PMD while the resultant second order PMD of the module becomes

$$\vec{\tau}_{\omega R} = 2\vec{\tau}_{\omega 2} \tag{5.32}$$

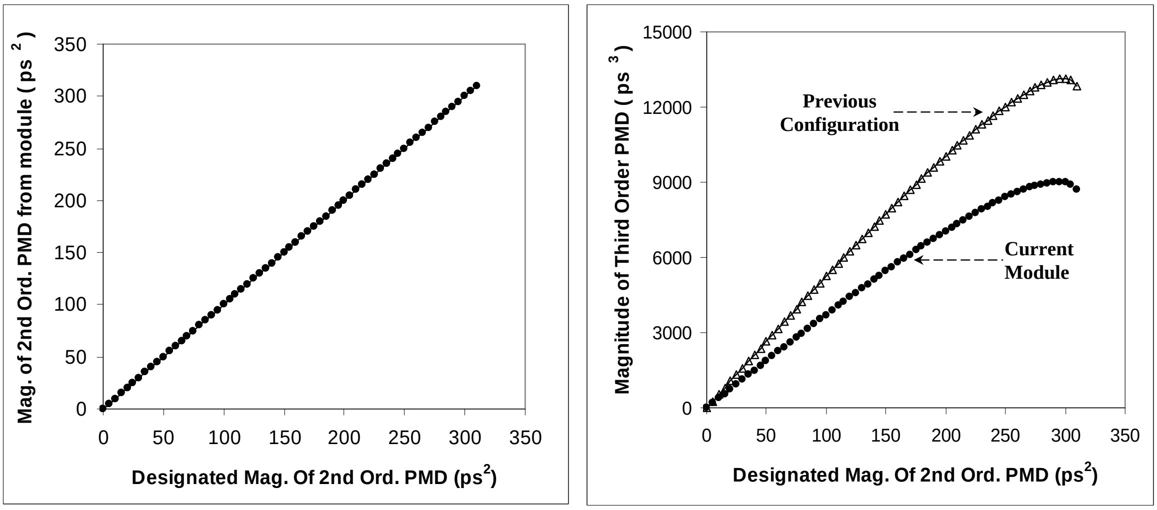

(a) **(b)**

Figure 5-5: (a) Magnitudes of second order PMD produced by our module for various designated magnitude values. (b) Magnitude of third order PMD vector produced by our module when it is controlled to produce the designated magnitude of second order PMD. For comparison purposes, we have also plotted the third order PMD produced by our previous 3-segments configuration (see Ref. [1]) for the same tuning range of 312.5 ps^2.

And since $R_2 = R^\dagger C_0 R^\dagger$, the solution of C is

$$C = RC_0^\dagger R^\dagger \tag{5.33}$$

To implement this polarization controller C, we need three phase plates as shown in Figure 5-4, where the rotation of fixed phase-plate 1 and fixed phase-plate 2 are $R^\dagger$ and R respectively, while the rotation of the second phase-plate is tunable as $C_0^\dagger$. Therefore, our approach to produce variable magnitude of second order PMD without any first order PMD can be summarized as follows: We arrange four identical fixed DGD segments (such as birefringence crystals) as shown in Figure 5-4. For any designated second order PMD magnitude, we adjust the rotation angle of C_0 as the only control parameter. Each of the blocks produces half of the designated magnitude of second order PMD, so that they add to give the designated value while their first order PMD cancel. The total tunable range of the magnitude of second order PMD is $2|\vec{\tau}|^2$. To produce any arbitrary second order PMD vector, we need an additional polarization controller to control the direction of the vector. Thus this polarization controller provides the other two degrees of freedom of the second order PMD vector.

Since the module is constructed with tunable phase-plates, which can either be electro-optic, magneto-optic or liquid crystal wave-plates, high speed tuning of the magnitude of second order PMD is possible. Moreover, instead of using polarization-maintaining fibers as fixed DGD segments, one could use birefringent crystals, which promise compactness and stability. Alternatively, one could integrate the whole variable DGD module on a wafer based on MEMS technology, since the fixed DGD segments are simply fixed delay lines in free space while the tunable phase-plates are finely-adjustable delay lines in free space as shown in [113].

In practical implementation, one may have difficulty in achieving the same rotation angle, θ_R, for all rotation matrices of the segments. Thus, for cases where we have different rotation angles for the various segments, the solution for C can be worked out to be

$$C = R^{\dagger}_{3rdSeg} C^{\dagger}_0 R^{\dagger}_{2ndSeg} \tag{5.34}$$

where $R^{\dagger}_{2ndSeg}$ is the transpose of the rotation matrix of the second fixed DGD segment while $R^{\dagger}_{3rdSeg}$ is the transpose of the rotation matrix of the third fixed DGD segment. This means that we need the rotation of the fixed phase-plate 1 and fixed phase-plate 2 in polarization controller, C, to be fixed as the transpose of the rotation matrices of the second and third segment of the module respectively. The rotation of the tunable phase-plate in polarization controller, C, is still $C^{\dagger}_0$. Note that the solution of C is independent of the rotation matrices of the first and last segment. If there are drifts in the rotation angles of the segments, the rotation of fixed phase-plate 1 and fixed phase-plate 2 can no longer be static but need to be tunable according to equation (5.34). However, drifts could be avoided by a temperature controlled and mechanically stabilized environment.

For any designated second order PMD magnitude, $|\vec{\tau}_{\omega R}| = 2\,|\vec{\tau}_{\omega 2}|$, we can solve

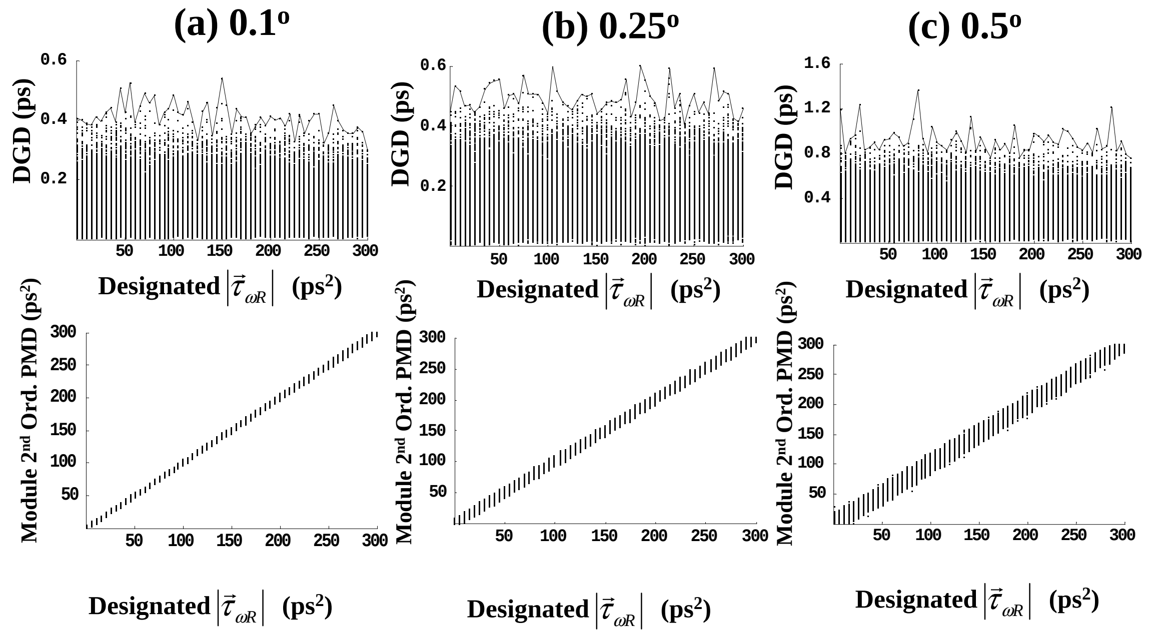

Figure 5-6: First and second order PMD generated by our module when there are angle standard deviations σ_{angle} of (a) 0.1°, (b) 0.25° and (c) 0.5° in the rotation angles of the phase-plates together, with DGD standard deviation σ_{DGD} of 0.06ps for all the DGD segments. All segments have identical $|\vec{\tau}|$ of 12.5ps.

the required rotation angle of C_0 using simple vector algebra,

$$\sin(\theta_{C_0}) = \frac{|\vec{\tau}_{\omega R}|}{2\,|\vec{\tau}|^2} \tag{5.35}$$

Since the rotation angle of C_0 is the only control parameter for the module, and from equation (5.35), the solution of C_0 is continuous, there is no issue of transient fluctuation when one changes the settings of the module's second order PMD magnitude, $|\vec{\tau}_{\omega R}|$.

Figure 5-5a shows the magnitudes of the second order PMD produced by our module for various designated values using the method discussed above. The DGD, $|\vec{\tau}|$, is 12.5ps for all four segments. Clearly, our module can produce the designated magnitude of second order PMD within the whole tuning range of zero to $2|\vec{\tau}|^2$, which, in this case is 312.5ps^2, while always maintaining zero first order PMD. Figure 5-6b shows the magnitude of third order PMD produced by our module. For comparison, we have also plotted the third order PMD produced by our previous 3-segments configuration discussed in Ref. [1]. In this 3-segments configuration, we rely on two fixed DGD segments to generate the required second order PMD and then use the variable DGD segment to cancel the unwanted first order PMD generated by these two fixed DGD segments. Thus, in order to produce the same second order PMD tuning range of 312.5ps^2, the DGD of the two fixed DGD segments are 17.68ps each. From Figure 4b, we can see that the present module produces a lower magnitude of third order PMD than the previous 3-segment configuration [1].

In practical implementation, there are three main considerations: (a) the tolerance in choosing DGD, (b) the errors in the rotation angles of the three tunable phase-plates in the phase plates, (c) the temperature changes that affect the rotation matrices of the fixed DGD segments. To study these tolerances, we have carried out Monte Carlo simulations, the results of which are shown in Figure 5-6. For a given magnitude of second order PMD, we first solve exactly the required rotation angle of C_0 using equation (5.35). We then introduce independent random Gaussian distributed angular errors of standard deviation σ_{angle} to all five phase-plates. At the same time, random Gaussian distributed DGD errors of standard deviation σ_{DGD} are introduced independently to all four segments. Using these perturbed angles and DGD, we calculate the first and second order PMD produced by our module. Figure 5-6 shows the first and second order PMD magnitudes generated for various standard deviations σ_{angle} of (a) 0.1^o, (b) 0.25^o and (c) 0.5^o together with σ_{DGD} of 0.06ps. All segments have identical $|\vec{\tau}|$ of 12.5ps. For each designated magnitude of second order PMD, we perform 1000 Monte-Carlo simulations. From these simulations, we can infer that the required tolerance of the DGD for each crystal is $< \pm 0.06$ps and the required accuracy of the rotation angle of all the five phase plates are $\sim \pm \sim 0.25^o$. With these tolerances, the magnitude of second order PMD produced is reasonably close to the designated value while the DGD is still tolerably small at < 0.6 ps. These parameters are realistic for practical implementation. For example, to build a pure second order PMD module that can generate a range of second order PMD from 0 to 312.5 ps^2, the required DGD of each segment is 12.5ps. For birefringence crystals, such as YVO$_{4,}$ whose birefringence is 0.2039, the required length of each crystal is

17.76mm. Commercial crystal suppliers can readily promise a dimension tolerance of ±0.05mm. This corresponds to DGD tolerance of ±0.035 ps for YVO $_{4,}$ which is better than the required tolerance of 0.06ps. For the tunable phase plates, one has the choice of a liquid crystal variable wave-plate or an electro-optic phase modulator. The required rotation angle accuracy of $\pm \sim 0.25^{o}$ is achievable with commercially available phase plates.

Temperature drifts can cause significant changes in the rotation angles of the birefringence crystals, and this is undesirable for the module. These drifts have to be avoided using a temperature controlled environment. Commercially available thermal electric cooler can provide temperature stability of better than ±0.005°C. Thus, for birefringence crystals such as YVO$_{4,}$ (whose thermal optical coefficients are dn/dT = 8.5x10^{-6}/K and dn/dT = 3.0x10^{-6}/K), the drift in the birefringence will be less than 2.75x10^{-8}, when it is temperature controlled. This corresponds to a polarization rotation angle drift of $< 0.1^{o}$. which is acceptable. Alternatively, one can also achieve low temperature dependence of the rotation angle by using a DGD segment that is a combination of birefringence crystals that have opposite temperature dependences. In summary, with existing commercially available components and careful design, it is practical to implement our module within the required tolerance.

5.4 Conclusion

We have described a procedure to exercise complete PMD compensation up to second order when the information of the first order PMD, $\vec{\tau}_f$, and second order PMD, $\vec{\tau}_{\omega f}$, of a long haul communication cable are known. Moreover, we have solved analytically the required rotation matrices of the polarization rotators and the required DGD of a variable delay line in a 3-segment compensator. The approach here is necessary for a PMD compensation system that uses feed-forward correction. In addition, we have also presented a module that generates variable second order PMD without producing any first order PMD. It is based on four identical fixed DGD segments arranged in a symmetrical manner. Only one control parameter varies the magnitude of second order PMD. This module is useful in a hybrid feed-forward/feedback compensation scheme, where first-order PMD compensation is carried out in a feed-forward manner and feedback compensation is used for the second order PMD.

Chapter 6

All-Frequency PMD Compensation in Feed-Forward Scheme

6.1 Background

Most PMD compensation techniques reported in the literature [88, 114, 2, 104], including those discussed in Chapter 4 and 5, are designed to compensate the first- and second- order PMD in a single channel. In general, regardless of single or multi-WDM channels, as long as the bandwidth of interest is much larger than the PSP bandwidth, all orders of PMD are important. In high PMD link where the PSP bandwidth is less than the WDM channel spacing, the PMD vectors of the different WDM channels are independent of each other. To compensate such WDM system, channels have to be demultiplexed and compensated individually. This results in an increased cost and complexity. To reduce cost, several authors [115, 116, 109, 10] proposed various broadband PMD compensators. Such inline broadband compensation over a tera-hertz bandwidth is attractive since it can achieve simultaneous compensation for several channels without the need of wavelength demultiplexing cum multiplexing. In such broadband applications, all orders of PMD need to be accounted for.

Most of the previous broadband compensators aim to generate the inverse of transmission fiber's Jones matrix over a range of frequency. They concentrate on the synthesis of a filter response to approximate the inverse of this unitary matrix

[115, 116, 109]. Recently, C.K. Madsen proposed an architecture using all-pass filters [109] to invert the complete Jones matrix $U(\omega)$. The approach is promising as it can be compactly integrated using planar waveguides. However, in terms of compensating for the PMD-induced signal's degradation, such inversion of the complete Jones matrix is not necessary since it also produces the same output polarizations as that of the input [117]. To avoid pulse distortion, what one really needs is to make the Jones matrix of the fiber/compensator combination independent of frequency (i.e. invert the "difference" of Jones matrices). This is equivalent to the cancellation of the PMD vectors. In [51], H.A. Haus discussed the three equivalent representations of PMD: Jones Space, Stokes Space and Energy Space and mentioned that, although the information about the isotropic dispersion is suppressed in the Stokes space formulation, the knowledge of the output PMD vector, $\vec{\tau}_f(\omega)$, as a function of frequency is sufficient for the construction of an all-frequency PMD compensator (AFPMD). Thus, in this chapter, we present the architecture of a compensator that can compensate PMD for all frequencies based solely on the knowledge of the output PMD vector.

Unlike previous works that concentrated on Jones Space representation, we propose to solve the all-frequency PMD compensation in Stokes space. This representation not only gives us good 3-D visualization of PMD vectors on the Poincaré sphere, it also offers us simple PMD concatenation rules when designing an all-frequency PMD compensator or emulator. In terms of PMD emulation, this preference is also reasonable since PMD statistics are mainly understood in terms of PMD vectors. In a feed-forward PMD compensation scheme [2, 4], there is also the advantage of real-time monitoring. In Madsen's approach, the complete Jones matrix $U(\omega)$ needs to be characterized as a function of frequency, while in our approach only the output PMD vector, $\vec{\tau}_f(\omega)$, needs to be characterized as a function of frequency. The latter is comparatively easier since it does not require any knowledge of the input state of polarization (SOP) and is monitored solely based on the measurements obtained at the receiver's end [4]. This also facilitates the use of random polarization scrambling of the input SOP to improve the estimation accuracy of the output PMD vector as discussed in Chapter 3.

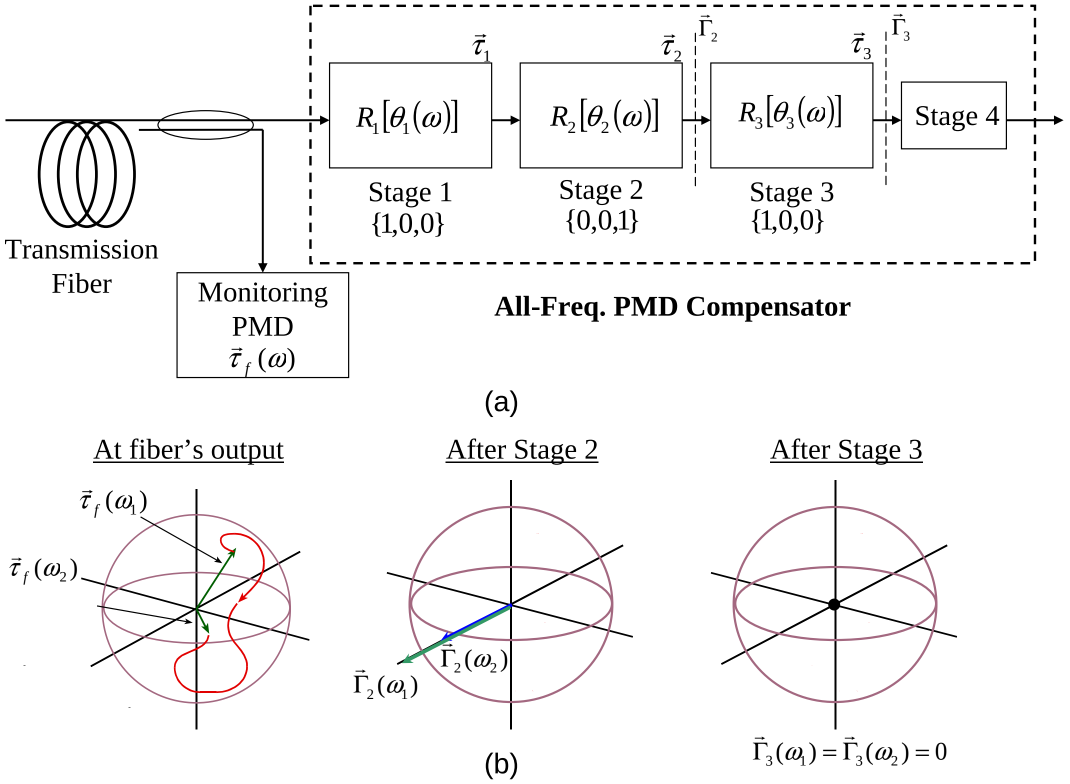

Figure 6-1: a) Schematic of our 4-stage all-frequency PMD compensator; b) PMD spectra after fiber, and composite PMD spectra after Stage 2 and 3 of compensator.

Our compensation scheme, as shown in Figure 6-1a, employs three stages of flexible frequency-dependent polarization rotation in Stokes space. These three stages provide the three degrees of freedom for compensating the PMD vector at each frequency. Intuitively, the net effect of the first two stages is equivalent to a frequency dependent polarization rotation that aligns all PMD vectors into a common direction, and the third stage compensates the frequency dependent variable DGD. The fourth stage basically compensates for the isotropic dispersion created by the first three stages.

6.2 Synthesis of Rotation Angle Profiles

Since there are so many degrees of freedom in a broadband compensator, the most viable approach is to carry out the compensation in a feed-forward manner. We assume that with the real-time PMD monitoring scheme proposed in Chapter 3, we have the required information of the fiber's output PMD vector, $\vec{\tau}_f(\omega)$, as a function of frequency. For simplicity, we neglect polarization-dependent losses. While the most common definitions of PMD orders is based on the Taylor expansion of the PMD vector in frequency [59], there is no reason to believe that this is the most useful description when the first order approximation is insufficient. We avoid the Taylor expansion since this introduces the complicated higher-order PMD terms such as $d\vec{\tau}/d\omega$, $d^2\vec{\tau}/d\omega^2$. Instead we simply treat the whole PMD spectrum as first order PMD vectors that vary from frequency to frequency. For this reason, we choose to call the proposed scheme "All-Frequency", instead of "All-Order", PMD compensator.

Figure 6-1a shows the schematic of the proposed architecture. A portion of the signal is tapped at the fiber output for real-time PMD monitoring. Based on the knowledge of the PMD vector data, we control the 4-stage compensator. At each angular frequency ω ($\omega = 2\pi f$ where f is the optical frequency), the fiber's output PMD vector, $\vec{\tau}_f(\omega)$, has three parameters $\{\tau_{fx}(\omega), \tau_{fy}(\omega), \tau_{fz}(\omega)\}$. The first three stages of the compensator provide the three degrees of freedom at each frequency for the PMD cancellation. In Stokes space, Stage 1 is a rotation about {1,0,0} with rotation angle $\theta_1(\omega)$ as a function of frequency while Stage 2 is a rotation about the {0,0,1} with rotation angle $\theta_2(\omega)$ which is also a function of frequency. The combined effect of stage 1 and 2 is equivalent to that of a frequency-dependent polarization controller that aligns the PMD of various frequencies into a common direction, in this case, we choose it to be {1,0,0}. Figure 6-1b illustrates this rotation effect. After aligning the PMD vectors, Stage 3 provides the necessary frequency dependent variable DGD $\tau_3(\omega) = d\theta_3(\omega)/d\omega$ in the {1,0,0} direction to cancel the PMD. Finally, Stage 4 compensates for the isotropic dispersion introduced by the first three stages due to imperfect fitting of the rotation angles, which will be discussed in later section. Since the rotation angles of Stage 1 and 2 are flexible functions of frequency, they possess substantial DGD that cannot be neglected. This is in contrary to polarization controllers that employ low-order wave-plates.

With the knowledge of the spectrum of the fiber's output PMD vector $\vec{\tau}_f(\omega)$, we need to synthesize the appropriate rotation angle profiles of the various stages for complete cancellation of the PMD vector at every frequency. This task is greatly simplified using the Stokes space representation. And we propose to use the PMD concatenation rules for this synthesis. In Stokes space, the rotation matrix of Stage 1 is

$$R_1(\omega) = \begin{pmatrix} 1 & 0 & 0 \\ 0 & \cos\theta_1(\omega) & -\sin\theta_1(\omega) \\ 0 & \sin\theta_1(\omega) & \cos\theta_1(\omega) \end{pmatrix} \tag{6.1}$$

and the rotation matrix of Stage 2 is

$$R_2(\omega) = \begin{pmatrix} \cos\theta_2(\omega) & -\sin\theta_2(\omega) & 0 \\ \sin\theta_2(\omega) & \cos\theta_2(\omega) & 0 \\ 0 & 0 & 1 \end{pmatrix} \tag{6.2}$$

Since $\vec{\tau}\times = \frac{dR}{d\omega}R^\dagger$ [17], the corresponding PMD vectors of stage 1 and 2 are $\vec{\tau}_1(\omega) = \left\{\frac{d\theta_1(\omega)}{d\omega}, 0, 0\right\}$ and $\vec{\tau}_2(\omega) = \left\{0, 0, \frac{d\theta_2(\omega)}{d\omega}\right\}$ respectively. We assume the fiber's PMD is known to be $\vec{\tau}_f(\omega) = \{\tau_{fx}(\omega), \tau_{fy}(\omega), \tau_{fz}(\omega)\}$. Using PMD concatenation rule, the PMD after Stage 2, $\vec{\Gamma}_2(\omega)$, is

$$\vec{\Gamma}_2(\omega) = \vec{\tau}_2(\omega) + R_2(\omega)\vec{\tau}_1(\omega) + R_2(\omega)R_1(\omega)\vec{\tau}_f(\omega) \tag{6.3a}$$

$$= \begin{pmatrix} \cos\theta_2\left(\frac{d\theta_1}{d\omega} + \tau_{fx}\right) - \sin\theta_2\left(\tau_{fy}\cos\theta_1 - \tau_{fz}\sin\theta_1\right) \\ \sin\theta_2\left(\frac{d\theta_1}{d\omega} + \tau_{fx}\right) + \cos\theta_2\left(\tau_{fy}\cos\theta_1 - \tau_{fz}\sin\theta_1\right) \\ \frac{d\theta_2}{d\omega} + \left(\tau_{fy}\sin\theta_1 + \tau_{fz}\cos\theta_1\right) \end{pmatrix} \tag{6.3b}$$

Since we want the PMD vector of all frequency to be aligned to {1,0,0} after Stage 2, we need

$$\sin\theta_2\left(\frac{d\theta_1}{d\omega} + \tau_{fx}(\omega)\right) + \cos\theta_2\left(\tau_{fy}(\omega)\cos\theta_1 - \tau_{fz}(\omega)\sin\theta_1\right) = 0 \tag{6.4}$$

and

$$\frac{d\theta_2}{d\omega} + \left(\tau_{fy}(\omega)\sin\theta_1 + \tau_{fz}(\omega)\cos\theta_1\right) = 0 \tag{6.5}$$

Solutions of equation (6.4) and (6.5) yield the required rotation angles $\theta_1(\omega)$ and

$\theta_2(\omega)$. To solve these equations, the following step-wise algorithm is proposed. At an initial frequency, $\omega_{initial}$, we determine the rotation angles of Stage 1 and 2 to bring $\vec{\tau}_f\left(\omega_{initial}\right)$ aligned to {1,0,0}. These $\theta_1(\omega_{initial})$ and $\theta_2(\omega_{initial})$ serve as the starting points for the algorithm. For subsequent frequency, we find the rotation angles in a step-wise manner:

$$\theta_1\left(\omega+\Delta\omega\right) \approx \theta_1\left(\omega\right) + \frac{d\theta_1}{d\omega}\left(\omega\right)\Delta\omega \tag{6.6}$$

$$\theta_2\left(\omega+\Delta\omega\right) \approx \theta_2\left(\omega\right) + \frac{d\theta_2}{d\omega}\left(\omega\right)\Delta\omega \tag{6.7}$$

where $d\theta_1/d\omega$ and $d\theta_2/d\omega$ are given by equation (6.4) and (6.5) as

$$\frac{d\theta_1}{d\omega}\left(\omega\right) = \cot\theta_2\left(\omega\right)\left[\tau_{fz}\left(\omega\right)\sin\theta_1\left(\omega\right) - \tau_{fy}\left(\omega\right)\cos\theta_1\left(\omega\right)\right] - \tau_{fx}\left(\omega\right) \tag{6.8}$$

and

$$\frac{d\theta_2}{d\omega}\left(\omega\right) = -\left[\tau_{fy}\left(\omega\right)\sin\theta_1\left(\omega\right) + \tau_{fz}\left(\omega\right)\cos\theta_1\left(\omega\right)\right] \tag{6.9}$$

In this way, we successively synthesize the rotation angles of Stage 1 and 2 to align all the PMD vectors into {1,0,0} and the PMD vector after Stage 2 becomes

$$\vec{\Gamma}_2(\omega) = \begin{pmatrix} \cos\theta_2\left(\frac{d\theta_1}{d\omega} + \tau_{fx}\right) - \sin\theta_2\left(\tau_{fy}\cos\theta_1 - \tau_{fz}\sin\theta_1\right) \\ 0 \\ 0 \end{pmatrix} \tag{6.10}$$

Since Stage 3 is a rotation about {1,0,0}, its rotation matrix has no effect on $\vec{\Gamma}_2(\omega)$. The PMD vector of Stage 3 is $\vec{\tau}_3\left(\omega\right) = \left\{\frac{d\theta_3(\omega)}{d\omega}, 0, 0\right\}$. After passing through Stage 3, the resultant PMD vector $\vec{\Gamma}_3(\omega)$ becomes

$$\begin{aligned} \vec{\Gamma}_3(\omega) &= \vec{\tau}_3\left(\omega\right) + R_3\left(\omega\right)\vec{\Gamma}_2(\omega) = \vec{\tau}_3\left(\omega\right) + \vec{\Gamma}_2(\omega) && \text{(6.11a)} \\ &= \begin{pmatrix} \frac{d\theta_3(\omega)}{d\omega} + \cos\theta_2\left(\frac{d\theta_1}{d\omega} + \tau_{fx}\right) - \sin\theta_2\left(\tau_{fy}\cos\theta_1 - \tau_{fz}\sin\theta_1\right) \\ 0 \\ 0 \end{pmatrix} && \text{(6.11b)} \end{aligned}$$

To have zero resultant PMD for all frequencies after Stage 3, $\vec{\Gamma}_3(\omega)$ must be zero for all frequencies. Making use of equation (6.8), this gives

$$\frac{d\theta_3\left(\omega\right)}{d\omega}=\csc\theta_2\left(\omega\right)\left[\tau_{fy}\left(\omega\right)\cos\theta_1\left(\omega\right)-\tau_{fz}\left(\omega\right)\sin\theta_1\left(\omega\right)\right] \tag{6.12}$$

Together with $\theta_1(\omega)$ and $\theta_2(\omega)$, $\theta_3\left(\omega\right)$ is synthesized by arbitrary fixing $\theta_3\left(\omega_{initial}\right)=0$ and subsequent frequency by

$$\theta_3\left(\omega+\Delta\omega\right)\approx\theta_3\left(\omega\right)+\frac{d\theta_3}{d\omega}\left(\omega\right)\Delta\omega \tag{6.13}$$

In summary of the synthesis algorithm, with equation (6.6)-(6.9) and (6.12)-(6.13), we can synthesize the required rotation angle of $\theta_1(\omega)$, $\theta_2(\omega)$ and $\theta_3(\omega)$ for the complete PMD compensation at all frequency.

6.3 Simulations to verify synthesis algorithm

PMD concatenation rules are commonly used to calculate the resultant PMD of the concatenation of birefringent elements. In this section, we show that it is equally valid for our concatenation of flexible frequency-dependent polarization rotation stages. And we verify our synthesis algorithm of the rotation angles by simulating the signal-degradation before and after the compensation

To test the synthesis algorithm, random fibers were generated with a mean DGD of 20 ps by cascading 20 randomly oriented birefringence sections. The birefringence of these sections was Gaussian distributed with a mean value of 4.85 ps and standard deviation of 20% of the mean. The input signal was a 40 Gbit/s RZ pseudo-random bit sequence (2^6-1) of Gaussian pulses of 10 ps (FHWM) pulse-width. For each generated fiber, we computed the output PMD vector, $\vec{\tau}(\omega)$, as a function of frequency with an optical frequency step-size of Δf =1.26 GHz. Based on this PMD vector spectrum, we synthesized the required rotation angles $\theta_1(\omega)$, $\theta_2(\omega)$ and $\theta_3(\omega)$ using equation (6.6)-(6.9) and (6.12)-(6.13). For illustration purpose, we randomly chose a fiber and the required rotation angles for the various stages are shown in Figure 6-2a-c. They

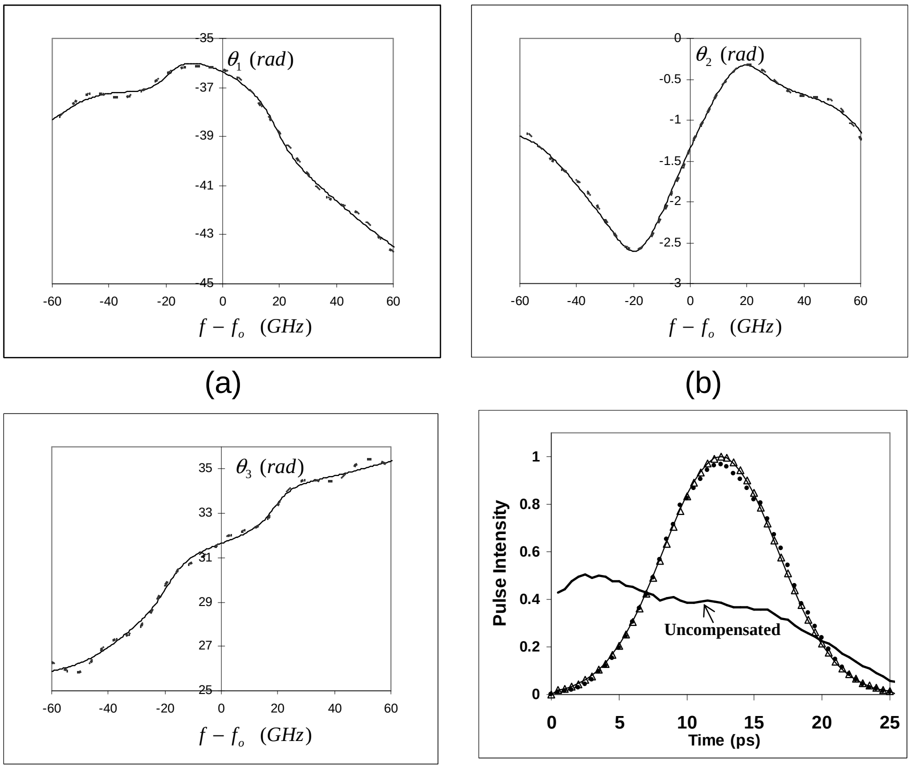

(a)

(b)

(c)

(d)

Figure 6-2: Required rotation angles of various stages for a randomly chosen fiber: (a) $\theta_1(\omega)$ of Stage 1 (b) $\theta_2(\omega)$ of Stage 2, (c) $\theta_3(\omega)$ of Stage 3. Solid curves are exact rotation angles computed using the synthesis algorithm while dashed curves are rotation angles approximated using APFs. f_o is the carrier's optical frequency. (d) shows the output optical signal before and after compensation. Thin solid curve is the input signal to fiber. Thick solid curve is output from fiber. Curve of unfilled triangles is after compensation using the exact rotation angles while the curve of filled circles is based on approximated rotation angles using APFs.

are presented in solid curves. Figure 6-2a is for $\theta_1(\omega)$ of Stage 1, Fig 6-2b is for $\theta_2(\omega)$ of Stage 2, and Fig 6-2c is for $\theta_3(\omega)$ of Stage 3. For the same chosen fiber, we show in Figure 6-2d the output signal from the fiber before compensation. It is the thick solid curve. For reference, the input signal is also shown in thin solid curve. Using the rotation angles $\theta_1(\omega)$, $\theta_2(\omega)$ and $\theta_3(\omega)$ calculated from our synthesis algorithm, the optical signal after passing through the AFPMD compensator is given by the curve of unfilled triangles. The compensation is nearly perfect.

To have a quantitative measure of the performance of the AFPMD compensator, we simulated the bit error rate (BER) by sending the output optical signals through

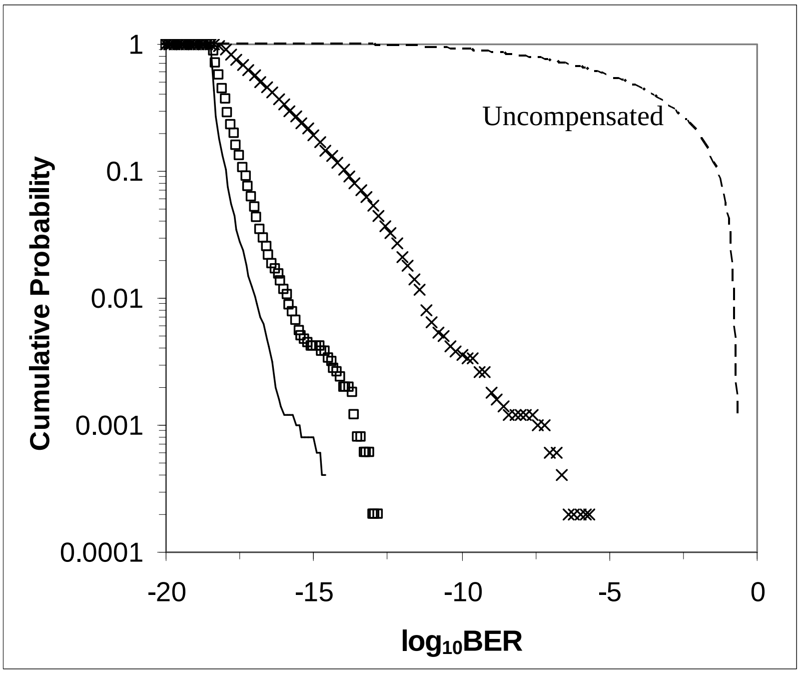

Figure 6-3: Cumulative Probability distribution of exceeding a certain BER value. Dashed curve is the uncompensated case. Performances of compensation using different Δf for the synthesis algorithm are investigated: Solid line curve is for $\Delta f =$ 0.63 GHz, curve of squares is for $\Delta f = 2.54$ GHz and curve of crosses is for $\Delta f =$ 6.3 GHz.

a 1 nm optical filter and an EDFA-preamplifier receiver (with noise figure of 3 dB) for detection. The electrical data was then low-pass filtered with an electrical fifth-order Bessel filter with a bandwidth of 0.5 B where B is the bit rate. Assuming the signal-spontaneous beat noise and spontaneous-spontaneous beat noise dominate, the noise variance in the detected signal was calculated analytically [118]. Only PMD and the signal-to-noise ratio were taken into account. Chromatic dispersion and nonlinearities were neglected. By assuming Gaussian noise statistics, the BER was calculated as the sum over all 2^6-1 bits, and as a function of the decision level and sampling time. We assume that the decision level and sampling time are optimized simultaneously to give the lowest BER for the bit sequence. Figure 6-3 shows the cumulative probability distribution of exceeding a certain BER value for a set of 5000 samples. This set was created by randomly generating 1000 fibers. For each fiber realization, there are 5 different random input SOPs. The power was set at 3 dB above the power

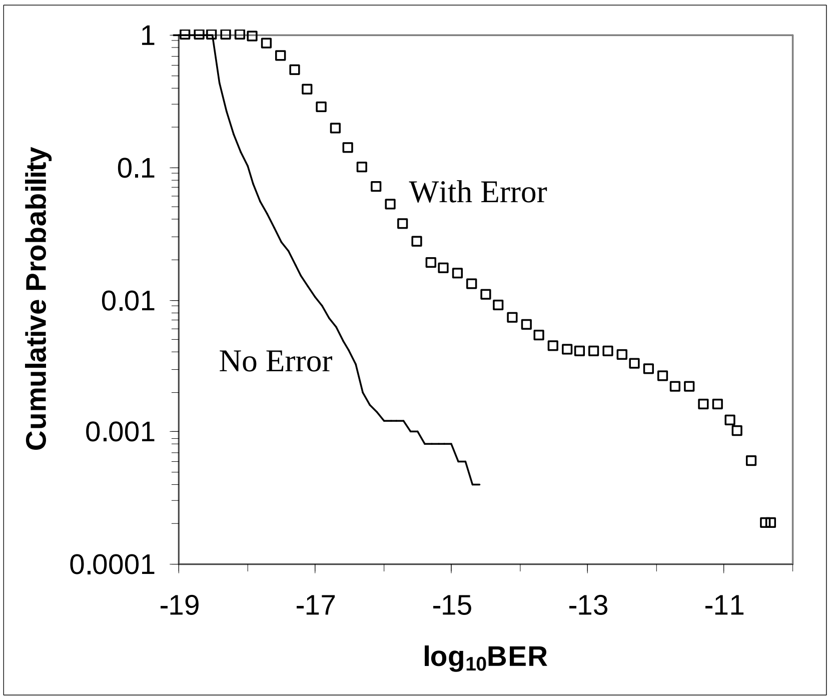

Figure 6-4: Performance of compensation when there are monitoring errors in the spectrum of PMD vectors. Curve of squares is for the case with error variance σ_{PMD} = 10ps. For reference, the compensated case without error is shown as the solid curve. The numerical simulation was carried out with Δf = 0.63 GHz, and the mean DGD was 20ps for the fiber ensemble.

that provides a BER of 10^{-9}. The dashed curve is for the uncompensated case while the curves of squares is for the compensated case. With a mean DGD value of the fiber ensemble set at 80% of the bit period, one would expect the presence of large amount of higher order PMD. The significant improvement of the signal quality after compensation indicates that the AFPMD compensator can handle the higher order PMD. The optical frequency resolution Δf required for the characterization of the spectrum of PMD vectors depends on the bandwidth of the PSP, which, in turn, depends on the mean DGD of the fiber ensemble. This frequency resolution affects the speed of monitoring. The step size used in the synthesis algorithm is equal to this frequency resolution. Therefore, it is interesting to study the performance of the compensation as a function of this step size.

The solid line curve in Figure 6-3 shows the compensated case when Δf is reduced to 0.63 GHz and the curve of crosses shows the compensated case when Δf is increased

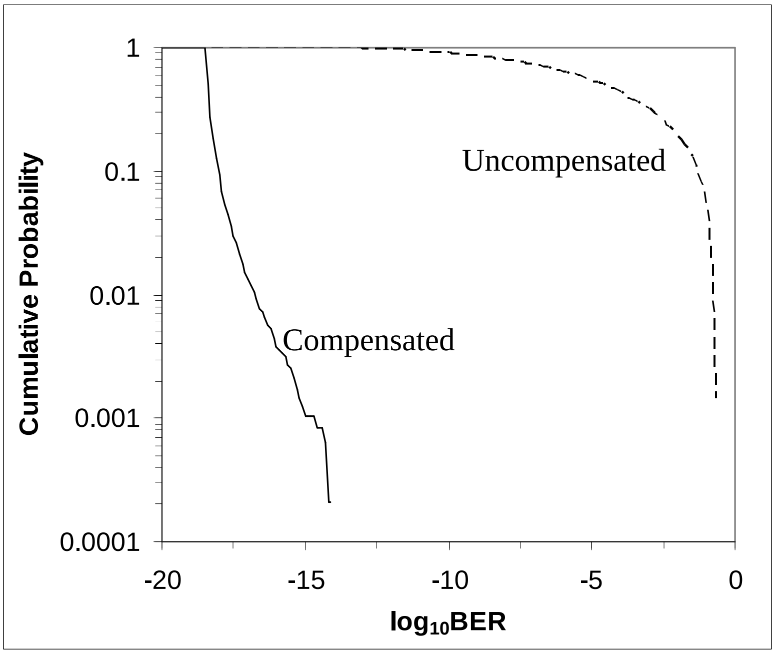

Figure 6-5: Cumulative probability distribution of BER curve for multi-channel PMD compensation over 1 Tera-Hertz bandwidth. The center wavelength of the 40 Gbit/s Gaussian pulse was randomly chosen within this 1 THz bandwidth. The numerical simulation was carried out with $\Delta f = 0.63$ GHz, and the mean DGD was 20ps for the fiber ensemble. The solid line curve is for the compensated case while the dashed curve is for the uncompensated case.

to 6.3 GHz. As expected, the performance of the compensation improves as the step-size is reduced. Since the mean DGD of the fiber ensemble is 20 ps, its corresponding PSP bandwidth Δf_{PSP} is ~6.25 GHz. From Figure 6-3, the required frequency resolution for good compensation is around $\Delta f_{PSP}/8$. In our numerical simulations, we restricted the value of $d\theta_i/d\omega$ to a maximum value of 100 ps in the synthesis algorithm. This is to avoid the singularity when θ_2 approaches 0 (see equation (6.8) and (6.12)). The significant improvement after compensation (as shown in Figure 6-3) indicates that this restriction has little impact on the performance of the AFPMD compensation.

In practice, there are always errors in the monitoring of the PMD vector spectrum. Therefore, it is useful to study the performance of the compensation in the presence of such errors. To simulate these monitoring errors, we first computed the exact output PMD vector, $\vec{\tau}(\omega)$, as a function of frequency for each randomly generated fiber.

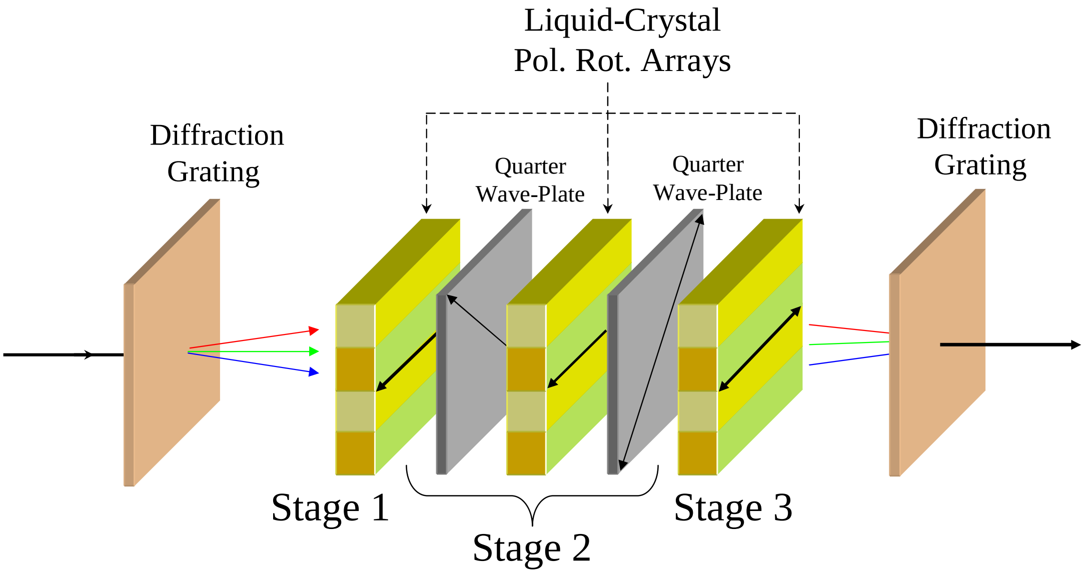

Figure 6-6: Implementation of PMD compensator using spatial arrays of liquid crystal polarization rotators with dispersive grating elements.

Then we introduced independent random Gaussian distributed errors of standard deviation σ_{PMD} to each component of the computed PMD vector. The perturbation was carried out independently for each frequency. Based on this perturbed spectrum of PMD vectors, we synthesized the required rotation angles $\theta_1(\omega)$, $\theta_2(\omega)$ and $\theta_3(\omega)$ using equation (6.6)-(6.9) and (6.12)-(6.13). The curve of squares in Figure 6-4 is for the case when σ_{PMD}= 10 ps. For comparison, the compensated case without monitoring error is shown in solid-line curve. The mean DGD of the fiber ensemble used in Figure 6-4 is 20 ps and the step-size Δf used is 0.63 GHz. This result shows that the performance of the AFPMD is quite tolerant of the monitoring errors.

Until now, our main focus has been on the application of our synthesis algorithm to the “All-frequency” compensation of a single channel. However, it is worthwhile to mention that our synthesis algorithm can be applied well across many channels, and it is suitable for broadband Tera-Hertz bandwidths. To simulate this, we computed the output PMD vector, $\vec{\tau}(\omega)$, as a function of frequency across a 1 THz bandwidth for each generated fiber. This is equal to a frequency range that spans 10 WDM channels. The optical frequency step-size used was $\Delta f = 0.63$ GHz. Based on this PMD vector spectrum, we synthesized the required rotation angles $\theta_1(\omega)$, $\theta_2(\omega)$

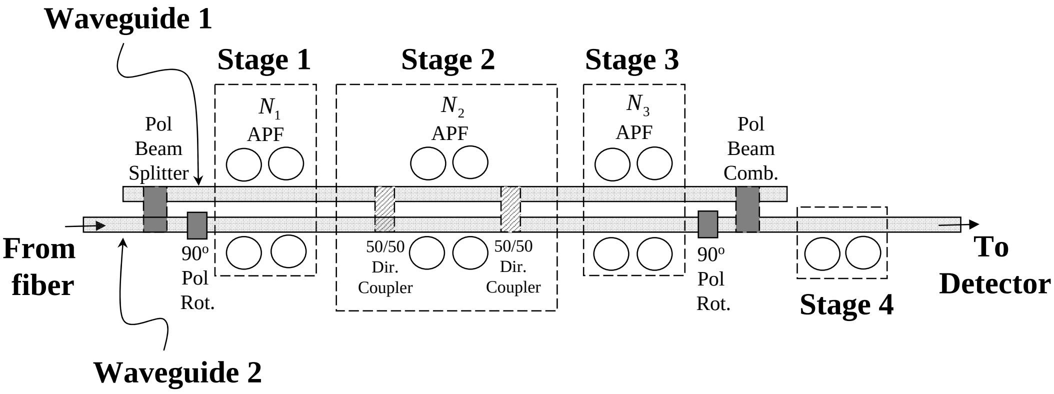

Figure 6-7: A possible implementation of Figure 1a using All-Pass filters integrated on planar waveguides.

and $\theta_3(\omega)$ using the same equation (6.6)-(6.9) and (6.12)-(6.13) for the whole terahertz bandwidth. We then sent 40 Gbit/s RZ pseudo-random bit sequences (2^6-1) of Gaussian pulses of 10 ps (FHWM) pulse-width. For each simulated fiber, in order to show that PMD was compensated across the whole Tera-Hertz range, the center wavelength of the Gaussian pulses was randomly chosen within this 1 THz bandwidth. Figure 6-5 show the cumulative probability distribution of the BER curve with and without compensation. The performance of the compensation is comparable to that of the single channel case (compare with the solid line curve in Figure 6-5). This illustrates that the synthesis algorithms can be applied for broadband multi-channel PMD compensation.

6.4 Practical implementations of AFPMD compensator

There are a few physical implementations of the proposed 4-stage AFPMD compensator. The first two implementations can be adapted from the femto-second pulse shaping schemes demonstrated experimentally by A. Weiner [119] using a spatial light modulator and by Zeek et al [120] using a deformable mirror. For stage 1 and 3, the light is polarization beam split into horizontal and vertical polarization. One polarization is then dispersed spatially by a diffraction grating to form a line spectrum across the deformable mirror or spatial light modulator. The mirror (or modulator) is programmed to produce the desired changes in the spectral phase across the bandwidth. When the two polarizations are combined using a polarization beam combiner, this creates frequency-dependent rotation about {1,0,0} in Stokes space. Stage 2 has the same setup as stage 1 and 3 except for two additional quarter-wave plates placed before and after the setup. The slow birefringent axis of the first quarter-wave plate is aligned at 45^o degree while the second is aligned at -45^o degree in physical space. This make stage 2 an equivalent rotation about {0,0,1} in Stokes space. Thus by programming appropriate spectral phase, we can produce the required rotation angles $\theta_1(\omega)$, $\theta_2(\omega)$ and $\theta_3(\omega)$ calculated from equation (6.6)-(6.9) and (6.12)-(6.13). An alternative setup using spatial arrays of liquid crystal polarization rotators with dispersive elements is shown in Figure 6-6. Another promising implementation is based on All-Pass Filters (APFs) integrated on a planar lightwave circuit as shown in Figure 6-7. In the next section, we focus on this particular implementation since they can be compactly integrated onto a chip. C.K. Madsen had demonstrated experimentally chromatic dispersion compensation using APFs in several papers [121, 122, 123].

6.5 AFPMD based on All-Pass Filter

An all-pass filter (APF) has unity magnitude response. By cascading them, one can engineer the phase response to approximate any desired response. This approach is common in the field of electrical circuit design and digital signal processing [124] and has been used extensively for phase equalization in these fields. C.K Madsen had extended it for optical filter application [121, 122, 123]. Two common implementations of optical APF are a) a ring resonator coupled to a straight waveguide [121, 122, 123] and b) an etalon that has a perfect mirror on one side [125]. The former is preferred for compact integrated optics. The latter is also known as a Gires-Tournois interferometer. The power coupling coefficient into the resonator and the resonant frequency are the two main filter parameters to adjust when engineering the phase response. C.K Madsen had demonstrated that the tuning of these two filter parameters is feasible using thermal heaters in a Mach-Zehnder interferometer configuration of APF [122]. In general, the phase response of a set of N_i APF is given by [124]:

$$\Phi_i(\omega) = N_i\left(\pi - \omega T\right) - \sum_{k}^{N_i}\left(\phi_k + 2\tan^{-1}\left(\frac{r_k \sin\left(\omega T + \phi_k\right)}{1 - r_k \cos\left(\omega T + \phi_k\right)}\right)\right) \qquad (6.14)$$

where ϕ_k determines the cavity's resonant frequency, r_k is the partial reflectance and is related to the power coupling ratio into the cavity, κ_k, by $r_k = \sqrt{1-\kappa_k}$ and T is the feedback path round trip delay and is related to the free spectral range (FSR) by $T = 1/FSR$. Any phase response can be engineered by varying the filter parameters ϕ_k and r_k.

The scheme shown in Figure 6-7 may look similar to that proposed by C.K. Madsen in Reference [109]. However, our synthesis algorithm of the phase responses of these filters is distinctly different from hers. Madsen's approach is to approximate the inverse Jones matrix while ours aims to compensate only its frequency-dependent part (i.e. $jU^{\dagger}U_{\omega}(\omega)$). In terms of signal distortion, the inversion of the Jones matrix is really not necessary as it also produces output polarizations that are equal to that of the input [117]. Our compensation of the output PMD vector is sufficient since it cancels the frequency dependent part of the Jones matrix. In this scheme, the output signals from the fiber are split into two waveguides (waveguide 1 and waveguide 2) by a polarization beam splitter. The polarization in waveguide 2 is rotated by 90^{o} [126] so that identical waveguide structures can be used for both polarizations. Stage 1 is comprised of a set of N_1 APFs for each of the waveguides to generate phase response of $\Phi_{1H}(\omega)$ for waveguide 1 and $\Phi_{1V}(\omega)$ for waveguide 2. The same number of APFs is used for both polarizations in an effort to minimize PDL. In Stokes space, transmission through Stage 1 corresponds to a rotation about {1,0,0} with rotation angle $(\Phi_{1V}(\omega) - \Phi_{1H}(\omega))$. Stage 2 is comprised of a 50/50 directional coupler with matched propagation constants, followed by another set of N_2 APFs for each of the waveguides, and then by another 50/50 directional coupler with matched propagation constants. For the same coupling constant, the length of the second 50/50 directional coupler is 3 times greater than that of the first 50/50 directional coupler. This

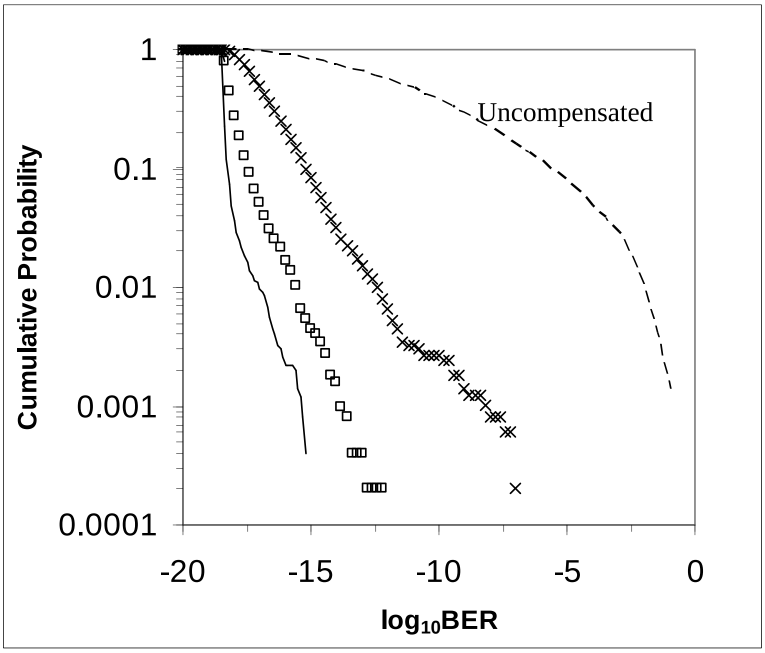

Figure 6-8: Cumulative probability distribution of BER curve when APFs are used to approximate the rotation angles calculated by the synthesis algorithm. The curve of crosses is for the compensated case using $N_1 = N_2 = N_3 = 3$ APFs, the curve of square is for the compensated case using $N_1 = 15$, $N_2 = 10$, and $N_3 = 15$ APFs, the solid line curve is for the compensated case using the exact rotation angles computed by the synthesis algorithm and the dashed curve is for the uncompensated case. The numerical simulation was carried out with $\Delta f = 1.26$ GHz, and the mean DGD was 11.5 ps for the fiber ensemble.

set of APFs generates a phase response of $\Phi_{2H}(\omega)$ for waveguide 1 and $\Phi_{2V}(\omega)$ for waveguide 2. In Stokes space, the first 50/50 directional coupler gives a 90^o rotation about {0,1,0}, the APF portion of Stage 2 is a rotation about {1,0,0} with rotation angle $(\Phi_{2V}(\omega) - \Phi_{2H}(\omega))$ and the second 50/50 directional coupler is designed to give a 270^o rotation about {0,1,0}. Thus the combined transformation of Stage 2 is equivalent to a rotation about {0,0,1} with rotation angle of $(\Phi_{2V}(\omega) - \Phi_{2H}(\omega))$. Stage 3 is again another set of N_3 APFs for each of the waveguides to generate phase response of $\Phi_{3H}(\omega)$ for waveguide 1 and $\Phi_{3V}(\omega)$ for waveguide 2. Transmission through Stage 3 again corresponds to a rotation about {1,0,0} with rotation angle $(\Phi_{3V}(\omega) - \Phi_{3H}(\omega))$. After Stage 3, the two polarizations are recombined on a single waveguide via a polarization rotator and a polarization beam combiner. Stage 4 is comprised of another set of APFs to compensate the isotropic dispersion accumulated through Stage 1 to 3. After knowing the required rotation angles of $\theta_1(\omega)$, $\theta_2(\omega)$ and $\theta_3(\omega)$ for all-frequency PMD compensation using equation (6.6)-(6.9) and (6.12)-(6.13), the corresponding $\Phi_{iH}(\omega)$ and $\Phi_{iV}(\omega)$ can be derived from

$$\Phi_{iV}(\omega) - \Phi_{iH}(\omega) = \theta_i(\omega) \tag{6.15}$$

We arbitrarily choose

$$\Phi_{iV}(\omega) + \Phi_{iH}(\omega) = 2N_i\left(\pi - \omega T\right) \tag{6.16}$$

for $i = 1, 2, 3$ so that the net isotropic dispersion introduced by the APFs in both waveguides is simply a group delay. From equations (6.15) and (6.16), we get

$$\Phi_{iV}(\omega) = N_i\left(\pi - \omega T\right) + \frac{\theta_i(\omega)}{2} \tag{6.17}$$

$$\Phi_{iH}(\omega) = N_i\left(\pi - \omega T\right) - \frac{\theta_i(\omega)}{2} \tag{6.18}$$

To obtain the parameters $\phi_k$and r_k for each APF in each waveguide, we fit equation (6.14) with equations (6.17) and (6.18) using a nonlinear fit subroutine that is available in standard mathematical software packages such as Mathematica. With small N_i, this nonlinear fit can be fast and efficient. Note that if the fitting is perfect, from equation (6.16), the first three stages only introduce isotropic dispersion $(\Phi_{iV}(\omega) + \Phi_{iH}(\omega))/2$ in the form of group delay. Thus Stage 4 is redundant. However, in reality, since the fitting is done separately for equation (6.17) and (6.18), this isotropic dispersion often deviates from a simple group delay, and Stage 4 is needed for compensating these accumulated isotropic dispersions.

To illustrate that the rotation angles calculated by our synthesis algorithm are feasible and can be approximated using APFs, we show the rotation angles produced by the APFs for the same randomly chosen fiber used in Figure 6-2. They are shown as dashed-line curves in Figure 6-2(a-c). The APF parameters used to approximate these rotation angles are found by fitting equation (6.17) and (6.18) using the “NonlinearFit” subroutine in Mathematica. The number of APFs used are $N_1 = N_2 = N_3 = 3$. To show that these approximated rotation angles are good enough for compensating pulse distortion, we simulated the signal after passing through the compensator using these APFs. The compensated signal is shown as the curve of filled circles in Figure 6-2d. The signal is almost recovered to its original shape. To obtain more statistics on the performance of the AFPMD compensator based on APFs, we created 1000 random fibers with mean DGD of 11.5 ps by cascading 20 randomly oriented birefringence sections. For each fiber realization, 5 different random input SOPs were used. Figure 6-8 shows the cumulative probability distribution of the BER for this set of 5000 samples. The power is set at 3 dB above the power that provides a BER of 10^{-9}. The step-size used is Δf =1.26 GHz. The dashed-line curve is for the uncompensated case and the curve of crosses is for the compensated case. There is a significant improvement in the signal quality after compensating using APFs, However, as one would expect, there is a drop in the performance when compared to the compensated case which uses the exact rotation angles profiles (see the solid line curve). This is reasonable since APFs can only approximate the rotation angles calculated from the synthesis algorithm. To improve the approximation of the rotation angles, one can introduce more APFs. For example, if we increase the number of APFs used to $N_1 = 15$, $N_2 = 10$, and $N_3 = 15$, the performance improves as shown by the curve of squares. It is worthwhile to note that, despite the simulation is performed with 40 Gbit/s RZ signal, all orders of PMD is also important in the case of in-line broadband compensation of 10 Gbit/s NRZ WDM system.

6.6 Fitting Algorithm for Broadband APF Application

The “NonlinearFit” subroutine in Mathematica used in Figure 6-2 is a simple fitting algorithm that is not optimized for our application. It lacks a weighting function

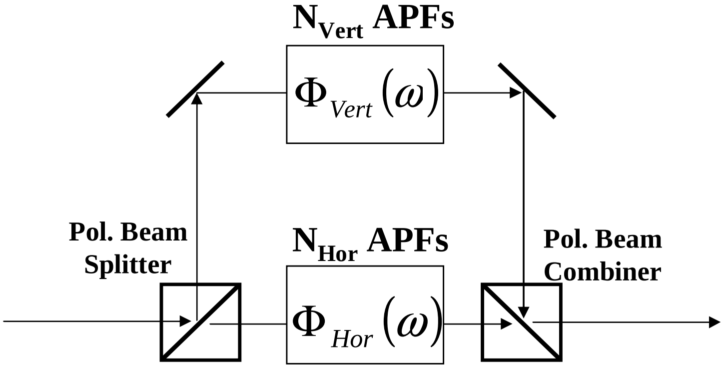

Figure 6-9: A common building block in the broadband PMD compensator

that allows flexibility in distributing APFs to maximize the approximation accuracy in certain frequency regions that have both large PMD and spectral power density. As shown in Figure 6-5, the same 4-stage architecture can be used without any demultiplexing for multi-channel broadband PMD compensation. However, to maintain a continuous PMD compensation over this broad bandwidth, we would need a large number of APFs for each stage since the approximation of the rotation angle spectra now spans a broader bandwidth. Thus the algorithm to find the optimum parameters of these APFs needs to be efficient and fast. This is especially true in the case of compensating for PMD, which are dynamically changing with time. Optimization algorithms, such as the "NonlinearFit" subroutine in Mathematica, tend to get trapped in local optima when the number of search parameters is large. For this reason, they are efficient only when a small number of APFs is involved

Fast fitting algorithms that based on recursive equations are desired. References [127, 128, 129] presented a simple and fast recursive method for designing digital allpass filters satisfying a given group delay specification using complex cepstrum [124]. The term *cepstrum* was introduced by Bogert et al. in 1963 [130] and has come to be accepted terminology for the inverse Fourier transform of the logarithm of the power spectrum of a signal. Cepstrum techniques have been applied extensively in speech analysis. The fundamental principle of these algorithms [127, 128, 129] is based on the relationship between the group delay of the minimum-phase denominator of a stable APF and the complex cepstral coefficients arising from its discrete Hilbert transform.

The main difference among the three algorithms lies in how the cepstral coefficients are computed. Reference [127] uses four Fast-Fourier Transforms (FFT) while [128] uses one FFT to approximate the cepstral coefficients in a least-square sense. Reference [129] requires no FFT and uses a weighted-least-square approximation.

To present the essence of the fitting algorithm, we focus on its application on a common building block in the broadband PMD compensator as shown in Figure 6-9. It is a frequency-dependent polarization rotator. The light is polarization beam-split into horizontal and vertical polarizations. Using cascaded APFs, different frequency-dependent phase profiles are created for the two polarization arms, $\Phi_H(\omega)$ for the horizontal and $\Phi_V(\omega)$ for the vertical. When the two polarizations are combined using a polarization beam combiner, this creates frequency-dependent rotation $\theta(\omega)$ about $\{1,0,0\}$ in Stokes space. This rotation profile $\theta(\omega)$ corresponds to the differential phase profile of the two arms (i.e. $\theta(\omega) = \Phi_V(\omega) - \Phi_H(\omega)$). The first derivative of $\theta(\omega)$ gives the Differential Group Delay (DGD) of the frequency-dependent polarization rotator. Fitting algorithms proposed in [127, 128, 129] are not optimized for fitting such a differential phase profile $\theta(\omega)$ for two reasons. Firstly, these algorithms assume pairs of poles that are complex conjugate to one another. Thus, the APFs have to mirror-image one another about the center frequency resulting in the group delay response of even-symmetry about the center frequency. This reduces the working frequency range to half of the Free Spectral Range (FSR) of the filters and doubles the number of APFs required. One common implementation of APFs in an optical integrated circuit is a ring resonator coupled to a waveguide [123]. The FSR of the APF is inversely proportional to the ring radius. Since rings with small radii tend to have more loss and are more difficult to fabricate, we would like to utilize as much of the FSR as possible. Secondly, these algorithms concentrate on the higher dispersion without accounting for the linear frequency dependence of the response. In applications such as chromatic dispersion compensation, this may not be an issue since this linear dependence corresponds to a group delay which does not distort the signal. However, in PMD compensation, the difference of the linear dependence in the two polarization arms, shown in Figure 6-9, creates a first order PMD. This will introduce polarization-dependent signal distortion if it is unaccounted for. In this section, we show how to rectify these two issues, and enhance the algorithms [128, 129] to efficiently fit the rotation angle profile of the frequency–dependent polarization rotator shown in Figure 6-9. This algorithm is equally valid for fitting the differential phase profile required for the frequency-dependent variable attenuator proposed in Chapter 10.

6.7 Group delay of APFs, Minimum-Phase Denominator and DGD

The transfer function in the z-transform domain of an all-pass filter of order N is given by

$$H(z) = z^{-N}\frac{N(z)}{D(z)} = z^{-N}\frac{\sum\limits_{n=0}^{N} a_n^* z^n}{\sum\limits_{n=0}^{N} a_n z^{-n}} \tag{6.19}$$

with $a_o = 1$. There are N poles and zeros. The zeros of $H(z)$ are reciprocal complex conjugates of its poles. In [127, 128, 129], a_n is taken as a real number resulting in a pair of poles that are complex conjugates of one another. This limits the fitting algorithm to accept only group delay that has even symmetry about the center frequency. In general, a_n is complex. From equation (6.19), when $z = e^{j\omega}$,

$$H(e^{j\omega}) = e^{-j\omega N}\frac{\sum\limits_{n=0}^{N} a_n^* e^{j\omega n}}{\sum\limits_{n=0}^{N} a_n e^{-j\omega n}} \tag{6.20}$$

where ω is the normalized frequency given by $2\pi\,(f - f_o)/FSR$ and f_o is the center optical frequency of the band of interest. Since the numerator $N(e^{j\omega})$ is the complex conjugate of the denominator $D(e^{j\omega})$, $H(e^{j\omega})$ has unity magnitude response for all frequencies. Moreover, the phase response of the overall filter $H(e^{j\omega})$ is given by

$$\phi_H(\omega) = -N\omega + \phi_N(\omega) - \phi_D(\omega) = -N\omega - 2\phi_D(\omega) \tag{6.21}$$

where $\phi_N(\omega)$ and $\phi_D(\omega)$ denote the phase response of the numerator $N(e^{j\omega})$ and the phase response of the denominator $D(e^{j\omega})$, respectively. The normalized group delay of the overall filter is given by

$$\tau_H(\omega) = \frac{-d\phi_H(\omega)}{d\omega} = N + 2\phi_D^{'}(\omega) \tag{6.22}$$

where $\phi_D^{'}(\omega) = d\phi_D(\omega)/d\omega = -\tau_D(\omega)$ is the negative group delay of the denominator $D(e^{j\omega})$. Hence, the group delay response of the denominator can be obtained from the group delay response of the all-pass filter using the relation

$$\tau_D(\omega) = \frac{-\tau_H(\omega)}{2} + \frac{N}{2} \tag{6.23}$$

The coefficient a_n of the denominator $D(z)$ and hence the filter $H(z)$ are completely determined from $\tau_D(\omega)$. From equation (6.19), for a stable APF, $H(z)$ has all its poles within the unit circle in the complex z-plane. This implies that the denominator $D(z)$ is a minimum phase function. A function is defined to be minimum phase when all its zeros and poles lies within the unit circle [124]. A minimum phase function is known to have zero average group delay over the FSR. From (6.23), this implies that the average group delay of a N^{th} -order APFs over a FSR is fixed at N.

To approximate a desired rotation angle profile $\theta(\omega)$ of the frequency-dependent polarization rotator shown in Figure 6-9, we cascade N_{Hor} APFs in the horizontal polarization arm to generate the phase response $\Phi_{Hor}(\omega)$ and N_{Vert} APFs in the vertical polarization arm to generate the phase response $\Phi_{Vert}(\omega)$ so that

$$\Phi_{Vert}(\omega) - \Phi_{Hor}(\omega) = \theta(\omega) \tag{6.24}$$

Differentiating equation (6.24) with respect to ω, we obtain their corresponding normalized group delay as

$$\tau_{Vert}(\omega) - \tau_{Hor}(\omega) = \tau_{DGD}(\omega) \tag{6.25}$$

which is the Differential Group Delay (DGD) of the frequency-dependent polarization rotator. We assume all APFs have the same FSR. Since the average group delay of an N^{th} order APF over the FSR is fixed at N, the average DGD over the FSR is fixed at $N_{Vert} - N_{Hor}$ which is an integer. On the other hand, since PMD is a stochastic process, the required rotation angle profile $\theta(\omega)$ for compensation is dynamically changing with an arbitrary non-integer value of the average DGD $\bar{\tau}_{DGD}$ over the frequency range of interest Δf_{int}. To overcome this incompatibility, the FSR of the APFs must be larger than Δf_{int}. We then express the required average DGD over Δf_{int} as $\bar{\tau}_{DGD} = N_{diff} + \Delta\bar{\tau}_{DGD}$ where N_{diff} is an integer. Since the frequency range outside Δf_{int} has no impact on the compensation, we appropriately extrapolate $\tau_{DGD}(\omega)$ outside the frequency range Δf_{int} to cancel $\Delta\bar{\tau}_{DGD}$, thus rounding the average value of $\tau_{DGD}(\omega)$ over the FSR to an integer value of N_{diff}. To account for this N_{diff} average DGD, we change the order of the APFs accordingly so that $N_{Vert} - N_{Hor} = N_{diff}$. One way to implement this is to have the same number of APFs in both polarization arms, and to "de-activate" N_{diff} APFs in the appropriate arms, depending on the sign of N_{diff}. From (6.25), if N_{diff} is a positive (negative) integer, we "de-activate" N_{diff} APFs from the horizontal (vertical) polarization arm, and vice versa. To "deactivate" an APF in an optical integrated circuit, we shift its resonant frequency out of Δf_{int} and decrease the power coupling of the ring resonator to the waveguide so that it does not contribute any group delay within Δf_{int}. The FSR of the APF is inversely proportional to the ring radius, and we would like to utilize the most of the FSR as Δf_{int} in order to reduce the ring bending loss and ease its fabrication. In our simulations, we typically choose the FSR to be ∼10% larger than Δf_{int}. After accounting for the linear frequency dependence of the rotation angle, we now focus on fitting its higher order differential dispersion. We have the freedom to choose $\Phi_{Hor}(\omega)$ and $\Phi_{Vert}(\omega)$ so that the isotropic dispersion of the frequency dependent polarization rotator is a group delay.

$$\tau_{Vert}(\omega) + \tau_{Hor}(\omega) = N_{Vert} + N_{Hor} \tag{6.26}$$

Using (6.25) and (6.26), we get

$$\tau_{Vert}(\omega) = \frac{N_{Vert} + N_{Hor}}{2} + \frac{\tau_{DGD}(\omega)}{2} \tag{6.27}$$

and

$$\tau_{Hor}(\omega) = \frac{N_{Vert} + N_{Hor}}{2} - \frac{\tau_{DGD}(\omega)}{2} \tag{6.28}$$

which are the corresponding desired group delays for the respective polarization arms. We show in the following how to fit the desired group delay for the vertical polarization, and the same procedures apply to the horizontal. For a desired group delay function $\tau_{Vert}(\omega)$, we use equation (6.23) to determine the corresponding group delay response $\tau_{DV}(\omega)$ of its minimum phase denominator function as

$$\tau_{DV}(\omega) = \frac{-\tau_{Vert}(\omega)}{2} + \frac{N_{Vert}}{2} \tag{6.29}$$

We then decompose it into a sum of even function $\tau_{DV}^{even}(\omega)$ and odd function $\tau_{DV}^{odd}(\omega)$ of the form,

$$\tau_{DV}^{even}(\omega) = \frac{\tau_{DV}(\omega) + \tau_{DV}(-\omega)}{2} \tag{6.30}$$

$$\tau_{DV}^{odd}(\omega) = \frac{\tau_{DV}(\omega) - \tau_{DV}(-\omega)}{2} \tag{6.31}$$

6.8 Relationship between Minimum-Phase Response and Cepstral Coefficients

Let $D(\omega)$ be a minimum phase frequency response. Since $D(\omega)$ is minimum phase with all its zeros and poles inside the unit circle, its natural logarithm $\hat{D}(\omega) = \ln D(\omega)$ also has all its poles inside the unit circle. Thus $\hat{D}(\omega)$ is a stable and causal frequency response. In addition, the inverse Fourier transform of $\hat{D}(\omega)$ (also known as the cepstrum) yields a causal sequence of cepstral coefficients $c(k)$. In terms of $c(k)$, we can express

$$\hat{D}(\omega) = \ln D(\omega) = c(0) + \sum_{k=1}^{\infty} c(k) e^{-jk\omega} \tag{6.32}$$

From $D(\omega) = |D(\omega)|\, e^{j\phi(\omega)}$, we see that the imaginary part of $\hat{D}\left(\omega\right)$ gives the phase term as

$$\phi\left(\omega\right) + 2v\pi = -\sum_{k=1}^{\infty} Re[c(k)] \sin k\omega + \sum_{k=1}^{\infty} Im[c(k)] \cos k\omega \tag{6.33}$$

where v is an integer. Its corresponding group delay is

$$\tau\left(\omega\right) = \sum_{k=1}^{\infty} kRe[c(k)] \cos k\omega + \sum_{k=1}^{\infty} kIm[c(k)] \sin k\omega \tag{6.34}$$

, and the real part of $\hat{D}\left(\omega\right)$ is given by

$$\ln|D(\omega)| = c(0) + \sum_{k=1}^{\infty} Re[c(k)] \cos k\omega + \sum_{k=1}^{\infty} Im[c(k)] \sin k\omega \tag{6.35}$$

From (6.34), we can see that the real part of $c(k)$ gives group delay of even symmetry while the imaginary part gives group delay of odd symmetry. In Reference [127, 128, 129], $c(k)$ is real since its group delay is only of even symmetry. For a given desired group delay $\tau_{Vert}(\omega)$, we determine the corresponding group delay $\tau_{DV}(\omega)$ of its minimum phase denominator response using (6.29). Then we decompose it into a sum of even group delay $\tau_{DV}^{even}(\omega)$ and odd group delay $\tau_{DV}^{odd}(\omega)$ using equations (6.30) and (6.31). Using equation (6.34), the even group delay function determines the real part

$$\tau_{DV}^{even}(\omega) = \sum_{k=1}^{\infty} kRe[c(k)] \cos k\omega \tag{6.36}$$

while the odd delay determines the imaginary part of the complex cepstral coefficients

$$\tau_{DV}^{odd}(\omega) = \sum_{k=1}^{\infty} kIm[c(k)] \sin k\omega \tag{6.37}$$

To compute the cepstral coefficients $c(k)$ from equations (6.36) and (6.37), we can either use an inverse Fast Fourier transform (IFFT) [128] or compute them using a weighted-least-square approximation [129]. From the computed complex cepstral coefficients $c(k)$, we can now derive the coefficients a_n of the denominator $D(z)$ using the recursive nonlinear difference equation [124] given by

$$a_n = \sum_{k=0}^{n} \left(\frac{k}{n}\right) c(k) a_{n-k} \quad n > 0 \tag{6.38}$$

where $c(0) = 0$ and $a_0 = 1$. To prove equation (6.38), we first differentiate $\hat{D}(z) = \ln\left(D\left(z\right)\right)$ with respect to z so that

$$\frac{d\hat{D}(z)}{dz} = \frac{1}{D(z)}\frac{dD(z)}{dz} \tag{6.39}$$

Using the z-Transform pairs,

$$nx\left[n\right] \Leftrightarrow -z\frac{dX\left(z\right)}{dz} \tag{6.40}$$

and

$$x_1\left[n\right] * x_2\left[n\right] \Leftrightarrow X_1\left(z\right).X_2\left(z\right), \tag{6.41}$$

the inverse z-transform of (6.39) gives the recursive nonlinear difference equation in (6.38). Once the sequence a_k is known, the parameters of the APFs are determined by finding the roots of the denominator $D(z)$. The magnitude of each root gives the reflection coefficient of each APF and its argument gives the resonant frequency of the APF.

6.9 Summary of fitting algorithm

The implementation procedure can be summarized as follows: let $\tau_{DGD}(\omega)$ be the desired differential group delay function over a frequency range Δf_{int}.

(1) Compute average $\tau_{DGD}(\omega)$ over Δf_{int} and express it in terms of an integer N_{diff} and $\Delta\bar{\tau}_{DGD}$. N_{diff} determines the required difference in orders of APFs used in the vertical and horizontal polarization arm. Since the frequency range outside does not affect the compensation, we extrapolate $\tau_{DGD}(\omega)$ outside Δf_{int} to cancel $\Delta\bar{\tau}_{DGD}$.

(2) From equation (6.27) and (6.28), compute the respective desired group delay for each polarization arm: $\tau_{Vert}(\omega)$ and $\tau_{Hor}(\omega)$.

(3) For $\tau_{Vert}(\omega)$ in the vertical polarization arm, use equation (6.29) to compute the corresponding group delay of the minimum phase denominator $\tau_{DV}(\omega)$.

(4) Perform an even-odd decomposition of $\tau_{DV}(\omega)$ using equations (6.30) and (6.31): $\tau_{DV}^{even}(\omega)$ and $\tau_{DV}^{odd}(\omega)$.

(5) Compute the complex cepstral coefficients $c(k)$ using equations (6.36) and (6.37). The real part of $c(k)$ is computed using the even function $\tau_{DV}^{even}(\omega)$ while the imaginary part using the odd function $\tau_{DV}^{odd}(\omega)$. This can be implemented using an IFFT [128] or computed in a weighted-least-square sense using a weighting function as in [129].

(6) Compute the denominator coefficients a_n using the recursive relation in equation (6.38).

(7) Compute the roots of the denominator $D(z)$. The magnitude of each root gives the reflection coefficient of each APF, and its argument gives the resonant frequency of each APF.

(8) Repeat Step 3 to 7 for the horizontal polarization arm.

6.10 Simulation

Figure 6-10 shows a sample of the rotation angle profile $\theta(\omega)$ required for one of the frequency dependent polarization rotators used in the broadband PMD compensator. The fiber to be compensated has a mean DGD of 6.75 ps. The desired rotation angle profile of $\theta(\omega)$ is shown by the solid curve while the profile approximated by the APFs

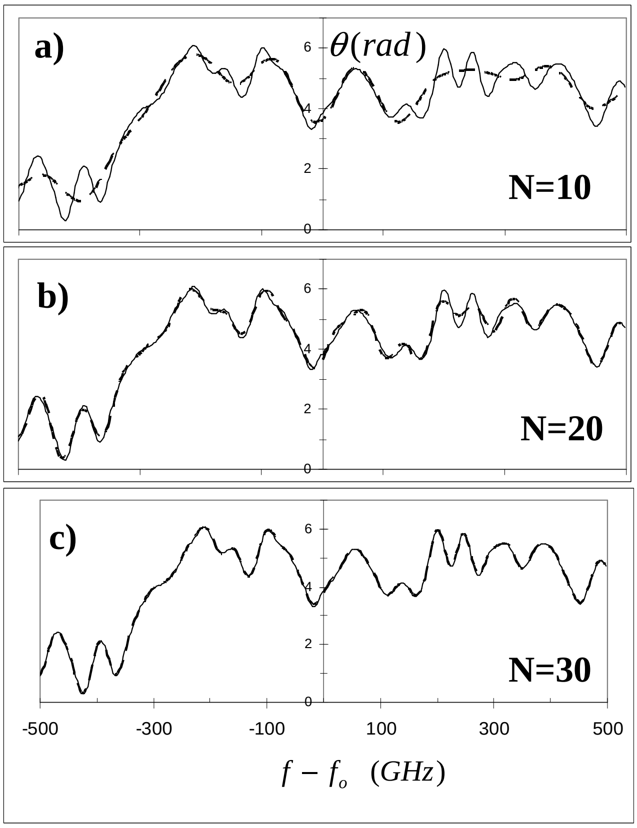

Figure 6-10: A random sample of the rotation angle profile $\theta(\omega)$ required for one of the frequency dependent polarization rotators used in the broadband PMD compensator. The desired rotation angle profile of $\theta(\omega)$ is shown by the solid curve while the profile approximated by the APFs is shown by the dashed-curve. The number of APFs used for each polarization arms is 10 for (a), 20 for (b) and 30 for (c).

is shown by the dashed-curve. The cepstral coefficients were computed using IFFT as in [128]. The number of APFs used for each polarization arms is 10 for Figure 6-10a, 20 for Figure 6-10b and 30 for Figure 6-10c. As expected, the approximation improves as the number of APFs increases. The FSR of the APFs is 1.0 THz while the frequency range of interest Δf_{int} is 0.9 THz. This broadband compensator is capable of covering nine 100 GHz-spaced WDM channels simultaneously. Rings with such Tera-Hz-scale FSR have been demonstrated in [131].

Since PMD is a stochastic process, the required rotation angle profile $\theta(\omega)$ for compensation is dynamically changing. To gain statistics on the performance of the APFs in approximating the rotation angle profile, we generated an ensemble of

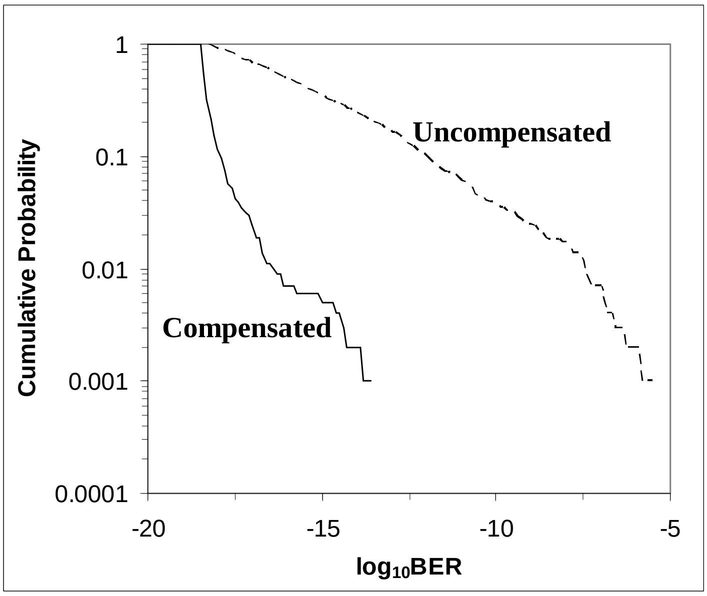

Figure 6-11: The cumulative probability distribution of the Bit Error Rate (BER) curve with and without PMD compensation.

1000 random fibers by cascading 20 randomly oriented birefringence sections. The mean DGD of the ensemble is of 6.75 ps. For each fiber, the input signal is a 40 Gbit/s RZ pseudo-random bit sequence (2^6-1) of Gaussian pulses of 10 ps (FHWM) pulse-width. PMD compensation is carried out at the fiber output. The broadband PMD compensator is comprised of three stages of frequency-dependent polarization rotators as shown in Figure 6-7, and the method to synthesize the required rotation angle profile $\theta(\omega)$ for each stage is described in Section 6.2. We then find the optimum parameters of the APFs to approximate these required rotation angle profiles using the recursive algorithm proposed here. The number of APFs used is 40 for each arm of the polarization rotators. In order to show that PMD was compensated across the whole Tera-Hertz range, the center wavelength of the Gaussian pulses was randomly chosen within this 0.9 THz bandwidth. Figure 6-11 shows the cumulative probability distribution of the Bit Error Rate (BER) curve with and without the PMD compensation. The power was set at 3dB above the power that provides a BER of 10^{-9}. The dashed curve is for the uncompensated case while the solid curve is for the compensated case. There is significant improvement in the signal quality after compensation, therefore illustrating the capability of the recursive algorithm in finding for the optimum fitting parameters of such large number of APFs.

6.11 Conclusion

We have presented the architecture of an All-Frequency PMD compensator in a feed-forward compensation scheme. It is comprised of 4 stages. The first two stages give an equivalent frequency dependent polarization rotation effect, the third stage provides the frequency dependent variable DGD while the last stage compensates for the isotropic dispersion created by the first three stages. In Stokes space formulation, we describe the algorithm to find the required rotation angles of each stage using the PMD concatenation rules. This synthesis algorithm is verified by simulating the PMD-induced signal degradation before and after the compensation. We discuss three possible practical implementations of the AFPMD compensator but only concentrate on the integrated optics approach of using APFs. We also show that the profiles of the rotation angles are practical and can be approximated using APFs. Again, through simulations, significant improvement of the signal quality was demonstrated using such 4-stage architecture based on APFs. To extend the architecture for broadband compensation, the number of APFs involved can be as large as 50 per stage. Thus we proposed a fast and efficient algorithm based on recursive equations to find the optimum of the large number of free parameters involved. This APF design algorithm is based on the complex cepstrum commonly used in digital signal processing.

Chapter 7

Combinatorial Polarization Scramblers for Many-Segment Emulator

7.1 Background

As the telecommunication industry continues to deploy higher bandwidth fiber optic systems, Polarization Mode Dispersion (PMD) becomes one of the major obstacles in 10Gbit/s and higher transmission systems. The evaluation of PMD mitigation techniques requires a method of emulating the PMD of the installed fiber links, especially since fiber with high PMD installed in the 1980's is no longer commercially available. PMD emulation has thus become an active area of research since the last few years. Much work has focused on emulating PMD using a concatenation of many birefringent segments with random coupling at each junction [95, 96, 132, 133]. There are various methods to achieve random coupling at the junctions: (i) several segments of Polarization Maintaining (PM) fiber can be connected using either mechanically rotatable connectors [95] or polarization controllers using fiber squeezers [134]; (ii) a series of free-space birefringence crystals separated by wave-plates mounted on motor-controlled rotation stages [96]; (iii) a long PM fiber with fiber-twisters placed periodically along the fiber to vary the polarization coupling between segments [133]; (iv) an electrically-controlled all-fiber PMD emulator constructed using thin-film micro-heaters to temperature tune the birefringence of the PM fiber segments [132]. One important feature of these emulators is that the number of segments concatenated has to be large. This is to give the key properties of a good PMD emulator [74] which include (i) a Maxwellian distributed DGD, (ii) accurate higher-order PMD statistics and (iii) a frequency autocorrelation function that tends toward zero after a frequency range that spans a few times the bandwidth of the principle state of polarization (PSP). On the other hand, practical considerations such as the size of the emulator, the cost of building it, the ease of implementation, the complexity involved in the controls and the insertion loss often limit the number of segments to typically ∼15 [95]. A polarization scrambler placed between segments is the one of the major components that determines its cost, size and complexity. Since the number of polarization scramblers required is linearly proportional to the number of segments used, these factors scale up linearly with the number of segments. Waddy [134] had demonstrated a dynamic PMD emulator using a total of 36 squeezers (3 squeezers in each of the 12 polarization controllers) while Noe used 64 motors to control the 64 fiber twisters in his experiment [133]. The cost to build and the complexity to control such many squeezers are substantial. In this paper, we investigate the combinatorial approach of building polarization scramblers, with the aim to reduce the number of phase-plates and the controls required in building a many-segment PMD emulator. This approach exploits the simple principle that the rotation matrices are non-commutative and there exist a large number of combinations involving just a few phase-plates in building polarization controllers. For instance, given 6 different phase-plates, one can build $6! = 720$ different polarization controllers. Thus, just by randomly varying the parameters of these 6 phase-plates, we effectively "scramble" hundreds of polarization controllers. Moreover, if duplicated use of each phase-plate is allowed, the total number of possible polarization controllers can be further increased. Although these hundreds of polarization controllers may be correlated to one another, we show in this paper, by numerical simulations and experiment, that with as few as 6 phase-plates for a 20-segment concatenation, there is sufficient polarization scrambling between segments to achieve the various key properties of a good emulator discussed earlier. This combinatorial approach to build polarization scramblers between birefringent segments allows us to reduce the number of phase-plates required, thus reducing the size, the cost, the complexity of building and controlling such emulator. In addition, it may now be relatively easier and cheaper to scale up the number of segments to 45-60 so as to further reduce the background correlation and improve the PMD statistics at the low-probability tails of the distributions [132].

7.2 Numerical simulation

Figure 7-1 shows a numerical simulation of concatenating 20 birefringent segments. The birefringence of these segments is Gaussian distributed with a mean value of 1.2 ps and with a standard deviation of 20% of this mean value. The unequal length of the segments is necessary to avoid the undesired periodicity in the frequency autocorrelation function of the PMD [74]. Random combinations of 6 phase-plates are chosen to form the 19 polarization scramblers. Each phase-plate is assumed to have a fixed birefringence axis while its retardation angle is tunable. In Stokes space representation, the birefringence axes of these phase-plates are randomly chosen on the Poincaré sphere; but, once chosen, they are fixed throughout the simulation. The number of phase-plates used to form a scrambler is randomly chosen from 6 to 9. It allows duplicated usage of any phase-plate. We generate random combinations of these phase-plates to form the polarization scramblers. Once the random set of polarization scramblers is chosen, it is also fixed throughout the simulation. The retardation angles of the six phase-plates are then randomly tuned for the different realizations of the fibers. The first- and second- order PMD of the concatenation are then computed using the PMD concatenation rule as a function of frequency. 100,000 random fiber realizations are used to generate the necessary statistics, as shown in Figure 7-1, for (a) one component of the first-order PMD vector, (b) the DGD, (c) the magnitude of the second order PMD and (d) the PMD frequency autocorrelation

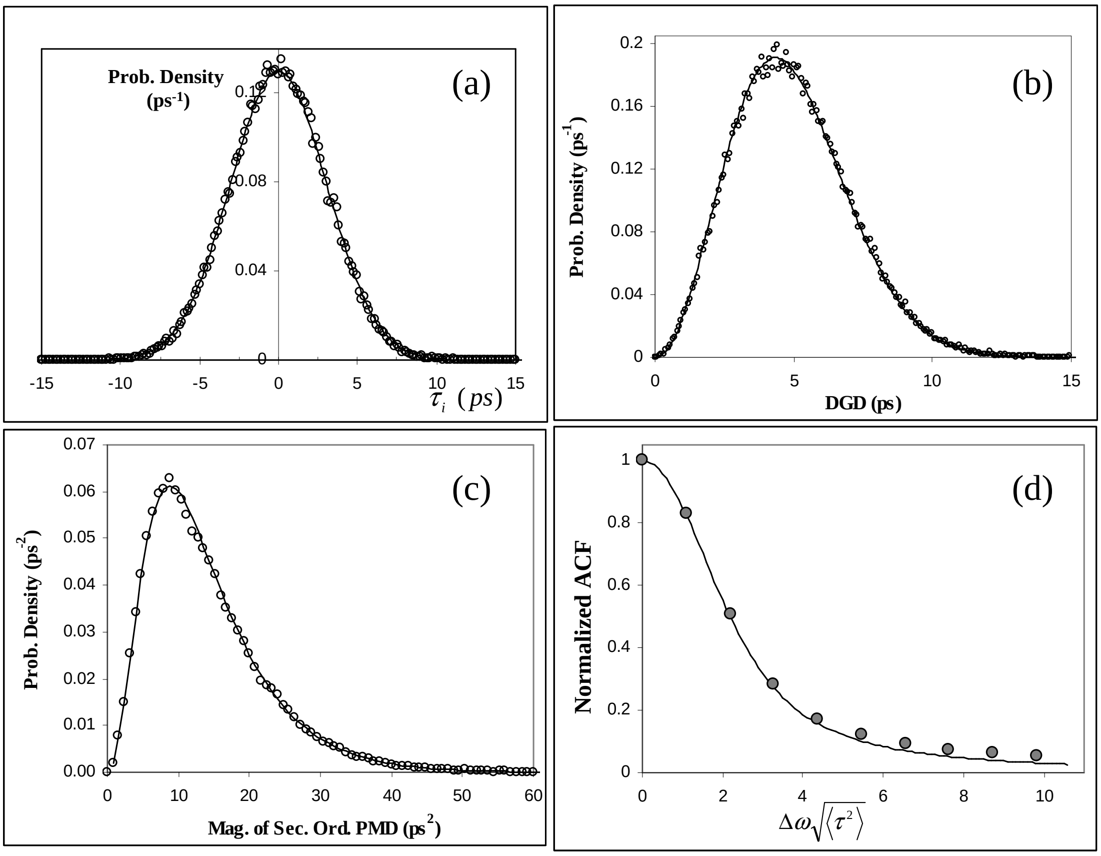

Figure 7-1: Simulated statistics of 100,000 random fiber realizations using the combinatorial polarization scramblers. Circles show the simulated distributions of (a) one of the components of the PMD vector, (b) the DGD, (c) magnitude of second order PMD. The number of bins used is 400. (d) shows the normalized frequency autocorrelation function. The corresponding theoretical curves are shown in solid line curves. The mean DGD used for fitting these theoretical curves is 4.9 ps.

function. One can see that the simulated statistics are in good agreement with the corresponding desired distributions [59] shown in the solid line curves. This result is encouraging as we can now generate the required PMD statistics using an order of magnitude fewer phase-plates. This would significantly reduce the cost, the size and the complexity of the emulator.

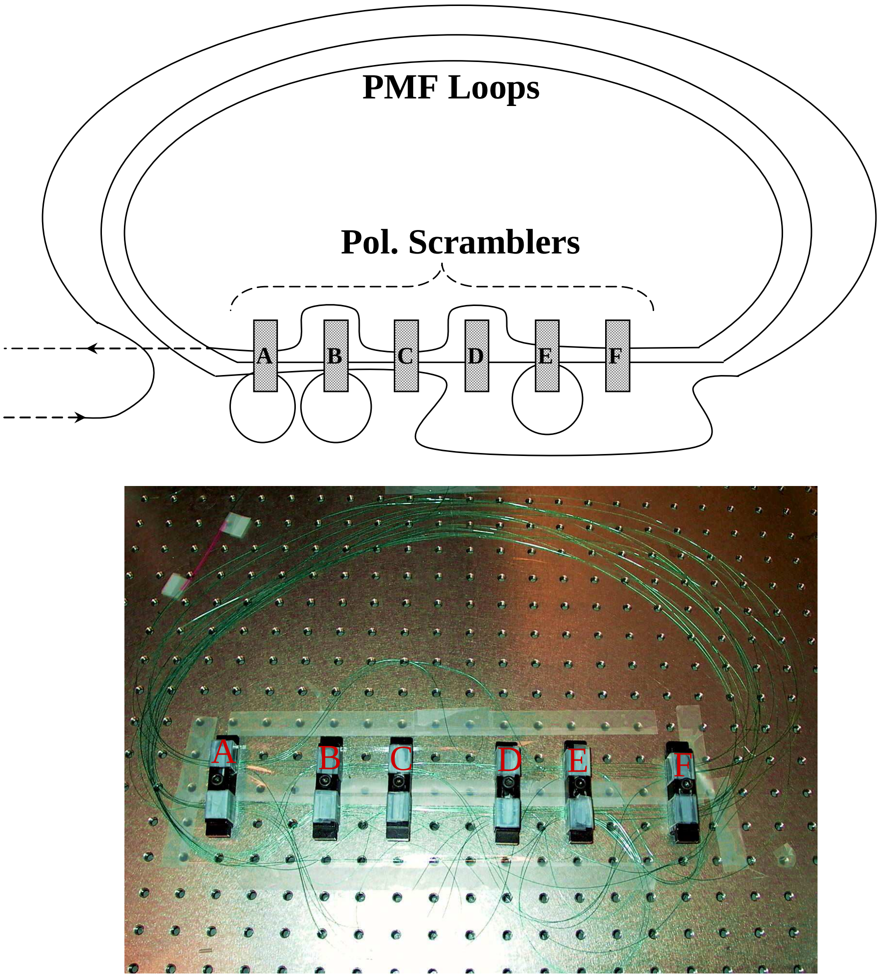

Figure 7-2: Top: Schematic of an all-fiber PMD emulator using combinatorial polarization scramblers. After each PM fiber loop, a different polarization scrambler is built by passing different sequence of the 6 fiber squeezers which are labelled letter "A" to "F"; Bottom: A photograph of such emulator

7.3 Experiment

There are a variety of ways to build an emulator with combinatorial polarization controllers. Figure 7-2 shows an all-fiber implementation using the fiber squeezing technique. A long 3M Tiger polarization maintaining fiber is arranged in loops. Between each loop, the fiber passes through a different sequence of the six fiber squeezers, this equivalently creates different polarization scramblers between loops of the PM fiber. For illustration purpose, after the first loop, the first polarization scrambler is built by passing through the squeezers in an arrangement C→B→B→A→A and after the second loop, the second polarization scrambler is built by passing through F→E→E→D→C→B→A and so on. We restrict the maximum number of squeezers experienced by any polarization controller to 7. This is to avoid excessive insertion loss. When a squeezer applies mechanical stress on the fiber, it induces stress birefringence and creates the equivalent of a tunable phase-plate and an effective polarization scrambling between the PM fiber loops. In the experiment, the DGD of each loop is randomly chosen with a Gaussian mean of 1.2 ps and a standard deviation 20% of this mean value. The total number of PM fiber loops is 16. The measured loss of the emulator is 5±2 dB depending on the stress applied to the squeezers. The polarization dependent loss is $\sim$ 0.2 dB. We manually vary the stresses applied by the 6 squeezers to generate different fiber realization. For each fiber realization, we characterize the spectrum of the PMD vectors by using the technique described in Chapter 3. Instead of using optically filtered telecommunication at the output end as described in Chapter 3, we use a Santec scanning wavelength laser at the input end. The polarization of the laser is randomly scrambled with a General Photonics polarization scrambler (Polarite II) before launching into the emulator. The output polarization is measured with a HP 8509B polarimeter. From measurements of the SOP versus frequency, we deduce the spectrum of the PMD vectors using the same algorithm described in Chapter 3. In this algorithm, we first compute the differential output SOP vectors for the various scrambled input polarization states and find the optimum normal axis to these differential SOP vectors in a least-square sense. This gives the PSP direction. Using this PSP direction, we then determine the DGD value from the length of the differential SOP vectors. Once the information of the PMD vectors with frequency is known, the higher-order PMD can then be computed. We verified experimentally the accuracy of this characterization using well-calibrated first- and higher-order PMD sources. For each fiber realization, we measured the PMD vectors over a range of 1440 nm to 1510 nm with a step size of 0.2nm. This step-size corresponds approximately to the PSP bandwidth of this emulator. The measured mean DGD of the emulator is 5 ps and its corresponding PSP bandwidth is $\sim$ 25 GHz. A hundred random fiber realizations were characterized. For each

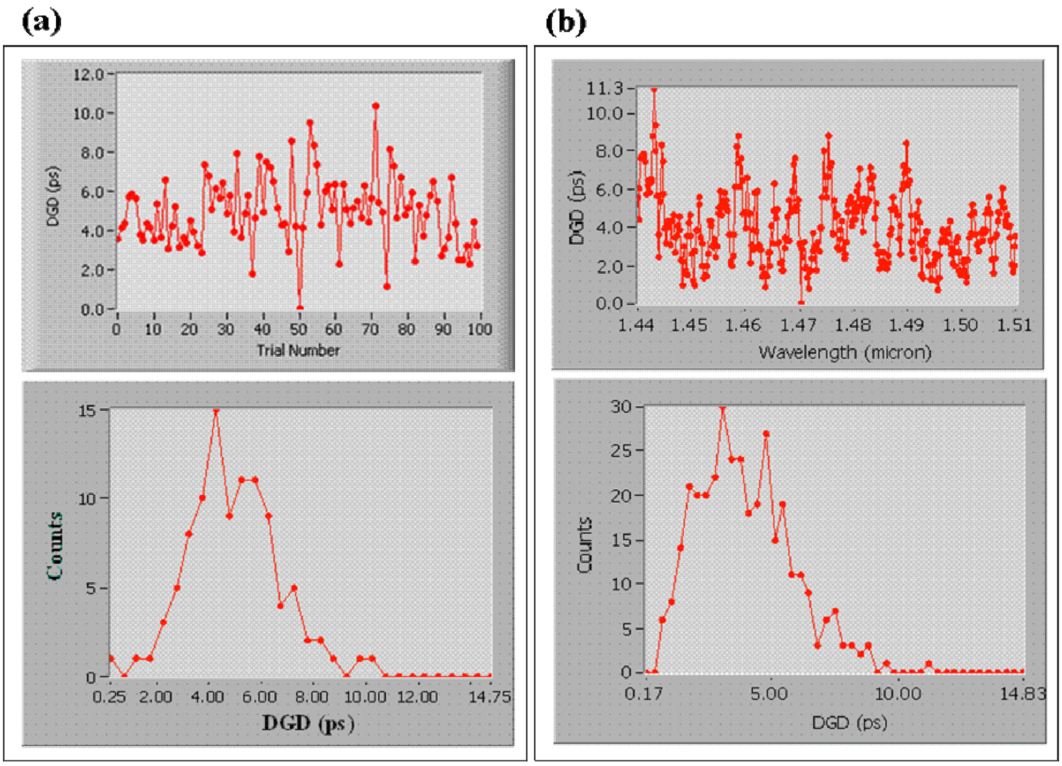

Figure 7-3: (a) Variation and distribution of DGD with fiber realizations at fixed wavelength; (b) Variation and distribution of DGD with wavelength for fixed fiber realizations

fiber realization, the DGD fluctuates with wavelength while, for each wavelength, the DGD fluctuates with the fiber realizations. In general, the observed distribution of the DGD at fixed wavelength or at fixed fiber realization has a trend that approximates a Maxwellian distribution with these limited statistics. Figure 7-3a shows a typical variation of DGD with fiber realization at a fixed wavelength while Figure 7-3b shows the DGD variation with wavelength for a fixed fiber realization. To improve the statistics, we combine the 350 wavelength samples of all the 100 fiber realizations to get a sample size of 35, 000. Figure 7-4a shows the distribution of one of the components of the PMD vector. It agrees well with the expected Gaussian distribution shown in the solid curve. Similarly, the other components of the PMD vector also follow this Gaussian distribution. Figure 7-4b shows the distribution of the DGD which agrees very well with the theoretical Maxwellian distribution depicted in the solid curve. Figure 7-4c shows the distribution of the magnitude of the second

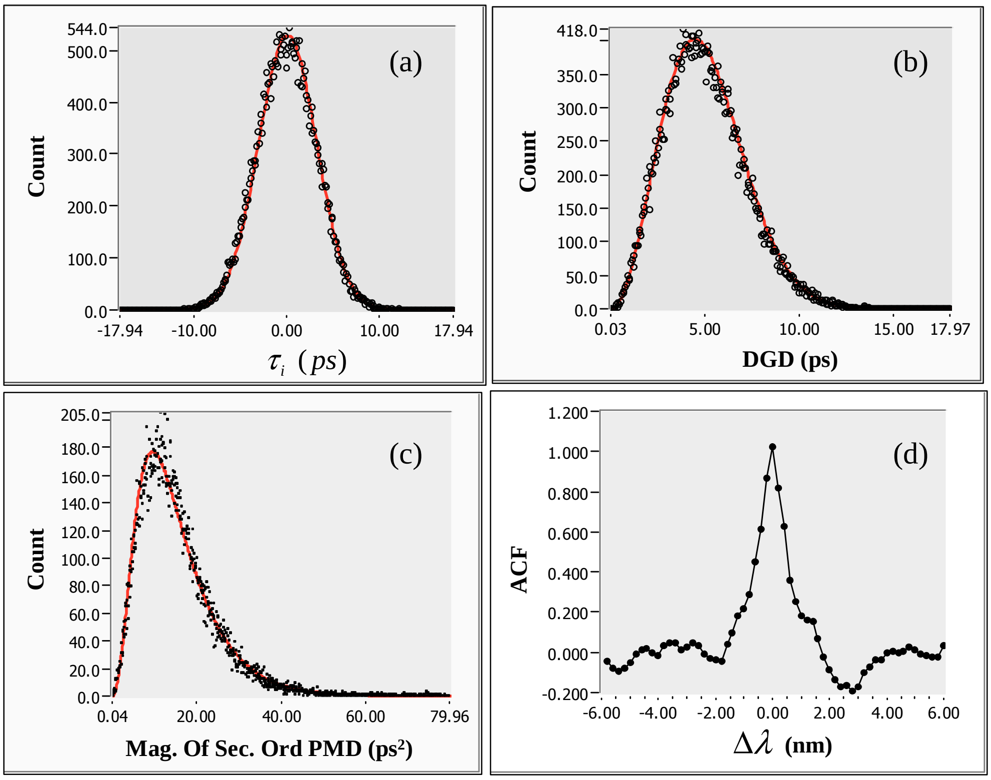

Figure 7-4: Measured statistics of the all-fiber PMD emulator using the combinatorial polarization scramblers. The sample size is 35000 and the number of bins used is 300. Circles show the simulated distributions of a) one of the component of the PMD vector, b) the DGD, c) the magnitude of second order PMD. Figure 3d) shows the measured frequency autocorrelation function in cricles. All the corresponding theoretical curves are shown in solid line curves. The mean DGD used for fitting these theoretical curves is 5ps.

order PMD which also agrees well with the theoretical distribution reported in [59]. All of the theoretical distributions shown as solid curves use the same mean DGD value of 5ps as their fitting parameter. The frequency autocorrelation function of the emulator, as shown in Figure 7-4d, indicates that outside the bandwidth of 1.2 nm, the PMD vectors are no longer correlated, thus the emulator is suitable for WDM applications. This 1.2 nm corresponds to between 6 and 7 times the PSP bandwidth of the emulator which is in good agreement with the theoretical results [18].

7.4 Conclusion

We have proposed a new approach for doing polarization scrambling between segments in a many-segment PMD emulator. It exploits the principles that rotation matrices are non-commutative and that numerous combinations are possible using only a few phase-plates for use in generating a polarization scrambler. With this combinatorial polarization scrambler approach, we demonstrated numerically and experimentally that good PMD statistics are still achievable when we reduce the number of phase-plates by as much as an order of magnitude. This can substantially reduce the cost, the size and the complexity of controlling the emulator. The ease of implementation is also shown by the fact that our emulator was built in less than 3 hours. Although our current setup utilizes manual squeezing, it can be readily implemented using automatic electrically controlled transducers to give a high speed operation. Furthermore, this combinatorial approach can also be adapted for emulation using thermal tuning, wave-plates and polarization controllers using paddles.

Chapter 8

Deterministic Emulator for First and Second Order PMD

8.1 Background

PMD emulators, including the one presented in Chapter 7, are built by physically concatenating as many as 15 segments of polarization maintaining fiber (PMF) with random polarization coupling between segments. The reason for using so many segments is to generate statistical distributions of PMD parameters that resemble those present in the real optical communication fiber. Previous research [95, 74] shows that a small number of concatenated PMF segments is not adequate to produce the tail in the Maxwellian distribution of the differential group delay (DGD) if only the polarization is scrambled between these segments. However, many-segment emulators tend to lack in repeatability and are unable to adjust for varying PMD statistics. In addition, they lack a "dial-in" feature. The ability to "dial-in" any PMD state is particularly useful, since it allows one to quickly examine a PMD compensator by investigating only PMD states that are of interest.

In this chapter, we propose an emulator that can be programmed to generate an arbitrary set of first and second order PMD emulators within its designed range. It is based on a configuration of 4 segments: one variable DGD segment concatenated with 3 fixed DGD segments. There are three polarization rotators, one at each junc-

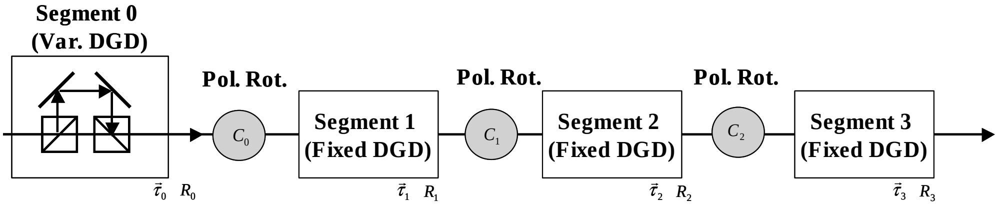

Figure 8-1: Schematics of 4-segment emulator. Segment 1, 2, and 3 have fixed DGD while Segment 0 has variable DGD.

tion of the segments. Instead of polarization scrambling at each junction, we set these polarization rotators according to a statistical schedule so as to produce the probability density functions (pdf) of first and second order PMD vectors that resemble those present in long haul transmission cable. The essence of this approach is to randomly select a pair of isotropically distributed 1^{st} and 2^{nd} order PMD vectors in Stokes space chosen to follow the pdf of real transmission cables. The 4-segment emulator is controlled to produce these PMD vectors. Thus, over a large number of independent samplings, the 1^{st} and 2^{nd} order PMD vectors generated by the emulator, will follow the pdf of the real transmission cable. In addition, since this is a deterministically controlled emulator, it can also be used with importance sampling [32, 33] to intentionally produce those low-probability events that create outages. In this approach to PMD emulation, we need to control the polarization rotators deterministically. Therefore, we need to solve the required 3×3 Mueller rotation matrices of polarization rotators to produce any given pair of 1^{st} and 2^{nd} order PMD vectors. In the following section, we discuss how to solve analytically for these required rotation matrices.

8.2 Theory

The emulator consists of 4 segments: one variable DGD segment and three concatenated segments of fixed DGD as shown in Figure 8-1. $\{\vec{\tau}_0, R_0\}$, $\{\vec{\tau}_1, R_1\}$, $\{\vec{\tau}_2, R_2\}$ and $\{\vec{\tau}_3, R_3\}$ are the first order PMD vectors and the 3×3 Mueller rotation matrices for each segment. They are fixed parameters, except for $|\vec{\tau}_0|$ which is adjustable.

We assume negligible second order PMD for each of the individual segments. Thus segment 1, 2 and 3 could be fixed group velocity delay lines in free space or polarization maintaining fibers with negligible second order PMD while segment 0 could be a variable delay line. There are three polarization rotators in the emulator whose rotation matrices are given by C_0, C_1 and C_2. These rotation matrices are assumed frequency independent over the frequency range of interest. In order for the emulator to generate a given first order PMD, $\vec{\tau}$, and second order PMD, $\vec{\tau}_\omega$, we need to work out the Mueller rotation matrices for the required polarization rotations, C_0, C_1, C_2, and the DGD ($|\vec{\tau}_0|$) of the variable delay line in the emulator. We analyse the emulator's PMD parameters by lumping segments together and calculate the PMD parameters using the PMD vector concatenation rules. From Figure 8-2a,

$$\vec{\tau}\,'' = \vec{\tau}_1 + R_1 C_0 \vec{\tau}_0 \tag{8.1}$$

$$\vec{\tau}_\omega\,'' = \vec{\tau}_1 \times \vec{\tau}\,'' \tag{8.2}$$

And from Figure 8-2b,

$$\vec{\tau}\,' = \vec{\tau}_2 + R_2 C_1 \vec{\tau}\,'' \tag{8.3}$$

$$\vec{\tau}_\omega\,' = R_2 C_1 \vec{\tau}_\omega\,'' + \vec{\tau}_2 \times \vec{\tau}\,' \tag{8.4}$$

The concatenation of all the segments produces the first order PMD vector $\vec{\tau}$ and second order PMD vector $\vec{\tau}_\omega$ as shown in Figure 8-2c.

$$\vec{\tau} = \vec{\tau}_3 + R_3 C_2 \vec{\tau}\,' \tag{8.5}$$

$$\vec{\tau}_\omega = R_3 C_2 \vec{\tau}_\omega\,' + \vec{\tau}_3 \times \vec{\tau} \tag{8.6}$$

Applying rotation transformation, $(R_3 C_2 R_2 C_1)$, on equations (8.1) and (8.2),

$$R_3 C_2 R_2 C_1 \vec{\tau}\,'' = R_3 C_2 R_2 C_1 \vec{\tau}_1 + R_3 C_2 R_2 C_1 R_1 C_0 \vec{\tau}_0 \tag{8.7}$$

$$R_3 C_2 R_2 C_1 \vec{\tau}_\omega\,'' = R_3 C_2 R_2 C_1 \vec{\tau}_1 \times R_3 C_2 R_2 C_1 \vec{\tau}\,'' \tag{8.8}$$

Applying (R_3C_2) on equations (8.3) and (8.4),

$$R_3C_2\vec{\tau}\,' = R_3C_2\vec{\tau}_2 + R_3C_2R_2C_1\vec{\tau}\,'' \tag{8.9}$$

$$R_3C_2\vec{\tau}_\omega{}' = R_3C_2R_2C_1\vec{\tau}_\omega{}'' + R_3C_2\vec{\tau}_2 \times R_3C_2\vec{\tau}\,' \tag{8.10}$$

Substituting (8.9) and (8.10) into (8.5) and (8.6), we obtain

$$\vec{\tau} - \vec{\tau}_3 = R_3C_2\vec{\tau}_2 + R_3C_2R_2C_1\vec{\tau}\,'' \tag{8.11}$$

$$\vec{\tau}_\omega - (\vec{\tau}_3 \times \vec{\tau}) = R_3C_2R_2C_1\vec{\tau}_\omega{}'' + R_3C_2\vec{\tau}_2 \times R_3C_2R_2C_1\vec{\tau}\,'' \tag{8.12}$$

To simplify notation, we denote

$$\vec{A} = R_3C_2R_2C_1R_1C_0\vec{\tau}_0 \tag{8.13}$$

$$\vec{B} = R_3C_2R_2C_1\vec{\tau}_1 \tag{8.14}$$

$$\vec{D} = R_3C_2\vec{\tau}_2 \tag{8.15}$$

Substituting (8.7) into (8.11), and making use of the above notations,

$$\vec{\tau} - \vec{\tau}_3 = \vec{A} + \vec{B} + \vec{D} \tag{8.16}$$

Similarly, substituting (8.7) and (8.8) into equation (8.12), we get

$$\vec{\tau}_\omega - (\vec{\tau}_3 \times \vec{\tau}) = (\vec{B} + \vec{D}) \times (\vec{B} + \vec{A}) \tag{8.17}$$

Vector $\vec{B}$ and $\vec{D}$ are adjustable in orientation using rotation matrices C_1 and C_2 respectively. Vector $\vec{A}$ is arbitrarily adjustable in orientation and magnitude using rotation matrix C_0 and the adjustable group delay $|\vec{\tau}_0|$. Our aim is to solve for $\vec{A}$, $\vec{B}$ and $\vec{D}$ from (8.16) and (8.17), so that we can compute their respective rotation matrices, C_0, C_1 and C_2 and $|\vec{\tau}_0|$, since we know R_3, $\vec{\tau}_2$, R_2, $\vec{\tau}_1$, R_1 of the individual segment. We also know the direction of $\vec{\tau}_0$. However, its magnitude is only known

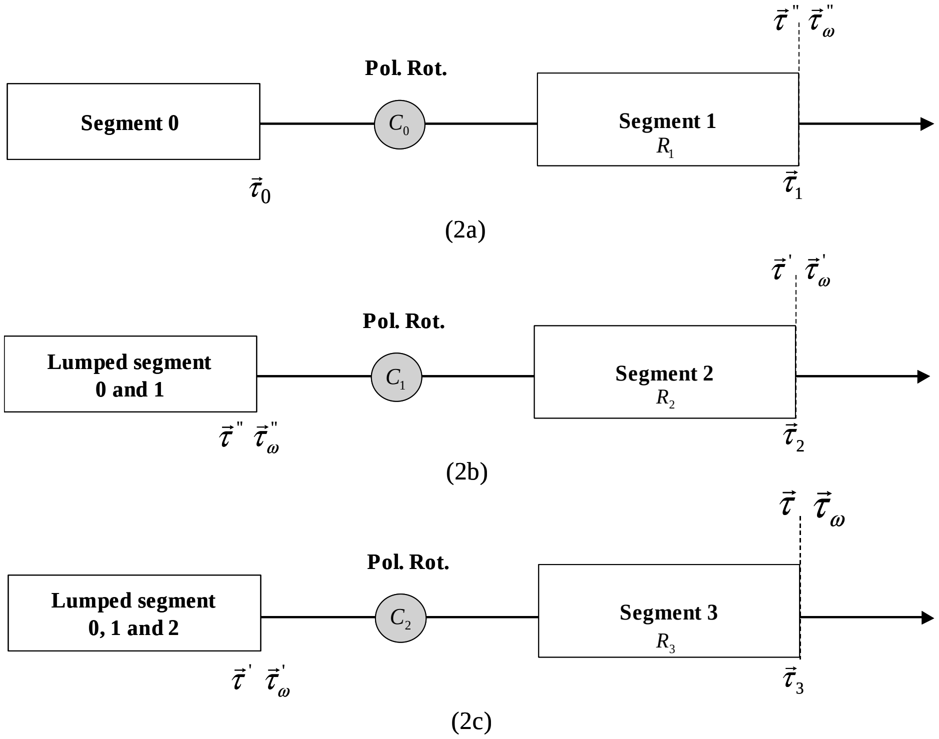

Figure 8-2: Sequences of combining segments for PMD analysis

when we have solved for $\vec{A}$ (i.e. $|\vec{\tau}_0| = \left|\vec{A}\right|$). Substitute (8.16) into (8.7) and with some algebraic manipulation, we obtain

$$(\vec{\tau}_\omega - (\vec{\tau}_3 \times \vec{\tau}) - \vec{D} \times (\vec{\tau} - \vec{\tau}_3)) = \vec{B} \times (\vec{\tau} - \vec{\tau}_3 - \vec{D}) \tag{8.18}$$

From (8.18), it is obvious that $(\vec{\tau}_\omega - (\vec{\tau}_3 \times \vec{\tau}) - \vec{D} \times (\vec{\tau} - \vec{\tau}_3))$ and $(\vec{\tau} - \vec{\tau}_3 - \vec{D})$ are perpendicular and thus by taking their dot product and set it to zero, we obtain a vector equation for $\vec{D}$

$$(\vec{\tau}_\omega - (\vec{\tau}_3 \times \vec{\tau})) \cdot (\vec{\tau} - \vec{\tau}_3 - \vec{D}) = 0 \tag{8.19}$$

To emulate any given $\vec{\tau}$ and $\vec{\tau}_\omega$, we just have to choose $\vec{D}$ such that $(\vec{\tau} - \vec{\tau}_3 - \vec{D})$ is perpendicular to $(\vec{\tau}_\omega - (\vec{\tau}_3 \times \vec{\tau}))$. Figure 8-3a helps us visualize the orientation of these vectors.

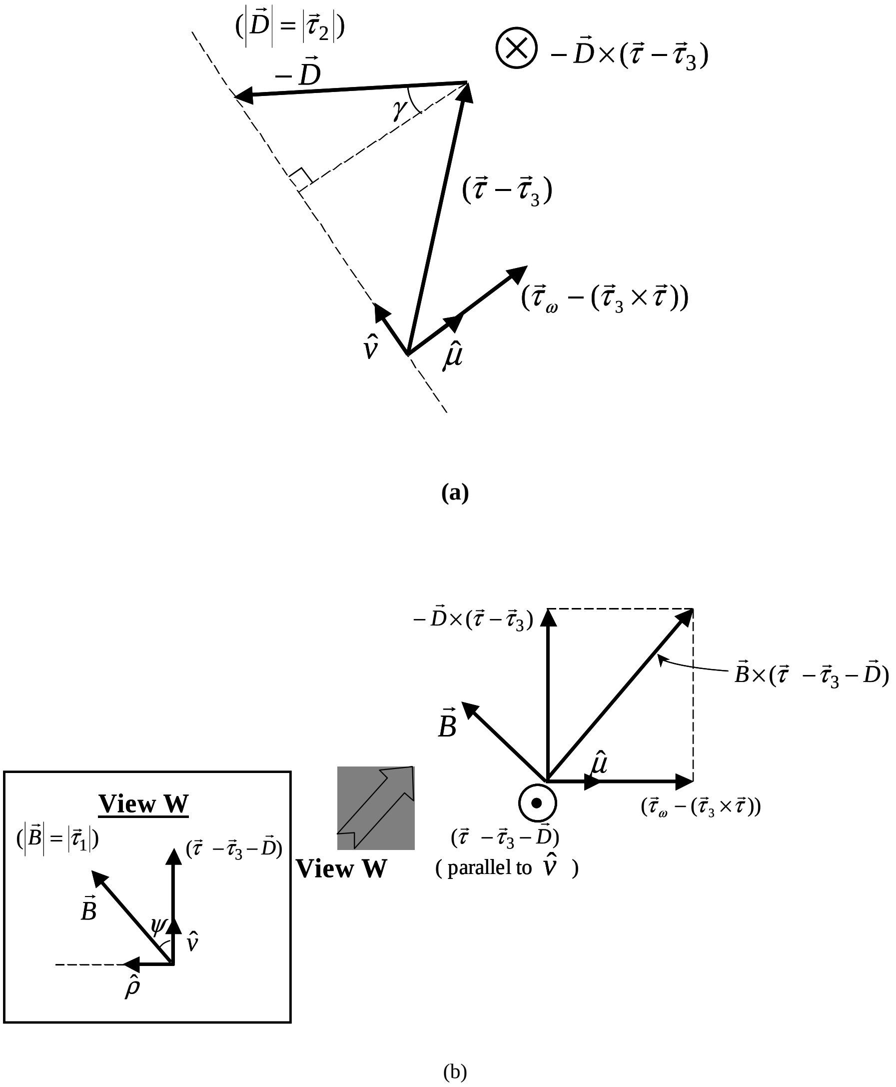

Figure 8-3: (a) Vector $\vec{D}$ is fixed to lie in the plane of $(\vec{\tau}-\vec{\tau}_3)$ and $(\vec{\tau}_\omega-(\vec{\tau}_3\times\vec{\tau}))$. It has fixed magnitude of $|\vec{\tau}_2|$ and is in the direction such that $(\vec{\tau}-\vec{\tau}_3-\vec{D}))$ is perpendicular to $(\vec{\tau}_\omega-(\vec{\tau}_3\times\vec{\tau}))$. (b) Vector $\vec{B}$ has fixed magnitude of $|\vec{\tau}_1|$ and, once $\vec{D}$ is solved, $\vec{B}$ lies in the orientation such that $\vec{B}\times(\vec{\tau}-\vec{\tau}_3-\vec{D})$ equals to $(\vec{\tau}_\omega-(\vec{\tau}_3\times\vec{\tau})-\vec{D}\times(\vec{\tau}-\vec{\tau}_3))$.

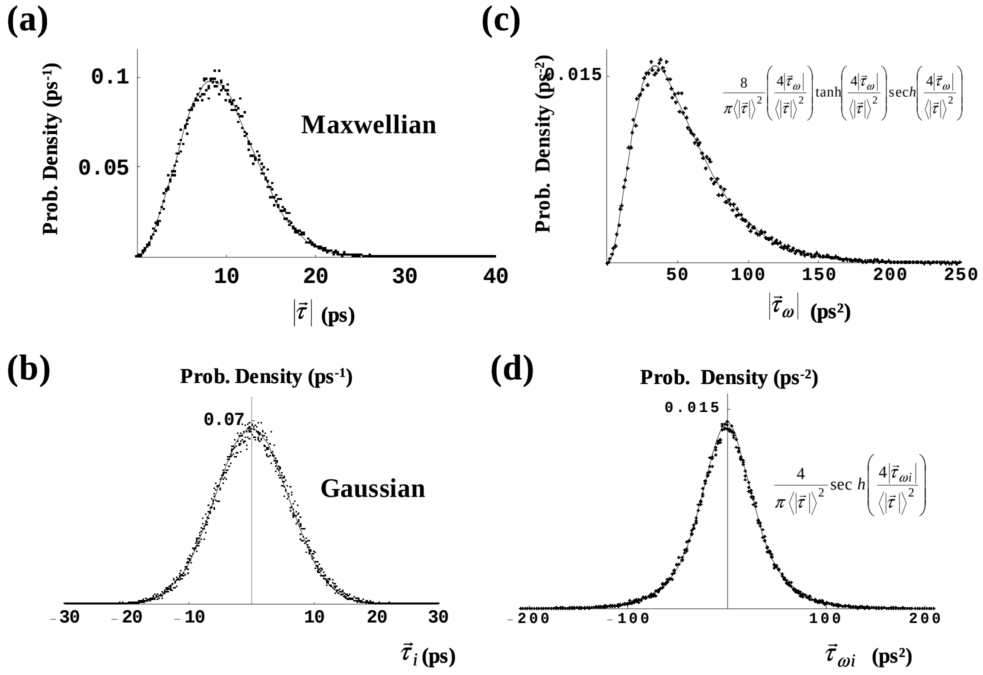

Figure 8-4: Monte Carlo simulation of 1st and 2nd order PMD generated by a concatenation of 100 1-ps DGD segments. (a) Probability density function (pdf) of DGD, $|\vec{\tau}|$; (b) pdf of vector components, $\vec{\tau}_i$, of $\vec{\tau}$. The pdf are identical for all the 3 vector components; (c) pdf of $|\vec{\tau}_\omega|$; and (d) pdf of vector components, $\vec{\tau}_{\omega i}$, of $\vec{\tau}_\omega$. Dots are simulation results while solid lines are the fitting curves.

It is worthwhile to note that the magnitude of $\vec{D}$ is fixed at $|\vec{\tau}_2|$ (see (8.15)) and that equation (8.19) does not uniquely define $\vec{D}$. For convenience, we fix $\vec{D}$ onto the plane containing $(\vec{\tau} - \vec{\tau}_3)$ and $(\vec{\tau}_\omega - (\vec{\tau}_3 \times \vec{\tau}))$. Thus we solve for $\vec{D}$ as

$$\vec{D} = |\vec{\tau}_2| \left(\cos\gamma\hat{\mu} - \sin\gamma\hat{v}\right) \tag{8.20}$$

where $\hat{\mu}$ is a unit vector in the direction of $(\vec{\tau}_\omega - (\vec{\tau}_3 \times \vec{\tau}))$, $\hat{v}$ is a unit vector perpendicular to $\hat{\mu}$ in the plane of $(\vec{\tau} - \vec{\tau}_3)$ and $(\vec{\tau}_\omega - (\vec{\tau}_3 \times \vec{\tau}))$ as shown in Figure 8-3a (which is parallel to $(\vec{\tau} - \vec{\tau}_3 - \vec{D})$). The angle γ, as in Figure 8-3a, is given by

$$\gamma = \cos^{-1}\left[\frac{((\vec{\tau} - \vec{\tau}_3) \cdot \hat{\mu})}{|\vec{\tau}_2|}\right] \tag{8.21}$$

To ensure that a solution always exists for equation (8.21), we need to choose $|\vec{\tau}_2|$ to be larger than any anticipated magnitude of $|\vec{\tau} - \vec{\tau}_3|$. Once we know $\vec{D}$, we solve $\vec{B}$

using (8.18). The solution is unique since the magnitude of $\vec{B}$ is $|\vec{\tau}_1|$. Thus $\vec{B}$, as in Figure 8-3b, is given by

$$\vec{B} = |\vec{\tau}_1| \left(\cos\psi\ \hat{v} + \sin\psi\ \hat{\rho}\right) \tag{8.22}$$

where $\hat{v}$ is the unit vector in the direction of $(\vec{\tau} - \vec{\tau}_3 - \vec{D})$, $\hat{\rho}$ is the unit vector in the direction of $\hat{v} \times [\vec{\tau}_\omega - (\vec{\tau}_3 \times \vec{\tau}) - \vec{D} \times (\vec{\tau} - \vec{\tau}_3)]$ and ψ is the angle between $\vec{B}$ and $(\vec{\tau} - \vec{\tau}_3 - \vec{D})$ given by

$$\sin\psi = \frac{\left|(\vec{\tau}_\omega - (\vec{\tau}_3 \times \vec{\tau}) - \vec{D} \times (\vec{\tau} - \vec{\tau}_3))\right|}{|\vec{\tau}_1| \left|\vec{\tau} - \vec{\tau}_3 - \vec{D}\right|} \tag{8.23}$$

Similarly, it is important to note that to ensure robust operation of the emulator, we need to choose an appropriate $|\vec{\tau}_1|$ so that a solution of equation (8.23) always exists for an anticipated range of the $\vec{\tau}$ and $\vec{\tau}_\omega$. After solving for $\vec{D}$ and $\vec{B}$, $\vec{A}$ is uniquely specified by equation (8.16) as

$$\vec{A} = \vec{\tau} - \vec{\tau}_3 - \vec{D} - \vec{B} \tag{8.24}$$

The magnitude of $\vec{A}$ gives the required DGD setting, $|\vec{\tau}_0|$, of segment 0 (refer to equation (8.13). Using the known R_3 and $\vec{\tau}_2$, and employing equation (8.15), we can now solve for the rotation matrix C_2 from

$$C_2\vec{\tau}_2 = R_3^\dagger \vec{D} \tag{8.25}$$

After we have solved C_2, with known R_2 and $\vec{\tau}_1$, and equation (8.14), we can find C_1 from

$$C_1\vec{\tau}_1 = (R_3 C_2 R_2)^\dagger \vec{B} \tag{8.26}$$

Similarly, using the known R_1 and known orientation of $\vec{\tau}_0$ (and whose magnitude from equation (8.23)), and (8.13), we can find C_0 from

$$C_0\vec{\tau}_0 = (R_3 C_2 R_2 C_1 R_1)^\dagger \vec{A} \tag{8.27}$$

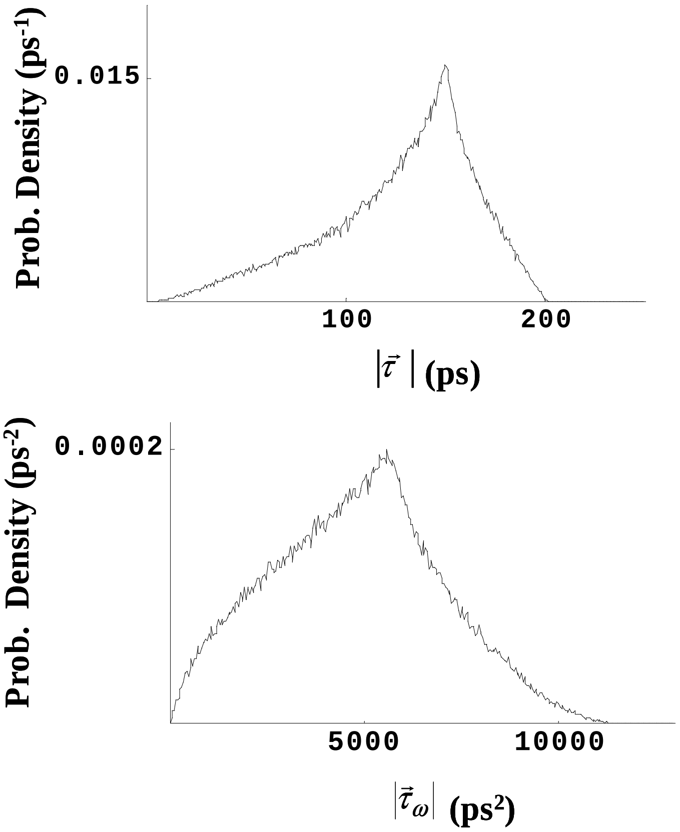

Figure 8-5: Monte Carlo simulation of 1st and 2nd order PMD generated by a concatenation of 4-DGD segments with polarization scramblers between them. The DGD values are 76.3 ps for segment 1, 73.5 ps for segment 2, 2.5 ps for segment 3 while the DGD for segment 0 is randomly chosen from 0 ps to 50 ps.

Thus we have found all the required rotation matrices, C_0, C_1, and C_2 (from equation (8.25), (8.26) and (8.27)) of the 3 polarization rotators as well as the required DGD value for segment 0, in order to generate any given pair of 1^{st} order PMD, $\vec{\tau}$, and 2^{nd} order PMD, $\vec{\tau}_\omega$ from the 4-segment emulator.

8.3 Simulations & Discussions

Real transmission fiber can be modeled as a concatenation of many randomly oriented birefringent elements. In Figure 8-4, we show the probability density functions (pdf) of the magnitudes of 1^{st} and 2^{nd} order PMD vectors, and of their respective vector components. The solid curves are the analytic results from Reference [53, 59, 63],

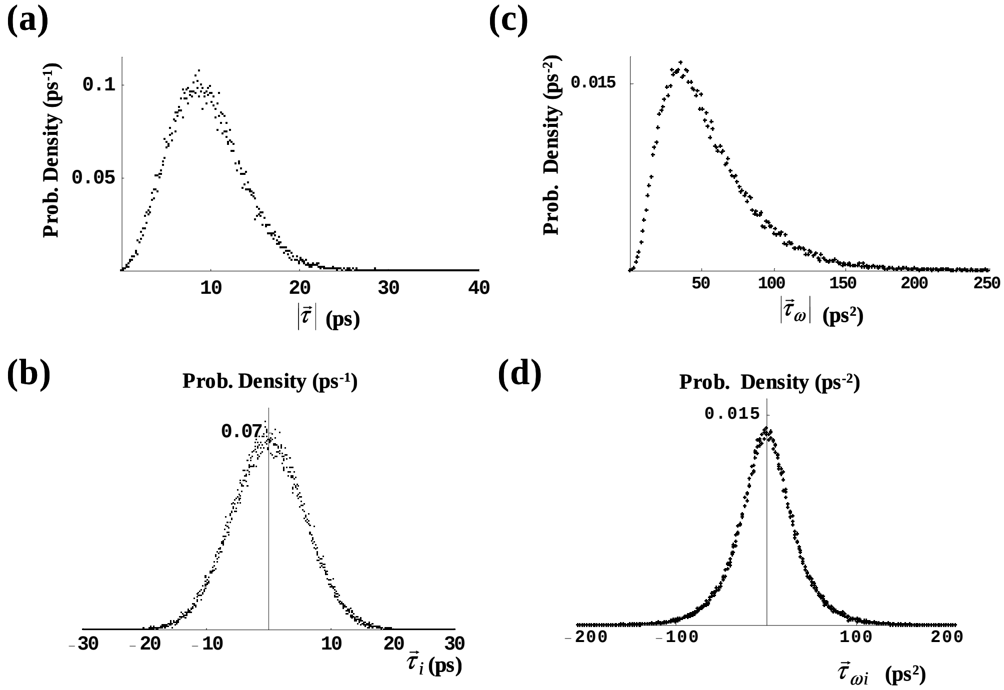

Figure 8-6: Monte Carlo simulation of 1st and 2nd order PMD generated by the same concatenation of 4-DGD segments used in Figure 8-5. However, here, the polarization rotators and DGD value of Segment 0 are controlled deterministically to produce the realistic pdf in Figure 8-4. (a) Probability density function (pdf) of DGD, $|\vec{\tau}|$; (b) pdf of vector components, $\vec{\tau}_i$, of $\vec{\tau}$. (c) pdf of $|\vec{\tau}_\omega|$; and (d) pdf of vector components, $\vec{\tau}_{\omega i}$, of $\vec{\tau}_\omega$.

the points are obtained using Monte Carlo simulations based on a concatenation of 100 randomly oriented 1-ps segments with polarization scramblers between segments. They are generated over 50000 independent samples. The magnitude $|\vec{\tau}|$ of 1^{st} order PMD, $\vec{\tau}$, follows a Maxwellian function,

$$\frac{8}{\pi^2 \langle|\vec{\tau}|\rangle}\left(\frac{2\,|\vec{\tau}|}{\langle|\vec{\tau}|\rangle}\right)^2 e^{-(2|\vec{\tau}|/\langle|\vec{\tau}|\rangle)^2/\pi} \tag{8.28}$$

while each of its vector components, $\vec{\tau}_i$, follows the Gaussian function

$$\frac{2}{\pi\,\langle|\vec{\tau}|\rangle} e^{-(2|\vec{\tau}_i|/\langle|\vec{\tau}|\rangle)^2/\pi} \tag{8.29}$$

$\langle|\vec{\tau}|\rangle$ is the mean DGD of the pdf function [53, 59, 63]. Indeed, our simulation results in Figure 8-4a and Figure 8-4b fit well to a Maxwellian and Gaussian function

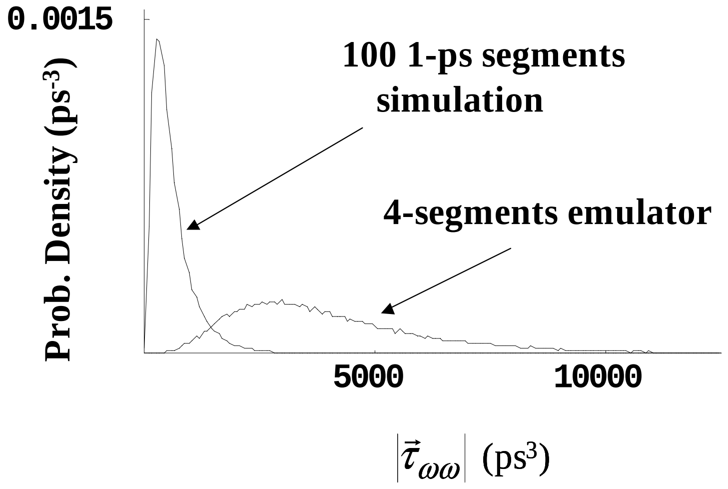

Figure 8-7: Probability density function (pdf) of the 3^{rd} order PMD magnitude, $|\vec{\tau}_{\omega\omega}|$ generated by 4-segments emulator when generating the 1^{st} and 2^{nd} order PMD shown in Figure 8-6. For comparison purposes, we also plotted the 3^{rd} order PMD pdf generated by the concatenation of 100 1-ps segments when generating the 1^{st} and 2^{nd} order PMD shown in Figure 8-4.

respectively, with $\langle|\vec{\tau}|\rangle$ of 9.3 ps. From Figure 8-4c and Figure 8-4d, we can see that the pdf of the magnitude of 2^{nd} order PMD, $|\vec{\tau}_{\omega}|$, follows the function of

$$\frac{8}{\pi\langle|\vec{\tau}|\rangle^2}\left(\frac{4|\vec{\tau}_{\omega}|}{\langle|\vec{\tau}|\rangle^2}\right)\tanh\left(\frac{4|\vec{\tau}_{\omega}|}{\langle|\vec{\tau}|\rangle^2}\right)\sec h\left(\frac{4|\vec{\tau}_{\omega}|}{\langle|\vec{\tau}|\rangle^2}\right) \tag{8.30}$$

while each of its vector components, $\vec{\tau}_{\omega i}$, follows the hyperbolic secant function of

$$\frac{4}{\pi\langle|\vec{\tau}|\rangle^2}\sec h\left(\frac{4|\vec{\tau}_{\omega i}|}{\langle|\vec{\tau}|\rangle^2}\right) \tag{8.31}$$

From Ref. [95, 135, 136], it is already known that a smaller number of concatenated segments, such as four segments, is not adequate to produce the ideal Maxwellian distribution of the DGD by polarization scrambling between the segments. We have once again verified this fact in Figure 8-5, which shows the results of a Monte-Carlo simulation of 4 concatenated segments with polarization scramblers between them. For this simulation, the DGD for the first segment is randomly chosen from 0 ps to 50 ps while the DGD values are 76.3 ps for second segment, 73.5 ps for third segment, 2.5 ps for last segment. The choice of these values will be discussed later. It is obvious, from Figure 8-5, that these pdfs' of 1^{st} and 2^{nd} order PMD are very different from the realistic pdfs of the transmission cable (shown in Figure 8-4). However, in Figure 8-6, we are able to produce these realistic pdf using the same four concatenated segments. This is achieved by controlling the polarization rotator in a deterministic manner, instead of randomly scrambling it. We first randomly select a pair of 1^{st} and 2^{nd} order PMD vectors whose directions are isotropically distributed over the Poincaré sphere and whose magnitudes are randomly chosen to follow their respective pdf over a large sample size. With this randomly chosen pair of 1^{st} and 2^{nd} order PMD vectors, we solve the required DGD for segment 0, $|\vec{\tau}_0|$, and the rotation matrices of the three polarization rotators, C_0, C_1, and C_2, as described in Section 8.2. These solutions are then used to set the polarization rotators and segment 0 of the emulator, so as to generate these vectors. The whole procedure is repeated independently over a large sample size, and eventually, we achieve the realistic pdf for the PMD vector magnitudes and their respective vector components. Figure 8-6 shows the probability distribution function of the magnitudes and the vector components of 1^{st} and 2^{nd} order PMD generated by this 4-segment emulator if it is controlled in the abovementioned manner. Comparing this with Figure 8-4, we see that it is obviously as good as a concatenated 100 1-ps segment. This approach is attractive since we can now generate realistic 1^{st} and 2^{nd} order distribution functions using a compact and simplified emulator. It is noteworthy that, for consistent comparison of results in Figure 8-5 and 8-6, we use the same four concatenated segments for simulations. The DGD for the first segment is adjusted from 0 ps to 50 ps while the DGD values are 76.3 ps for second segment, 73.5 ps for third segment, 2.5 ps for last segment. The choice of the DGD values for the fixed segments and the variable DGD range for segment 0, is to ensure solutions of C_0, C_1, and C_2, and $|\vec{\tau}_0|$, always exist for all values of DGD, $|\vec{\tau}|$, ranging from 0 to 50 ps and second order PMD magnitude, $|\vec{\tau}_\omega|$, ranging from 0 to 600 ps^2, for the case of Figure 8-6. While we control the 4-segment emulator to produce realistic 1^{st} and 2^{nd} pdfs of transmission fiber, there are insufficient degrees of freedom to control the 3^{rd} order and higher order PMD. Thus this emulator is more suitable for PMD study of single channel systems than for multi-channel wavelength

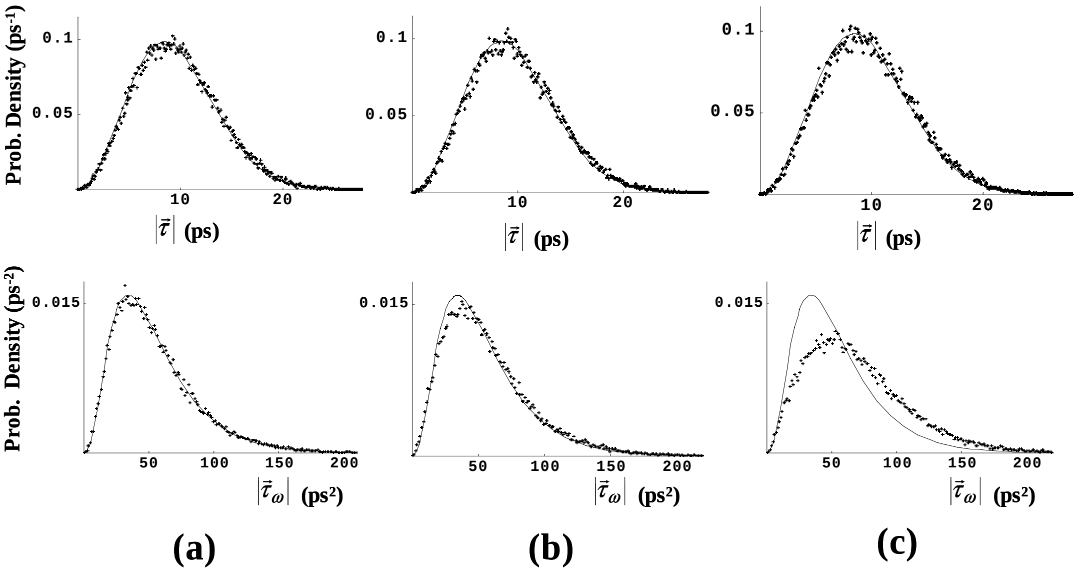

Figure 8-8: 1st and 2nd order PMD probability density functions generated by 4-segments emulator using fixed phase-plates polarization rotators when there is a random Gaussian distributed angular error of standard deviation σ_{angle} in the rotation of the birefringence axes. (a) $\sigma_{angle} = 0.3$ arc min degree, (b) $\sigma_{angle} = 1.5$ arc min degree and (c) $\sigma_{angle} = 4.5$ arc min degree. For all these cases, a random Gaussian distributed error of standard deviation 0.12 ps is also introduced to the DGD value in the variable DGD segment 0.

division multiplexing systems. Particularly, it is useful to know the type of 3^{rd} order PMD, $\vec{\tau}_{\omega\omega}$, pdf generated by this 4-segment emulator as compared to the realistic pdf of the 3^{rd} order PMD. Figure 8-7 shows the pdf of the 3^{rd} order PMD magnitude, $|\vec{\tau}_{\omega\omega}|$, generated by the 4-segment emulator when it is producing the pdf of 1^{st} and 2^{nd} order PMD shown in Figure 8-6. For comparison purposes, we have also plotted the 3^{rd} order PMD pdf generated by the concatenation of 100 1-ps segments while it is generating the 1^{st} and 2^{nd} order PMD shown in Figure 8-4. The 3^{rd} order PMD generated by this 4-segment emulator pdf is generally larger than its 100-segments counterpart, and its maximum magnitude is around 4 times larger. This is expected since we are now using fewer segments of larger DGD values and also because this 4-segment emulator is designed to produce a larger range of 1^{st} and 2^{nd} order PMD than those in Figure 8-4. From Figure 8-7, it is also evident that, even if we do not control the 3^{rd} order PMD generated from the 4-segment emulator, we are not going to generate excessively large value of 3^{rd} order PMD with a proper selection of the DGD value for the segments. Thus, another objective in selecting the DGD values for the fixed segments and the variable DGD range for segment 0, is to minimize the 3^{rd} order PMD generated while trying to achieve sufficient working range for the 1^{st} and 2^{nd} order PMD.

When we instruct the polarization rotators to carry out the rotation transformations solved in Section 8.2, there are bound to be some inaccuracies. Therefore, for practical purposes, it is useful to know the sensitivity of our 4-segment emulation to these deviations. In this study, we consider two types of polarization rotator: (1) polarization rotators that consists of a combination of three fixed phase-plates where a half-wave plate is sandwiched by two quarter-wave plates, and (2) polarization rotators that consists of a combination of three tunable phase-plates whose birefringence axes are in $\{1,0,0\}$, $\{0,1,0\}$ and $\{1,0,0\}$ in Stokes space. For a fixed phase-plate polarization rotator, we can transform any polarization state to any polarization state on the Poincaré sphere by changing the angular orientations of their birefringent axes. For a tunable phase-plate polarization rotator, we fix the birefringence axes, but tune its phase angle to carry out any polarization transformation on the Poincaré sphere. Thus, our goal is to know the required angular accuracy in the rotation of birefringence axes for the case of fixed phase-plate polarization rotator, and in the tuning of phase angle for the case of tunable phase-plate polarization rotator. To study this angular sensitivity, we first solve exactly the angles of all phase-plates in the three polarization rotators of the emulator required to generate the randomly selected pair of PMD vectors. We then introduce a random Gaussian distributed angular error of standard deviation σ_{angle} to the angles of all phase plates. Using these perturbed angles, we calculate the 1^{st} and 2^{nd} order PMD produced. Figure 8-8, shows the 1^{st} and 2^{nd} order PMD pdf generated by the 4-segment emulator using fixed phase-plate rotators, for various standard deviation σ_{angle} of 0.3, 1.5 and 4.5 arc min degree. Figure 8-9 shows the 1^{st} and 2^{nd} order PMD pdf generated by the emulators using tunable phase-plate polarization rotators, for various standard deviation σ_{angle} of 6, 9 and 12 arc min degree. For all these cases, we have also introduced a random Gaussian

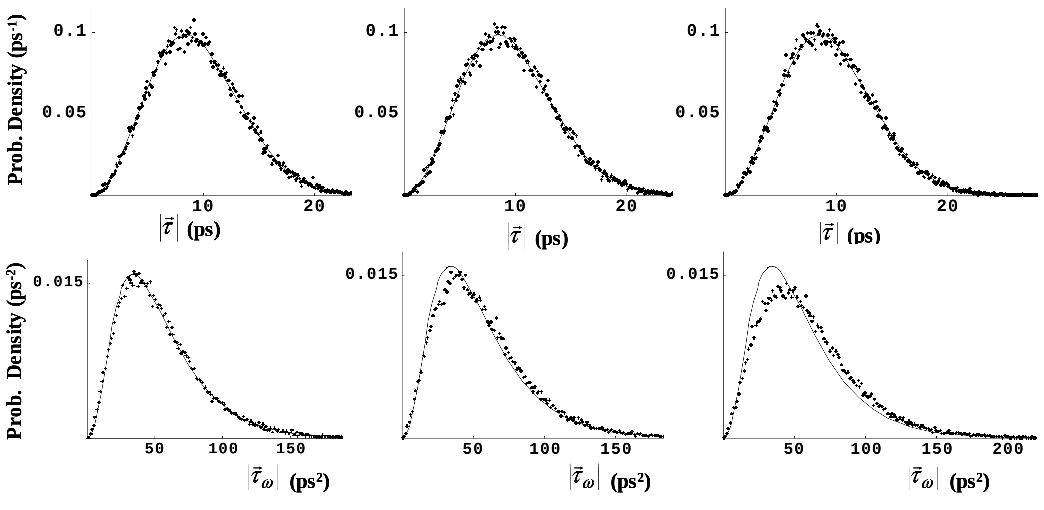

(a) (b) (c)

Figure 8-9: 1st and 2nd order PMD probability density functions generated by 4-segments emulator using tunable phase-plates polarization rotators when there is a random Gaussian distributed angular error of standard deviation, σ_{angle}, in the tuning phase angle. The birefringence axes of the three tunable phase-plates are fixed at 1,0,0, 0,1,0 and 0,0,1 direction in the Stokes space. (a) σ_{angle} =6 arc min degree, (b) σ_{angle} = 9 arc min degree and (c) σ_{angle} = 12 arc min degree. For all these cases, a random Gaussian distributed error of standard deviation 0.12 ps is also introduced to the DGD value in the variable DGD segment 0.

distributed error of standard deviation 0.12ps to the DGD value in the variable DGD segment 0. From Figure 8-8, we know that if we built our 4-segment emulators based on fixed phase-plate polarization rotators, we would need an angular accuracy of $\sim$ 1.5 arc min degree for the birefringence axes rotation. On the other hand, if we build it based on tunable phase-plate polarization rotator, we would require an accuracy of $\sim$ 9 arc min degree in the tuning of the phase angle. From Figure 8-8 and 8-9, we can note that the first order PMD pdf is not so sensitive to angular errors and remains a Maxwellian function for all the considered σ_{angle}. Second order PMD pdf, on the other hand, is less tolerant to angular errors. This is expected since second order PMD is the sum of vector cross-products, which is more sensitive to angle variations between vectors.

It is worthwhile to note that small length changes of fixed DGD segments would result in different rotation matrices, R_i, for each DGD segment. And this will affect the generated 1^{st} and 2^{nd} order PMD vectors. Thus accurate prior knowledge of R_i of each fixed DGD segment must be obtained by measuring the output SOP of each DGD segment for known input SOP. And, subsequent changes of R_i should be minimized, for example, by having a temperature controlled environment. Alternatively, we may recalibrate R_i when need arises. In principle, we could also use a three-segment emulator to perform the same function since it has sufficient degrees of freedom. However, our experience with 3-segments emulator is that, when it produces the same range of 1^{st} and 2^{nd} order PMD, it produces a larger third order PMD statistics than its 4-segments counterpart. The reason of using a variable DGD element as a first segment in our emulator is to simplify the analytical solution. We could replace the variable DGD segment with fixed DGD segments, but we could only manage to solve the solution analytically with more segments (∼6 to 8).

8.4 Conclusion

We have proposed a new concept of PMD emulation where the first and second order PMD vectors are generated using 4 concatenated segments (1 variable DGD segment and 3 fixed DGD segments). The emulator is deterministically controlled to produce the probability density functions of the 1^{st} and 2^{nd} order PMD of a real transmission cable. To control the emulator deterministically, we have solved analytically the required rotation matrices of the polarization rotators and DGD value of the variable delay line in the emulator. Through Monte Carlo simulations, we have demonstrated that our emulator is, indeed, capable of generating realistic probability density functions for the 1^{st} and 2^{nd} order PMD. While we do not control the 3^{rd} order PMD generated by the emulator, we have shown that the 3^{rd} order PMD is somewhat larger than the realistic distribution. In addition, we have also studied the sensitivity of the emulator to angular inaccuracy in the polarization rotators.

Chapter 9

Deterministic Broadband PMD Emulator

9.1 Background

In Chapter 8, we describe a deterministically controlled PMD emulator for generating an arbitrary set of 1^{st} and 2^{nd} order PMD vectors. In this chapter, we extend the same concept to broadband emulation. This Deterministic Broadband PMD emulator (DBPMD) can approximate a desired PMD vector for every frequency within a certain band of interest. In the other words, one can "dial-in" the spectrum of an arbitrary PMD vector that comprises all orders of PMD. This emulator employs three stages of flexible frequency-dependent polarization rotation in Stokes space, which provide the three degrees of freedom for emulating the PMD vector at each frequency. The fourth stage compensates for the isotropic dispersion created by the first three stages as shown in Figure 9-1.

9.2 Theory

At each angular frequency ω ($\omega = 2\pi f$ where f is the optical frequency), the "dial-in" PMD vector $\vec{\tau}_e(\omega)$ has three parameters. In Stokes space, Stage 1 and 3 are rotations about {1,0,0} with rotation angle $\theta_1(\omega)$ and $\theta_3(\omega)$ respectively. Stage 2 is

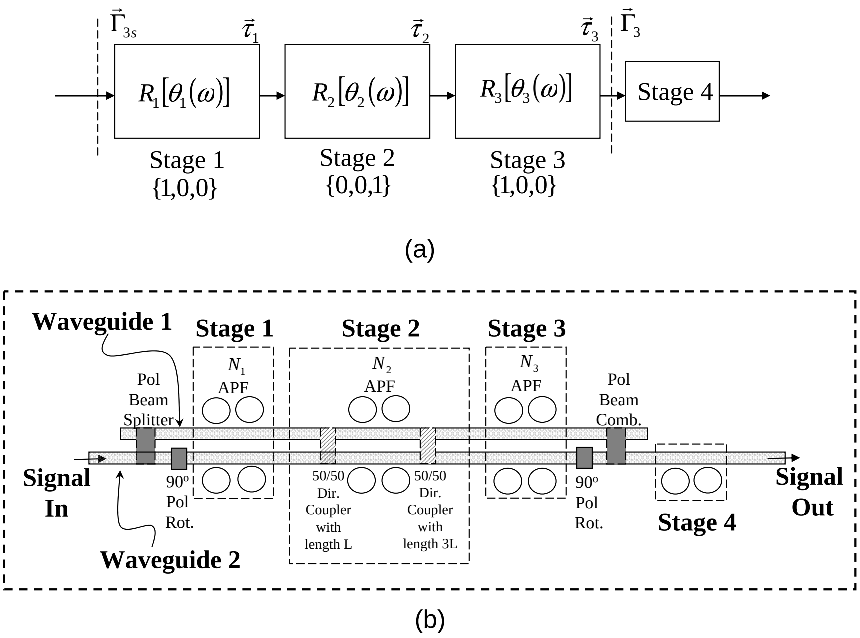

Figure 9-1: a) Block diagram of the 4-stage All-Frequency PMD emulator; b) A practical implementation using All-Pass filters integrated on planar waveguides.

a rotation about the $\{0,0,1\}$ with rotation angle $\theta_2(\omega)$. Rotation angles $\theta_1(\omega)$, $\theta_2(\omega)$ and $\theta_3(\omega)$ are general functions of frequency, in contrast to the linear dependence on frequency of a birefringent element. The rotation matrices of Stage 1 and 3 are

$$R_i(\omega) = \begin{pmatrix} 1 & 0 & 0 \\ 0 & \cos\theta_i\left(\omega\right) & -\sin\theta_i\left(\omega\right) \\ 0 & \sin\theta_i\left(\omega\right) & \cos\theta_i\left(\omega\right) \end{pmatrix} \tag{9.1}$$

for $i = 1$ and 3 and the rotation matrix of Stage 2 is

$$R_2(\omega) = \begin{pmatrix} \cos\theta_2\left(\omega\right) & -\sin\theta_2\left(\omega\right) & 0 \\ \sin\theta_2\left(\omega\right) & \cos\theta_2\left(\omega\right) & 0 \\ 0 & 0 & 1 \end{pmatrix} \tag{9.2}$$

Since $\vec{\tau}\times = \left(dR/d\omega\right)R^{+}$, the corresponding PMD vectors of Stage 1, 2, and 3 are this is $\vec{\tau}_1\left(\omega\right) = \left\{\frac{d\theta_1}{d\omega}, 0, 0\right\}$, and $\vec{\tau}_2\left(\omega\right) = \left\{0, 0, \frac{d\theta_2}{d\omega}\right\}$ and $\vec{\tau}_3\left(\omega\right) = \left\{\frac{d\theta_3}{d\omega}, 0, 0\right\}$ respectively. To account for the input state of polarization (SOP), we transform the concatenated

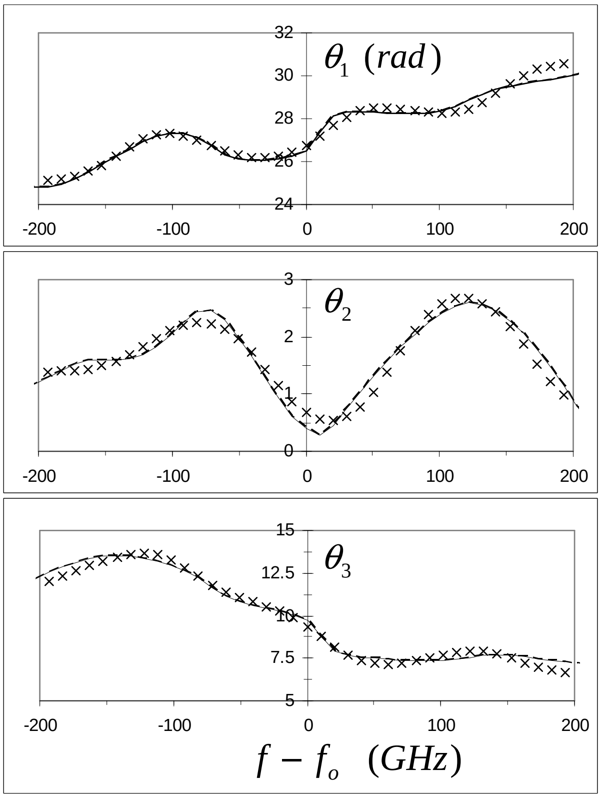

Figure 9-2: Required rotation angles of various stages for a randomly chosen fiber: $\theta_1(\omega)$ of Stage 1, $\theta_2(\omega)$ of Stage 2 and and $\theta_3(\omega)$ of Stage 3. Solid curves are exact rotation angles calculated using the synthesis algorithm while curves of crosses are those approximated using $N_1 = N_2 = N_3 = 3$ AFPs. f_o is the carrier's optical frequency and corresponds to a wavelength of 1550nm.

PMD to the input plane. With the PMD concatenation rule, the PMD vector after Stage 3 is transformed to the input plane of the emulator is given as

$$\begin{aligned} \vec{\Gamma}_{3s}(\omega) &= \vec{\tau}_1(\omega) + R_1^+(\omega)\,\vec{\tau}_2(\omega) + R_1^+(\omega)\,R_2^+(\omega) && \text{(9.3a)} \\ &= \begin{pmatrix} \frac{d\theta_1}{d\omega} + \cos\theta_2 \frac{d\theta_3}{d\omega} \\ \sin\theta_1 \frac{d\theta_2}{d\omega} - \cos\theta_1 \sin\theta_2 \frac{d\theta_3}{d\omega} \\ \cos\theta_1 \frac{d\theta_2}{d\omega} + \sin\theta_1 \sin\theta_2 \frac{d\theta_3}{d\omega} \end{pmatrix} && \text{(9.3b)} \end{aligned}$$

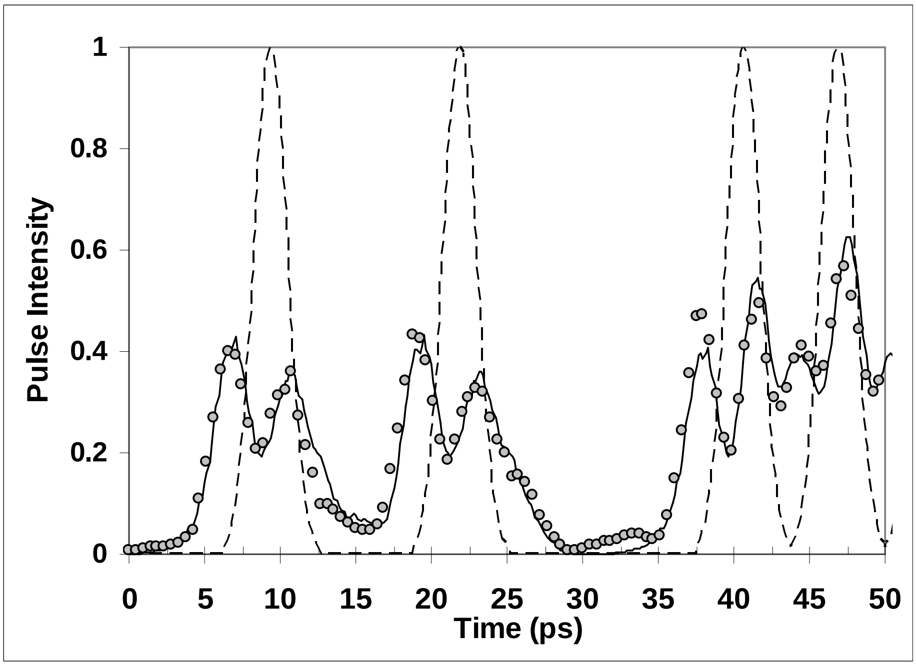

Figure 9-3: Output signals of simulated fiber of 30 sections and the DBPMD emulator. The dashed line is for the input signal. The solid line curve is the output from a simulated fiber of 30 sections while the curve of filled circles is the output from the DBPMD emulator using the approximated rotation angles by APFs shown in Figure 9-2

Given a "dial-in" PMD vector spectrum $\vec{\tau}_e(\omega) = \{\tau_{ex}(\omega), \tau_{ey}(\omega), \tau_{ez}(\omega)\}$, we set $\vec{\Gamma}_{3s}(\omega) = \vec{\tau}_e(\omega)$ and obtain

$$\frac{d\theta_1}{d\omega}(\omega) = \cot\theta_2(\omega)\left[\tau_{ey}(\omega)\cos\theta_1(\omega) - \tau_{ez}(\omega)\sin\theta_1(\omega)\right] + \tau_{ex}(\omega) \tag{9.4a}$$

$$\frac{d\theta_2}{d\omega}(\omega) = \tau_{ey}(\omega)\sin\theta_1(\omega) + \tau_{ez}(\omega)\cos\theta_1(\omega) \tag{9.4b}$$

$$\frac{d\theta_3}{d\omega}(\omega) = \csc\theta_2(\omega)\left[\tau_{ez}(\omega)\sin\theta_1(\omega) - \tau_{ey}(\omega)\cos\theta_1(\omega)\right] \tag{9.4c}$$

Note that this "dial-in" PMD vector spectrum $\vec{\tau}_e(\omega)$ is for the input plane. The synthesis algorithm for the required rotation angles of the three stages is similar to that in Chapter 6. It is as followed: At an initial frequency, $\omega_{initial}$, we arbitrarily fix the rotation angles of Stage 1, 2 and 3 to be 0, $\pi/2$ and 0 respectively. These $\theta_1(\omega_{initial})$, $\theta_2(\omega_{initial})$ and $\theta_3(\omega_{initial})$ serve as the starting points for the algorithm.

For subsequent frequencies, we find the rotation angles in a step-wise manner:

$$\theta_i (\omega + \Delta\omega) \approx \theta_i (\omega) + \frac{d\theta_i}{d\omega} (\omega) \Delta\omega \tag{9.5}$$

for $i = 1, 2$ and 3 where the $\frac{d\theta_i}{d\omega}$ are given by equation (9.4). In this way, we successively synthesize the required profiles of the rotation angles of the first three stages to generate the desired PMD vector spectra $\vec{\tau}_e (\omega)$ within a certain band of interest.

As described in Chapter 6, there are at least three practical implementations of the proposed 4-stage DBPMD emulator: 1) using a spatial light modulator, 2) using a deformable mirror and 3) using All-Pass Filters (APFs) integrated on a planar lightwave circuit as shown in Figure 9-1b. A broadband spectral phase profile may be achieved by cascading multiple APFs with appropriately displaced resonant frequencies and appropriately adjusted Q's over a frequency range that is less than the free spectral range of any of the individual APF's. As in Chapter 6, we only concentrate on the implementation that based on APFs. The optimum parameters for the APFs are found using the fitting algorithm described in Chapter 6.

9.3 Simulations and Discussions

To test the DBPMD emulator, we randomly simulated fibers by cascading 30 randomly oriented birefringence sections. The birefringence of these sections is Gaussian distributed with a mean value of 0.86 ps and with a standard deviation of 20 % of this mean value. This corresponds to a mean differential group delay of 4.35 ps. The concatenated PMD vectors of this simulated fiber are computed over a frequency range of ±230GHz about the carrier's optical frequency f_o with a step-size Δf=2.54 GHz. The PMD vectors are transformed to the input plane. This spectrum serves as the "dial-in" PMD vector spectrum for the DBPMD emulator. Based on this spectrum, we computed the required rotation angles $\theta_1(\omega)$, $\theta_2(\omega)$ and $\theta_3(\omega)$ using the synthesis algorithm (i.e. equation (9.4) and equation (9.5)). Figure 9-2 shows the rotation angles required for a simulated fiber randomly chosen from the ensemble. The solid

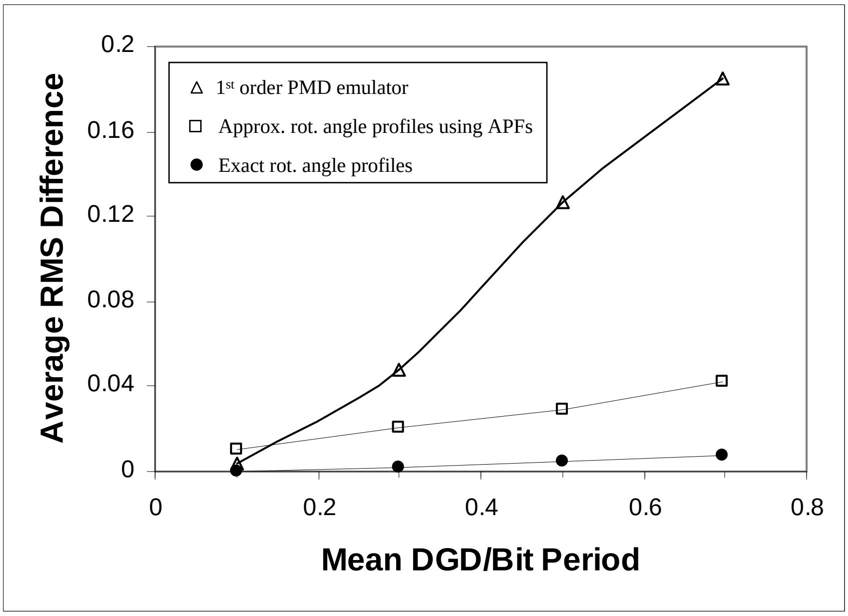

Figure 9-4: Average rms difference of DBPMD emulator's output signal and that of the simulated fiber taken over an ensemble of 1000 randomly chosen fiber states as a function of the mean DGD.

line curves are the rotation angles computed using the synthesis algorithm while the curves of crosses are the rotation angles approximated by the APFs. The number of APFs used are $N_1 = N_2 = N_3 = 3$. All APFs have the same FSR of 500 GHz. It is worthwhile to note that the frequency band of interest corresponds to slightly less than one FSR of the filters. In the synthesis algorithm, we restrict the value of $\frac{d\theta_i}{d\omega}$ to a maximum value of 100 ps to avoid the singularity when θ_2 approaches 0, as can be seen in equation (9.4). This restriction is determined from our simulations to have little impact on the fidelity of the emulation.

If the emulator were built experimentally, a reasonable way to check its fidelity would be to measure its PMD spectrum and compare that with the "dial-in" spectrum. However, since the work presented here is still only theoretical, the PMD produced by our emulator can only be computed. To calculate the emulator's PMD, we can use the inverse of the same PMD concatenation rule (equations (9.3)) that we used to synthesize the required rotation angle of the stages in our emulator. If the fitting is perfect, it is obvious that the emulator will reproduce the same PMD spectrum. Such comparison of the PMD spectrum is therefore not convincing, especially since the way we apply the PMD concatenation rule to the stages of flexible frequency-dependent polarization rotation itself needs verification. So, instead, we investigate the performance of the DBPMD emulator by generating an input train of 160 Gbit/s RZ pseudo-random bit sequence (2^6-1) of Gaussian pulses of 2.5 ps (FHWM) pulse-width and sending it through the simulated fiber and also through the DBPMD emulator using the same input SOP. We then compare the PMD-induced signal degradation of the two cases. The difference of the two temporal output signals is used to gauge the fidelity of the DBPMD emulator. This is a reasonable way of checking fidelity since the signal degradation is ultimately the main concern in PMD emulation.

For the same randomly chosen fiber used in Figure 9-2, we show the output signals of this particular fiber versus that of the DBPMD emulator. Both cases have the same input SOP. They are presented in Figure 9-3. The solid line curve is for the simulated fiber of 30 sections while the curve of filled circles is for the DBPMD emulator which uses $N_1 = N_2 = N_3 = 3$ AFPs to approximate the rotation angles calculated by the synthesis algorithm. For reference, the input signal is shown as the dashed curve. The two output signals match closely, thereby illustrating that the DBPMD emulator is capable of approximating an arbitrary PMD spectrum. Good agreements are also observed for other fiber realizations in our simulations. To obtain a quantitative measure of the match, we compute the root mean square (rms) difference of the two output signals for the whole (2^6-1) bit sequences. If the match is perfect, this rms difference should be zero. Figure 9-4 shows the average rms difference of the DBPMD emulator's output signal with that of the simulated fiber taken over an ensemble of 1000 randomly chosen fiber states. It is presented as a function of the mean DGD (normalized to the bit period) of the ensemble. We use a true first-order PMD emulator as a benchmark. For every random state of the simulated fiber, this first-order PMD emulator is set to produce the PMD vector at the carrier frequency f_o. The curve of unfilled triangles is for the first-order PMD emulator. As expected, this first-order PMD emulator performs well when the mean DGD of the ensemble is less than ~ 15 % of the bit period, but its performance degrades significantly as the mean DGD increases. The curve of filled circles is for the DBPMD emulator using the exact rotation angles profiles of $\theta_1(\omega)$, $\theta_2(\omega)$ and $\theta_3(\omega)$ calculated from the synthesis algorithm. The match is nearly perfect even for large mean DGD value. While the PMD concatenation rule is commonly used for cascading birefringent elements, the near-perfect match shows that it is equally valid for our concatenation of flexible frequency-dependent polarization rotation stages. This result not only verifies our synthesis algorithm of the rotation angles, it also confirms that the restriction on the maximum value of $\frac{d\theta_i}{d\omega}$ in the algorithm has little impact on its performance. The curve of unfilled squares is for the DBPMD emulator which employs $N_1 = N_2 = N_3 = 3$ APFs to approximate the rotation angle profiles calculated by the synthesis algorithm. The reasonably good emulation shows that the rotation angle profiles generated by the synthesis algorithm are feasible and can be approximated using a practical number of APFs even at large mean DGD value. It is also worthwhile to mention that the total rotation angle accumulated by a single APF is fixed at 2π over a frequency range of FSR. Thus, if the fluctuation rate of the PMD spectrum is too large for a given number of APFs to handle, one has to either increase the number of APFs or decrease the frequency range of fitting. This is the fundamental trade-off between the group delay and the bandwidth of APFs [123].

In conclusion, we have presented the architecture of a deterministic broadband PMD emulator based on a four-stage architecture. By numerical simulations, we demonstrated good fidelity of this DBPMD emulator in approximating arbitrary spectrum of PMD vectors over a wide frequency band of interest.

Chapter 10

Deterministic Broadband PDL Compensator

10.1 Background

Until now, for the sake of simplicity, we have assumed negligible Polarization Dependent Loss (PDL) present in the fiber. However, the deployment of optical amplifiers in lightwave systems has significantly increased the number and variety of optical components distributed along the link. As a result, small polarization effects, such as polarization dependent loss (PDL) [21, 20, 22, 23, 36], associated with the individual components may accumulate to produce noticeable performance degradation. These optical components include optical isolators, add/drop filters, switches, WDM multiplier, and couplers, which could have PDL up to 0.3 dB. The presence of non-negligible PDL induces the signals to be attenuated in a way that differs from that of the unpolarized noise, resulting in OSNR fluctuations at the end of the link. This leads to a potential system degradation effect. This degradation is aggravated when low-frequency polarization scrambling ($\sim$ 20 kHz) is used at the transmitter end [35, 102, 101, 100] . Polarization scrambling of the input State-Of-Polarization (SOP) may be applied for various reasons: to suppress the polarization-hole burning in erbium-doped fiber amplifiers [101, 100], and to facilitate the real-time monitoring of PMD in feed-forward PMD compensation schemes [2, 103, 104, 4]. In terms of

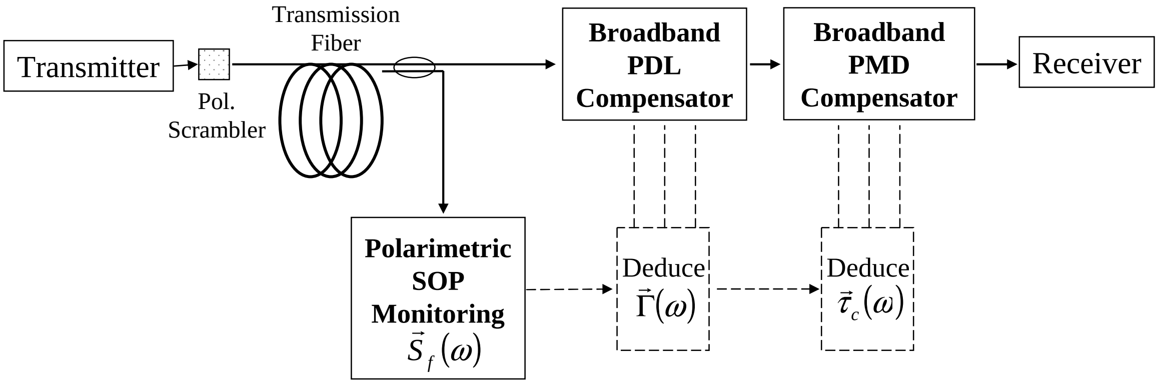

Figure 10-1: Schematic of the feed-forward compensation scheme for both PDL and PMD

real-time monitoring of PMD, the presence of PDL also has its deleterious effects. It causes the principal states of polarization (PSP) to become complex vectors in Stokes space. As a result, the PSPs are no longer orthogonal to one another and no longer represent the fastest and slowest propagating polarization states [20]. This affects the accuracy of the PMD characterization and thus compromises the effectiveness of the feed-forward PMD compensation.

In addition, the system penalty due to the coexistence of PMD and PDL is found to be higher than the summation of the PMD-only penalty and the PDL-only penalty [21, 36]. The presence of PDL may also discount the performance of some PMD compensators discussed in [99]. Therefore, in cases where PDL becomes non-negligible, a compensation scheme for PDL may be desired. Although the PDL of an individual component is relatively constant in time and frequency, when they interact with polarization mode dispersion (PMD) present in the fiber, the global PDL becomes frequency-dependent and time-varying on the same time-scale as PMD. This makes the compensation of both PMD and PDL [20, 22] particularly challenging. The physics of the mutual interaction of PMD and PDL in the fiber is complex as evidenced in Reference [20]. Fortunately, the polar decomposition theorem of a complex matrix provides a simple way to separate the effects of PMD and PDL [137, 21], making it feasible to perform lumped compensation of the global PDL and PMD at the receiver's end. Based on this theorem, we propose in this chapter a module

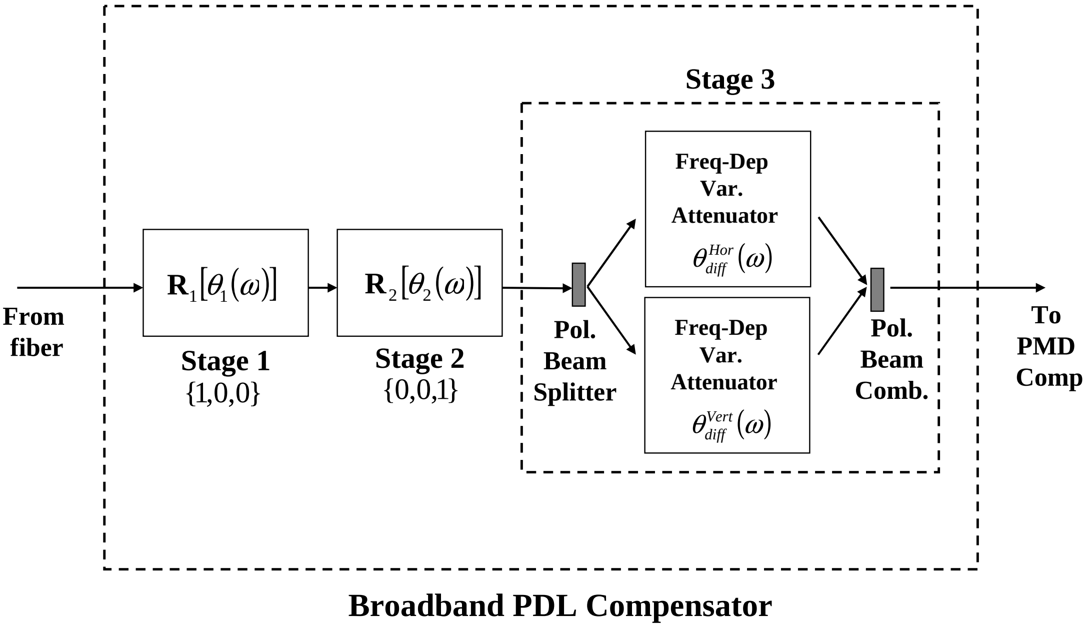

Figure 10-2: Schematic of the broadband PDL compensation module

that can compensate PDL for a broadband frequency range. We then show that by performing appropriate transformations on the monitored polarimetric data, we can determine the composite PMD of the fiber and the PDL compensator that is needed for the subsequent lumped PMD compensation described in Chapter 6.

Figure 10-1 shows the schematic of the overall feed-forward compensation scheme for both PDL and PMD. We employ polarization scrambling at the transmitter's end for characterizing the feed-forward information. A portion of the optical signal is tapped at the fiber output for real-time spectrally resolved polarimetric SOP monitoring [105, 106, 107, 4] as described in Chapter 3. Reference [108] reported such a spectrally resolved polarimeter using dispersive elements together with detector arrays. From these polarimetric measurements, we know the maximum and minimum attenuation and its associated polarization states. Thus we can characterize the PDL of each frequency component. Yan et al. demonstrated the feasibility of this real-time PDL monitoring technique in Reference [35]. Based on this information, we compensate the global PDL using the broadband PDL compensation module shown in Figure 10-2. This module consists of three stages. Stage 1 and 2 comprise the frequency-dependent polarization controller that aligns all the different PDL vectors into the

$\{1,0,0\}$ direction in Stokes space. Stage 3 involves polarization beam splitting, different frequency-dependent variable attenuation for each polarization, and subsequent polarization beam combining. This stage eliminates both the PDL magnitude and the frequency dependence in the isotropic attenuation. Using the Poincaré sphere representation, we illustrate in Figure 10-3 the motion of the PDL vectors of different frequencies after each stage of compensation. By applying the known transformation of each stage to the monitored polarimetric data, we then use the transformed SOP to deduce the composite PMD as a function of frequency by the method given in Chapter 3. The composite PMD spectrum serves as the input parameter for subsequent broadband PMD compensation as described in Chapter 6. It is worthwhile to note that in this compensation scheme, the PDL compensation utilizes exactly the same polarimetric data required in the case of PMD compensation as described in Chapter 6 [10]. Thus no additional monitoring is required. Moreover, all real-time polarimetric monitoring is carried out solely at the fiber's output without any knowledge of the input SOP.

The organization of the chapter is as followed: In Section 10.2, we present the theory of PDL compensation both in Jones space and Stokes space. Using the Stokes space representation, we synthesize the required rotation angle profiles of the frequency- dependent polarization rotators, Stage 1 and Stage 2, and the required transmission profiles of the frequency-dependent variable attenuators in Stage 3 once the information on the PDL is gathered. In Section 10.3, we verify this synthesis algorithm by simulating the PDL as a function of frequency before and after compensation. And we also verify our method to deduce the composite PMD of the fiber and the PDL compensator by simulating the PMD-induced signal distortion. In Section 10.4, we discuss the various practical implementations of the PDL compensator using a) a deformable mirror [120], b) a spatial phase modulator [119] or c) an All-Pass Filter (APF) [121, 122, 123]. We concentrate on the integrated optics approach of using APFs and show that the computed phase difference profiles using the synthesis algorithm are practical, and can be approximated using APFs.

10.2 Synthesis Algorithm

Without PDL, the transmission matrix of the fiber is always unitary. However, when the fiber PMD is intertwined with PDL elements, the transmission matrix loses its unitary property. Nevertheless, by the polar decomposition theorem [137], we can always decompose a complex 2 by 2 matrix $\mathbf{T}(\omega)$ into

$$\mathbf{T}(\omega) = \mathbf{A}(\omega)\mathbf{U}(\omega) \tag{10.1}$$

where $\mathbf{A}(\omega)$ is a positive definite Hermitian (self-adjoint) matrix (i.e. $\mathbf{A}(\omega) = \mathbf{A}^{\dagger}(\omega)$) and $\mathbf{U}(\omega)$ is a unitary matrix (i.e. $\mathbf{U}(\omega)\mathbf{U}^{\dagger}(\omega) = 1$). $\mathbf{A}(\omega)$ represents the effective PDL while $\mathbf{U}(\omega)$ represents the effective PMD. $\mathbf{U}(\omega)$ is not equal to the concatenation of all the PMD elements nor is $\mathbf{A}(\omega)$ equal to the concatenation of the PDL elements. In terms of compensation, this is an important result since it indicates the feasibility of lumped compensation of the global PDL followed by a lumped compensation of the global PMD all carried out at the receiver's end. Since $\mathbf{A}(\omega)$ is a hermitian matrix, we can always diagonalize it to

$$\mathbf{A}(\omega) = \mathbf{P}\left(\omega\right)\mathbf{D}\left(\omega\right)\mathbf{P}^{\dagger}\left(\omega\right) \tag{10.2}$$

where $\mathbf{D}\left(\omega\right)$ is a diagonal matrix with diagonal elements given by the eigenvalues (i.e. $\alpha_{\max}\left(\omega\right)$ and $\alpha_{\min}\left(\omega\right)$) of $\mathbf{A}(\omega)$, while $\mathbf{P}(\omega)$ is an unitary matrix whose columns are formed by the corresponding eigen-axes of $\mathbf{A}(\omega)$. $\mathbf{A}(\omega)$ is always invertible, except for perfect polarizer, which is not considered here. It is also easy to show that $\mathbf{A}^{-1}(\omega)$ has the same eigen-axes as $\mathbf{A}(\omega)$ and its eigen-values are the reciprocals of the eigenvalues of $\mathbf{A}(\omega)$. To verify that all the PDL information is embedded in the matrix $\mathbf{A}(\omega)$, we compute

$$\langle s_{in} \mid s_{in}\rangle = \langle s_{out}|\left(\mathbf{T}\mathbf{T}^{\dagger}\right)^{-1}|s_{out}\rangle = \langle s_{out}|\left(\mathbf{A}^{2}\right)^{-1}|s_{out}\rangle \tag{10.3}$$

where $|s_{in}\rangle$ and $|s_{out}\rangle$ are the 2-D complex Jones vectors in bra-ket notation for the input and output of the fiber respectively. From equation (10.3), the eigen-axes of matrix $\mathbf{A}(\omega)$ correspond to the two orthogonal output polarization states that have maximum and minimum transmission. Therefore these eigen-axes correspond to the PDL axes at the output. Moreover, the square of the eigenvalues of $\mathbf{A}(\omega)$ (i.e. $\alpha_{\max}^2(\omega)$ and $\alpha_{\min}^2(\omega)$) correspond to the maximum and minimum intensity transmission of the fiber. Thus the PDL value in dB is

$$PDL(dB) = 10Log_{10}\left(\frac{\alpha_{\max}(\omega)}{\alpha_{\min}(\omega)}\right)^2 \tag{10.4}$$

The frequency dependence of matrix $\mathbf{A}(\omega)$ results in the PDL axes and its magnitude changing with frequency. To be consistent with previous literature [20, 21], we define the PDL vector $\vec{\Gamma}(\omega)$ as parallel to the least-attenuated polarization state on the Poincaré sphere and of magnitude defined by

$$\left|\vec{\Gamma}(\omega)\right| = \frac{\alpha_{\max}^2 - \alpha_{\min}^2}{\alpha_{\max}^2 + \alpha_{\min}^2} \tag{10.5}$$

Moreover, we also defined the transmission coefficient for depolarized light as

$$T_{depol} = \frac{\alpha_{\max}^2 + \alpha_{\min}^2}{2} \tag{10.6}$$

Since all PDL properties of the system $\mathbf{T}(\omega)$ are given by $\mathbf{A}(\omega)$alone, if we are able to monitor the global PDL at the output, we can determine the matrix $\mathbf{A}(\omega)$ regardless of the PMD of the system. Yan et al. have demonstrated such a real-time monitoring scheme for PDL [35]. Using spectrally resolved polarimetric measurements [105, 106, 107, 4], one can extend the monitoring spectrally to obtain the complete matrix $\mathbf{A}(\omega)$ and its frequency dependence. With this information gathered, we can perform lumped PDL compensation at the output by applying the unitary transformation $\mathbf{P}^\dagger(\omega)$ followed by the inverse of $\mathbf{D}(\omega)$. From equation (10.1) and (10.2), we get

$$\mathbf{D}^{-1}(\omega)\,\mathbf{P}^\dagger(\omega)\,\mathbf{T}(\omega) = \mathbf{P}^\dagger(\omega)\,\mathbf{U}(\omega) \tag{10.7}$$

We define $\mathbf{V}(\omega) \equiv \mathbf{P}^\dagger(\omega)\,\mathbf{U}(\omega)$ as the resultant transmission matrix after the lumped PDL compensator. Since $\mathbf{U}(\omega)$ and $\mathbf{P}^\dagger(\omega)$ are both unitary, $\mathbf{V}(\omega)$ is also unitary; and

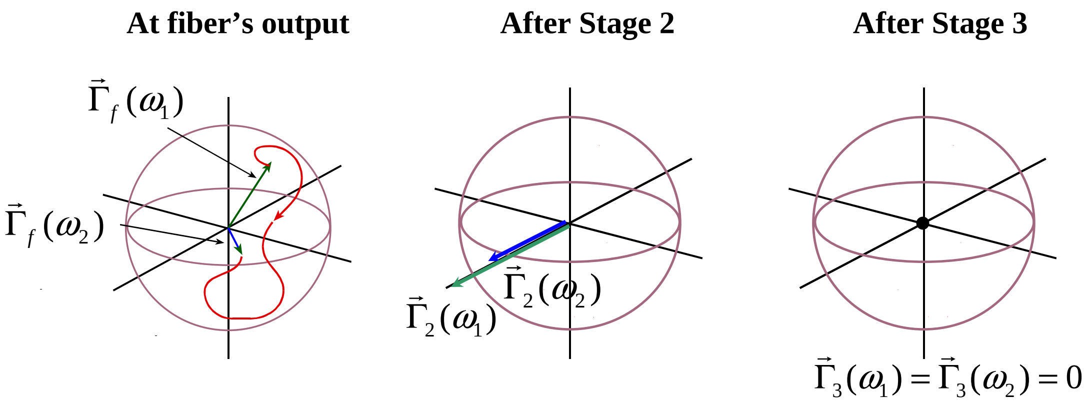

Figure 10-3: The motion of PDL vectors of different frequency after each stage of compensation in Poincaré sphere representation

it is related to the composite PMD $\vec{\tau}_c(\omega)$ of the fiber system and the PDL compensator (at the plane just after the PDL compensator) by $\vec{\tau}_c(\omega) = j\,(d\mathbf{V}/d\omega)\,\mathbf{V}^\dagger$.

In Stokes space representation, one obtains an equivalent but more intuitive picture of the transformations carried out by the lumped PDL compensator. This representation is particularly useful since all the real-time polarimetric monitoring information is gathered using this representation. A unitary transformation in Jones space corresponds to a rotation in Stokes space [17]. The matrix $\mathbf{P}^\dagger(\omega)$ applied by the PDL compensator is a unitary transformation that maps the eigen-axes of matrix $\mathbf{A}(\omega)$ into the horizontal and vertical polarization axes in physical space. Since the eigen-axes of $\mathbf{A}(\omega)$ are the PDL axes at the output and since $\mathbf{P}^\dagger(\omega)$ is frequency-dependent, in Stokes space representation, $\mathbf{P}^\dagger(\omega)$ corresponds to a frequency-dependent polarization controller that rotates the output PDL axes of different frequency components to align with the {1,0,0} direction in Stokes space. To build this frequency-dependent polarization controller, we use two stages: Stage 1 and Stage 2 in Figure 10-2. Stage 1 is a rotation about {1,0,0} axis with frequency-dependent rotation angle $\theta_1(\omega)$ while Stage 2 is a rotation about {0,0,1} with frequency-dependent rotation angle $\theta_2(\omega)$. Stage 1 rotates the different output PDL axes onto the equatorial plane while Stage 2 subsequently rotates them into {1,0,0} direction. In Stokes space, the rotation matrix of Stage 1 is

$$\mathbf{R}_1(\omega) = \begin{pmatrix} 1 & 0 & 0 \\ 0 & \cos\theta_1(\omega) & -\sin\theta_1(\omega) \\ 0 & \sin\theta_1(\omega) & \cos\theta_1(\omega) \end{pmatrix} \tag{10.8}$$

and the rotation matrix of Stage 2 is

$$\mathbf{R}_2(\omega) = \begin{pmatrix} \cos\theta_2(\omega) & -\sin\theta_2(\omega) & 0 \\ \sin\theta_2(\omega) & \cos\theta_2(\omega) & 0 \\ 0 & 0 & 1 \end{pmatrix} \tag{10.9}$$

Through the real-time monitoring, we assume we have the knowledge of the spectrum of the fiber's output PDL vector $\vec{\Gamma}(\omega) = \{\Gamma_x(\omega), \Gamma_y(\omega), \Gamma_z(\omega)\}$. To synthesize the appropriate rotation angle profiles to align the PDL vectors, $\vec{\Gamma}(\omega)$ of all frequencies with the {1,0,0} direction, we need,

$$\mathbf{R}_2(\omega)\mathbf{R}_1(\omega)\vec{\Gamma}(\omega) = \left|\vec{\Gamma}(\omega)\right| \begin{pmatrix} 1 \\ 0 \\ 0 \end{pmatrix} \tag{10.10}$$

Solving equation (10.10) yields the required rotation angles

$$\theta_1(\omega) = \cos^{-1}\left(\frac{\Gamma_y(\omega)}{\sqrt{\Gamma_y^2(\omega) + \Gamma_z^2(\omega)}}\right) \quad \text{for } \Gamma_{\mathrm{z}}(\omega) \leqslant 0 \tag{10.11a}$$

$$= \pi + \cos^{-1}\left(\frac{-\Gamma_y(\omega)}{\sqrt{\Gamma_y^2(\omega) + \Gamma_z^2(\omega)}}\right) \quad \text{for } \Gamma_{\mathrm{z}}(\omega) > 0 \tag{10.11b}$$

and

$$\theta_2(\omega) = \pi + \cos^{-1}\left(\frac{-\Gamma_x(\omega)}{\left|\vec{\Gamma}(\omega)\right|}\right) \tag{10.12}$$

After Stage 2, the linear horizontal polarization becomes the least-attenuated polarization state while the linear vertical polarization becomes the most-attenuated polarization state for all frequencies. Note that we have assumed that the PDL com-

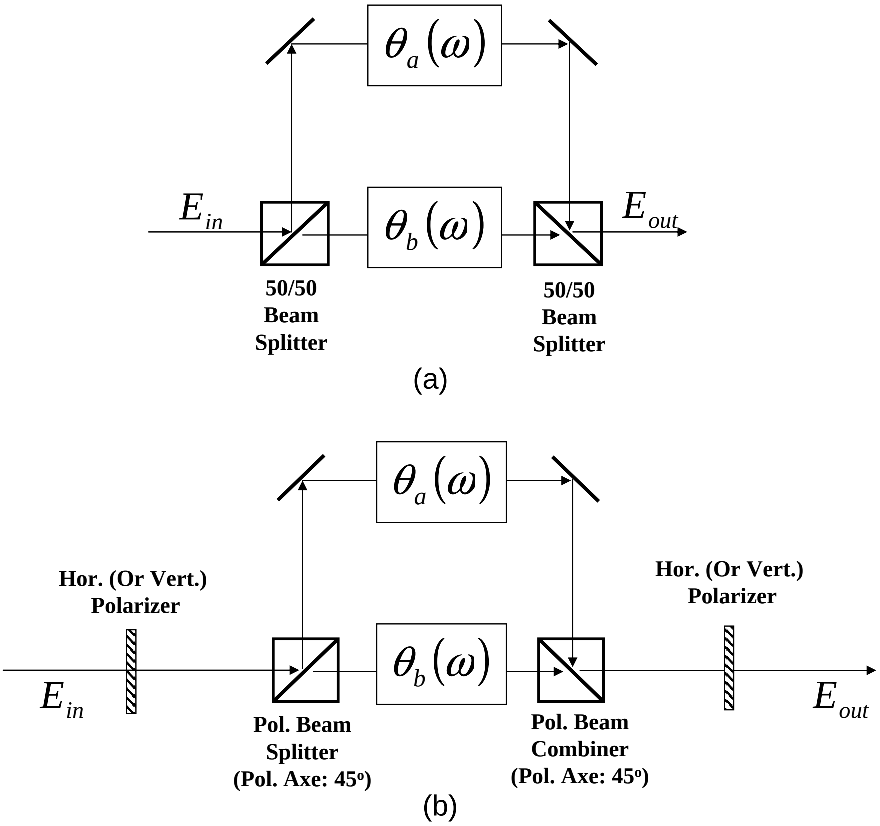

Figure 10-4: Two possible configurations of fequency-dependent variable attenuation: (a) A Mach-Zehnder interferometer with programmable frequency-dependent phases on both arms (b) A frequency-dependent polarization rotation about {0,1,0} sandwiched between two perfect polarizers oriented in the {1,0,0} (or {-1,0,0}) direction in Stokes space.

pensator produces small PDL compared to that of fiber so that, after Stage 2, the orientation of $\vec{\Gamma}(\omega)$ may be changed but its magnitude is preserved. From the definitions (10.5) and (10.6), the horizontal polarization now has a maximum transmission of $T_{\max}(\omega) = T_{depol}(\omega)\left(1 + \left|\vec{\Gamma}(\omega)\right|\right)$ while the vertical polarization has a minimum transmission of $T_{\min}(\omega) = T_{depol}(\omega)\left(1 - \left|\vec{\Gamma}(\omega)\right|\right)$. The goal of Stage 3 is to make these transmissions independent of polarization and of frequency. Stage 3 consists of a polarization beam splitter to split the polarization into horizontal and vertical, and then introduce separate frequency-dependent variable attenuations to each polarization arm (see Figure 10-2) so that the transmissions for both polarizations become a constant value T_{const} for all frequencies within the range of interest. Unless a gain

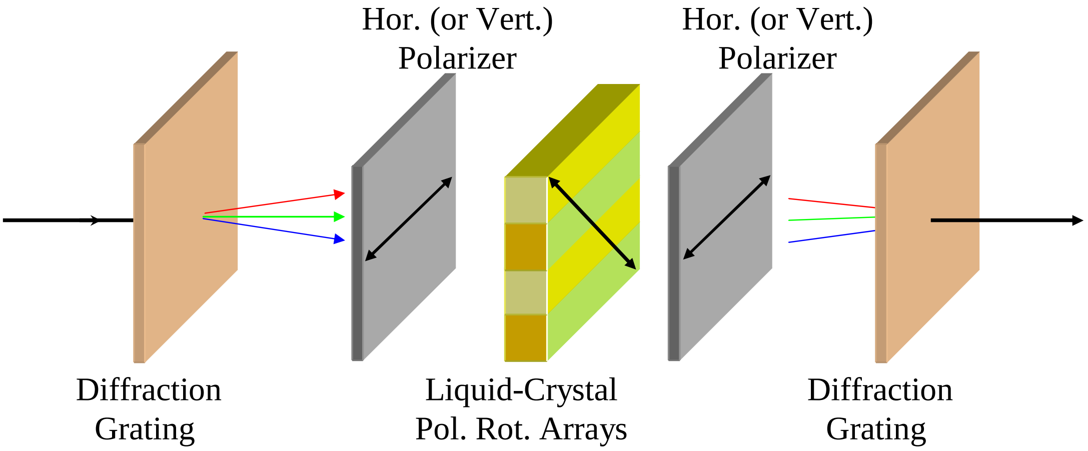

Figure 10-5: Light is spatially dispersed by grating onto a array of liquid-crystal polarization rotators sandwiched between two polarizers.

medium is used in a PDL compensator, the compensation introduces attenuation in order to compensate for PDL. Thus the value for T_{const} has to be appropriately chosen to account for the statistics of the PDL and, at the same time, not to introduce excessive loss to the system. Figure 10-4 shows two possible configurations to accomplish a frequency-dependent variable attenuation: (a) a Mach-Zehnder interferometer (MZI) with programmable frequency-dependent phases in both arms [138]; (b) a frequency-dependent polarization rotation about {0,1,0} sandwiched between two perfect polarizers oriented in the {1,0,0} (or {-1,0,0}) direction in Stokes space. In terms of transmission profiles, these two configurations are equivalent. Figure 10-5 depicts an example of configuration (b) using a spatial array of liquid-crystal polarization rotators with polarizers.

In the following, we consider only the MZI and calculate the required phase difference between its two arms for any given attenuation profile. The output field E_{out} of this 4-port MZI system is related to the input field E_{in} by

$$\frac{E_{out}}{E_{in}} = -ie^{-i\left(\frac{\theta_a+\theta_b}{2}\right)} \sin\left(\frac{\theta_a-\theta_b}{2}\right) \tag{10.13}$$

Thus the "transmission" of this MZI is given by

$$\left|\frac{E_{out}}{E_{in}}\right|^2(\omega) = \sin^2\left(\frac{\theta_{diff}(\omega)}{2}\right) \tag{10.14}$$

where $\theta_{a,b}(\omega)$ are the phases of the two MZI arms and $\theta_{diff}(\omega)$ is their phase difference. Since the transmission of the MZI depends only on the phase difference between the two arms, if we can program arbitrary profile of $\theta_{diff}(\omega)$ versus frequency, we can engineer the frequency-dependent attenuation profile of the MZI to eliminate PDL and the frequency dependence in $T_{depol}(\omega)$. The required phase difference profile for the MZI in the horizontal polarization branch is

$$\theta_{diff}^{Hor}(\omega) = 2\sin^{-1}\left(\sqrt{\frac{T_{const}}{T_{\max}(\omega)}}\right) \tag{10.15}$$

and for the MZI in the vertical polarization branch is

$$\theta_{diff}^{Vert}(\omega) = 2\sin^{-1}\left(\sqrt{\frac{T_{const}}{T_{\min}(\omega)}}\right) \tag{10.16}$$

With equations (10.11), (10.12), (10.15) and (10.16), we have now synthesized the required phase difference profiles of all the three stages to compensate for any PDL spectrum $\vec{\Gamma}(\omega)$ and also the frequency dependence in the isotropic attenuation given by $T_{depol}(\omega)$. After the PDL compensation, what remains to be compensated is the composite PMD spectrum $\vec{\tau}_c(\omega)$ of the fiber and the PDL compensator. To deduce the composite PMD spectrum $\vec{\tau}_c(\omega)$, we transform the Stokes vectors $\vec{S}_f(\omega) = \{S_0, S_1, S_2, S_3\}$ that we have monitored at the output of the fiber, by the known transformations of the PDL compensator

$$\vec{S}_c(\omega) = \mathbf{M}_3(\omega)\mathbf{M}_2(\omega)\mathbf{M}_1(\omega)\vec{S}_f(\omega) \tag{10.17}$$

where $\mathbf{M}_1(\omega)$ is the 4-by-4 Mueller matrix for the rotation transformation of Stage 1 given as

$$\mathbf{M}_1(\omega) = \begin{pmatrix} 1 & 0 & 0 & 0 \\ 0 & 1 & 0 & 0 \\ 0 & 0 & \cos\theta_1(\omega) & -\sin\theta_1(\omega) \\ 0 & 0 & \sin\theta_1(\omega) & \cos\theta_1(\omega) \end{pmatrix} \tag{10.18}$$

and $\mathbf{M}_2(\omega)$ is Mueller matrix for the rotation transformation of Stage 2 given as

$$\mathbf{M}_2(\omega) = \begin{pmatrix} 1 & 0 & 0 & 0 \\ 0 & \cos\theta_2(\omega) & -\sin\theta_2(\omega) & 0 \\ 0 & \sin\theta_2(\omega) & \cos\theta_2(\omega) & 0 \\ 0 & 0 & 0 & 1 \end{pmatrix} \tag{10.19}$$

and $\mathbf{M}_3(\omega)$ is Mueller matrix of Stage 3, which acts like a partial polarizer [45], given as

$$\mathbf{M}_3(\omega) = \frac{1}{2}\begin{pmatrix} K_H + K_V & K_H - K_V & 0 & 0 \\ K_H - K_V & K_H + K_V & 0 & 0 \\ 0 & 0 & 2\sqrt{K_H K_V} & 0 \\ 0 & 0 & 0 & 2\sqrt{K_H K_V} \end{pmatrix} \tag{10.20}$$

where $K_H = \sin^2\left(\theta_{diff}^{Hor}/2\right)$ and $K_V = \sin^2\left(\theta_{diff}^{Vert}/2\right)$. The transformed $\vec{S}_c(\omega)$ is then normalized onto the unit Poincaré sphere to give $\hat{s}_c(\omega)$. Once $\hat{s}_c(\omega)$ is known, the corresponding composite PMD $\vec{\tau}_c(\omega)$ can be deduced. In principle, the principal state of polarization (PSP) of the composite PMD at frequency ω_o can be obtained by the direction of the cross product of differential SOP vectors $(\hat{s}_c(\omega_o) - \hat{s}_c(\omega_o - \Delta\omega))$ and $(\hat{s}_c(\omega_o + \Delta\omega) - \hat{s}_c(\omega_o))$. The DGD at frequency ω_o can be deduced from the length of these differential SOP vectors. In practice, these changes in the differential SOP vectors with frequency may be too small for accurate estimation of $\vec{\tau}_c(\omega)$, especially in the presence of high-order PMD. To improve the estimation accuracy, random scrambling of the launched SOP is carried out at the transmitter end of the fiber [4]. Since the input polarization scrambling does not change the fiber's properties, it will not affect the PMD of the fiber, and therefore the composite PMD. On the

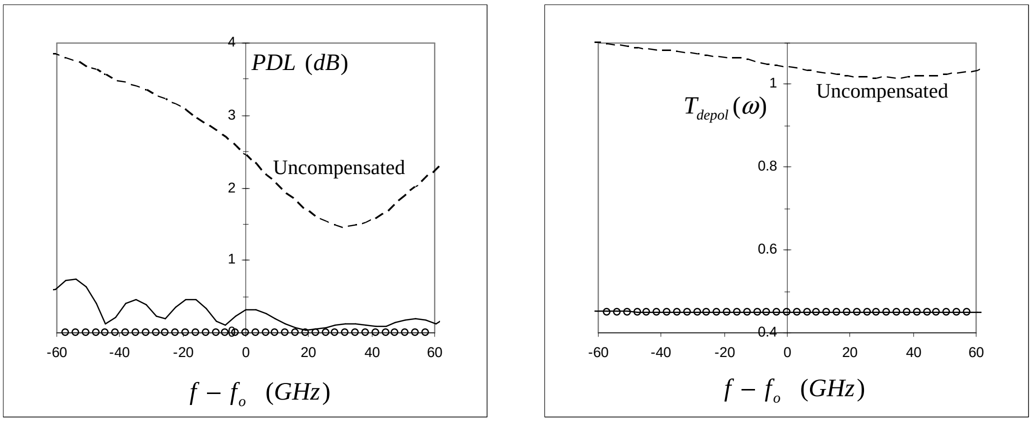

Figure 10-6: The spectrum of PDL and the transmission of depolarized light T_{depol} for a randomly generated fiber. f_o is the carrier's optical frequency. Dashed curve for before PDL compensation, curve of circles for after PDL compensation using exact phase difference profiles, solid curve for after PDL compensation using phase difference profiles approximated by APFs.

other hand, the trajectory of the transformed SOP changes to $\hat{s}_c{}'(\omega)$. For a given frequency, the trajectories of $\hat{s}_c(\omega)$ and $\hat{s}_c{}'(\omega)$ produce different arcs, however, both arcs possess a common axis. This common axis gives the composite PSP at that frequency, and can be found by the cross product of $(\hat{s}_c(\omega_o + \Delta\omega) - \hat{s}_c(\omega_o - \Delta\omega))$ and $(\hat{s}_c{}'(\omega_o + \Delta\omega) - \hat{s}_c{}'(\omega_o - \Delta\omega))$. Often more than two different scrambled input SOPs are used. By finding a unit vector that is normal to all the various differential SOP vectors, $(\hat{s}_c^j(\omega_o + \Delta\omega) - \hat{s}_c^j(\omega_o - \Delta\omega))$, one can determine their common axis (which is aligned to the PSP) with much better accuracy. The DGD estimation can also be improved by averaging the individual DGD values deduced from the various $(\hat{s}_c^j(\omega_o + \Delta\omega) - \hat{s}_c^j(\omega_o - \Delta\omega))$ [4].

10.3 Simulations to verify synthesis algorithm

To verify our synthesis algorithm for $\theta_1(\omega)$, $\theta_2(\omega)$, $\theta_{diff}^{Vert}(\omega)$, $\theta_{diff}^{Hor}(\omega)$, random fibers were generated with a mean DGD of 10 ps and a mean global PDL of 2.5 dB by cascading 20 segments. Each segment contains a randomly oriented birefringent element and a randomly oriented PDL element of 0.54 dB. The birefringence of these segments was Gaussian distributed with a mean value of 2.42 ps and standard deviation of 20%

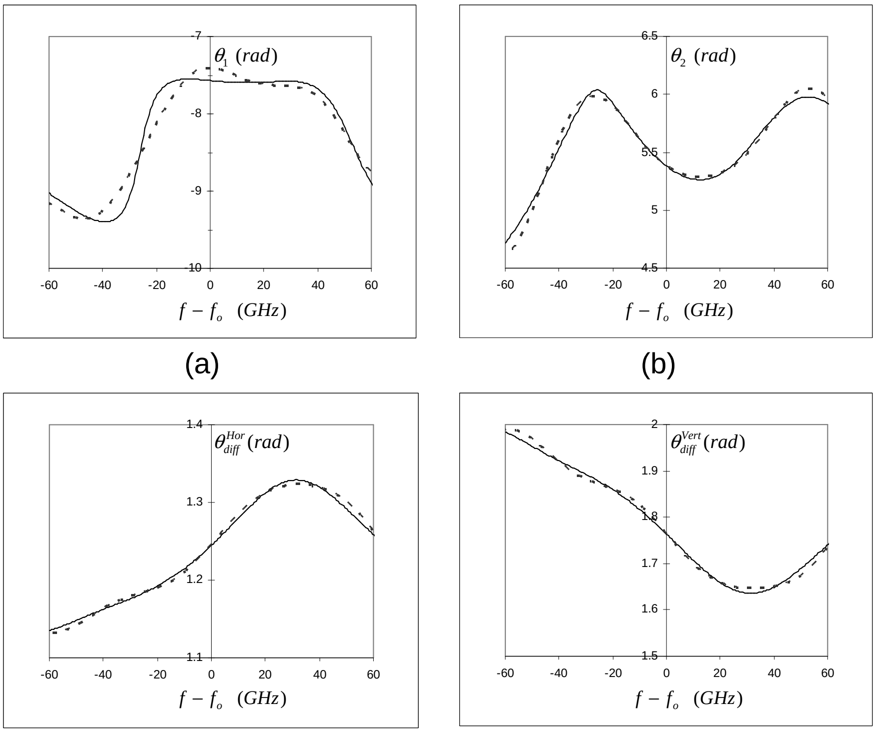

(a) (b)

(c) (d)

Figure 10-7: Required phase difference profiles for a randomly generated fiber: (a) $\theta_1(\omega)$ of Stage 1 (b)$\theta_2(\omega)$ of Stage 2, (c) $\theta_{diff}^{Hor}(\omega)$ of the horizontal polarization branch of Stage 3, (d) $\theta_{diff}^{Vert}(\omega)$ of the vertical polarization branch of Stage 3. Solid curves are exact phase difference profiles computed using the synthesis algorithm while dashed curves are profiles approximated using APFs.

of the mean. For each segment, we assume the transmission for the depolarized light is unity. We then sent input signals with randomly scrambled polarization through each randomly generated fiber and simulate the Stokes SOP $\vec{S}_f(\omega)$ at the output as a function of frequency with an optical frequency step-size of Δf =0.63 GHz. Following the Power Max-Min method, we determine the global PDL vector, $\vec{\Gamma}(\omega)$, and the transmission for depolarized light, $T_{depol}(\omega)$, as a function of frequency. Two hundred randomly scrambled input polarization states were used for each spectrum characterization. The frequency band of interest is ±60 GHz about the optical carrier frequency f_o. Based on this PDL vector spectrum, we synthesized the required $\theta_1(\omega)$, $\theta_2(\omega)$, $\theta_{diff}^{Vert}(\omega)$, $\theta_{diff}^{Hor}(\omega)$ using equations (10.11), (10.12), (10.15) and (10.16). For illustration purpose, the PDL spectrum of a randomly generated fiber, and its transmission of depolarized light $T_{depol}\left(\omega\right)$ are shown as dashed curves in Figure 10-6. The corresponding required phase difference profiles for this particular fiber are shown as solid curves in Figure 10-7a-d. Figure 10-7a is for $\theta_1(\omega)$ of Stage 1, Figure 10-7b is for $\theta_2(\omega)$ of Stage 2, and Fig 10-7c for $\theta_{diff}^{Hor}\left(\omega\right)$ of the horizontal polarization branch of Stage 3 and Fig 10-7d for $\theta_{diff}^{Vert}\left(\omega\right)$ of the vertical polarization branch of Stage 3. The value of T_{const} used in the Stage 3 of the compensator is 0.45. Using these phase difference profiles, we performed the lumped PDL compensation. We then determine the PDL spectrum and the transmission spectrum for depolarized light after compensation, using the same Power Max-Min method. Figure 10-6 shows that the PDL is clearly compensated and that the frequency dependence of depolarized light transmission is removed. Using these phase difference profiles, we also transformed Stokes vectors $\vec{S}_f\left(\omega\right)$ into $\vec{S}_c\left(\omega\right)$ to deduce the composite PMD of the fiber and the PDL compensator at the plane just after the PDL compensator. This information serves as the input parameters for subsequent broadband PMD compensator proposed in Chapter 6. To verify that the composite PMD spectrum is correctly deduced, we sent a gaussian pulse of 10 ps (FHWM) pulse-width through the same fiber used in Figure 10-6 and studied its signal distortion. The dashed curve in Figure 10-8 shows the output signal from the fiber. The optical signal after passing through both the PDL and PMD compensator is given by the solid curve. The Gaussian shape is restored almost perfectly except for the fact that the power of the pulse is reduced by T_{const}. To further confirm that PDL is compensated, we randomly scrambled the input polarization of this gaussian pulse, and observed that the power of the pulse is insensitive to the input polarization. To present this result, we overlap the output signals of 20 different input polarizations (each output signal is plotted in dots). Figure 10-9a shows the overlapped signals before compensation. As expected, due to the presence of PMD and PDL, there is no distinct pattern in the overlapped output signal. On the other hand, the overlapped signal after both PDL and PMD compensation in Figure 10-9b preserves a distinct Gaussian shape with a constant peak power, regardless of the input polarization. This showed that PDL is compensated and the information on the composite PMD spectrum is accurate for subsequent PMD compensation. To

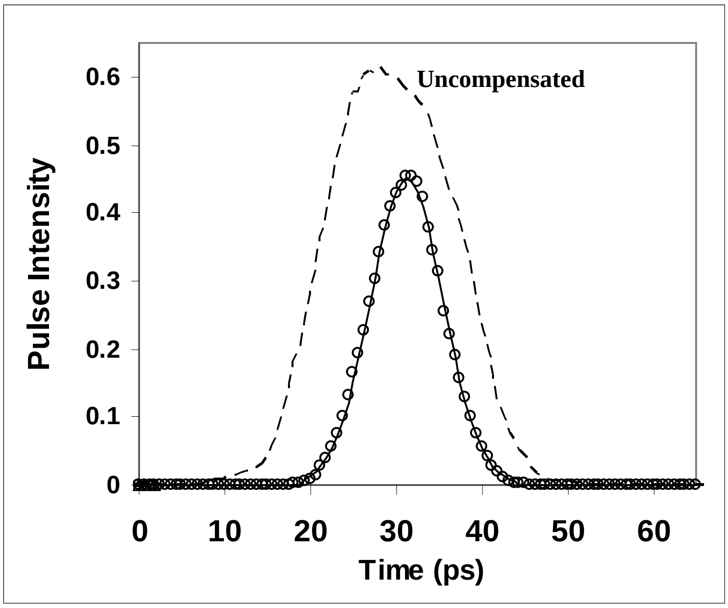

Figure 10-8: Output optical signal before and after PML+PMD compensation. Dashed curve is output from fiber. Solid curve is after compensation using the exact phase difference profiles while the curve of circles is based on approximated phase difference profiles using APFs. The number of APFs for the various stages of the PMD compensator is $N_1 = 15, N_2 = 10, N_3 = 15$.

show that the same result is applicable to arbitrary fibers, we repeated the same simulations for another 500 randomly generated fibers (with 5 different input polarizations for each fiber) and then overlapped the output signals in the same manner. Figure 10-10 confirms that the PDL is compensated and the composite PMD spectrum is determined accurately for all the 500 fibers. Figure 10-11 shows the mean PDL spectrum and its standard deviation for the 500 fibers ensemble before and after compensation.

10.4 Practical Implementations

As in Chapter 6, there are at least three physical implementations of the proposed 3-stage PDL compensator. The first two implementations can be adapted from the femtosecond pulse shaping schemes using a spatial light modulator [119] or using a deformable mirror [120]. With diffraction gratings, one can disperse the various fre-

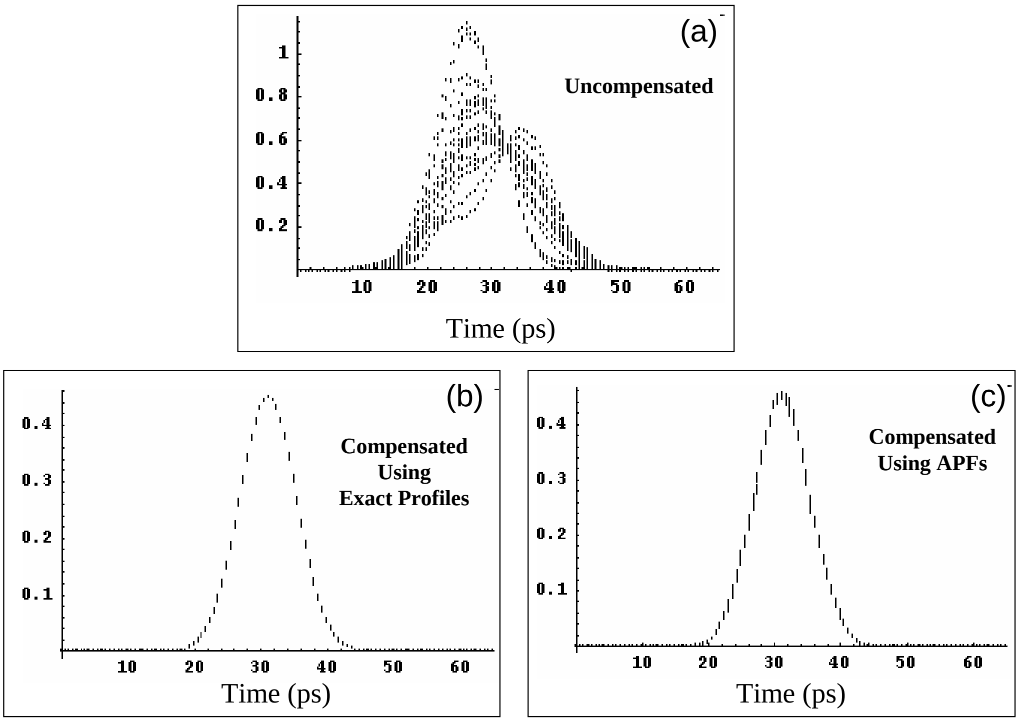

Figure 10-9: Overlapped signals of 20 different input polarizations launched into the randomly generated fiber. (a) for before compensation, (b) for after both PDL and PMD compensation using exact phase difference profiles, (c) for after both PDL and PMD compensation based on approximated phase difference profiles using APFs.

quency components spatially onto the spatial phase modulator (or deformable mirror) and program appropriate spectral phase to achieve the required phase difference profiles of $\theta_1(\omega)$, $\theta_2(\omega)$ and $\theta_{diff}^{Vert}(\omega)$ and $\theta_{diff}^{Hor}(\omega)$. The third promising implementation is based on All-Pass Filters (APFs) integrated on a planar lightwave circuit as shown in Figure 10-12. In this chapter, we focus only on this particular implementation since they can be compactly integrated onto a chip. In this scheme, the output signals from the fiber are split into two waveguides (waveguide 1 and waveguide 2) by a polarization beam splitter. The polarization in waveguide 2 is rotated by 90°. Stage 1 is comprised of a set of N_1 APFs for each of the waveguides to generate a phase response of $\Phi_{1H}(\omega)$ for waveguide 1 and $\Phi_{1V}(\omega)$ for waveguide 2. In Stokes space, transmission through Stage 1 corresponds to a rotation about {1,0,0} with rotation angle $(\Phi_{1V}(\omega) - \Phi_{1H}(\omega))$. Stage 2 is comprised of a 50/50 directional coupler with matched propagation constants, followed by another set of N_2 APFs for each of the

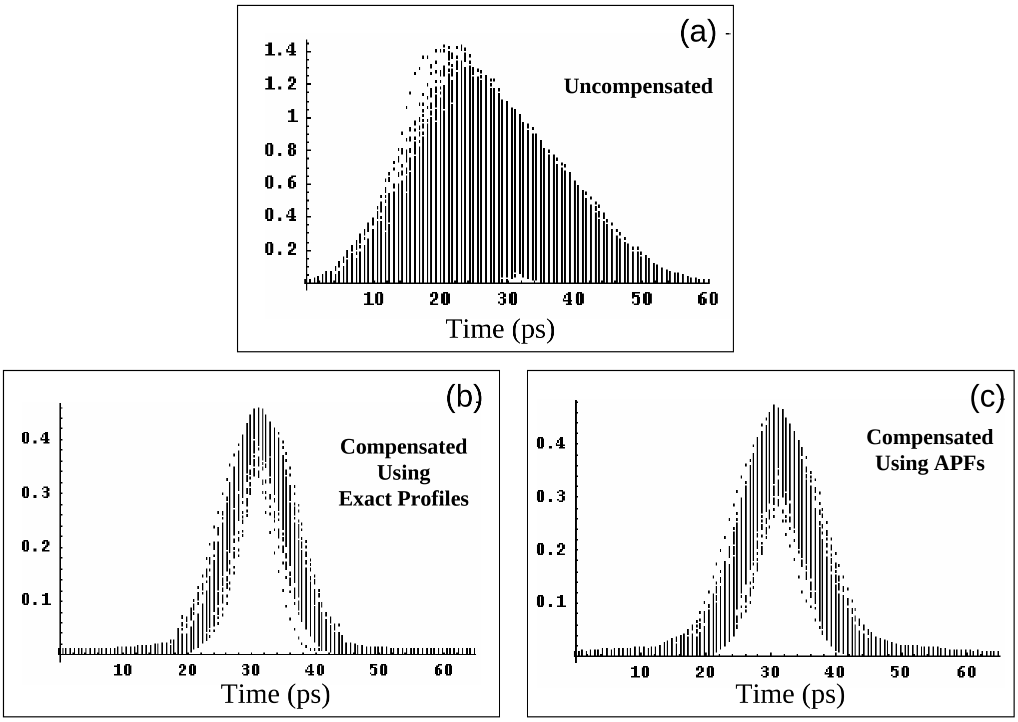

Figure 10-10: Overlapped signals of 2500 cases (500 random fibers with 5 random input polarizations per fiber): (a) for before compensation, (b) for after both PDL and PMD compensation using exact phase difference profiles, (c) for after both PDL and PMD compensation based on approximated phase difference profiles using APFs. The number of APFs for the various stages of the PMD compensator [16] is $N_1 = 15, N_2 = 10, N_3 = 15$.

waveguides, and then by another 50/50 directional coupler with matched propagation constants. For the same coupling constant, the length of the second 50/50 directional coupler is 3 times greater than that of the first 50/50 directional coupler. This set of APFs generates a phase response of $\Phi_{2H}(\omega)$ for waveguide 1 and $\Phi_{2V}(\omega)$ for waveguide 2. In Stokes space, the first 50/50 directional coupler gives a 90° rotation about {0,1,0}, the APF portion of Stage 2 is a rotation about {1,0,0} with rotation angle $(\Phi_{2V}(\omega) - \Phi_{2H}(\omega))$ and the second 50/50 directional coupler is designed to give a 270° rotation about {0,1,0}. Thus the combined transformation of Stage 2 is equivalent to a rotation about {0,0,1} with rotation angle of $(\Phi_{2V}(\omega) - \Phi_{2H}(\omega))$. Stage 3 consists of a Mach-Zehnder interferometer (MZI) on each of the waveguide. Each MZI has set of N_3 APFs in each of its arms. For the MZI on waveguide 1, the APFs generate phase response of $\Phi_{3a}^{Hor}(\omega)$ on one arm and $\Phi_{3b}^{Hor}(\omega)$ on the other. This

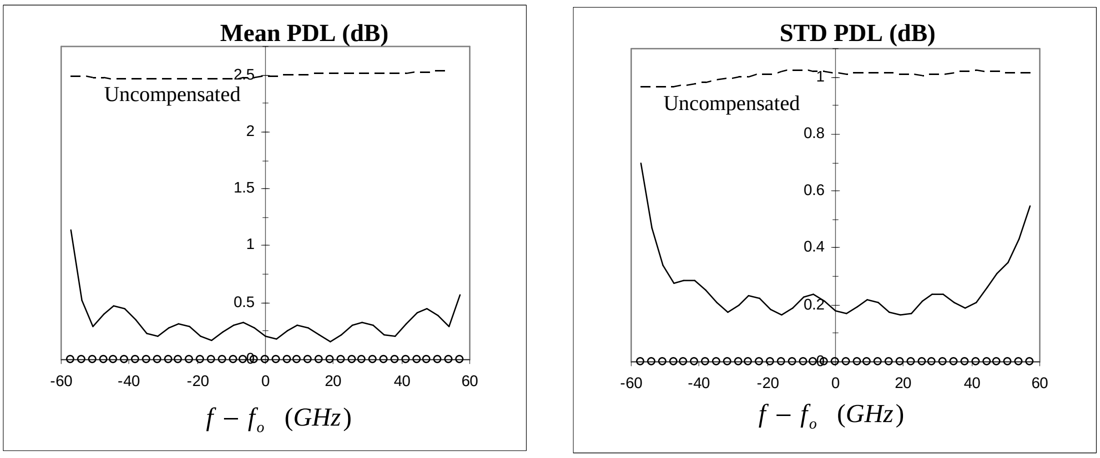

Figure 10-11: Mean and standard deviation of the PDL as a function of frequency for the 500 fibers ensemble. Dashed curve for before PDL compensation, curve of circles for after PDL compensation using exact phase difference profiles, solid curve for after PDL compensation using phase difference profiles approximated by APFs

gives a frequent-dependent attenuation of $\sin^2\left(\left(\Phi_{3a}^{Hor}(\omega) - \Phi_{3b}^{Hor}(\omega)\right)/2\right)$. Similarly, for the MZI on waveguide 2, its APFs generate a phase response of $\Phi_{3a}^{Vert}(\omega)$ on one arm and $\Phi_{3b}^{Vert}(\omega)$ on the other, and thus a frequency-dependent attenuation of $\sin^2\left(\left(\Phi_{3a}^{Vert}(\omega) - \Phi_{3b}^{Vert}(\omega)\right)/2\right)$. After Stage 3, the two polarizations are recombined into a single waveguide via a polarization rotator and a polarization beam combiner. To illustrate that the phase difference profiles calculated by our synthesis algorithm are feasible and can be approximated using APFs, we show the phase difference profiles produced by the APFs for the same randomly chosen fiber used in Figure 10-7. They are shown as dashed-line curves in Figure 10-7(a-d). The APF parameters used to approximate these phase differences are found by the fitting algorithm described in Chapter 6. The number of APFs used are $N_1 = N_2 = N_3 = 3$. All APFs have the same FSR of 150 GHz. It is worthwhile to note that the frequency band of interest corresponds to less than one FSR of the filters. Using these approximated phase difference profiles, the curves showing the respective performance of the APF compensation can also be found in the Figure 10-6-10-11. All these results show the feasibility of implementing the compensation scheme using APFs.

Until now, our main focus has been on the PDL compensation of a single channel.

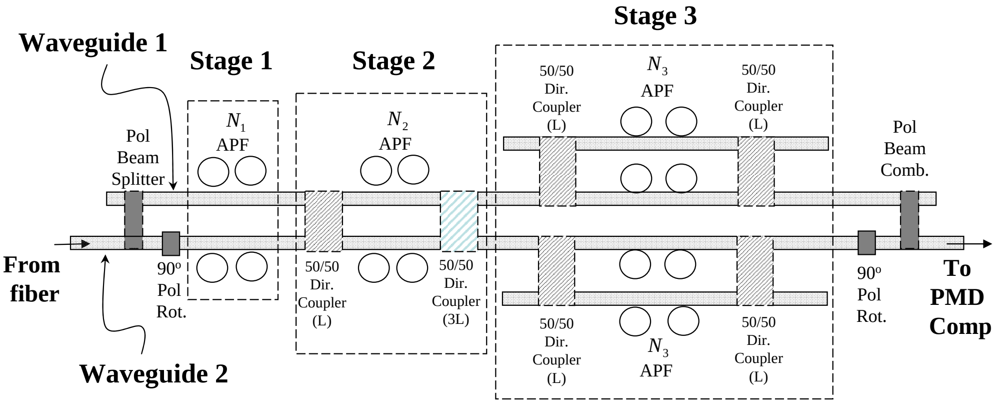

Figure 10-12: A possible implementation of broadband PDL compensator using All-Pass filters integrated on planar waveguides.

However, it should be apparent that the compensation can be extended to cover many channels simultaneously. The same compensation scheme and synthesis algorithms apply except that more APFs are needed and the FSR of the APFs has to be increased, in order to cover a broader spectral range. It is also worthwhile to mention that, by combining with the deterministic broadband PMD emulator presented in Chapter 9, this architecture can be used for deterministically controlled PDL+PMD emulation.

10.5 Conclusion

In this chapter, we have proposed a method for compensating PDL and PMD in a feed-forward scheme. By the polar decomposition theorem, we showed that lumped PDL followed by PMD compensation at the receiver's end is feasible. Our proposed PDL compensator consists of three stages: Stage 1 and 2 are the frequency-dependent polarization rotators that align all the different PDL vectors into the {1,0,0} direction in Stokes space. Stage 3 eliminates both the PDL magnitude and the frequency dependence in the isotropic attenuation by introducing different frequency-dependent variable attenuation to each polarization. For real-time monitoring, we use random polarization scrambling at the input end of the fiber and measure the SOP at the output of the fiber as a function of frequency. We then determine the PDL spectrum by finding the polarization states with the maximum and minimum attenuation. Using this monitored PDL spectrum, we synthesize the required phase difference profiles of the three stages of the PDL compensator using equations (10.11), (10.12), (10.15) and (10.16) to compensate for the PDL over a certain frequency range of interest. The resultant intensity transmission after passing through the PDL compensator is polarization- and frequency-insensitive. We then apply the known Mueller transformations of the PDL compensator to the same set of monitored SOP data to deduce the composite PMD as a function of frequency. This composite PMD spectrum provides the input parameters for the subsequent broadband PMD compensator described in Chapter 6. By numerical simulations, we verified the synthesis algorithm of the required phase difference profiles and the procedure to deduce the composite PMD spectrum. We also showed that these phase difference profiles are practical and can be approximated by APFs.

Chapter 11

Conclusion

In this thesis, we presented a deterministic approach to both PMD compensation and emulation. Despite the fact that most of the PMD compensation schemes, demonstrated in the literature, rely on feedback scheme, there is an emerging interest of compensating PMD in a deterministic manner, especially in the presence of the higher-order PMD. This is because adding control parameters in feedback scheme to enable higher-order PMD compensation increases the complexity of the feedback algorithm and also lowers its response time. As PMD can vary as fast as in a millisecond time scale, there are difficult tracking problems associated due to too many search parameters with too little feedback information. In terms of PMD emulation, a deterministic approach is attractive because it allows one to quickly evaluate a particular PMD compensator by investigating only the PMD states that are of interest, especially those in the tail of the PMD distribution.

A deterministic approach to PMD compensation means that the PMD parameters have to be first characterized, and then the compensator are set appropriately to compensate for the fiber PMD. In Chapter 3, we presented a real-time estimation technique to predict the first- and second- order PMD parameters. At the output end of the fiber, the signal is tapped and filtered. Three filters are used: a high-pass filter, a low-pass filter and a narrowband filter. The averaged SOP of the filtered signals are then measured using a polarimeter. We repeat the measurement for several different input SOP's using a polarization scrambler at the input end of the fiber. From these measurements, we deduce the first order PMD, and subsequently the second order PMD. Using Monte Carlo simulations, we have shown that this technique offers significant improvements over the previous ellipsoid method [2] in terms of measurement accuracy, lower required polarization scrambling rate and capability to estimate more PMD parameters. The search algorithm used is simple and requires little computation time, thus making the technique feasible for real-time PMD characterization. We also discussed how to extend the scheme for broadband monitoring of PMD vectors. We also demonstrated the accuracy of the characterization technique experimentally using well-calibrated first- and higher- order PMD sources.

In terms of building PMD compensator, we presented in Chapter 4 a variable DGD module which is useful for first-order PMD compensation. It is based on a novel way to concatenate four identical fixed DGD segments so that the resultant DGD is variable while no second order PMD is produced. In addition, the third order PMD generated is only half the value of the one produced by the conventional two fixed segments concatenation. The 4-segment module is based totally on tunable phase-plates and fixed DGD segments. By simulation, we analyzed the required accuracies of the tunable phase-plates used in this variable DGD module and illustrated that the 4-segment module has better performance in PMD compensation than the conventional two-segment concatenation, when there is frequency chirp presented in the system.

In Chapter 5, we described a procedure to exercise complete PMD compensation up to second order when the information of the first order PMD and second order PMD of a long haul communication cable are known. Moreover, we have solved analytically the required rotation matrices of the polarization rotators and the required DGD of a variable delay line in a 3-segments compensator. The approach here is necessary for a PMD compensation system that uses feed-forward correction. To allow for a hybrid feed-forward/feedback compensation scheme, where first-order PMD compensation is carried out in a feed-forward manner and feedback compensation is used for the second order PMD. We also presented a module that generates variable second order PMD without producing any first order PMD. It is based on four identical fixed DGD segments arranged in a symmetrical manner. Only one control parameter varies the magnitude of second order PMD. This module is useful to decouple the compensation of second- order PMD from first- order PMD.

In Chapter 6, we presented the architecture of an All-Frequency PMD compensator in a feed-forward compensation scheme. This scheme can handle the compensation of all orders of PMD. It is comprised of 4 stages. The first two stages give an equivalent frequency-dependent polarization rotation effect, the third stage provides the frequency dependent variable DGD while the last stage compensates for the isotropic dispersion created by the first three stages. In Stokes space formulation, we described the algorithm to find the required rotation angles of each stage using the PMD concatenation rules. This synthesis algorithm is verified by simulating the PMD-induced signal degradation before and after the compensation. We discussed three possible practical implementations of the AFPMD compensator but only concentrated on the integrated optics approach of using APFs. We also showed that the profiles of the rotation angles are practical and can be approximated using APFs. Again, through simulations, significant improvement of the signal quality is demonstrated using such 4-stage architecture based on APFs. To extend the architecture for broadband WDM compensation, the number of APFs involved can be as large as 50 per stage. Thus we presented a fast and efficient algorithm based on recursive equations to find the optimum of the large number of APFs parameters involved. This APFs design algorithm is based on the complex cepstrum commonly used in digital signal processing.

For many-segment PMD emulator, we presented in Chapter 7 a new approach of doing polarization scrambling between segments. It exploits the principle that rotation matrices are non-commutative and there are numerous possible combinations of using a few phase-plates to generate polarization controller. With this combinatorial polarization scrambler approach, we demonstrated numerically and experimentally that good PMD statistics is still achievable when we reduce the number of phase-plate by as much as an order of magnitude. This can substantially reduce the cost, the size, the complexity of building and controlling such many-segment PMD emulator.

We presented in Chapter 8 a new concept of PMD emulation where the first and second order PMD vectors are generated using 4 concatenated segments (1 variable DGD segment and 3 fixed DGD segments). The emulator is deterministically controlled to produce the probability density functions of 1st and 2nd order PMD of a real transmission cable. To control the emulator deterministically, we have solved analytically the required rotation matrices of the polarization rotators and DGD value of the variable delay line in the emulator. Through Monte Carlo simulations, we demonstrated that our emulator is, indeed, capable of generating realistic probability density functions for the 1st and 2nd order PMD. In addition, we have also studied the sensitivity of the emulator to angular inaccuracy in the polarization rotators.

In Chapter 9, we presented the architecture of a deterministic broadband PMD emulator based on a four-stage architecture. We show how to synthesize the required rotation profile of the stages for arbitrary "dial-in" spectrum of PMD vectors. By numerical simulations, we demonstrated good fidelity of this broadband PMD emulator.

In Chapter 10, we account for PDL which has often being neglected in the PMD compensation for simplicity sake. We proposed a method for compensating PDL and PMD in a feed-forward scheme. By the polar decomposition theorem, we showed that lumped PDL followed by PMD compensation at the receiver's end is feasible. Our proposed PDL compensator consists of three stages: Stage 1 and 2 are the frequency-dependent polarization rotators that align all the different PDL vectors into the $\{1,0,0\}$ direction in Stokes space. Stage 3 eliminates both the PDL magnitude and the frequency dependence in the isotropic attenuation by introducing different frequency-dependent variable attenuation to each polarization. For real-time monitoring, we use random polarization scrambling at the input end of fiber, and measure the SOP at the output of the fiber as a function of frequency. We then determine the PDL spectrum by finding the polarization states with the maximum and minimum attenuation. Using this monitored PDL spectrum, we show how to synthesize the required phase difference profiles of the three stages of the PDL compensator in order to compensate for the PDL over a certain frequency range of interest. The resultant intensity transmission after passing through the PDL compensator is polarization- and frequency- insensitive. We then apply the known Mueller transformations of the PDL compensator to the same set of monitored SOP data to deduce the composite PMD as a function of frequency. This composite PMD spectrum provides the input parameters for the subsequent broadband PMD compensator. By numerical simulations, we verified the synthesis algorithm of the required phase difference profiles and the procedure to deduce the composite PMD spectrum. We also showed that these phase difference profiles are practical and can be approximated by APFs.

Bibliography

[1] P. B. Phua and H. Haus, "Deterministic approach to pure 2nd order polarization mode dispersion," Proceeding of Optical Fiber Communication Conference 2002, Anaheim, ThGG98.

[2] P. C. Chou, J. M. Fini, and H. A. Haus, "Real-time principal state characterization for use in pmd compensators," *IEEE Photonics Technology Letters*, vol. 13, no. 4, pp. 568–570, 2001.

[3] P. C. Chou, *Optical Pulse Distortion and Manipulation Through Polarization Effects and Chromatic Dispersion.* PhD dissertation, Massachusetts Institute of Technology, Department of Electrical Engineering and Computer Science, Feb 2001.

[4] P. B. Phua, J. M. Fini, and H. A. Haus, "Real-time first and second order pmd characterization using averaged state-of-polarization of filtered signal and polarization scrambling," *IEEE/OSA Journal of Lightwave Technology*, vol. 21, no. 4, pp. 982–989, 2003.

[5] P. B. Phua, J. M. Fini, H. A. Haus, and E. P. Ippen, "New 1^{st} and 2^{nd} order pmd characterization using time-averaged state-of-polarization variation with signal's bandwidth," Proceedings of OSA Annual Meeting 2001, Long Beach CA, TuY4.

[6] P. B. Phua and H. A. Haus, "Variable differential-group-delay module without second-order pmd," *IEEE/OSA Journal of Lightwave Technology*, vol. 20, no. 9, pp. 1788–1794, 2002.

[7] P. B. Phua and H. A. Haus, “Variable differential-group-delay module without second-order pmd,” Venice Summer School on Polarization Mode Dispersion, 2002, Italy.

[8] P. B. Phua and H. A. Haus, “Deterministic approach to first and second order pmd compensation,” *IEEE Photonics Technology Letters*, vol. 14, no. 9, pp. 1270–1272, 2002.

[9] P. B. Phua and H. A. Haus, “Variable second-order pmd module without first-order pmd,” *IEEE/OSA Journal of Lightwave Technology*, vol. 20, no. 11, pp. 1951–1956, 2002.

[10] P. B. Phua, H. A. Haus, and E. P. Ippen, “All-frequency pmd compensator in feedfoward scheme,” *IEEE/OSA Journal of Lightwave Technology*, vol. 22, no. 5, pp. 1280–1289, 2004.

[11] P. B. Phua and E. P. Ippen, “Fast recursive algorithm for broadband apfs using complex cepstrums.” Submitted for publication.

[12] P. B. Phua and E. P. Ippen, “Combinatorial polarization scramblers for pmd emulator.” Submitted for publication.

[13] P. B. Phua and H. A. Haus, “A deterministically controlled four-segment polarization-mode dispersion emulator,” *IEEE/OSA Journal of Lightwave Technology*, vol. 20, no. 7, pp. 1132–1140, 2004.

[14] P. B. Phua, H. A. Haus, and E. P. Ippen, “Deterministic broad-band pmd emulator,” *IEEE Photonics Technology Letters*, vol. 16, no. 6, pp. 1486–1488, 2004.

[15] P. B. Phua and E. P. Ippen, “A deterministic broadband polarization-dependent-loss compensator.” Accepted for publication in IEEE/OSA Journal of Lightwave Technology.

[16] I. P. Kaminow and T. L. Koch, *Optical Fiber Telecommunications IIIA*. 2002. Chapter 6.

[17] J. P. Gordon and H. Kogelnik, "Pmd fundamentals : Polarization mode dispersion in optical fibers," *Proceeding of the National Academy of Science*, vol. 97, no. 9, pp. 4541–4550, 2000.

[18] L. E. Nelson and R. M. Jopson, "Introduction to polarization mode dispersion in optical systems," Venice Summer School on Polarization Mode Dispersion, 2002, Italy.

[19] C. D. Poole and R. E. Wagner, "Phenomenological approach to polarization dispersion in long single-mode fibers," *Electronics Letters*, vol. 22, pp. 1029–1030, 1986.

[20] N. Gisin and B. Huttner, "Combined effects of polarization mode dispersion and polarization dependent losses in optical fibers," *Optics Communications*, vol. 142, pp. 119–125, 1997.

[21] B. Huttner, C. Geiser, and N. Gisin, "Polarization-induced distortions in optical fiber networks with polarization-mode dispersion and polarization-dependent losses," *IEEE Journal of Selected Topics in Quantum Electronics*, vol. 6, no. 2, pp. 317–329, 2000.

[22] A. E. Willner, S. M. R. M. Nezam, L. S. Yan, Z. Q. Pan, and M. C. Hauer, "Monitoring and control of polarization-related impairments in optical fiber systems," *IEEE/OSA Journal of Lightwave Technology*, vol. 22, no. 1, pp. 106–125, 2004.

[23] E. Lichtman, "Limitations imposed by polarization-dependent gain and loss on all-optical ultralong communication systems," *IEEE/OSA Journal of Lightwave Technology*, vol. 13, no. 5, pp. 906–913, 1995.

[24] H. Bulow, "Operation of digital optical transmission system with minimal degradation due to polarization mode dispersion," *Electronics Letters*, vol. 31, no. 3, pp. 214–215, 1995.

[25] H. Bulow, "System outage probability due to first and second order pmd," *IEEE Photonics Technology Letters*, vol. 10, no. 5, pp. 696–698, 1998.

[26] H. Sunnerud, M. Karlsson, and P. A. Andrekson, "A comparison between nrz and rz data formats with respect to pmd-induced system degradation," *IEEE Photonics Technology Letters*, vol. 13, pp. 448–450, 2001.

[27] H. Sunnerud, P. A. Andrekson, and M. Karlsson, "Optimum receiver decision point in presence of pmd in fiber-optics communication systems," *IEEE Photonics Technology Letters*, vol. 15, no. 11, pp. 1651–1653, 2003.

[28] C. Vassallo, "Pmd pulse deformation," *Electronics Letters*, vol. 31, no. 18, pp. 1597–1598, 1995.

[29] H. Bulow, W. Baumert, F. M. H. Schmuck, F. K. T. Schulz, and W. Weiershausen, "Measurement of the maximum speed of pmd fluctuation in installed field fiber," Proceeding of Optical Fiber Communication Conference 1999, W 83-85.

[30] C. D. Poole, N. S.Bergano, R. E. Wagner, and H. J. Schulte, "Polarization dispersion and principal states in a 147km undersea lightwave cable," *IEEE/OSA Journal of Lightwave Technology*, vol. 6, no. 7, pp. 1185–1190, 1988.

[31] M. Karlsson, J. Brentel, and P. A. Andrekson, "Long-term measurement of pmd and polarization drift in installed fibers," *IEEE/OSA Journal of Lightwave Technology*, vol. 18, no. 7, pp. 941–951, 2000.

[32] I. T. Lima, G. Biondini, B. S. Marks, W. L. Kath, and C. R. Menyuk, "Analysis of pmd compensators with fixed dgd using importance sampling," *IEEE Photonics Technology Letters*, vol. 14, no. 5, pp. 627–629, 2002.

[33] S. L. Fogal, G. Biondini, and W. L. Kath, “Importance sampling for polarization mode dispersion,” Venice Summer School on Polarization Mode Dispersion, 2002, Italy.

[34] I. T. Lima, A. O. Lima, G. Biondini, C. R. Menyuk, and W. L. Kath, “A comparative study of single-section polarization-mode dispersion compensators,” *IEEE/OSA Journal of Lightwave Technology*, vol. 22, no. 4, pp. 1023–1032, 2004.

[35] L. S. Yan, Q.Yu, and A. E. Willner, “Demonstration of in-line monitoring and compensation of polarization-dependent loss for multiple channels,” *IEEE Photonics Technology Letters*, vol. 14, no. 6, pp. 864–866, 2002.

[36] L. S. Yan, Q.Yu, Y.Xie, and A. E. Willner, “Experimental demonstration of the system performance degradation due to the combined effect of polarization-dependent loss with polarization mode dispersion,” *IEEE Photonics Technology Letters*, vol. 14, no. 2, pp. 224–226, 2002.

[37] X. Fu, M. O’Sullivan, and J. Goodwin, “Equivalent first order lumped-elements model for networks with both pmd and pdl,” *IEEE Photonics Technology Letters*, vol. 16, no. 3, pp. 939–941, 2004.

[38] A. Yariv, *Optical Electronics in Modern Communications.* Oxford University Press, fifth ed., 1997.

[39] J. A. Kong, *Electromagnetic Wave Theory.* EMW Publishing, first ed., 2000.

[40] W. Eickhoff, Y. Yen, and R. Ulrich, “Wavelength dependence of birefringence in single-mode fiber,” *Applied Optics*, vol. 20, pp. 3428–3435, 1981.

[41] J. Sakai and T. Kimura, “Birefringence and polarization characteristics of single-mode fibers under elastic deformations,” *IEEE Journal of Quantum Electronics*, vol. 17, pp. 1041–1051, 1981.

[42] S. C. Rashleigh, "Origins and control of polarization effects in single-mode fibes," *IEEE/OSA Journal of Lightwave Technology*, vol. 1, pp. 312–331, 1983.

[43] R. Ulrich and A. Simon, "Polarization optics of twisted single-mode fibers," *Applied Optics*, vol. 18, pp. 2241–2251, 1979.

[44] W. A. Shurcliff, *Polarized Light.* Harvard University Press, first ed., 1962.

[45] D. Clarke and J. F. Grainger, *Polarized Light and Optical Measurement.* Pergamon Press, first ed., 1971.

[46] M. Martinelli and R. A. Chipman, "Polarization control for coherent systems using nematic liquid crystal," *IEEE/OSA Journal of Lightwave Technology*, vol. 8, pp. 459–465, 1990. March.

[47] M. Martinelli and R. A. Chipman, "Endless polarization control algorithm using adjustable linear retarders with fixed axes," *IEEE/OSA Journal of Lightwave Technology*, vol. 21, no. 9, pp. 2089–2096, 2003.

[48] N. G. Walker and G. R. Walker, "Polarization control for coherent communications," *IEEE/OSA Journal of Lightwave Technology*, vol. 8, no. 3, pp. 438–458, 1990.

[49] R. Noe, H. Heidrich, and D. Hoffmann, "Endless polarization control systems for coherent optics," *IEEE/OSA Journal of Lightwave Technology*, vol. 6, pp. 1199–1208, 1988.

[50] H. A. Haus, "Group velocity, energy, and polarization mode dispersion," *Journal of the Optical Society of America B*, vol. 16, no. 11, pp. 1863–1867, 1999. November.

[51] H. A. Haus and P. B. Phua, "Three representations of polarization mode dispersion," Venice Summer School on Polarization Mode Dispersion, 2002, Italy.

[52] F. Curti, B. Diano, G. D. Marchis, and F. Matera, “Statistical treatment of the evolution of the principal states of polarization in single mode fibers,” *IEEE/OSA Journal of Lightwave Technology*, vol. 8, pp. 1162–1166, 1990.

[53] C. D. Poole, J. H. Winters, and J. A. Nagel, “Dynamical equation for polarization dispersion,” *Optics Letters*, vol. 16, pp. 372–374, 1991.

[54] S.Betti, F. Curti, B. Daino, E. I. G D. Marchis, and F. Matera, “Evolution of the bandwidth of the principal states of polarization in single-mode fibers,” *Optics Letters*, vol. 16, pp. 467–469, 1991.

[55] F. Bruyere, “Impact of first and second order pmd in optical digital transmission systems,” *Optical Fiber Technology*, vol. 2, pp. 269–280, 1996.

[56] M. Karlsson and J. Brentel, “Autocorrelation function of the polarization-mode dispersion vector,” *Optics Letters*, vol. 24, no. 14, pp. 939–941, 1996.

[57] R. Jopson, L. Nelson, and H. Kogelnik, “Measurement of second order pmd vectors in optical fibers,” *IEEE Photonics Technology Letters*, vol. 11, pp. 1153–1155, 1999.

[58] M. Shtaif, A. Mecozzi, and J. Nagel, “Mean-square magnitude of all orders of pmd and the relation with the bandwidth of the principal states,” *IEEE Photonics Technology Letters*, vol. 12, pp. 53–55, 2000.

[59] G. J. Foschini and C. D. Poole, “Statistical theory of polarization dispersion in single mode fibers,” *IEEE/OSA Journal of Lightwave Technology*, vol. 9, no. 11, pp. 1439–1456, 1991.

[60] C. D. Poole and C. R. Giles, “Polarization-dependent pulse compression and broadening due to polarization dispersion in dispersion-shifted fiber,” *Optics Letters*, vol. 13, no. 2, pp. 155–157, 1988.

[61] B. L. Heffner, “Automated measurement of polarization mode dispersion using jones matrix eigenanalysis,” *IEEE Photonics Technology Letters*, vol. 4, pp. 1066–1069, 1992.

[62] D. Andresciani, F. Curti, F. Matera, and B. Daino, “Measurement of the group-delay difference between the principal states of polarization on a low-birefringence terrestrial fiber cable,” *Optics Letters*, vol. 12, pp. 844–846, 1987.

[63] G. J. Foschini, L. E. Nelson, R. M. Jopson, and H. Kogelnik, “Probability densities of second order polarization mode dispersion including polarization dependent chromatic fiber dispersion,” *IEEE Photonics Technology Letters*, vol. 12, no. 3, pp. 293–295, 2000.

[64] D. Waddy, P. Lu, L. Chen, and X. Bao, “The measurement of fast state of polarization changes in aerial fiber,” Proceeding of Optical Fiber Communication Conference 2001, Paper ThA3.

[65] J. Cameron, L. Chen, X. Bao, and J. Stears, “Time evolution of polarization mode dispersion in optical fibers,” *IEEE Photonics Technology Letters*, vol. 10, pp. 1265–1267, 1998.

[66] C. D. Poole, R. W. Tkach, A. R. Chraplyvy, and D. A. Fishman, “Fading in lightwave systems due to polarization-mode dispersion,” *IEEE Photonics Technology Letters*, vol. 3, pp. 68–70, 1991.

[67] H. Blow, “System outage probability due to first and second order pmd,” *IEEE Photonics Technology Letters*, vol. 10, pp. 696–698, 1998.

[68] L. E. Nelson, R. M. Jopson, H. Kogelnik, and G. J. Foschini, “Measurement of depolarization and scaling associated with second-order polarization mode dispersion in optical fibers,” *IEEE Photonics Technology Letters*, vol. 11, no. 12, pp. 1614–1616, 1999.

[69] H. Kogelnik, L. E. Nelson, and P. J. Winzer, “Second-order pmd outage of first-order compensated fiber systems,” *IEEE Photonics Technology Letters*, vol. 16, no. 4, pp. 1053–1055, 2004.

[70] J. Hansryd, H. Sunnerud, P. A. Andrekson, and M. Karlsson, “Impact of pmd on four-wave-mixing-induced crosstalk in wdm systems,” *IEEE Photonics Technology Letters*, vol. 12, pp. 1261–1263, 2000.

[71] R. Khosravani, Y. Xie, L. S. Yan, Y. W. Song, A. E. Willner, and C. R. Menyuk, “Limitations to first-order pmd compensation in wdm systems due to xpm-induced psp changes,” Proceeding of Optical Fiber Communication Conference 2001, Paper WAA5.

[72] B. C. Collings and L. Boivin, “Nonlinear polarization evolution induced by cross phase modulation and its impact on transmission systems,” *IEEE Photonics Technology Letters*, vol. 12, pp. 1582–1584, 2000.

[73] M. J. Li and D. A. Nolan, “Fiber spin designs for producing fibers with low polarization mode dispersion,” *Optics Letters*, vol. 23, pp. 1659–1661, 1998.

[74] A. E. Willner and M. C. Hauer, “Pmd emulation,” Venice Summer School on Polarization Mode Dispersion, 2002, Italy.

[75] Y. N. H. Taga, M. Suzuki, “Polarization mode dispersion tolerance of 10 gbit/s nrz and rz optical signals,” *Electronics Letters*, vol. 34, no. 22, pp. 2098–2100, 1998.

[76] D. Dahan and G. Eisenstein, “Numerical comparison between distributed and discrete amplification in a point-to-point 40-gb/s 40-wdm-based transmission system with three different modulation formats,” *IEEE/OSA Journal of Lightwave Technology*, vol. 20, no. 3, pp. 379–388, 2002.

[77] H. Sunnerud, J. Li, C. Xie, and P. Andrekson, “Soliton robustness to the polarization-mode dispersion in optical fibers,” *IEEE/OSA Journal of Lightwave Technology*, vol. 19, no. 10, pp. 1453–1461, 2001.

[78] H. K. C Xie and P. A. Andrekson, “Soliton robustness to the polarization-mode dispersion in optical fibers,” *IEEE Photonics Technology Letters*, vol. 12, no. 7, pp. 801–803, 2000.

[79] Y. Xie, Q. Yu, L. S. Yan, O. H. Adamczyk, Z. Pan, S. lee, and A. E. Willner, "Enhanced pmd migitation using forward error correction coding and a first order compensator," Proceeding of Optical Fiber Communication Conference 2001, Paper WAA2.

[80] K.-P. Ho and C. Lin, "Performance analysis of optical transmission system with polarization-mode dispersion and forward error correction," *IEEE Photonics Technology Letters*, vol. 9, no. 9, pp. 1288–1290, 1997.

[81] H. Sunnerud, M. Karlsson, C. Xie, and P. Andrekson, "Polarization-mode dispersion in high-speed fiber-optic transmission systems," *IEEE/OSA Journal of Lightwave Technology*, vol. 20, no. 12, pp. 2204– 2219, 2002.

[82] A. Lima, I. J. Lima, T. Adali, and C. Menyuk, "A novel polarization diversity receiver for pmd mitigation," *IEEE Photonics Technology Letters*, vol. 14, no. 4, pp. 465 – 467, 2002.

[83] B. W. Hakki, "Polarization mode dispersion compensation by phase diversity detection," *IEEE Photonics Technology Letters*, vol. 9, no. 1, pp. 121 – 123, 1997.

[84] J. Winters and M. Santoro, "Experimental equalization of polarization dispersion," *IEEE Photonics Technology Letters*, vol. 2, no. 8, pp. 591–593, 1990.

[85] H. Bullow, D. Schlump, J. weber, B. wedding, and R. Heidemann, "Electronic equalization of fiber pmd-induced distortion at 10gbit/s," Proceeding of Optical Fiber Communication Conference 1998, pp. 151-152.

[86] J. Winters and R. D. Gitlin, "Electrical signal processing techniques in long-haul fiber-optics system," *IEEE Trans. Commun.*, vol. 38, pp. 1439–1453, 1990.

[87] M. Shtaif, A. Mecozzi, M. Tur, and J. A. Nagel, "A compensator for the effects of high-order polarization mode dispersion in optical fibers," *IEEE Photonics Technology Letters*, vol. 12, no. 4, pp. 434–436, 2000.

[88] F. Heismann, D. A. Fishman, and D. L. Wilson, “Automatic compensation of first order polarization mode dispersion in 10gbit/s transmission system,” Proceeding of ECOC’98, pp. 529-530.

[89] T. Takahashi, T. Imai, and M. Aiki, “Automatic compensation technique for timewise fluctuating polarisation mode dispersion in in-line amplifier systems,” *Electronics Letters*, vol. 30, no. 4, pp. 348–349, 1994.

[90] S. Lanne, W. Idler, J. P. Thiery, and J. P. Hamaide, “Fully automatic pmd compensation at 40 gbit/s,” *Electronics Letters*, vol. 38, no. 1, pp. 40–41, 2002.

[91] J. Patscher and R. Eckhardt, “Component for second-order compensation of polarisation-mode dispersion,” *Electronics Letters*, vol. 33, no. 13, pp. 1157–1159, 1997.

[92] C. Francia, F. Bruyere, J. Thiery, and D. Penninckx, “Simple dynamic polarisation mode dispersion compensator,” *Electronics Letters*, vol. 35, no. 5, pp. 414–415, 1999.

[93] F. Buchali, S. Lanne, J. P. Thiery, W. Baumert, and H. Bulow, “Fast eye monitor for 10gbit/s and its application for optical pmd compensation,” Proceeding of Optical Fiber Communication Conference 2001, Paper TuP5.

[94] M. C. Hauer, Q. Yu, E. R. Lyons, C. H. Lin, A. A. Au, H. P. Lee, and A. E. Willner, “Compact, all-fiber pmd emulator using an integrated series of thin-film micro-heaters,” Proceeding of Optical Fiber Communication Conference 2002, Paper ThA3.

[95] R. Khosravani, I. T. Lima, P. Ebrahimi, E. Ibragimov, C. R. Menyuk, and A. E. Willner, “Time and frequency domain characteristics of polarization-mode dispersion emulators,” *IEEE Photonics Technology Letters*, vol. 13, no. 2, pp. 127–129, 2001.

[96] J. N. Damask, "A programmable polarization mode-dispersion emulator for systematic testing of 10gb/s pmd compensators," Proceeding of Optical Fiber Communication Conference 2000, Paper ThB3.

[97] M. G. Taylor, "Observation of new polarization dependence effect in long haul optically amplified system," *IEEE Photonics Technology Letters*, vol. 5, pp. 1244–1246, 1993.

[98] D. Q. Chowdhury and L. Bhagavatula, "Polarization dependent loss induced gain ripple statistics in erbium-doped fiber amplifiers," *IEEE Photonics Technology Letters*, vol. 13, no. 12, pp. 1301–1303, 2001.

[99] N. Y. Kim, D. Lee, H. Yoon, J. Park, and N. Park, "Limitation of pmd compensation due to polarization-dependent loss in high-speed optical transmission links," *IEEE Photonics Technology Letters*, vol. 14, no. 1, pp. 104–106, 2002.

[100] F. Bruyere, O. Audouin, V. Letellier, G. Bassier, and P. Marmier, "Demonstration of an optimal polarization scrambling for long-haul optical amplifier systems," *IEEE Photonics Technology Letters*, vol. 6, pp. 1156–1158, 1994.

[101] M. G. Taylor, "Improvement in q with low frequency polarization modulation on transoceanic edfa link," *IEEE Photonics Technology Letters*, vol. 6, pp. 860–862, 1994.

[102] L. S. Yan, Q. Yu, J. E. McGeehan, and A. E. Willner, "Deleterious system effects due to low-frequency polarization scrambling in the presence of nonnegligible polarization-dependent loss," *IEEE Photonics Technology Letters*, vol. 15, pp. 464–466, 2003.

[103] H. Pua, K. Peddanarapp, B. Zhu, C. Allen, K. Demarest, and R. Hui, "An adaptive first-order polarization mode dispersion compensation system aided by polarization scrambling: Theory and demonstration," *IEEE/OSA Journal of Lightwave Technology*, vol. 8, pp. 832–841, 2000.

[104] H. Rosenfeldt, R. Ulrich, E. Brinkmeyer, U. Feiste, C. Schubert, J. Berger, R. Ludwig, H. Weber, and A. Ehrhardt, “Feedforward approach for automatic pmd compensation at 80gbit/s over 45km installed single mode fiber,” Proc. European Conference on Optical Communication 2001, pp. 68.

[105] L. Moller and L. Buhl, “Spectral resolved pmd vector monitoring using a scanning fabry-perot filter and a polarimeter,” LEOS Society 2000 Annual Meeting,Vol. 1, p220-221.

[106] I. Roudas, G. Piech, M. Mlejnek, Y. Zhu, and D. Q. Chowdhury, “Coherent heterodyne frequency-selective polarimeter for error signal generation in higher-order pmd compensators,” Optical Fiber Communication Conference 2002, Anaheim, Paper WQ2, p299-301.

[107] S. M. Nezam, L. S. Yan, Y. Q. Shi, A. E. Willner, and S. Yao, “Wide dynamic range dgd monitoring by partial optical signal spectrum dop measurement,” Optical Fiber Communication Conference 2002 Postdeadline Papers, Anaheim, Paper FD8.

[108] X. Wang and A. M. Weiner, “Fast multi-wavelength polarimeter for polarization mode dispersion compensation systems,” 2003 Digest of the LEOS Summer Topical Meetings, 14-16 July 2003, p163 - 164.

[109] C. K. Madsen and P. Oswald, “Optical filter architecture for approximating any 2×2 unitary matrix,” *Optics Letters*, vol. 28, no. 7, pp. 534–536, 2003.

[110] L. Moller and H. Kogelnik, “Pmd emulator restricted to first and second order pmd generation,” ECOC’99, Vol.2, Sept. 1999, pg 64 - 65.

[111] Q. Yu, L. S. Yan, Y. Xie, M. Hauer, and A. E. Willner, “Higher order polarization mode dispersion compensation using a fixed time delay followed by a variable time delay,” *IEEE Photonics Technology Letters*, vol. 13, no. 8, pp. 863–865, 2001.

[112] L. S. Yan, C. Yeh, G. Yang, L. Lin, Z. Chen, Y. Q. Shi, and X. S. Yao, "Fast digitally variable differential group delay module using polarization switching," Optical Fiber Communication Conference 2002, Anaheim, Postdeadline Paper FA5-1.

[113] C. Pu, L. Y. Lin, E. L. Goldstein, N. J. Frigo, and R. W. Tkach, "Micromachined integrated optical polarization-state rotator," *IEEE Photonics Technology Letters*, vol. 12, no. 10, pp. 1358–1360, 2000.

[114] T. Merker, A. Schwarzbeck, and P. Meissner, "Pmd compensation up to second order by tracking the principle states of polarization using a two-section compensator," *Optics Communications*, vol. 198, pp. 41–47, 2001.

[115] A.Eyal and A.Yariv, "Design of broad-band pmd compensation filters," *IEEE Photonics Technology Letters*, vol. 14, no. 8, pp. 1088–1090, 2000.

[116] L. Moller, "Filter synthesis for broad-band pmd compensation in wdm systems," *IEEE Photonics Technology Letters*, vol. 12, no. 9, pp. 1258–1260, 2000.

[117] H. Kogelnik, L. E. Nelson, and J. P. Gordon, "Emulation and inversion of polarization-mode dispersion," *IEEE/OSA Journal of Lightwave Technology*, vol. 21, no. 2, pp. 482–495, 2003.

[118] G. P. Agrawal, *Fiber-Optics Communication System 2*. New York:Wiley, 2002.

[119] A. Weiner, "Pulse shaping using lcd light modulators," *IEEE Journal of Quantum Electronics*, vol. 28, p. 908, 1992.

[120] E. Zeek, K. Maginnis, S. Backus, U. Russek, M. Murnane, G. Mourou, H. Kapteyn, and G. Vdovin, "Pulse compression by use of deformable mirrors," *Optics Letters*, vol. 24, pp. 493–495, 1999.

[121] C. Madsen, "Integrated waveguide allpass filter tunable dispersion compensators," Optical Fiber Communication Conference 2002, Anaheim, Paper TuT1.

[122] C. K. Madsen, G. Lenz, A. J. Bruce, M. A. Capuzzo, L. T. Gomez, and R. E. Scotti, “Integrated all-pass filters for tunable dispersion and dispersion slope compensation,” *IEEE Photonics Technology Letters*, vol. 11, no. 12, pp. 1623–1625, 1999.

[123] C. Madsen and J. Zhao, *Optical Filter Design and Analysis: A Signal Processing Approach.* New York:Wiley, 1999.

[124] A. Oppenheim and R. W. Schafer, *Discrete-Time Signal Processing.* Prentice Hall, 1989.

[125] C. K. Madsen, J. A. Walker, J. E. Ford, K. W. Goossen, T. N. Nielsen, and G. Lenz, “A tunable dispersion compensating mems all-pass filter,” *IEEE Photonics Technology Letters*, vol. 12, no. 6, pp. 651–653, 2000.

[126] M. R. Watts and H. A. Haus, “Integrated mode-evolution-based polarization rotators.” To be published in Optics Letters.

[127] G. R. Reddy and M. N. S. Swamy, “Digital all-pass filter design through discrete hilbert transform,” Proc. IEEE Int. Conf. Acoustics, Speech Signal Processing, 1990, p646-649.

[128] K. Rajamani and Y. S. Lai, “A novel method for designing allpass digital filters,” *IEEE Signal Processing Letters*, vol. 6, no. 8, pp. 207–209, 1999.

[129] G. J. Dolecek and J. D. Carmona, “Digital all-pass filter design method based on complex cepstrums,” *Electronics Letters*, vol. 39, no. 8, pp. 695–697, 2003.

[130] B. P. Bogert, M. J. R. Healy, and J. W. Tukey, “The quefrency analysis of time series for echoes: Cepstrum, pseudoautocovariance, cross-cepstrum, and saphe cracking,” Proc. Symposium Time Series Analysis, M. Rosenblatt, Ed., John Wiley and Sons, New York, p209-243, 1963.

[131] T. Barwicz, M. A. Popovi, P. T. Rakich, M. R. Watts, H. A. Haus, E. P. Ippen, and H. Smith, “Microring-resonator-based add-drop filters in sin: fabrication and analysis,” *Optics Express*, vol. 12, no. 7, pp. 1437–1442, 2004.

[132] M. C. Hauer, Q. Yu, E. R. Lyons, C. H. Lin, A. A. Au, H. P. Lee, and A. E. Willner, "Electrically controllable all-fiber pmd emulator using a compact array of thin film microheaters," *IEEE/OSA Journal of Lightwave Technology*, vol. 22, pp. 1059–1065, 2004.

[133] R. Noe, D. Sandel, M. Y. Dierolf, S. Hinz, V. Mirvoda, A. Schopflin, C. Glingener, E. Gottwald, C. Scheerer, G. Fischer, T. Weyrauch, and W. Haase, "Polarization mode dispersion compensation at 10, 20 and 40 gbit/s with various optical equalizers," *IEEE/OSA Journal of Lightwave Technology*, vol. 17, no. 9, pp. 1602–16016, 1999.

[134] D. S. Waddy, L. Chen, and X. Bao, "A dynamical polarization mode dispersion emulator," *IEEE Photonics Technology Letters*, vol. 15, no. 4, pp. 534–536, 2003.

[135] M. Karlsson, "Probability density functions of the differential group delay in optical fiber communication systems," *IEEE/OSA Journal of Lightwave Technology*, vol. 19, no. 3, p. 324, 2000.

[136] A. Djupsjobacka, "On differential group-delay statistics for polarization-mode dispersion emulators," *IEEE/OSA Journal of Lightwave Technology*, vol. 19, no. 2, p. 285, 2001.

[137] G. Fano, *Mathematical Methods of Quantum Mechanics.* McGraw-Hill Book Company.

[138] C. K. Madsen, "Efficient architectures for exactly realizing optical filters with optimum bandpass designs," *IEEE Photonics Technology Letters*, vol. 10, pp. 1136–1138, 1998.